MIXING IN GAS PHASE TURBULENT JETS

Thesis by

David Russell Dowling

In Partial Fulfillment

of the Requirements for the Degree of

Doctor of Philosophy

California Institute of Technology

Pasadena California

1988

(Submitted April 1, 1988)

ACKNOWLEDGEMENTS

Many people provided support, encouragement, and ideas from the time that the design of the experiment was begun to the point at which the final corrections were made in this manuscript. The leading contributor was my advisor, Professor Paul Dimotakis, who provided many creative suggestions and was a constant source of motivation. Dr. J. E. Broadwell and Professor E. Zukoski also contributed good ideas which led to fruitful discussions and important experimental design changes.

I am thankful for the help received from the postdoctoral fellows and the other graduate students in the Aeronautics Department. The most important among these was Dr. Daniel B. Lang, whose understanding and capabilities in linear and digital electronics appear to be almost magical. Special mention is also deserved by Dr. Godfrey Mungal, Dr. Werner Dahm, Dr. John Torczynski, Dr. Thomas Roesgren, Dr. Manooch Koochesfahani, Cliff Frieler, and Dr. Richard Miake-Lye, all of whom contributed to my understanding of fluid mechanics, experimental engineering and design, and laser and computer technology.

Additionally, I would like to acknowledge the personal financial support of the W. F. Marlar Fellowship and the A.R.C.S. Fellowship. This research was jointly supported by the Gas Research Institute through grant no. 5083-260-0878, and by the Air Force Office of

Scientific Research through grant no. 83-0213.

On a more personal level, I must recognize the contribution of my wife, Catherine, whose devotion and patience were essential in all phases of this effort. And finally, I want to thank the good Lord for providing the challenge of curiosity and the strength to persevere through the completion of my graduate studies.

ABSTRACT

This work is an experimental investigation of the mixing of the nozzle fluid of a round, turbulent jet with the entrained reservoir fluid, using laser-Rayleigh scattering methods. The measurements, at Reynolds numbers of 5,000 and 16,000, cover the axial range from 20 to 90 jet exit diameters and resolve the full range of temporal and spatial concentration scales. The measured mean and rms values of the concentration, and the mean scalar dissipation rate, when estimated from the time derivative of concentration, are consistent with jet similarity laws. Concentration fluctuation power spectra are found to be self-similar along rays emanating from the virtual origin of the jet, and are consistent with the universal form of scalar spectra proposed by Gibson (1968 II). The probability density functions for the concentration, the time derivative of concentration, and the square of the time derivative of concentration, are compiled and are also found to be self-similar along rays. Features of the measured distributions and spectra are consistent with the existence of large-scale structures within the flow that span the local diameter of the jet's turbulent cone. On the centerline of the jet, the scaled probability density function of jet gas concentration is found to be almost independent of the Reynolds number while the local mixing rate in the inner part of jet is not. The usual assumptions concerning isotropy and correlation of derivatives are found to lead to erroneous results for the probability density function of the scalar dissipation rate.

TABLE OF CONTENTS

Page

Copyright....ii

Acknowledgements....iii

Abstract....v

Table of Contents....vi

List of Figures....x

List of Tables....xviii

List of Variables and Symbols....xix

1.0 INTRODUCTION....1

1.1 Background....1

1.2 Present Experiments....5

2.0 EXPERIMENTAL FACILITY....8

2.1 The Main Apparatus....8

2.2 The Jet Gas Delivery System....11

2.3 The Coflow Delivery System....15

2.4 The Exhaust System....16

2.5 The Laser-Rayleigh Scattering Diagnostic....18

2.6 The Laser System....19

2.7 The Collection Optics and Photosensor....20

2.8 Processing Electronics....23

2.9 Procedures and Parameter Selection....25

3.0 BASIC PROPERTIES OF THE CONCENTRATION FIELD OF THE JET.....28

3.1 The Mean Jet Fluid Concentration Field.....28

3.2 The Root Mean Square Concentration Fluctuation Level.....34

3.3 Shadowgraph Flow Visualization.....41

4.0 POWER SPECTRA OF CONCENTRATION FLUCTUATIONS.....46

4.1 Normalization and Scaling of Power Spectra.....46

4.2 The Measured Spectra at Reynolds Number 5,000 and 16,000...48

4.3 Comparison of Scalar Power Spectra with Jet Scaling.....57

4.4 Comparison of Scalar Power Spectra with Universal Scaling..62

5.0 PROBABILITY DENSITY FUNCTION OF CONCENTRATION.....66

5.1 Results at Reynolds number 5,000 and 16,000.....67

5.2 Reynolds Number and Schmidt Number Comparisons.....73

5.3 The Structure of the Probability Density Function.....75

5.4 Implications for Turbulent Jet Mixing.....82

6.0 THE TIME DERIVATIVE OF CONCENTRATION.....88

6.1 Results at Reynolds Number 5,000 and 16,000.....89

6.2 Comparisons and Comments.....96

7.0 THE ESTIMATED SCALAR DISSIPATION RATE.....99

7.1 The Mean Estimated Scalar Dissipation Rate.....103

7.2 The Instantaneous Value of $(dC/dt)^2$.....107

7.3 Power Spectra of ε_c.....111

7.4 The Probability Density Function of $\log\left[(dC/dt)^2\right]$.....119

7.5 The Correlation of C(t) and $(dC/dt)^2$.....142

8.0 CONCLUSIONS AND DISCUSSION.....145

APPENDICES

A.0 EXPERIMENTAL DESIGN AND PARAMETER SELECTION.....155

A.1 Resolution.....156

A.2 Spatial Range and Similarity.....161

A.3 Reynolds Number.....161

A.4 Run Time.....163

A.5 Momentum and Buoyancy.....165

A.6 Momentum and Coflow.....167

A.7 Signal-to-Noise Ratio.....168

A.8 Laboratory.....169

A.9 The Jet Nozzles.....171

A.10 Experimental Parameters.....174

B.0 PERFORMANCE PREDICTION AND MEASUREMENT.....177

B.1 Relating Current, Concentration, and the RSNR.....178

B.2 The Dynamic Range of the Jet.....180

B.3 The Intensity of Rayleigh Scattered Light.....181

B.4 The Two light Sensing Systems.....183

B.4.1 The Photodiode System.....184

B.4.2 The Photomultiplier Tube System.....188

B.4.3 Measurements and Comparisons.....189

C.0 COMPUTATION OF POWER SPECTRA.....197

C.1 High Frequency Spectral Estimation.....198

C.2 Low Frequency Spectral Estimation.....201

C.3 Comments.....204

D.0 THE COFLOW TEMPERATURE CONTROL SYSTEM.....206

E.0 DATA ACQUISITION SYSTEM AND PROCESSING TECHNIQUES.....211

E.1 The First Stage Electronics.....211

E.2 Analog Processing.....213

E.3 Digital Processing.....213

E.3.1 Analog-to-Digital Converter Corrections.....214

E.3.2 Conversion to Mass-Weighted Concentration.....215

E.3.3 The Removal of the Effects of Particles.....216

E.4 Statistical Processing.....219

F.0 A MOMENTUM-INTEGRAL ANALYSIS OF THE FREE-JET MEAN VELOCITY FIELD.....224

REFERENCES.....235

LIST OF FIGURES

Figure	Title	Page
1-1	Experimental jet flow coordinates	3
2-1	Schematic of jet flow facility	8
2-2	Photograph of jet flow facility	9
2-3	Mechanical setup of the nozzle	14
2-4	Reduced blueprints of the exhaust system	17
2-5	Diagram of collection optics and photosensor	22
2-6	Analog signal processing	24
3-1	Mean concentration profile at Re_0 = 5,000	29
3-2	Mean concentration profile at Re_0 = 16,000	30
3-3	Comparison of the fitted mean profile with the results of other experiments	31
3-4	Comparison of the scaled mean centerline concentration with the results of other experiments	33
3-5	Root mean square concentration fluctuation level plotted with the same axis scaling that collapses $\overline{C}$, at Re_0 = 5,000	35
3-6	Root mean square concentration fluctuation level plotted with the same axis scaling that collapses $\overline{C}$, at Re_0 = 16,000	36
3-7	Comparison of the centerline rms concentration fluctuation level, divided by the mean centerline concentration, with the results of other experiments	37

3-8 Comparison of the rms concentration fluctuation level, divided by its centerline value, with the results of other experiments 38

3-9 Schematic of the shadowgraph setup 42

3-10 Shadowgraph picture of the jet at Re_0 = 5,000 for $0 \leq x/d \leq 40$ 44

3-11 Shadowgraph picture of the jet at Re_0 = 16,000 for $0 \leq x/d \leq 100$ 45

4-1 Scaled power spectra of the concentration fluctuations on the jet centerline at Re_0 = 5,000 48

4-2 Scaled power spectra of the concentration fluctuations at 3.4^0 off the jet centerline at Re_0 = 5,000 49

4-3 Scaled power spectra of the concentration fluctuations at 7^0 off the jet centerline at Re_0 = 5,000 50

4-4 Scaled power spectra of the concentration fluctuations on the jet centerline at Re_0 = 16,000 54

4-5 Scaled power spectra of the concentration fluctuations at 3.4^0 off the jet centerline at Re_0 = 16,000 54

4-6 Scaled power spectra of the concentration fluctuations at 6.3^0 off the jet centerline at Re_0 = 16,000 56

4-7 Comparison of the centerline concentration fluctuation power spectra to the results of other experiments with jet parameter scaling of the axes 58

4-8 Comparison of concentration fluctuation spectra from $\sim 7^0$ off the centerline to the results of Lockwood and Moneib

(1980) with jet parameter scaling of the axes 59

4-9 Comparison of centerline concentration fluctuation power spectra to the results of Clay (1973) with universal Kolmogorov coordinate scaling of the axes 63

5-1 Probability density function of the scaled concentration on the jet centerline at Re_0 = 5,000 67

5-2 Probability density function of the scaled concentration 3.4^0 off the jet centerline at Re_0 = 5,000 68

5-3 Probability density function of the scaled concentration 7^0 off the jet centerline at Re_0 = 5,000 69

5-4 Probability density function of the scaled concentration on the jet centerline at Re_0 = 16,000 70

5-5 Probability density function of the scaled concentration 3.4^0 off the jet centerline at Re_0 = 16,000 71

5-6 Probability density function of the scaled concentration 6.3^0 to 7^0 off the jet centerline at Re_0 = 16,000 72

5-7 Averaged and smoothed probability density functions of the scaled concentration on centerline of the jet at Re_0 = 5,000 and 16,000 73

5-8 Time traces of C(t) and accumulated PDFs at Re_0 = 5,000 on the jet centerline with about .25 τ_D per line 76

5-9 Time traces of C(t) and accumulated PDFs at Re_0 = 5,000 on the jet centerline with about 1 τ_D per line 77

5-10 Time traces of C(t) and accumulated PDFs at Re_0 = 5,000 on the jet centerline with about 4 τ_D per line 78

5-11 Time traces of C(t) and accumulated PDFs at Re_0 = 16,000 on the jet centerline with about .25 τ_D per line 79

5-12 Time traces of C(t) and accumulated PDFs at Re_0 = 16,000 on the jet centerline with about 1 τ_D per line 80

5-13 Time traces of C(t) and accumulated PDFs at Re_0 = 16,000 on the jet centerline with about 4 τ_D per line 81

5-14 Comparison of flame lengths reported by Dahm et al. (1984) with those estimated from the measured PDFs of this study 85

6-1 Probability density function of the scaled time derivative of concentration on the jet centerline at Re_0 = 5,000 90

6-2 Probability density function of the scaled time derivative of concentration 3.4° off the jet centerline at Re_0 = 5,000 91

6-3 Probability density function of the scaled time derivative of concentration 7° off the jet centerline at Re_0 = 5,000 92

6-4 Probability density function of the scaled time derivative of concentration on the centerline of the jet at Re_0 = 16,000 93

6-5 Probability density function of the scaled time derivative of concentration 3.4° off the jet centerline at Re_0 = 16,000 94

6-6 Probability density function of the scaled time derivative of concentration 6.3° off the jet centerline at

Re_0 = 16,000 95

6-7 Time traces of C(t) 3.4° off the jet centerline at Re_0 = 5,000 97

6-8 Time traces of C(t) 3.4° off the jet centerline at Re_0 = 16,000 98

7-1 The scaled mean value of ε_c verses $r/(x - x_0)$ 104

7-2 Time traces of C(t) and $\varepsilon_c(t)$ on the jet centerline at Re_0 = 5,000 107

7-3 Time traces of C(t) and $\varepsilon_c(t)$ on the jet centerline at Re_0 = 16,000 108

7-4 Distribution of time intervals between peaks of $(dC/dt)^2$ 109

7-5 Power spectra of ε_c on the jet centerline at Re_0 = 5,000 111

7-6 Power spectra of ε_c 3.4° off centerline at Re_0 = 5,000 112

7-7 Power spectra of ε_c 7° off centerline at Re_0 = 5,000 113

7-8 Power spectra of ε_c on the jet centerline at Re_0 = 16,000 114

7-9 Power spectra of ε_c 3.4° off centerline at Re_0 = 16,000 115

7-10 Power spectra of ε_c 6.3° to 7° off the centerline at Re_0 = 16,000 116

7-11 Probability density function of the logarithm of the scaled value of $(dC/dt)^2$ on the jet centerline at Re_0 = 5,000 120

7-12 Probability density function of the logarithm of the scaled value of $(dC/dt)^2$ 3.4° off the jet centerline

at Re_0 = 5,000 121

7-13 Probability density function of the logarithm of the scaled value of $(dC/dt)^2$ 7° off the jet centerline at Re_0 = 5,000 122

7-14 Probability density function of the logarithm of the scaled value of $(dC/dt)^2$ on the jet centerline at Re_0 = 16,000 123

7-15 Probability density function of the logarithm of the scaled value of $(dC/dt)^2$ 3.4° off the jet centerline at Re_0 = 16,000 124

7-16 Probability density function of the logarithm of the scaled value of $(dC/dt)^2$ 6.3° to 7° off the centerline at Re_0 = 16,000 125

7-17 Logarithm of the probability density function of the logarithm of the scaled value of $(dC/dt)^2$ on the centerline at Re_0 = 5,000 128

7-18 Logarithm of the probability density function of the logarithm of the scaled value of $(dC/dt)^2$ on the centerline at Re_0 = 16,000 129

7-19 Probability density functions of the logarithm of Σ_3 for $\frac{1}{3} \leq \omega_1 \leq 1$ 134

7-20 Probability density functions of the logarithm of Σ_3 for $0 \leq \omega_1 \leq \frac{1}{3}$ 135

7-21 Logarithm of the probability density functions of the logarithm of Σ_3 for $\frac{1}{3} \leq \omega_1 \leq 1$ 136

7-22 Logarithm of the probability density functions of the logarithm of Σ_3 for $0 \leq \omega_1 \leq 1/3$ 137

7-23 Reynolds number comparison of the probability density function of the logarithm of Σ_3 at $\omega_1 = 1$ 139

7-24 Reynolds number comparison of the probability density function of the logarithm of Σ_3 at $\omega_1 = 1/3$ 140

7-25 Reynolds number comparison of the probability density function of the logarithm of Σ_3 at $\omega_1 = 0$ 141

7-26 Contour plot of the joint PDF of $C/\overline{C}$ and the logarithm of the scaled value of $(dC/dt)^2$ on the jet centerline at $Re_0 = 16,000$ 142

7-27 Contour plot of the joint PDF of $C/\overline{C}$ and the logarithm of the scaled value of $(dC/dt)^2$ 7° off the centerline of the jet at $Re_0 = 16,000$ 144

8-1 Comparison of the reported probability density functions of the scaled concentration for the centerline of the jet 151

8-2 Comparison of the reported probability density functions of concentration for the centerline of the jet with the concentration axis scaled by $\overline{C}$ 152

A-1 Schematic of the collection lens testing setup 160

A-2 Results of the design analysis for the 0.30" nozzle 172

B-1 Linearity of the photodetectors 190

B-2 Comparison of the measured and predicted rms noise current from the photodiode system 191

B-3 Comparison of the measured and predicted signal to noise ratio for the photomultiplier tube system 192

B-4 Comparison of the expected RSNR from the two photodetection systems for both of the chosen gas pairs. 193

B-5 Comparison of the noise power spectra from the photomultiplier tube system, and the 1^{st} and 2^{nd} photodiode systems 195

C-1 Flow chart for the high frequency portion of the spectral estimation software 201

C-2 Flow chart for the low frequency portion of the spectral estimation software 204

D-1 Schematic of the coflow temperature control system 209

E-1 Frequency response of both photodiode systems 212

E-2 The effects of dust removal and optimal filtering on the instantaneous concentration signal 218

E-3 A typical optimal filter kernel in the time domain. ($\Delta t/\tau_D = 3.47 \times 10^{-4}$) 220

E-4 The effects on the optimally filtered concentration of taking the time derivative, squaring the time derivative, and taking the logarithm of the square of the time derivative 222

LIST OF TABLES

Table	Title	Page
3-1	Turbulent Jet Mixing Experiments	32
5-1	Values of $\overline{C}_m/\overline{C}$	83
A-1	Parameter Summary at Re_0 = 5,000	175
A-2	Parameter Summary at Re_0 = 16,000	176

LIST OF VARIABLES AND SYMBOLS

English Alphabet

a_0, a_1, a_2	parameters in a log-normal distribution
A	total available Rayleigh scattering extinction coefficient
A_0	exit area of the jet nozzle
B	buoyancy flux
C, C(t)	instantaneous mass-weighted concentration of jet gas (mass fraction)
$\overline{C}_m$	mean concentration of the mixed fluid in the jet
C_n	instantaneous mole fraction of jet gas (molecular number-weighted concentration)
C'_{rms}	root mean square concentration fluctuation level
$\overline{C'^2}$	mean square concentration level ($= C'^2_{rms}$)
$\overline{C}(\chi,\eta), \overline{C}$	local mean value of jet gas concentration
c_0 to c_6	coefficients in the polynominal for $r_i(z)$
c_p	specific heat of the coflow gas
C_0	jet exit concentration (usually assumed to be equal to one but is explicitly included in Chapter 1 and 8)
$\overline{C}_{cl}$	mean centerline concentration of jet gas
C_{max}	local maximum concentration of jet gas
C_t	total input capacitance of transimpedance amplifier
d	geometrical jet nozzle exit diameter
d^*	momentum diameter of the jet nozzle
$D_{j\infty}$	diffusivity of jet gas into reservoir gas

$D(x)$	diameter of the jet's turbulent cone
e_a	amplifier equivalent noise voltage (volts/$\sqrt{Hz}$)
$E_c(f)$	concentration-fluctuation power spectrum
$E_{\varepsilon_c}(f)$	power spectrum of $\varepsilon_c(t)$
E_ζ	power spectrum of $\zeta(t)$
E_{ph}	photon energy
f	frequency (Hertz)
f_e	estimated passage frequency of Δy, $f_e = \bar{U}_{cl}/\Delta y$
f_o	knee frequency of the electronic filtering
g	mean concentration profile function, acceleration of gravity
G	Görtler parameter for a curved boundary layer
G_h	gain of the coflow, temperature-control, heating system
G_{PMT}	gain of the photomultiplier tube
i	counting or summing index
i_a	amplifier noise current (ampere/$\sqrt{Hz}$)
i_n	noise current (ampere/$\sqrt{Hz}$)
I_L	leakage current
I_r	residual current
I_S	signal current
J_c	conserved momentum flux in a coflowing jet
J_o	nozzle exit momentum flux
J_∞	jet momentum flux transmitted to the far field
k	wave number, $2\pi f/U_{cl}$ or $2\pi E_{ph}/(\text{Planck's constant} \cdot \text{speed of light})$
k_K	dimensionless wave number, $k \cdot \lambda_K$

k_B	Boltzmann's constant
L_b	buoyancy length scale
m	$\frac{\partial I}{\partial C}$, slope of the detector's concentration-current characteristic
$\dot{m}$	mass flow rate of the coflow gas
$\dot{m}(R)$	mass flux in the jet a distance R from its origin
$\dot{m}_0$	jet exit mass flux
M_w	molecular weight
n	index of refraction
N	# density of molecules, # of measurements in a data set
N_w	normalization of the window function
p	pressure
P_L	laser output power (watts)
P(y)	local power in the laser beam
Pr	Prandtl number, ν_∞/(thermal difusivity)
q_e	charge of an electron (coulombs)
$\dot{Q}$	rate of heat input to the coflow gas
Q_0	exit volume flux of the jet
Q_v	volume flux in the jet
r	radial distance in cylindrical coordinates, Appendix F only: radial distance in spherical coordinates
r_e	exit radius of the jet nozzle
$r_i(z)$	inner radius of the jet nozzle contour
r_0	entrance radius of the jet nozzle
r_u	U_0/U_c

R	radius of spherical control volume
Re_0	jet exit Reynolds number $(U_0 d/\nu_\infty)$
Re_θ	Reynolds number of the boundary layer on the inside of the nozzle based on its momentum thickness
R_h	electrical resistance of the coflow heater
R_L	load resistor of the transimpedance amplifier
RSNR	relative signal-to-noise ratio
s	exponent of $\Phi_1(\xi)$ near $\xi = 0$, $\Phi_1(\xi) = \Phi_o \xi^s$ as $\xi \to 0$
S	surface of the control volume V
S_0	$\frac{d^2C}{dt^2}$ near $dC/dt = 0$
Sc	molecular Schmidt number, $(\nu_\infty/D_{j\infty})$
SE	*Scalar energy*, $\int_V \rho_\infty C^2 \, dV$
SNR	signal-to-noise ratio
t	time
Δt	time between samples, (A/D conversion rate)$^{-1}$
t_0	a time when dC/dt equal zero
t_1	transmissivity of one coated glass interface
T	temperature (degrees Kelvin)
ΔT_p	preset temperature rise for the coflow heating system
T_{ref}	temperature of the thermocouple reference junction
$\underline{u}$	vector velocity
$\underline{u}'$	fluctuating vector velocity
$\underline{U}$	mean vector velocity
U_c	coflow velocity
$\overline{U}_{cl}$	centerline velocity for density matched jets taken

from Chen and Rodi (1980), $\bar{U}_{cl} = 6.2U_0 d/(x - x_0)$

U_j	jet nozzle exit velocity profile
U_m	mean axial velocity in the nozzle contraction
U_o	jet exit velocity for a "top-hat" profile
$\bar{U}_x$	mean axial component of velocity in cylindrical coordinates
U_θ	mean polar angle velocity in spherical coordinates
U_r	mean radial velocity in spherical coordinates
V	a fixed control volume, a spherical control volume
$\dot{V}_c$	"volume flux" of the conserved scalar
V_h	voltage across the resistive heater
V_{sp}	set point voltage for the coflow heating system
V_{tc}	thermocouple voltage
w	1/e width of the laser beam
W(i)	window function
x	axial distance from nozzle exit in cylindrical coordinates
x_o	virtual origin of the jet
Δy	length of laser beam imaged onto the photodiode
y	distance along the path of the laser beam
z	distance along the nozzle axis from the start of the nozzle contraction
z_e	length of the jet nozzle contraction

Greek Alphabet

α	Rayleigh scattering extinction coefficient

α_j, α_∞ extinction coefficients of jet and reservoir gases

β efficiency of the focal volume

γ polarization recovery factor

$\Gamma(k)$ Scalar-fluctuation, power spectrum with wave number as the independent variable

$\Gamma_K(k)$ Universal, scalar-fluctuation, power spectrum, $\Gamma_K(k) = \Gamma(k)/\Sigma_K^2 \cdot \lambda_K$

$\delta(\ )$ small change in ( )

$\varepsilon(t)$ error signal of the coflow temperature controller

ε_c estimated scalar dissipation rate, $6D_{j\infty}\left(\frac{\dot{C}(t)}{\bar{U}_{cl}}\right)^2$

$\bar{\varepsilon}$ mean energy dissipation rate from Friehe et al. (1971)

ζ true scalar dissipation rate, $2D_{j\infty}|\nabla C|^2$, transmissivity of the photodetector window

η $r/(x - x_0)$, normalized radial coordinate

η_d, η_t quantum efficiencies of the photodiode and photomultiplier tube

θ polar angle in spherical coordinates (Appendix F), momentum thickness of the nozzle boundary layer (Appendix A)

θ_j half-angle of the jet's turbulent cone

Θ_c momentum thickness for a coflowing jet

κ mean concentration decay constant

κ_ε mean centerline decay constant for $\bar{\varepsilon}_c$

λ_K Kolmogorov length scale, $\left(\frac{\nu_\infty^3}{\bar{\varepsilon}}\right)^{1/4}$

λ_B Batchelor length scale, $\lambda_K/\sqrt{Sc}$

μ Universal parameter for the power law of $E_\zeta(k)$

$\Delta\nu$	bandwidth (Hertz)
ν_∞	kinematic viscosity of the reservoir gas
ξ	random variable, $0 < \xi < \infty$
π	3.1415926 . . .
$\rho_0, \rho_1(t)$	density of measurement points with respect to time
ρ_2	density of measurement points with respect to $(dC/dt)^2$
ρ_j, ρ_∞	densities of the jet and reservoir gases
$\Delta\rho$	$\rho_j - \rho_\infty$
σ	thermocouple sensitivity (40 μmVolt/K)
Σ_3	weighted sum of derivatives, $\sum_{i=1}^{3} \omega_i (dC/dt)_i^2$
Σ_K	Kolmogorov scalar scale, $\left(\bar{\varepsilon}_c \sqrt{\nu_\infty / \bar{\varepsilon}}\right)^{1/2}$
τ	time constant of the coflow temperature-control system
τ_K	passage time for a Kolmogorov length scale
τ_D	large scale time of the jet, $D(x)/\bar{U}_{cl}$
υ	width parameter for a Gaussian kernel
Υ	half of the total time over which data are collected
ϕ	pressure ratio ($\phi = 1$ implies atmospheric conditions)
Φ_o	a real constant
Φ_1	probability density of ξ
Φ_2	probability density of $\log\xi$
χ	$(x - x_0)/d^*$, normalized downstream coordinate
Ψ	number of beam passes through the focal volume
ω	temporal radian frequency, $2\pi f$ or $2\pi\Delta\nu$
ω_i	weighting coefficients in Σ_3, $\sum_{i=1}^{3} \omega_i = 1$
Ω	solid angle subtended by the collection optics

Other Symbols

$\overline{(\ )}$	mean value of ( )
$\dot{(\ )}$	time derivative of ( )
$(\ )'$	fluctuating part of ( ), dummy integration variable for ( )
PDF( )	probability density function of ( )
log( )	natural logarithm of ( )
$\log_{10}(\ )$	base ten logarithm of ( )
CDF( )	cumulative distribution function of ( )

CHAPTER 1

INTRODUCTION

1.1 Background

The momentum-driven, free turbulent jet, a small source of high speed fluid issuing into a large, quiescent reservoir, is one of the classical free shear flows. It has been the subject of experimental work for more than 50 years (Ruden 1933, Kuethe 1935) and has found broad application in combustion systems as a means of mixing reactants.

The momentum-driven, free turbulent jet is a special turbulent flow for several reasons. In the far field, the evolution of the maximum mean velocity and the largest scale of the motion conspire to give the flow a single Reynolds number independent of the distance from the jet nozzle (e.g., Landau and Lifshitz 1959). Another special property of the jet flow is that measured mean profiles of velocity and jet fluid concentration are self-similar when collapsed on rays that emanate from the origin of the jet (Wilson and Danckwerts 1964, Becker et al. 1967, Wygnanski and Fiedler 1969, Townsend 1976, Birch et al. 1978, Lockwood and Moneib 1980, Chen and Rodi 1980 and references cited therein). The measured self-similarity of the mean velocity field, and the decay of the mean concentration within the jet are consistent with the equations of motion for an incompressible fluid (Appendix F).

In the cylindrical coordinates that will be used in the body of this work, the self-similar profile of the mean concentration of jet fluid takes the following form:

$$\overline{C}(x,r) = \kappa \frac{C_0 d^*}{x - x_0} g\left(\frac{r}{x - x_0} \right), \tag{1.1}$$

where κ is a constant determined by experiment, d^* is the momentum diameter of the nozzle exit, C_0 is the jet exit concentration, $g(\eta)$ is a function that has a maximum value of 1 at $\eta = 0$ and is determined by experiment, x is the distance from the jet nozzle along the axis of the jet, r is the radial distance from the axis of the jet, and x_0 is the virtual origin of the jet flow similarity. A schematic of this coordinate system is given as Figure 1-1.

The momentum diameter is defined by:

$$d^* = \frac{2 \dot{m}_0}{\sqrt{\pi \rho_\infty J_0}}, \tag{1.2}$$

where ρ_∞ is the density of the reservoir fluid and $\dot{m}_0$ and J_0 are the nozzle mass and momentum fluxes. It was introduced in a limited way by Thring and Newby (1953), used by Avery and Faeth (1974), and modified to the form presented here by Dahm and Dimotakis (1987). The momentum diameter can be used to collapse the results of many different jet experiments (see Dahm and Dimotakis 1987) and is assumed to be the proper length scale for normalizing the downstream distance in the jet. The constants in Equation (1.2), 2 and π, were chosen so that d^* reduces to the geometrical nozzle diameter, d, for density matched jet and reservoir fluids and a perfect "top-hat" exit velocity profile.

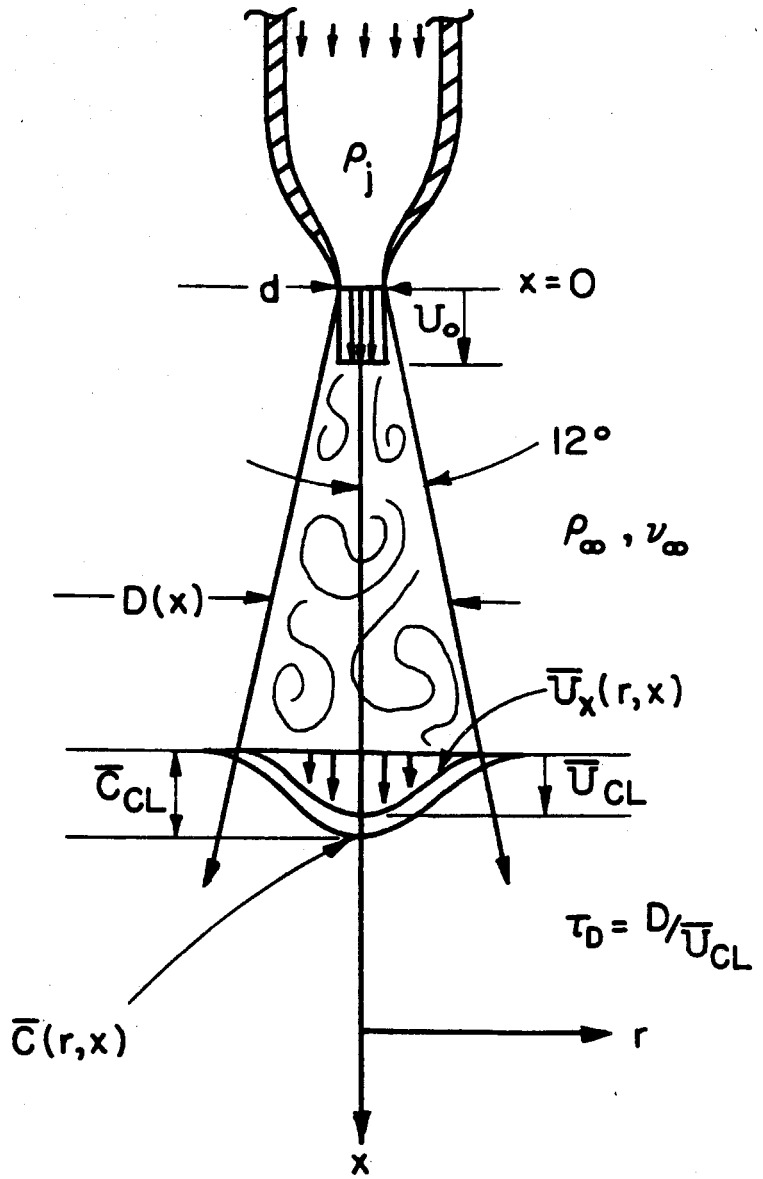

Experimental Jet Flow Coordinates

Figure 1-1.

The virtual origin is determined by the far-field behavior of the jet and is a correction for the influence of the near field of the jet. Some parameters that affect the virtual origin are the external shape of the jet nozzle, the exit turbulence level, and the exit velocity profile.

In the body of this work, the following substitutions will often be made:

$$\chi = \frac{x - x_0}{d^*}, \qquad \eta = \frac{r}{x - x_0}. \tag{1.3 \& 1.4}$$

These allow Equation (1.1) to be simplified to:

$$\overline{C}(\chi,\eta) = \kappa \frac{C_0}{\chi} g(\eta). \tag{1.5}$$

The jet far field is defined here as that portion of the jet flow that is influenced only by the momentum flux of the jet. Far-field measurements are usually verified by a satisfactory collapse of the measured means with the scaling suggested by Equation (1.1) or (1.5).

While the similarity of the mean profiles is on a solid experimental footing, the picture is not yet complete. For most experimental data, the root mean square (rms) fluctuation profile cannot be collapsed with the same scaling used to collapse the means. There are also conflicts between the reported rms levels from different experiments. No clear consensus exists as to whether the ratio of the rms to mean concentration of the jet fluid ($C'_{rms}/\overline{C}$) is a constant in the far field of the jet (see Figure 3-7, Chen and Rodi 1980, Dahm 1985).

These problems could arise from many sources, including: Reynolds number effects, contamination of the flow by buoyancy forces, insufficient resolution of all of the fluctuating scales, unsteadiness in the jet source or the quiescent reservoir, the effects of the molecular Schmidt number (kinematic viscosity divided by species diffusivity), or the possible failure of similarity.

1.2 **Present Experiments**

The experiments described here were designed to address these concerns about the self-similar nature of turbulent mixing in the far field of the jet. In the design of this experiment, the dual requirements of resolution down to the smallest theoretical concentration scales and high signal-to-noise ratio were strictly followed. This meant that the choices of the exit Reynolds numbers, nozzle sizes and other experimental parameters were based on the dynamic range limitations of the chosen diagnostic and the resolution requirements of the fluid mechanical mixing process. The jet and reservoir gases and the overall size of the experiment were chosen to minimize buoyancy forces while allowing for sufficient downstream range in the jet for the mean concentration profile to properly establish the similarity of Equation (1.1). Appendix A describes how these requirements were met and how the rest of the experimental parameters were chosen. The topics presented in Appendix A include: calculation of the resolution requirements, scaling the momentum and buoyancy forces in the jet, estimation of the effects of placing the jet in a coflowing

stream, and designing the jet nozzles.

This work is an experimental investigation of mixing and structure within the turbulent jet concentration field, as it is diluted with entrained reservoir fluid. In particular, it is a study of the similarity of the mean concentration of jet fluid, $\overline{C}(\chi,\eta)$, the rms concentration fluctuation level, $C'_{rms}(\chi,\eta)$, the power spectrum of concentration fluctuations, $E_c(f)$, the probability density function of jet fluid concentration, the probability density function of the time derivative of concentration, and the statistical properties of the estimated scalar dissipation rate, ε_c, computed from $(dC/dt)^2$. Some features of these statistical measures show evidence of a large-scale motion in the flow that spans the local jet diameter.

This work addresses three types of similarity in the jet and it is necessary to present the terminology that will be used in each case.

Specific similarity. This term is applied to the specific properties of the turbulent mixing process in the jet that allow a collapse of the statistical measures of the fluctuating concentration field with downstream distance *at a fixed Reynolds number*.

General Similarity. This term refers to properties of jet mixing that are *independent of the Reynolds number*.

Universal Similarity. This term describes properties of jet mixing that are *independent of Reynolds number and independent of the jet flow geometry*.

The actual measurements, single-point concentration time histories, were made with a nonintrusive laser-Rayleigh scattering diagnostic in a steady, gas phase, axisymmetric, momentum-driven jet that issued into a large enclosure. The diagnostic was sensitive to the mole fraction or molecular number-weighted concentration, C_n. To correct for the small density differences that existed between the jet and reservoir gases, all of the results are presented in terms of the mass-weighted concentration, C, since that is the variable that best represents constant density conditions (see Pitts 1986). The details of the conversion from C_n to C are contained in Appendix E. The measurements cover the downstream range from 20 to 90 jet exit diameters at Reynolds numbers of 5,000 and 16,000. The Reynolds numbers were computed from the jet exit velocity, U_0, the geometrical nozzle exit diameter, d, and the reservoir kinematic viscosity, ν_∞:

$$Re_0 = \frac{U_0 d}{\nu_\infty} . \tag{1.6}$$

A complete discussion of the experimental design is given in Appendix A. The performance details of the diagnostic are contained in Appendix B. The data processing techniques are described in Appendix C and Appendix E.

CHAPTER 2

EXPERIMENTAL FACILITY

2.1 The Main Apparatus

These experiments were performed in the gas phase, jet-mixing apparatus shown schematically in Figure 2-1 and pictured in Figure 2-2. This facility, specially designed for these experiments, was constructed in part with the aid of Mr. Earl Dahl.

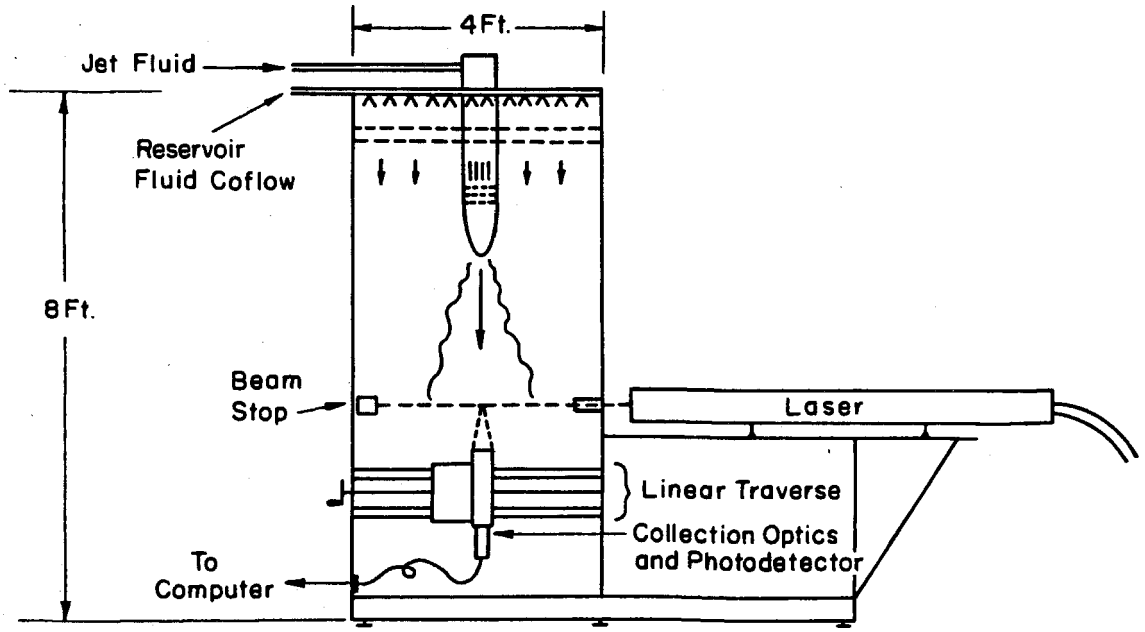

Figure 2-1. Schematic of the jet flow facility.

The main apparatus consisted of a large, relatively airtight,

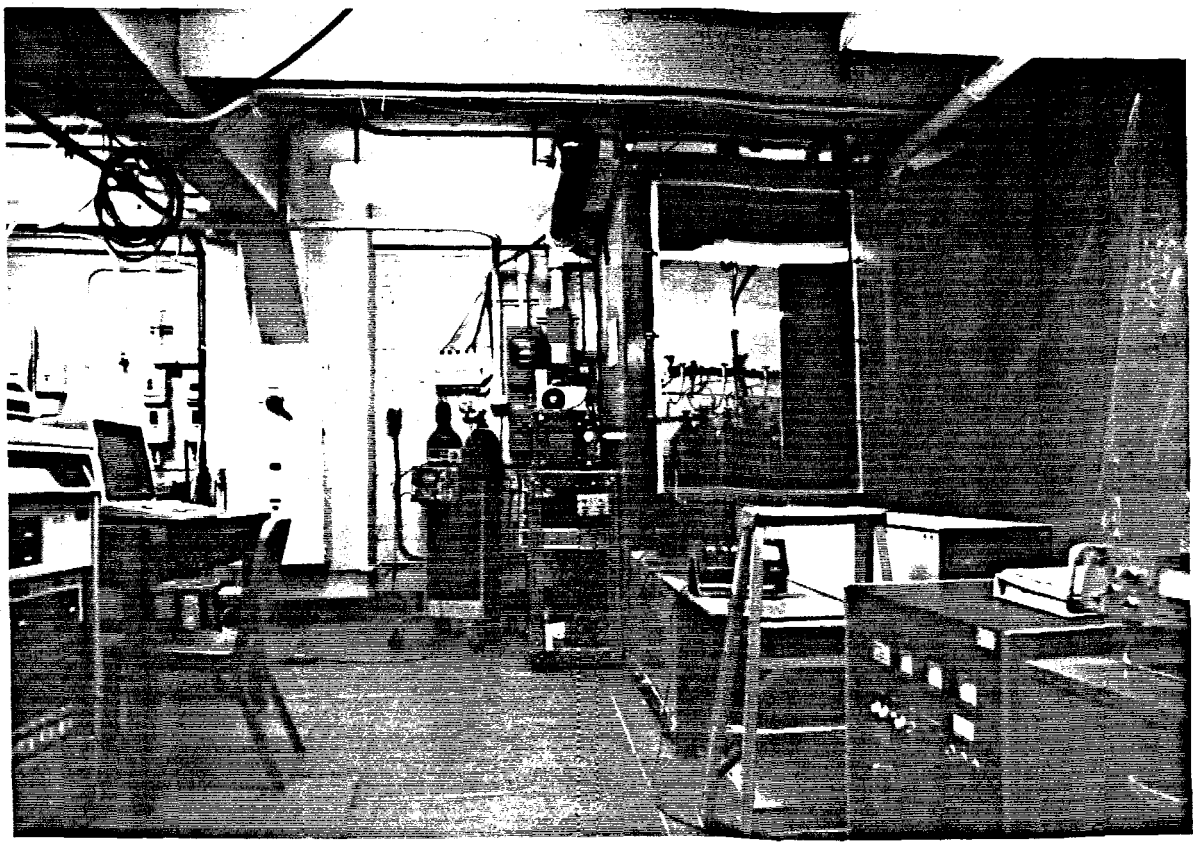

Figure 2-2. Photograph of the jet flow facility.

varnished plywood enclosure, with an interior volume of about 120 cubic feet (7.5′ x 4′ x 3′11"), and an adjoining rigidly attached laser platform. The test section was about 5 1/2′ long and extended from 6" below the top, to 18" above the bottom of the enclosure. The jet was produced by a vertically adjustable nozzle, which was inserted downward into the test section through the center of the top of the apparatus. A mild coflow was produced over the entire 15.7 ft^2 cross section of the

top of the test section to provide the jet entrainment requirements (Ricou and Spalding 1961) to a point below the farthest measuring station. The internal cross section of the experiment was mildly contracted (peak area reduction of 13%) over the lower two-thirds of the test section. The sudden change in area at the end of the contraction provided a fixed separation point for the coflow as it decelerated in the pressure field produced by the jet. Fixing the separation point of the coflow helped prevent unsteady interactions between the entrainment field of the jet and the walls of the main enclosure. The measuring station was located about 4" above the end of the contraction, and this height was fixed with respect to the wooden structure. The largest ratio of the cross-sectional area of the jet's turbulent cone to the cross-sectional area of the test section was about 0.26 .

The laser platform, built as an integral part of the main enclosure, supported the 65 kg laser head. The laser beam crossed the test section horizontally and was stopped after a single pass through the test section. The collection optics and the photosensor were supported 4 1/2" below the laser beam by a large linear traverse used for horizontal positioning of the sensing volume.

The inside wooden surfaces were painted flat black, and a rubber glove-box glove was installed near the bottom on one of the vertical sides for internal manipulations while the experiment was sealed. This permitted most adjustments to be made without opening the enclosure, thereby minimizing the introduction of dust particles. Large 3' x 5'

plexiglas windows were located on opposite sides of the test section to allow shadowgraph imaging of the jet flow.

2.2 **The Jet Gas Delivery System**

The jet gas was ethylene (C_2H_4) for the $Re_0 = 5,000$ experiments and propylene (C_3H_6) for the $Re_0 \approx 16,000$ experiments. Both gases were packed under vapor pressure in size 1A or 1S cylinders (9" diameter and 51" length), whose thermal mass was sufficient to provide the necessary "boil-off" during a run. A single-stage regulator (Matheson model # 1L) was used to stabilize the delivery pressure. After passing through about 300 diameters of 3/8" copper tubing, the flow of jet gas was filtered (Matheson model # 6190, 100% efficiency at .02 micron), regulated by a fine metering valve (Nupro # B-4L) with a micrometer handle (Nupro # NY-2M-S6), passed through an explosion-proof solenoid valve (ASCO Red Hat # 8211C93) used to initiate the flow, and plumbed to the jet nozzle. Measurements of the dynamic head of the jet using a Barocel sensor and manometer allowed the metering value to be calibrated. Changes in the jet flow rate during a run, and variations between runs at the same Reynolds number, were less than ±2% of the jet exit velocity.

Two nozzles were used to increase the range of jet Reynolds numbers that could be reached without rebuilding the large enclosure. A 0.75" diameter nozzle was used for the runs at $Re_0 = 5,000$ and a 0.30" diameter nozzle was used for the runs at $Re_0 = 16,000$. The inner contours of both

nozzles were designed by a method developed by Professor Paul Dimotakis. The larger nozzle was made of plexiglas and machined by the Disney corporation, while the other was made of aluminum and machined by Mr. George Lundgren of the GALCIT machine shop. The design of the inner contours was based on an optimized 6^{th} order polynomial (7 adjustable coefficients). The details of this optimization can be found in Appendix A, Section 9. The outer contour was a simple circular arc that started near the lip of the nozzle exit and met smoothly with the supporting 3" diameter pipe. Inside the nozzle, the flow was manipulated with a 6" section of cruciform, several inches of open pore foam (100 pores per inch), a half-inch section of honeycomb, and 3 screens. The exit turbulence level for both nozzles was about .2% in the Reynolds number range where each was used. The jet exit velocities were 4.04 m/sec at $Re_0 = 5,000$ and 28.6 m/sec at $Re_0 = 16,000$.

Because it can be used to collapse the results of many different jet experiments (see Dahm and Dimotakis 1987), perhaps the most important parameter determined by the jet nozzle is the momentum diameter d^* (see Equation 1.2). The momentum diameter, d^*, reduces to the geometric exit diameter, d, for $\rho_{jet} = \rho_\infty$ and a perfect "top-hat" velocity exit profile. The use of pure gases in these experiments insured that the exit density profiles from both nozzles were ideal. An axisymmetric Thwaites calculation was used to estimate the boundary layer corrections to the velocity profile for both nozzles yielding; $d^* = .960\, d$ for the 0.75" nozzle, flowing ethylene into nitrogen at $Re_0 = 5,000$, and $d^* = 1.005\, d$ for the 0.30" nozzle, flowing propylene into

argon at $Re_0 = 16,000$.

Either nozzle could be suspended in the test section on the end of a 3" diameter pipe made up of a variable number of 6" long threaded sections. The operational length of the pipe was determined by the placement of a ring clamp. The distance between the measuring station and the tip of the nozzle was continuously adjustable by moving the ring clamp, and adding or removing pipe sections as necessary. This whole assembly (nozzle and pipe sections) was supported by a special collar mounted on top of the main enclosure. A seal was made against one of the pipe sections by a greased o-ring at the base of this collar. The weight of the nozzle assembly was carried by the ring clamp, which rested on top of the support collar. The angular orientation of the nozzle could be adjusted by using 3 thumb screws near the top of the support collar to orient the nozzle assembly as necessary. The pivot point for this tilting was provided by the o-ring at the base of the support collar. Figure 2-3 is a drawing of the mechanical setup of the jet nozzle.

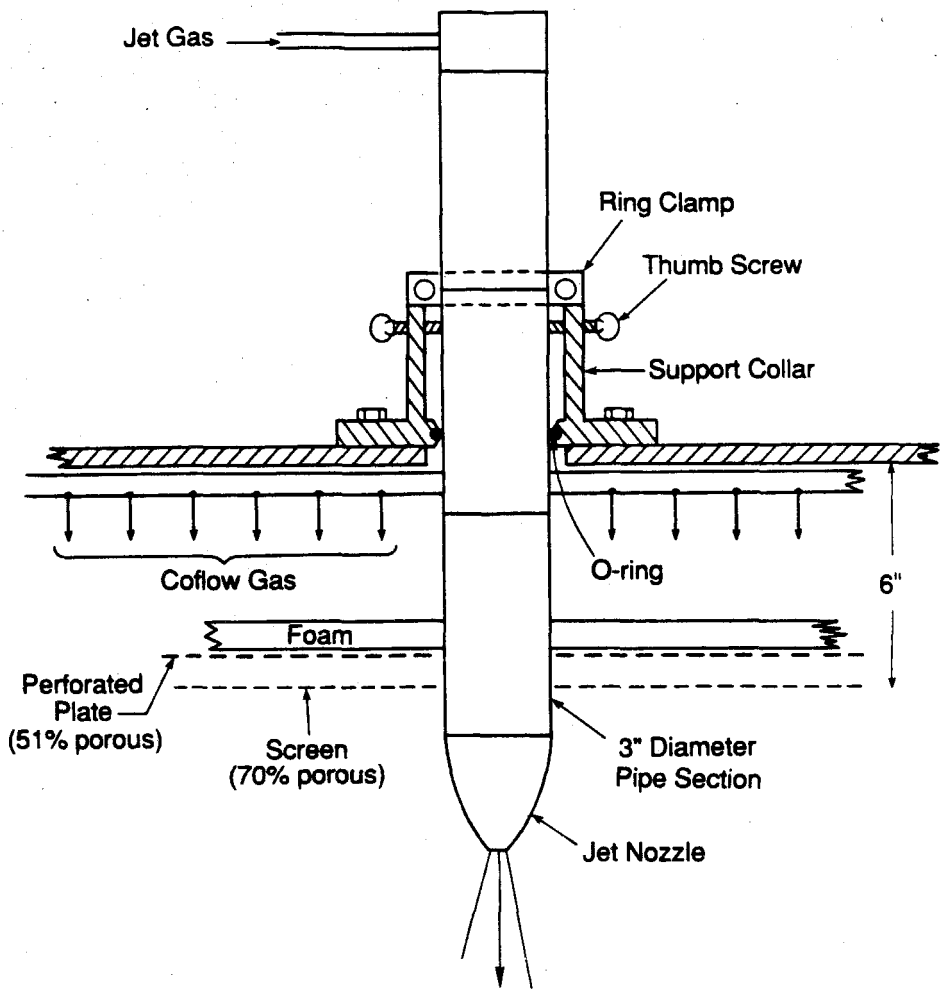

Figure 2-3. Mechanical setup of the nozzle.

2.3 The Coflow Delivery System

The reservoir or coflow gas was nitrogen for the experiments at $Re_0 = 5,000$ and argon for the experiments at $Re_0 = 16,000$, because these were the least expensive pure gasses that were safe to deal with in large quantities. The coflow gas originated in a high-pressure (2500 psig), 4 bottle manifold (Matheson) mated to a high flow-rate, single-stage regulator (Matheson # SP-2369-1). The flow was filtered (Matheson # 6124-P12FF, 100% efficient at .2 micron) and heated "on-the-fly" by a special feedback, temperature-control system. A complete description of the coflow temperature-control system is contained in Appendix D. An explosion-proof, solenoid valve (ASCO Red Hat # 8211B26) was used to initiate the coflow at the start of a run.

The coflow was introduced into the top of the flow facility by a special manifold. The incoming gas was converted from 3/4" diameter copper tubing to a 6 1/4" internal diameter PVC pipe, which fed 30 smaller PVC pipes with an internal diameter of about 5/8". Each of these smaller pipes, which were inserted into the coflow settling chamber at the top of the main enclosure, had 30 1/16" diameter holes that pointed vertically downward. These 900 holes, arrayed in a square, produced 900 little jets, which had about 3 1/4" to develop before impinging on a 1" layer of open-pore foam (100 pores per inch) supported by a perforated plate (49% solidity). The final coflow manipulator, a high porosity (about 70% open) screen was placed 1" below the perforated plate. The whole coflow manipulation system was contained in the top 6" of the main enclosure (see Figure 2-3).

The velocity of the coflow was checked by floating balloons on an intentionally produced density gradient in the test section and by measuring the distance they traveled when the coflow was cycled on for a known time. The velocity of the coflow was set to about 2 cm/sec for the runs at $Re_0 = 5,000$ and to between 5 and 6 cm/sec for the runs at $Re_0 = 16,000$. These rates were achieved by adjusting the output pressure of the regulator on the high-pressure manifold.

2.4 **The Exhaust System**

The spent gases exited at the bottom of the main enclosure through 4 symmetricly placed 6.5" diameter holes. These holes fed two ducts that discharged into a large plastic bag with a capacity of about 300 cubic feet. The contents of the bag were vented on the roof of the laboratory at the end of each run by a special explosion-proof suction system with a capacity of about 50 cubic feet per minute. Because the experiments involved explosive hydrocarbon gases, and because the suction line traveled through 4 floors of the occupied areas, it was made from galvanized, 3" IPS, schedule 40, steel pipe, which had the strength to contain a detonation wave with a safety factor of more than 10. Figure 2-4 is a reduction of the blueprints for this system.

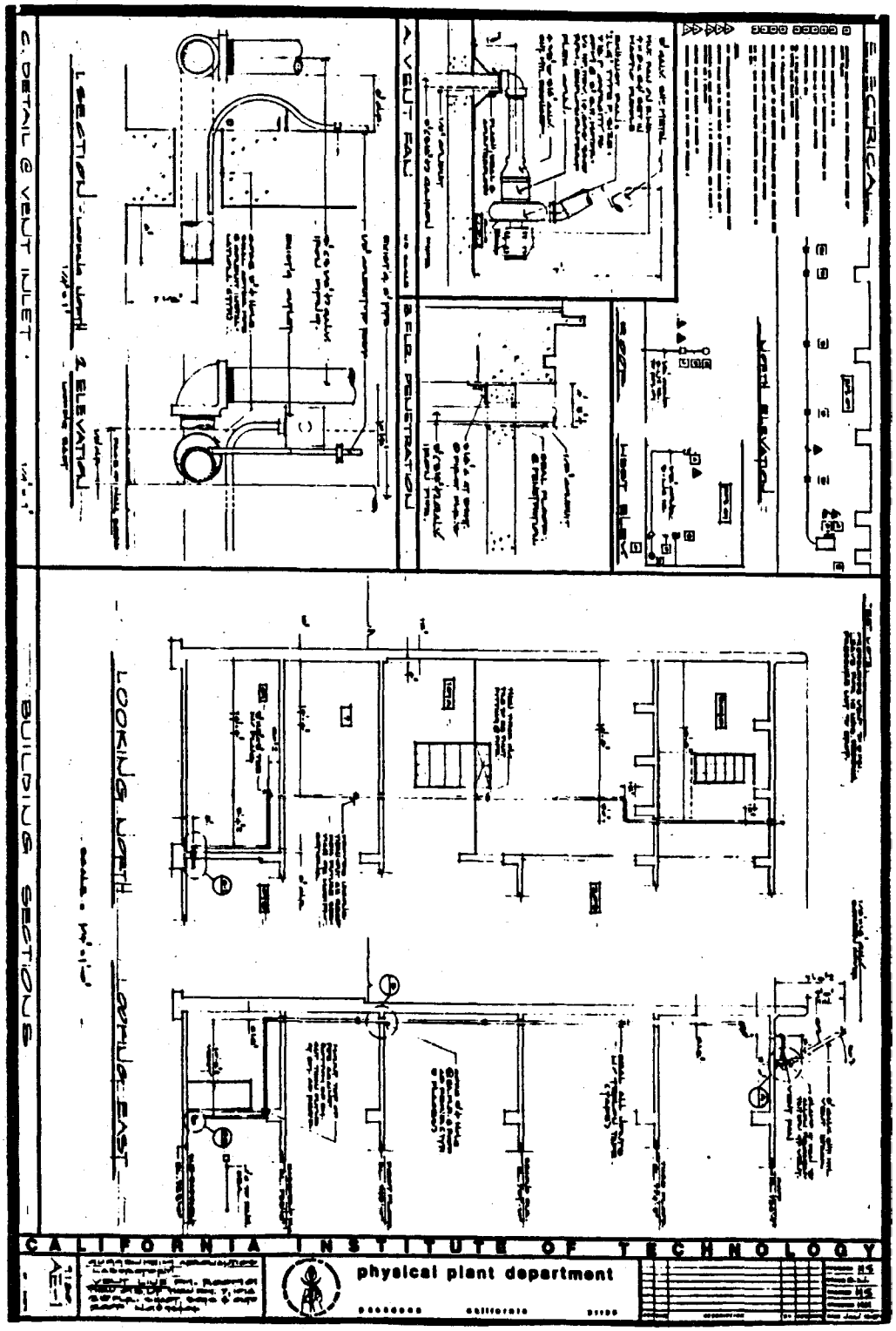

Figure 2-4. Reduced blueprints of the exhaust system.

2.5 The Laser-Rayleigh Scattering Diagnostic

In these experiments, laser-Rayleigh scattering was used to determine the time- and space-resolved, mole fraction of a binary gas mixture by measuring the amount of light that the mixture scatters. The intensity of the scattered light is proportional to the scattering cross section of the gas mixture and the incident light intensity. For these experiments, the Rayleigh scattered light from a small section of a constant-power, focused laser beam was imaged onto a small aperture photosensor, that produced a current that was linearly related to the mole fraction of jet gas in the focused laser beam. This photocurrent was amplified and measured. A complete description of the performance of the photodetection system is contained in Appendix B.

This diagnostic has four main advantages over other types of concentration probes.

1. It is nonintrusive.

2. It is capable of exceedingly high spatial resolution.

3. It exhibits a very large dynamic range for density-matched gas pairs.

4. It has almost perfectly linear characteristics.

Nonlinearity might arise through multiple scattering of detected photons or ionization of the gas in the focal volume. Both of these effects were unimportant at the gas and laser power densities used for these

measurements.

The major difficulty with the diagnostic comes from the fact that the Rayleigh cross sections of gases are small from an experimental standpoint when compared, for example, to the resonant cross sections of fluorescent dyes used quite successfully in liquid phase experiments (Robben et al. 1976, Liu et al. 1977, Koochesfahani 1984, Dahm 1985, and others). For Rayleigh scattering at room temperature and pressure, about 1 part in 10^4 or 10^5 of the incident beam power is scattered per meter of gas that is traversed, while about 1 to 10 percent of the beam power is scattered per meter by typical concentrations of the fluorescent dyes used in liquids. The Rayleigh cross sections of gases are also orders of magnitude smaller than the Mie cross sections of dust particles. This necessitated the use of well-filtered gases to minimize the number of dust particles that passed through the focal volume during a run. The technique for removing the effects of the dust from the data is the subject of Appendix E, Section 3.3 .

2.6 **The Laser System**

A Coherent Radiation CR-10, water-cooled, argon-ion laser system was used for all the measurements. It was run with the "all-lines" mirror in place and delivered about 18 watts of power for the $Re_0 = 5,000$ runs and about 23 watts for the $Re_0 = 16,000$ runs. The laser head was fixed with respect to the wooden structure, and the distance between the beam and the bottom of the main enclosure was 22". Before the beam

entered the test section, its polarization was rotated with a half-wave plate. A small focusing lens was used to bring the beam to a waist in the vicinity of the measurement volume. An iris placed beyond the lens cut down on the stray light scattered from the other optics. The focusing lens and the iris were mounted on a sliding tube that could be moved horizontally a few inches to adjust the position of the beam waist. A removable prism on a kinematic mount was used to divert the beam to a power meter to check the power level before each run. The beam was dumped on the far side of the test section in a special, high-quality beam stop, designed by Dr. Richard Miake-Lye, which minimized reflections.

2.7 **The Collection Optics and Photosensor**

The collection optics, placed directly below the focal volume, were a one-to-one imaging system based on two identical, antireflection-coated, achromatic doublet lenses (Ealing # 23-9749) of focal length 120 mm and diameter 50 mm. These lenses were chosen as a tradeoff between the minimization of f# and the minimization of flow blockage. The collection efficiency (collected solid angle/4π) of these lenses used in tandem was about 1% (f# = 2.5). The lenses were held by a special 2.5" diameter pipe that mated to the housing for the photodiode and the custom, first-stage amplifier designed by Dr. Daniel Lang for these experiments. The gain of this stage was 10^8 volts/ampere, and it was located as physically close to the photodiode as possible. The performance of this amplifier is discussed in detail in Appendix B. The

photodiodes used in the studies had 200, 500, and 1000 μm diameter, sensitive apertures, which respectively defined, along with the laser-beam waist size, the spatial resolution of the measurements. Figure 2-5 is a diagram of the collection optics and the photosensor.

The optics pipe was mounted on a 3 axis positioning system. A large custom translation stage with more than 30" of travel was used for positioning along the laser beam. Two precision 1" travel translation stages (Newport Corporation # 420-1) were used for adjustments parallel to the jet axis and perpendicular to the plane defined by the jet axis and the laser beam. These two smaller stages were used to align the collection optics with respect to the laser beam. The large stage was securely bolted to the wooden structure of the main enclosure. The whole optical system (laser head, beam optics, wooden platform, 3-axis traverse and collection optics) was mechanically stable enough to maintain optical alignment of the beam and the photosensor for periods of longer than 24 hours, even if the laser was turned off and later turned back on.

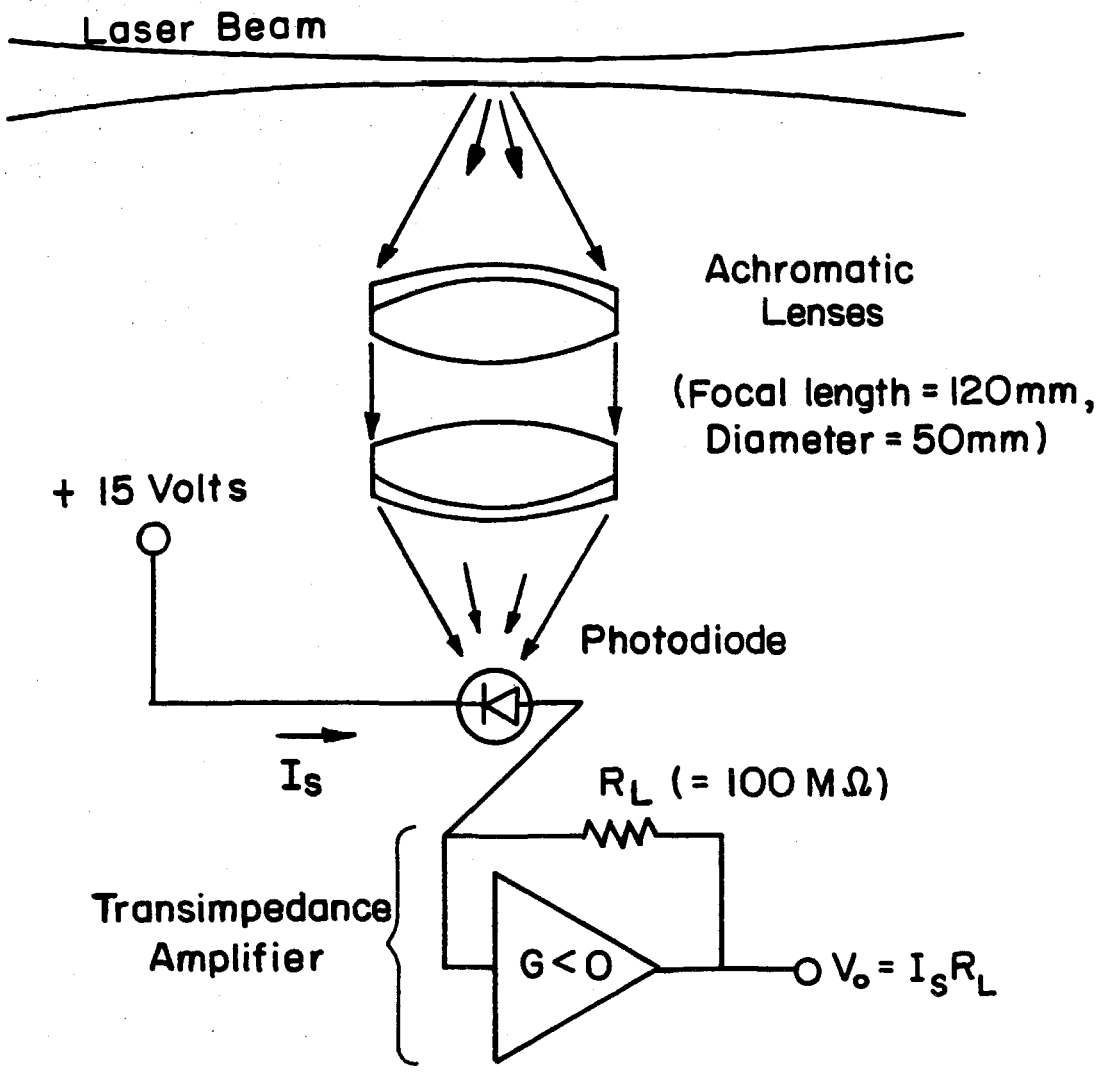

Diagram of Collection Optics
and Photosensor

Figure 2-5.

2.8 **Processing Electronics**

The analog signal processing followed the simple scheme shown schematically in Figure 2-6. The signal from the first stage was brought out of the main enclosure by a 10' cable. The second stage of electronics provided DC offsets and variable amplification to match the signal to the voltage range of the analog-to-digital converter. The signal was also filtered in the second-stage electronics by a 3-pole Butterworth filter with the knee frequency placed at half the digitization rate in accordance with the Nyquist criterion. The offset, amplified and filtered signal was sent to an LSI PDP 11/73 CPU-based computer system, where the analog-to-digital conversion was done by a 12-bit, 250 KHz A/D board (Data Translation # 3382). This computer system was used to control most of the aspects of the data acquisition and system calibration. A more complete description of the signal processing is contained in Appendix E.

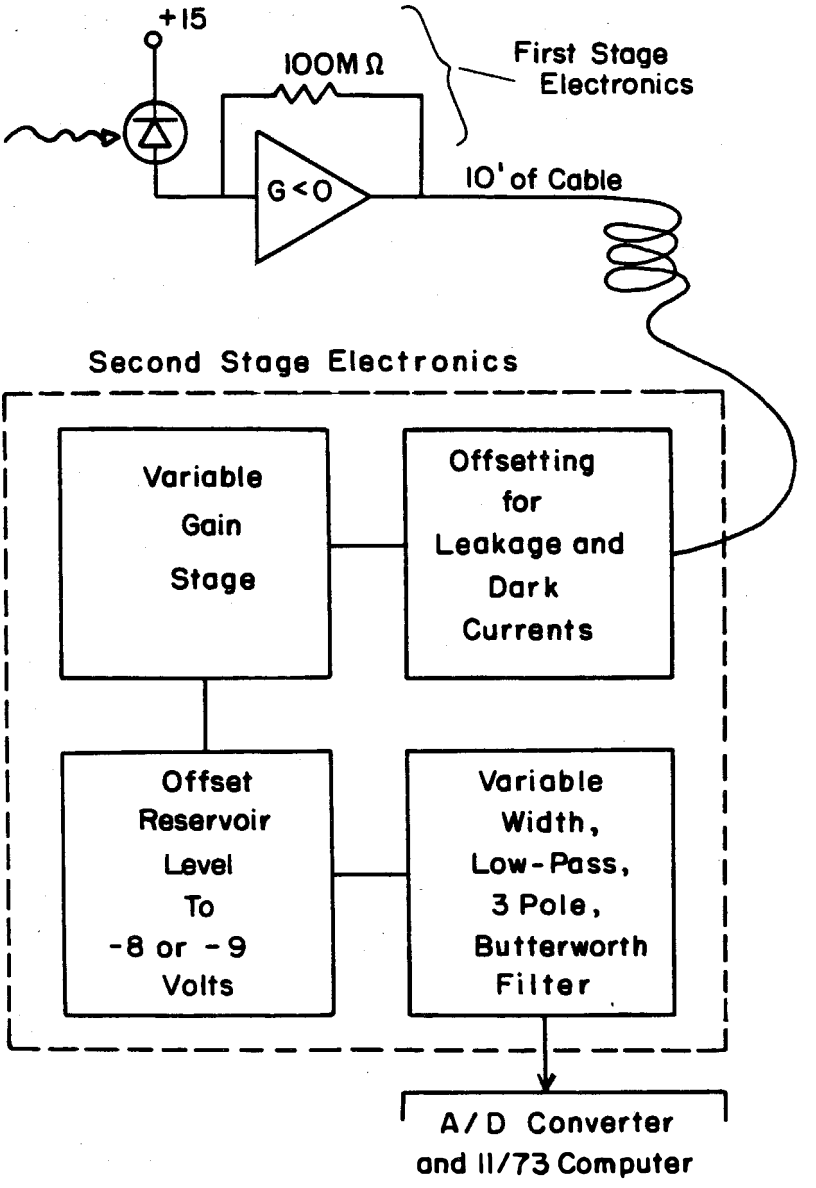

Figure 2-6. Analog signal processing.

2.9 **Procedures and Parameter Selection**

The vertical placement of the nozzle was determined by physically measuring the distance from its tip to the laser beam. The angular alignment of the nozzle was adjusted with the three thumb screws on the support collar until the sides of the 3" supporting pipe were parallel to the string of a plumb bob when viewed in two nearly orthogonal planes. This insured that the jet was pointed vertically downward.

The required spatial and temporal resolution for each run was estimated based on calculated values of the Kolmogorov length scale and the passage frequency for that length scale. For almost all of the studies at $Re_0 = 5,000$, the diameter of the sensitive area of the photodiode was chosen to be less than or equal to the calculated Kolmogorov length scale. A few runs were made at x/d = 20 with the spatial and temporal resolution relaxed by a factor of 2.5 . The focusing lens for the laser beam was chosen so that the beam waist was also smaller than the calculated Kolmogorov length scale. The sampling frequency was chosen to exceed 8 times the local passage frequency of a Kolmogorov scale, when convected by the local mean centerline velocity of the jet. Based on the results of the data from $Re_0 = 5,000$, the resolution requirements were relaxed by a factor of 3 for the runs at $Re_0 = 16,000$. The details of how the Kolmogorov scale and the resolution requirements were estimated are contained in Appendix A, Section 1.

The horizontal position of the focal volume was determined by a pointer and a scale ruled in inches. Fine positioning was achieved by counting revolutions of the hand crank on the 1/2"-13 lead screw, which moved the optics car on the large linear traverse. The absolute alignment of the jet flow and the focal volume was deduced from the mean concentration values of several runs that spanned the centerline of the jet. The true centerline ray of the jet was presumed to intersect the laser beam at the horizontal location that made the measured mean concentration profile the most symmetric. In practice, the true centerline ray of the jet was typically only a few tenths of a degree from its presumed orientation.

The experiment was set up by positioning the nozzle, mounting the correct photodiode in the sensor housing, putting the correct beam focusing lens in place, setting the gain, offsets and filtering of the second stage electronics, purging the experiment with as much as 400 cubic feet of reservoir gas, positioning the collection optics with respect to the jet and aligning them with respect to he laser beam. The absolute sensitivity of the whole system was measured by introducing pure jet and reservoir gases into the focal volume and digitizing the voltage level from each gas. A run was made by starting the jet and coflow together, letting the jet establish a steady state, and then collecting about 200,000 to 500,000 individual measurements. After the run, the spent gases were exhausted through the suction system and the main enclosure was purged with reservoir gas. The data were converted to concentration (mass fraction) on the 11/73 and were checked to insure

that the mean and rms concentration values were relatively stationary throughout the data set.

The inspected data sets were then transferred to a PDP 11/44 computer, where the rest of the processing was done. This typically included removing the effects of Mie scattered light, computing the concentration fluctuation power spectrum, optimal filtering, taking and squaring the temporal derivative, and compiling various probability density functions. The method for power spectral estimation is described in Appendix C. The rest of the data processing techniques are covered in Appendix E.

CHAPTER 3

BASIC PROPERTIES OF THE CONCENTRATION FIELD OF THE JET

3.1 The Mean Jet Fluid Concentration Field

The mean value was computed from each data set by dividing the sum of the measurements by the number of measurements. The computed mean values were then plotted with the axis scaling suggested by Equation (1.5).

$$\overline{C}(\chi,\eta) = \kappa \frac{C_0}{\chi} g(\eta) \qquad (1.5)$$

The results are displayed on Figure 3-1 for the data at $Re_0 = 5,000$ with $\kappa = 5.11 \pm 0.05$ and $x_0 = -3.7d$ and on Figure 3-2 for the data at $Re_0 = 16,000$ with $\kappa = 4.73 \pm 0.1$ and $x_0 = .5d$. The value of κ at $Re_0 = 16,000$ is not as certain as at $Re_0 = 5,000$ because it is based on only two downstream measurement locations, x/d = 30 and 90. The transformation used to collapse the data points is based only on the fitted values of κ and x_0 at each Reynolds number. Separate normalizations by the local centerline mean, or concentration profile radius at half-maximum were not necessary. Figures 3-1 and 3-2 show that the experimental apparatus and technique produced a turbulent jet with the accepted general similarity form of the mean concentration field. The solid curve on Figures 3-1 and 3-2 is a least squares fit to the data at $Re_0 = 5,000$.

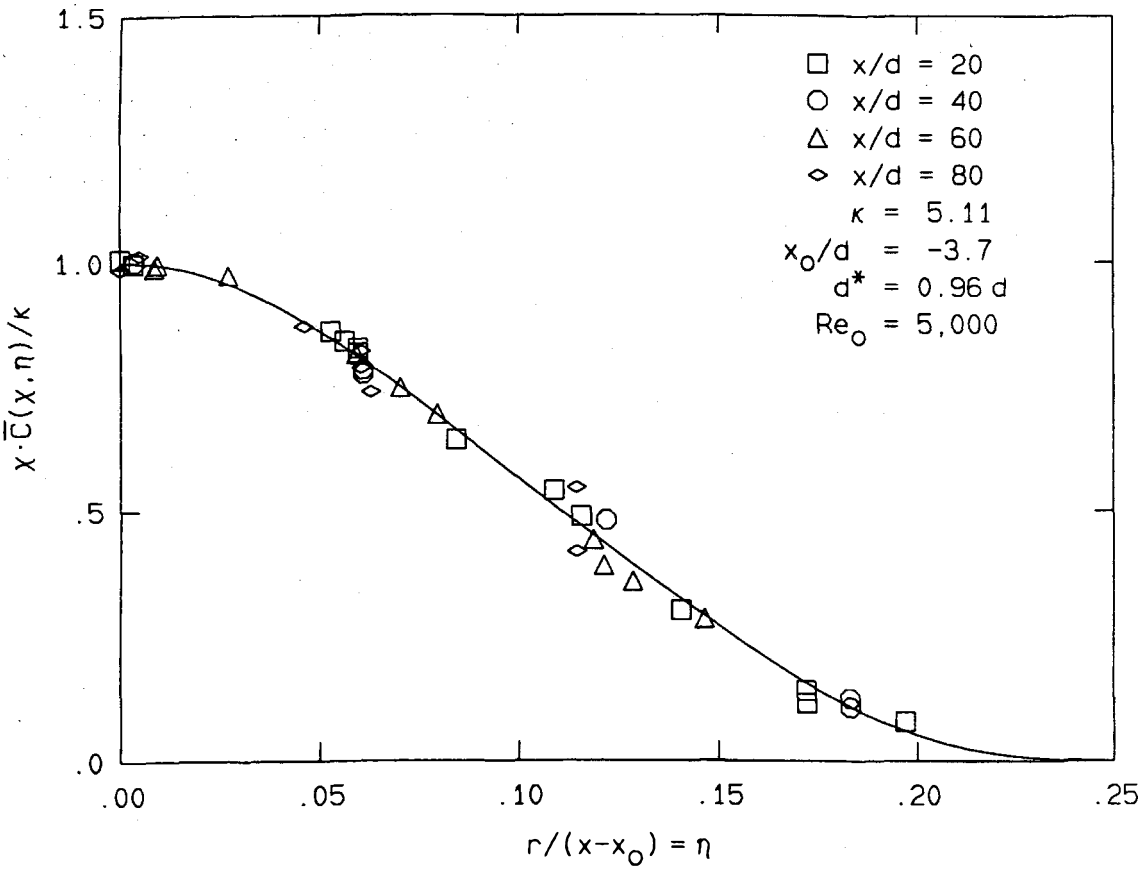

Figure 3-1. Mean concentration profile at Re_0 = 5,000.

A comparison of the fitted mean profile with the published profiles of other experiments is given on Figure 3-3. The digitization of the results from the experiments before 1985 plotted on Figures 3-3, 3-4, 3-7, and 3-8 was performed by Dr. W. Dahm. Similar figures appear in his Ph.D. thesis (Dahm 1985). The agreement between profiles is good and the small differences can probably be attributed to the differing experimental conditions and techniques of each experiment. Table 3-1 lists some of the important parameters of the experiments used for

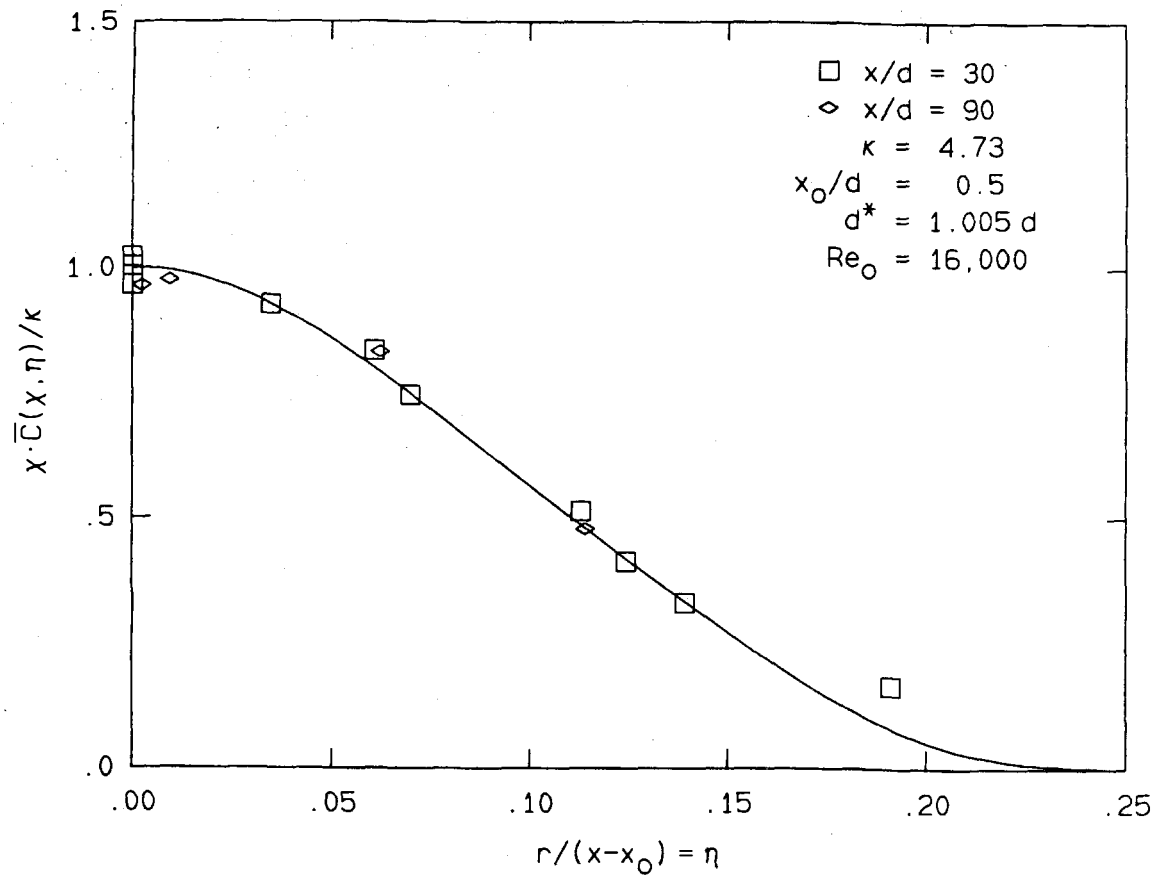

Figure 3-2. Mean concentration profile at Re_0 = 16,000.

comparison with the current studies. The published literature on turbulent jets is very extensive and the studies in Table 3-1 were selected based on the following criteria.

1. A coflowing stream must not effect the measurements.

2. The jet must be nonbuoyant over a significant downstream range.

3. The reported measurements must extend beyond x/d = 20.

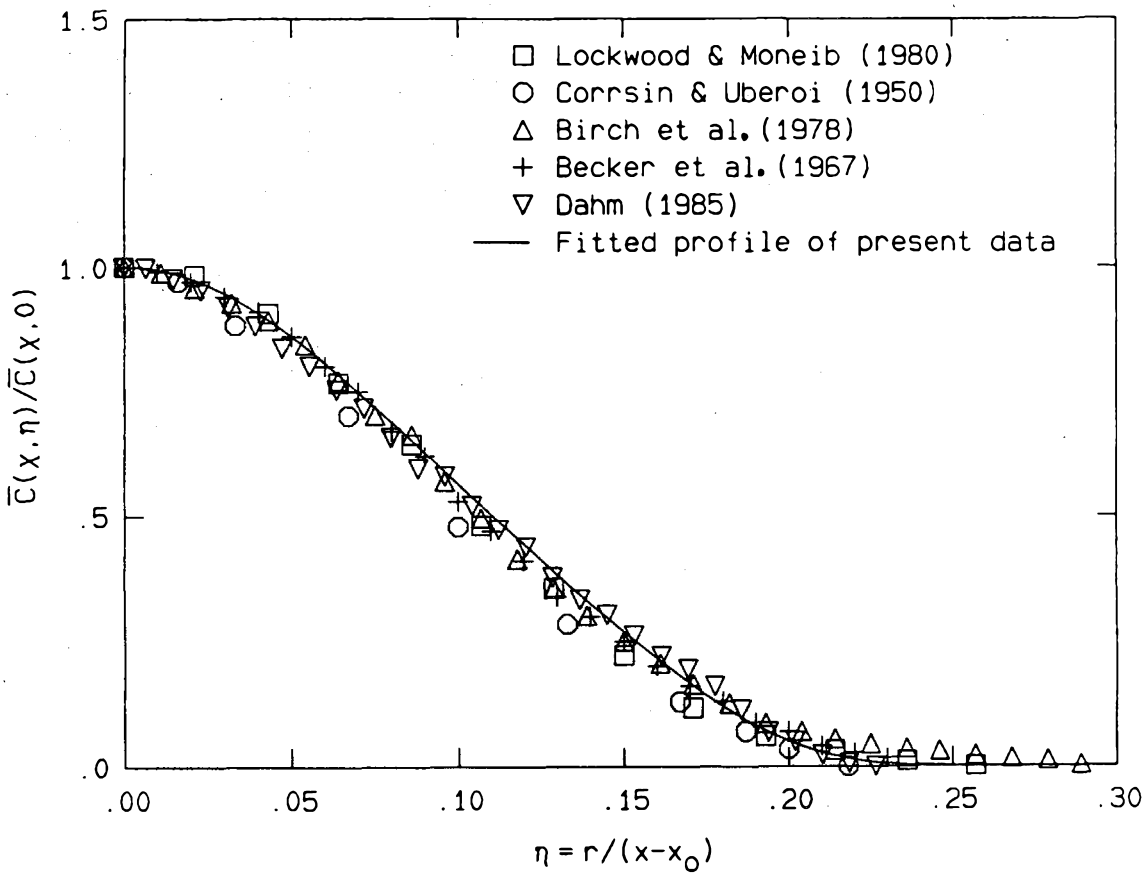

Figure 3-3. Comparison of the fitted mean profile with the results of other experiments

4. The jet Reynolds number must be greater than 2,500.

A comparison of the current and published results for the mean centerline concentration, $\bar{C}(\chi,0)$, is provided as Figure 3-4. The vertical axis is scaled so that the measured data will fall on curves that become horizontal when the far-field behavior of the jet is

Table 3-1: Turbulent Jet Mixing Experiments

Author	Re_o	Sc or Pr	Diagnostic
Becker et al.(1967)	54,000	38,000	Smoke Scattering
Birch et al.(1978)	16,000	0.70	Raman Scattering
Corrsin & Uberoi (1950)	33,000 and ↑	0.7	Thermometry (air)
Dahm (1985)	5,000	600-800	Laser Induced Fluorescence
Lockwood & Moneib (1980)	50,000	0.7	Thermometry (air)
Wilson & Danckwerts (1964)	20,000-60,000	0.7	Thermometry (air)
Papanicolaou & List (1987)	10,000-16,000	7.0	Thermometry (H_20)
Papanicolaou & List (1988)	2,600 - 3,600	$\sim 10^3$	Laser Induced Fluorescence
Present study (1988)	5,000 & 16,000	1.0 & 1.2	Rayleigh Scattering

attained. The ordinate of the horizontal portion of the curves occurs at the value of κ. The current data fall within the scatter of the results from the other experiments.

The Reynolds number above which the mean mixing properties of the jet become independent of Reynolds number is not yet accurately known. Dahm et al. (1984), using their own data and the data of Weddell (1952) find this threshold to be at about $Re_0 = 3,000$ while the entrainment studies of Ricou and Spalding (1961) suggest a value that is roughly an order of magnitude higher. This means that differences in the reported values of κ, and variations in the shape of the mean concentration profile could be due in part to Reynolds number effects. For the current experiments, the value of κ at $Re_0 = 16,000$ is about 8% lower

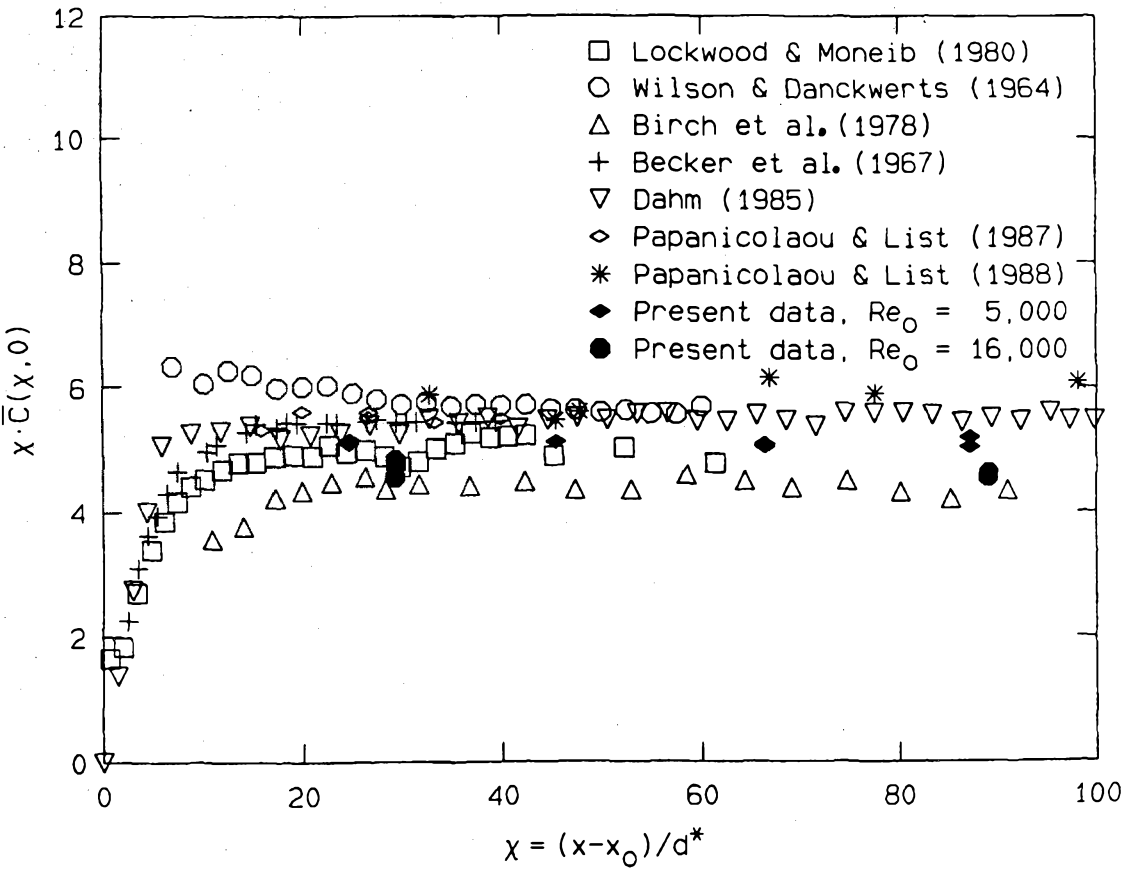

Figure 3-4. Comparison of the scaled mean centerline concentration with the results of other experiments.

than that obtained at Re_0 = 5,000. Further discussion of the disagreement in the measured values of κ is contained in Chapter 8. If not controlled, the effects of a coflowing stream, buoyancy forces, and unsteadiness of the source and reservoir conditions could also influence the mean profile shape and the value of κ. In the present experiments these parameters were tightly controlled (see Appendix A).

3.2 The Root Mean Square Concentration Fluctuation Level

The root mean square (rms) fluctuation level was computed for each data set from:

$$C'_{rms} = \left[\frac{1}{N} \sum_{i=1}^{N} (C_i - \overline{C})^2 \right]^{1/2}, \qquad (3.1)$$

where N is the number of points in the data set. Figures 3-5 and 3-6 are plots of the current data at $Re_0 = 5,000$ and 16,000. The axis scaling on each plot and the values of κ and x_0 are identical to those used for the mean concentration profiles at each Reynolds number. Separate normalization by the centerline fluctuation level was not necessary. The fact that the rms fluctuation data cluster about a single curve, in the specific similarity coordinates of the mean concentration profile, for both Reynolds numbers, implies that C'_{rms} and $\overline{C}$ conform to the same specific similarity law and that $C'_{rms}/\overline{C}$ is a general similarity variable for the jet. This issue will be addressed further in Chapter 5.

Many previous experimental investigations have not found this behavior (see discussion in Dahm 1985 and Lockwood and Moneib 1980) Figure 3-7 is a plot of the centerline fluctuation level divided by the centerline mean for several experiments. The present data at $Re_0 = 5,000$ and 16,000 fall on horizontal lines, indicating that the rms and mean centerline concentration values have the same specific similarity behavior. The value of $C'_{rms}/\overline{C}$ on the centerline is found to be $.230 \pm .007$ at $Re_0 = 5,000$ and $.237 \pm .005$ at $Re_0 = 16,000$. Because the

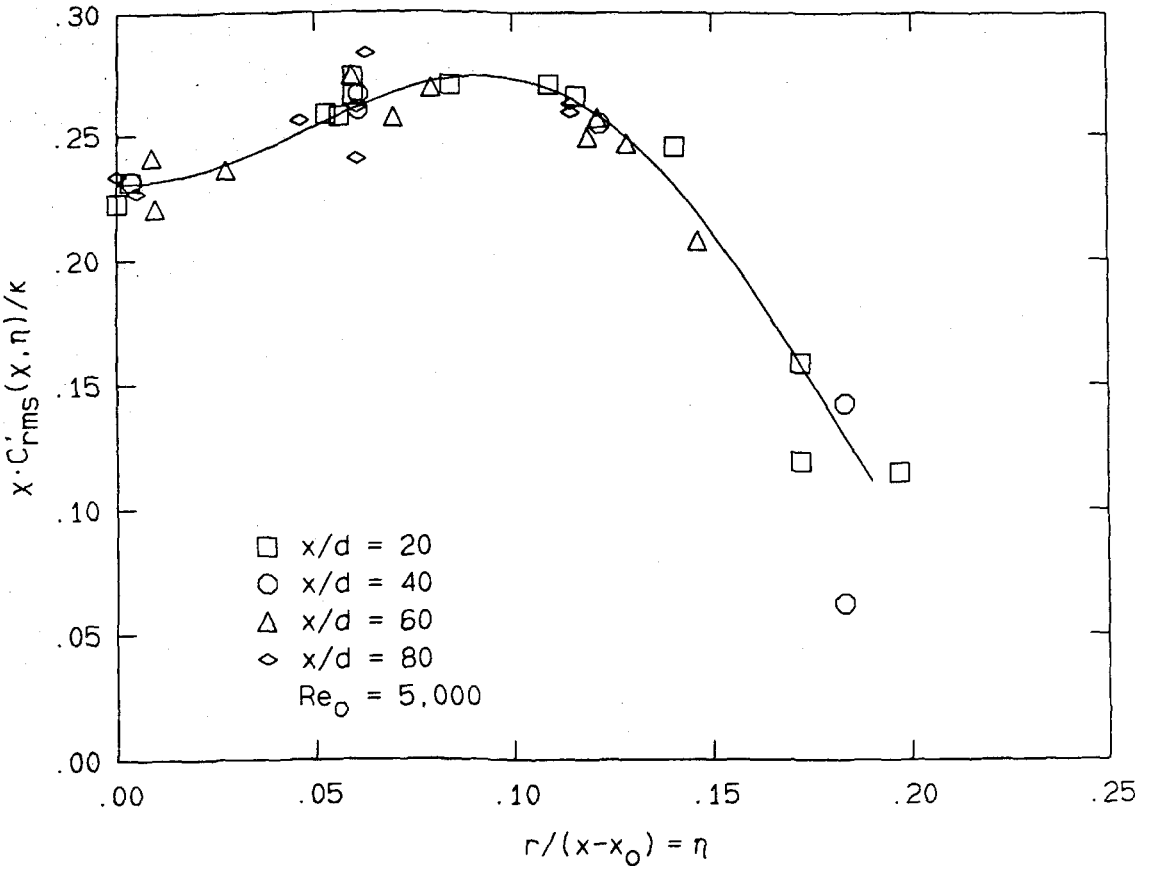

Figure 3-5. Root mean square concentration fluctuation level plotted with the same axis scaling that collapses $\overline{C}$, at Re_o = 5,000.

resolution requirements in the jet become more difficult to meet when the distance from the nozzle to the measurement point is decreased (see Appendix A, Section 1), the failure of previous studies to find a constant value of $C'_{rms}/\overline{C}$ on the centerline may be a result of inadequate resolution in those studies. The present experiments were designed to resolve all of the diffusive scales within the jet and do not suffer

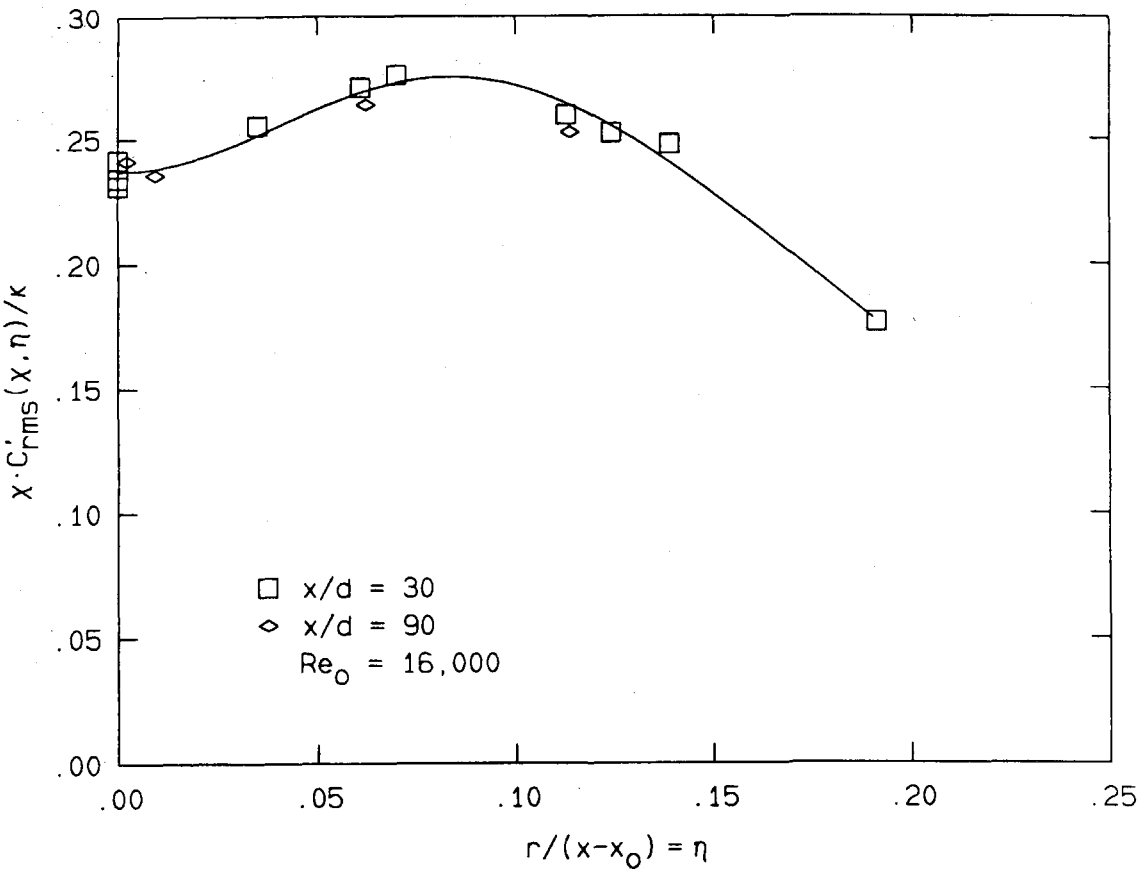

Figure 3-6. Root mean square concentration fluctuation level plotted with the same axis scaling that collapses $\overline{C}$, at Re_o = 16,000.

from such resolution difficulties. This claim will be further supported in the next chapter.

If the fluctuation levels of other experiments are normalized by their centerline value, the rms profiles of other experiments can be compared with the present results. Figure 3-8 is a plot of the curves

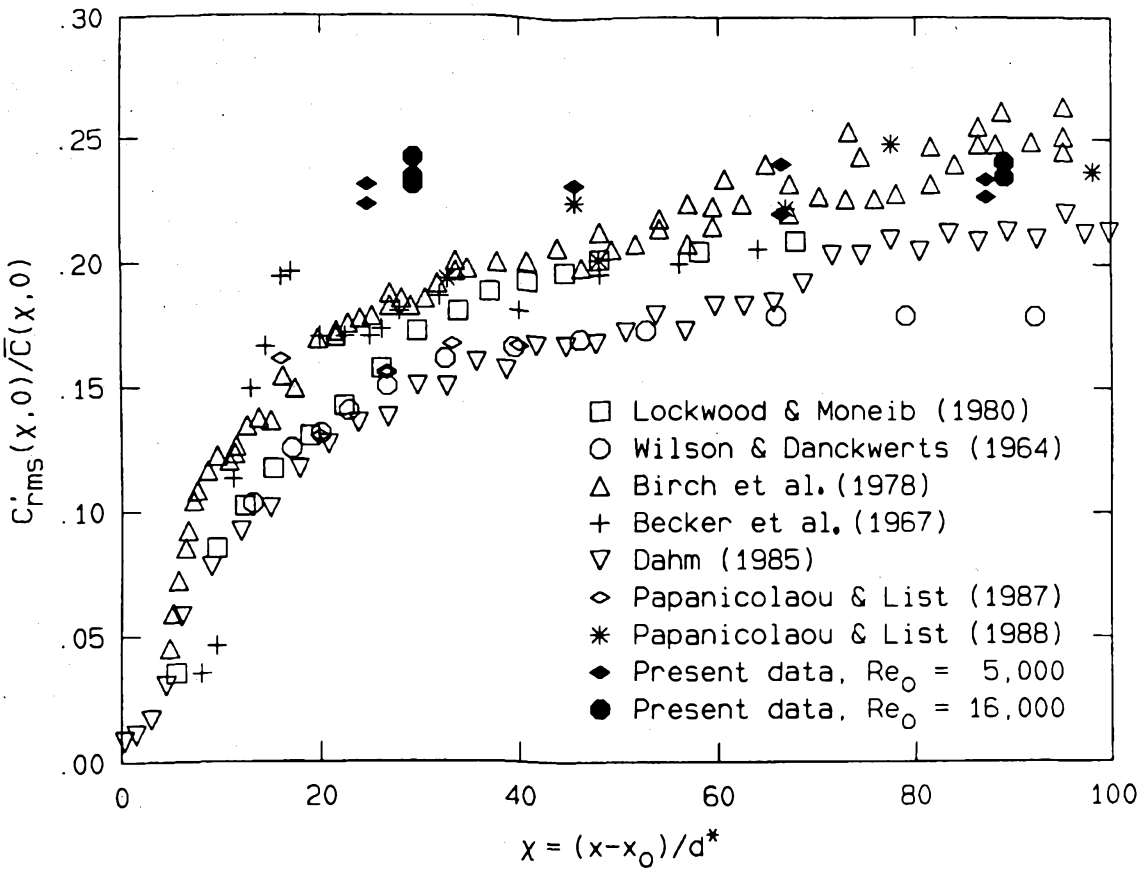

Figure 3-7. Comparison of the centerline rms concentration fluctuation level, divided by the mean centerline concentration, with the results of other experiments.

fitted to the present data along with similar results from other experiments. The fact that the collapse on Figure 3-8 is less than perfect is not surprising because the six experiments plotted were performed at different Reynolds and Schmidt numbers using different techniques with varying resolution.

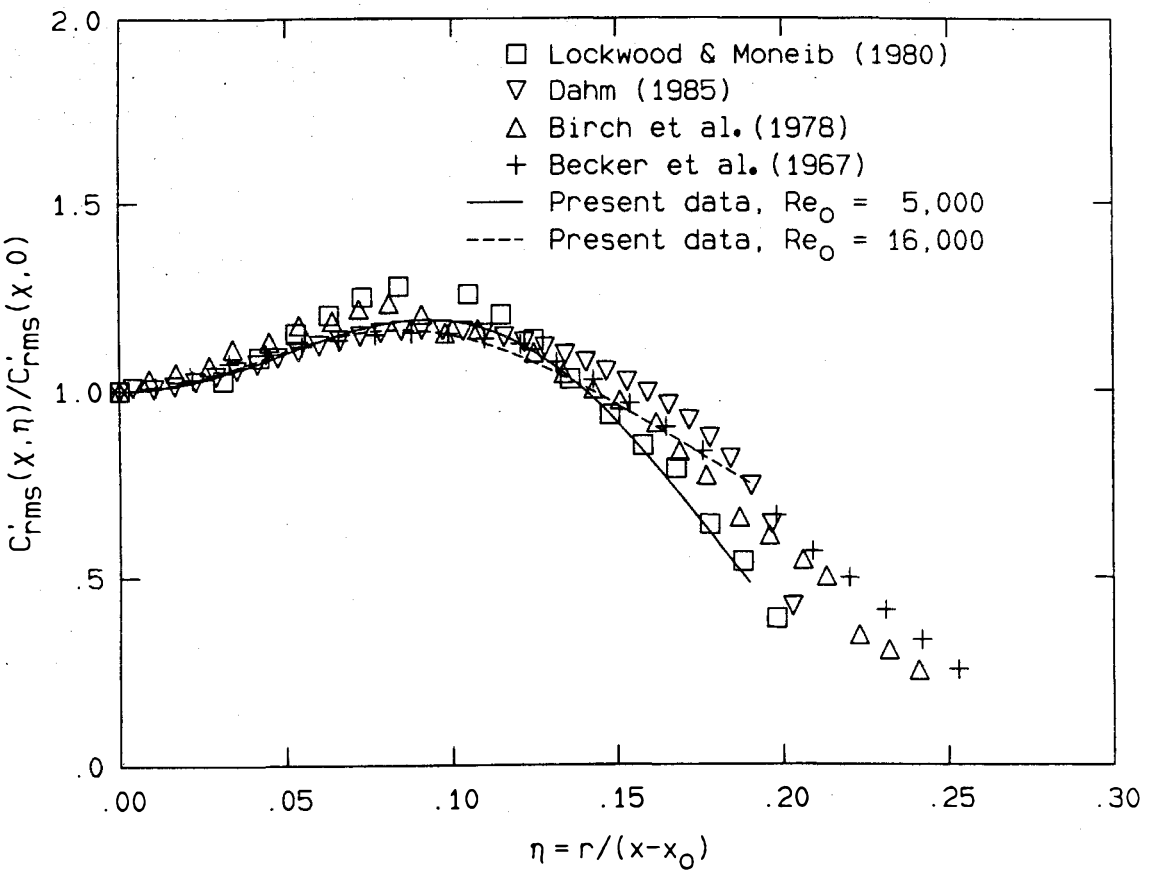

Figure 3-8. Comparison of the rms concentration fluctuation level, divided by its centerline value, with the results of other experiments.

An interesting comparison can be made between the present data at $Re_o = 5,000$ and the results of Dahm (1985), who worked at the same Reynolds number, but in a liquid phase experiment where the molecular Schmidt number is about 600 to 800. Assuming that the spatial resolution of the experiments were comparable with respect to the

smallest diffusion scale in each flow, the Batchelor scale (see appendix A, section 1), one effect of increasing the Schmidt number seems to be an increase in the concentration fluctuation level near the edge of the jet.

This can be understood in terms of the different rates of diffusion in liquids and gases. The matched Reynolds numbers insure that the fluid mechanics in both flows will be statistically the same. Therefore, fluid with a relatively high concentration is tossed to the edge of the jet with the same frequency in both flows. The edge of the jet is a region of low mean velocity and shear, so diffusion is relatively more important in the transport of concentration when compared to the inner regions of the jet. Diffusive transport, which is proportional to $\sqrt{D_{j\infty}}$, proceeds about 20 to 30 times faster in the gas phase flow, so local maxima and minima of the concentration field are smoothed out more quickly. This leads to lower rms values near the edges of the gas phase jet, when compared to the liquid phase jet, at the same Reynolds number.

Another interesting comparison is between the present data at $Re_0 = 5,000$ and $Re_0 = 16,000$. The increase in Reynolds number causes a broadening of the rms profile. This might also be explained using diffusion-time ideas. Increasing the Reynolds number decreases all of the time scales in the jet; hence, the high concentration chunks of fluid thrown to the edge of the jet have less time to diffuse before being reentrained. This creates larger concentration fluctuations,

relative to the local mean, near the edge of the jet when compared to lower Reynolds number flow at the same Schmidt number.

These simple diffusion-time ideas suggest that the flow with the lowest Reynolds and Schmidt numbers should have the narrowest rms profile. Figure 3-8 supports this contention since the narrowest rms profile comes from the current data at $Re_0 = 5,000$ and $Sc = 1.0$.

It is also worth comparing the current data at $Re_0 = 16,000$ and the results of Birch et al. (1978), who worked at the same Reynolds number and nearly the same Schmidt number. The mean values and profiles from both experiments agree reasonably well but the rms results do not. The disagreement in the rms profile might be the result of resolution problems (see discussion below). The mismatch of the centerline rms levels at the farthest downstream locations (see Figure 3-7) might be due to the influence of buoyancy forces in the experiments of Birch et al.

The parameters of the jet flow can be used to form a buoyancy length scale, L_b, and a buoyancy criterion (see Papanicolaou and List 1987 and 1988, Chen and Rodi 1980, or Appendix A, Section 5). The result for the flow of Birch et al., $L_b \approx 55\,d$, suggests that their jet may not be momentum-dominated beyond $x/d = 55$ and is possibly in a transitional state between momentum-driven and buoyant beyond about $x/d \approx 30$. By comparison, L_b/d for the present experiment at $Re_0 = 16,000$ is about 440.

Returning to Figure 3-8, it can be seen that the peak values of the rms profiles do not coincide. While this might be the result of Schmidt and Reynolds number effects, resolution difficulties near the centerline could also cause the observed differences between experiments. At a given downstream distance, the passage frequency of diffusive scales is greatest where the convection velocity is the greatest (the jet centerline). As the measurement point is moved toward the edge of the jet, the convection velocity decreases, so the bandwidth necessary to capture all of the fluctuations is smaller. If the estimated rms value on the centerline is low, possibly because of insufficient measurement time/space resolution, the rest of the rms profile is elevated when normalized by the artificially lower value.

3.3 **Shadowgraph Flow Visualization**

For several reasons, the shadowgraph method was the preferred visualization technique for this flow. It could be successfully applied to the mixing region of two clear gases, was optically clean (no smoke, dust or vapor was needed), and was capable of large aperture imaging at low cost. The shadowgraph system for this experiment exploited the 3′ by 5′ windows on opposite sides of the test section, a 200 watt arc lamp, a first-surface mirror (17" by 30") and a rear-projection screen. Photographic recording of the images produced on the screen were realized using a 90 mm lens, a Nikon FE 35 mm camera, and ASA 400 black and white print film. Figure 3-9 is a schematic of the set up.

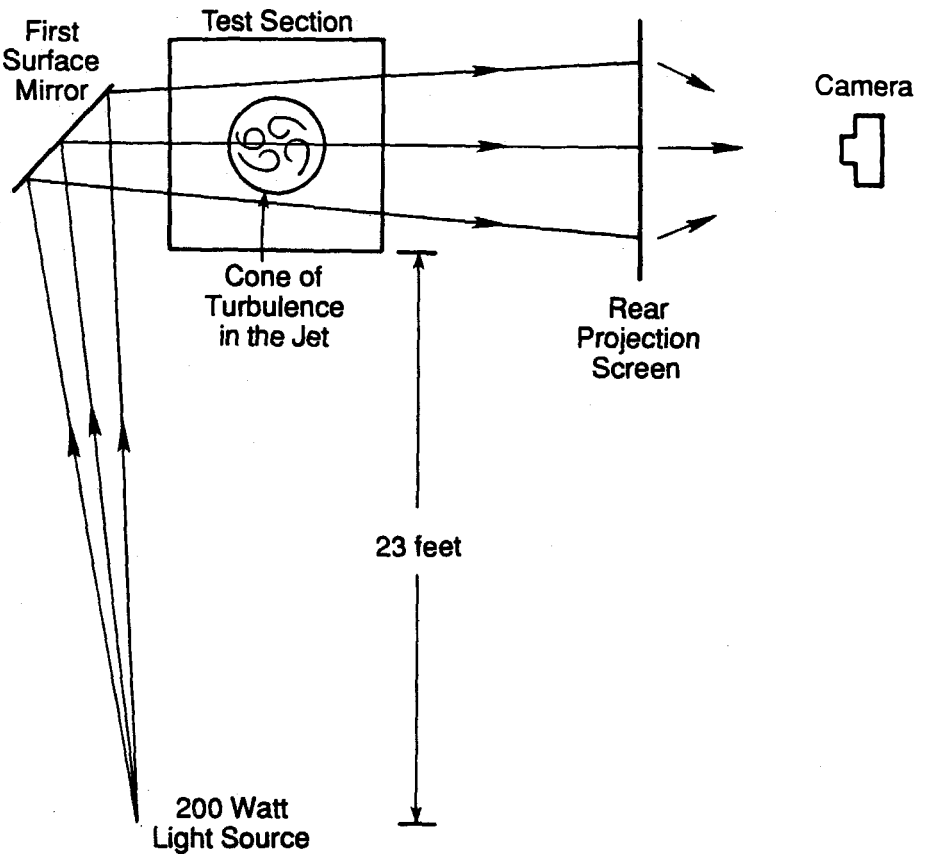

Figure 3-9. Schematic of the shadowgraph setup.

The shadowgraph image was formed as the spherically diverging white light from the arc lamp was refracted by index of refraction gradients at the interfaces between the jet and reservoir gases. The gases selected for the jet and reservoir for their Rayleigh scattering properties were also good choices for the shadowgraph technique. A more complete description of shadowgraph flow visualization can be found in Liepmann and Roshko (1957).

Figures 3-10 and 3-11 are shadowgraph pictures of the jet at $Re_0 = 5,000$ and 16,000. The visible full angle of the cone of turbulence is about 23^0 to 24^0 in both cases. The field of view is from 0 to 40 jet exit diameters for the picture at $Re_0 = 5,000$ and from 0 to 100 jet exit diameters for the picture at $Re_0 = 16,000$. The portion of the flow that is imaged in Figures 3-10 and 3-11 covers about half of the test section's length and less than one-third of its width.

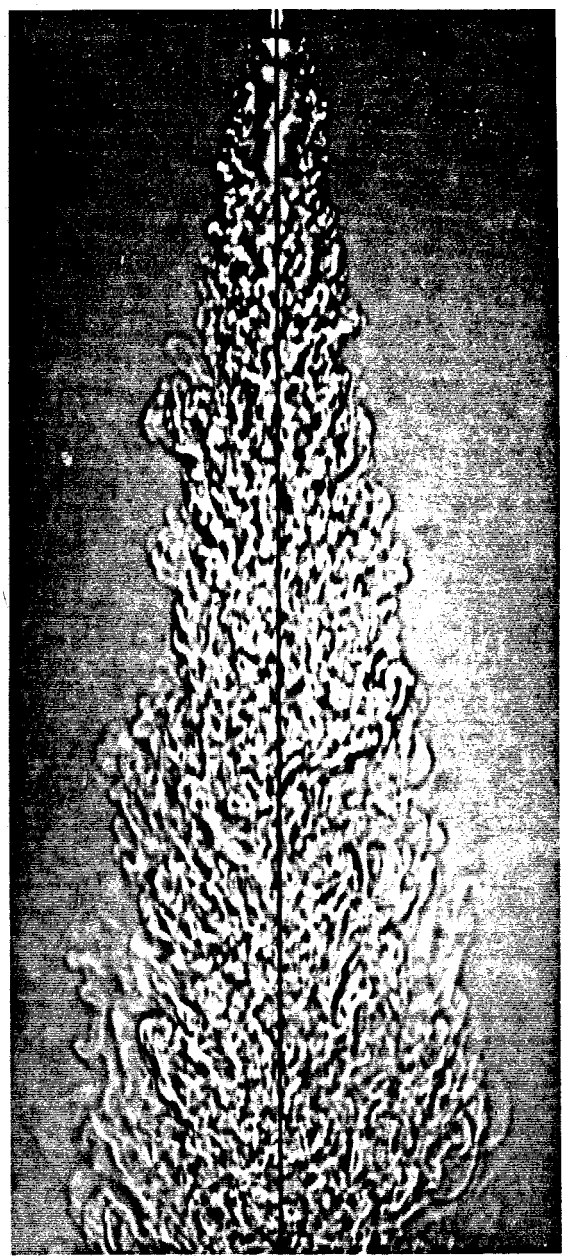

Figure 3-10. Shadowgraph picture of the jet at Re_0 = 5,000 for $0 \leq x/d \leq 40$.

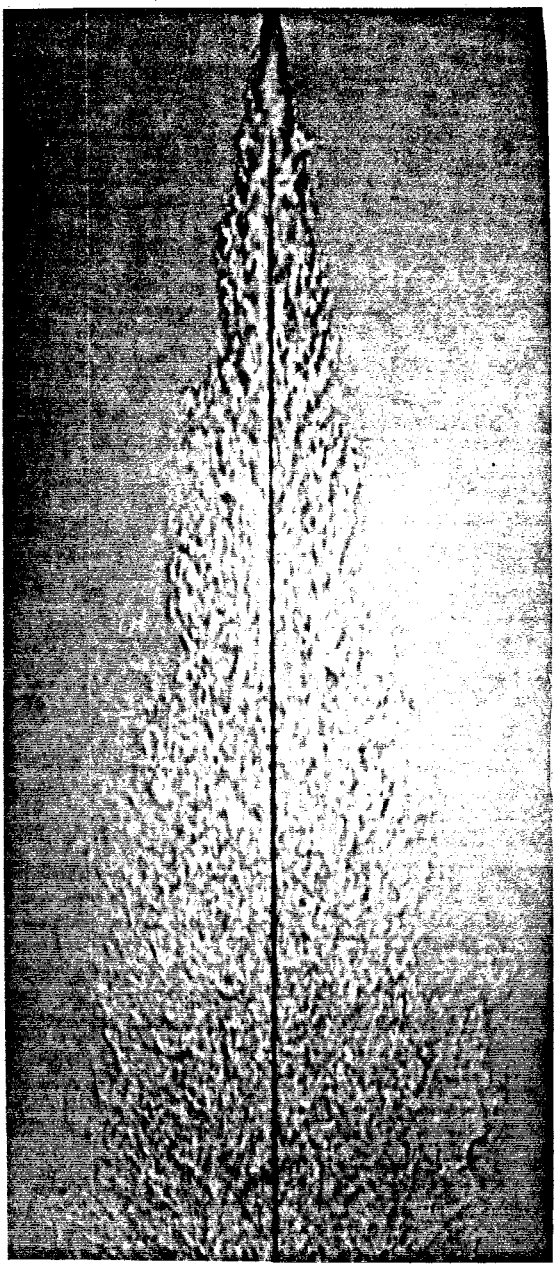

Figure 3-11. Shadowgraph picture of the jet at $Re_0 = 16{,}000$ for $0 \leq x/d \leq 100$.

CHAPTER 4

POWER SPECTRA OF CONCENTRATION FLUCTUATIONS

4.1 Normalization and Scaling of Jet Spectra

The power spectrum of concentration fluctuations, $E_c(f)$, was calculated from each of the sampled data sets using the method described in Appendix C. The overall normalization chosen was:

$$\left[2 \int_0^\infty E_c(f)\, df \right]^{1/2} = C'_{rms}, \tag{4.1}$$

which makes the connection between the power spectrum and the rms level of each data set. The independent variable is the frequency, f (in Hertz).

If the spectra have the same similarity as the mean concentration, they should collapse when scaled by the mean concentration and an appropriate time scale. The unscaled spectra have the units of concentration squared, multiplied by time (see Equation C.1). The time scale chosen, τ_D, is defined by:

$$\tau_D = \frac{D}{\bar{U}_{cl}}, \tag{4.2}$$

where D is the local diameter of the jet's turbulent cone (see Figure 1-1), and $\bar{U}_{cl}$ is the estimated mean centerline line velocity calculated from the formula suggested by Chen and Rodi (1980). τ_D should be the largest time scale associated with the jet flow for any particular downstream location. The actual numerical expression used to compute τ_D

is given in Appendix A, Section 4.

In the far field of the jet, the local diameter grows linearly with $(x - x_0)$ and the centerline velocity decays like $1/(x - x_0)$, so τ_D is proportional to $(x - x_0)^2$. Because there is a single Reynolds number associated with the far field of the jet, *the general mean-flow similarity actually dictates that all jet time scales, which are related by a power of the Reynolds number, will have a quadratic dependence on the downstream coordinate.* For example, the passage time of the Kolmogorov scale, τ_K, also increases quadratically with $(x - x_0)$ and is related to τ_D by a factor of $Re_0^{-3/4}$.

The plots presented in the next section display $E_c(f)$ on the vertical axis divided by the local value of $\bar{C}^2 \cdot \tau_D$, and f on the horizontal axis multiplied by τ_D. This scaling makes both axes dimensionless. The spectral plots were made in log-log coordinates, so the numerical factors involved in computing the time scale, τ_D, only shift the plots relative to the numerical values on the axes and do not affect the spectral shapes. Consequently, other time scales with the same quadratic dependence on the downstream coordinate will produce the same collapse seen in the spectra presented on Figures 4-1 to 4-6.

4.2 The Measured Spectra at Reynolds Number 5,000 and 16,000

For the data at $Re_0 = 5{,}000$, the power spectra of the concentration fluctuations at x/d = 20, 40, 60, and 80, along the three rays at $r/(x-x_0) \approx 0$ (centerline), .06 (3.4° off the centerline) and .12 (7° off the centerline) are plotted on Figures 4-1, 4-2 and 4-3. The visual

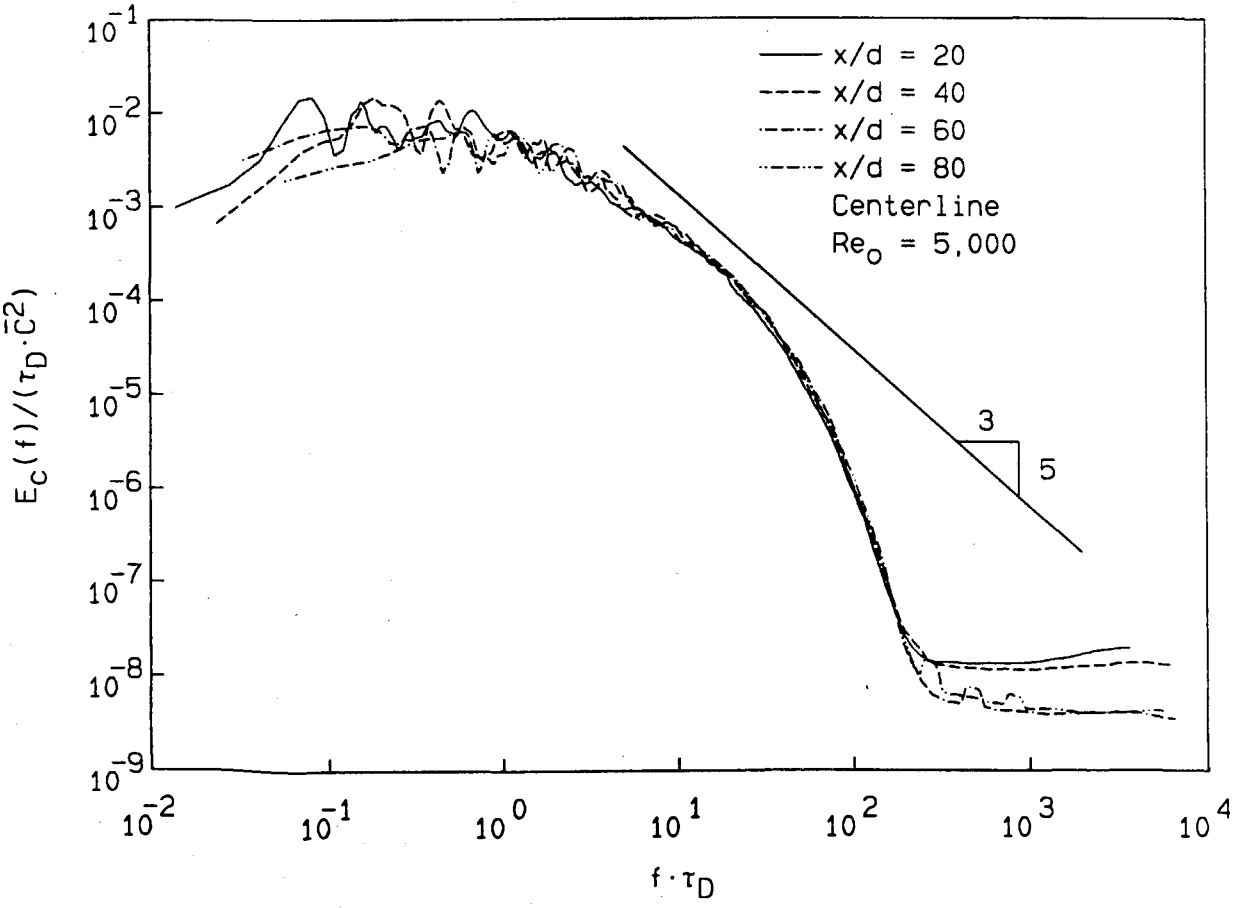

Figure 4-1. Scaled power spectra of the concentration fluctuations on the jet centerline at $Re_0 = 5{,}000$.

edge of the jet is about 12° from the centerline (e.g., White 1974, or

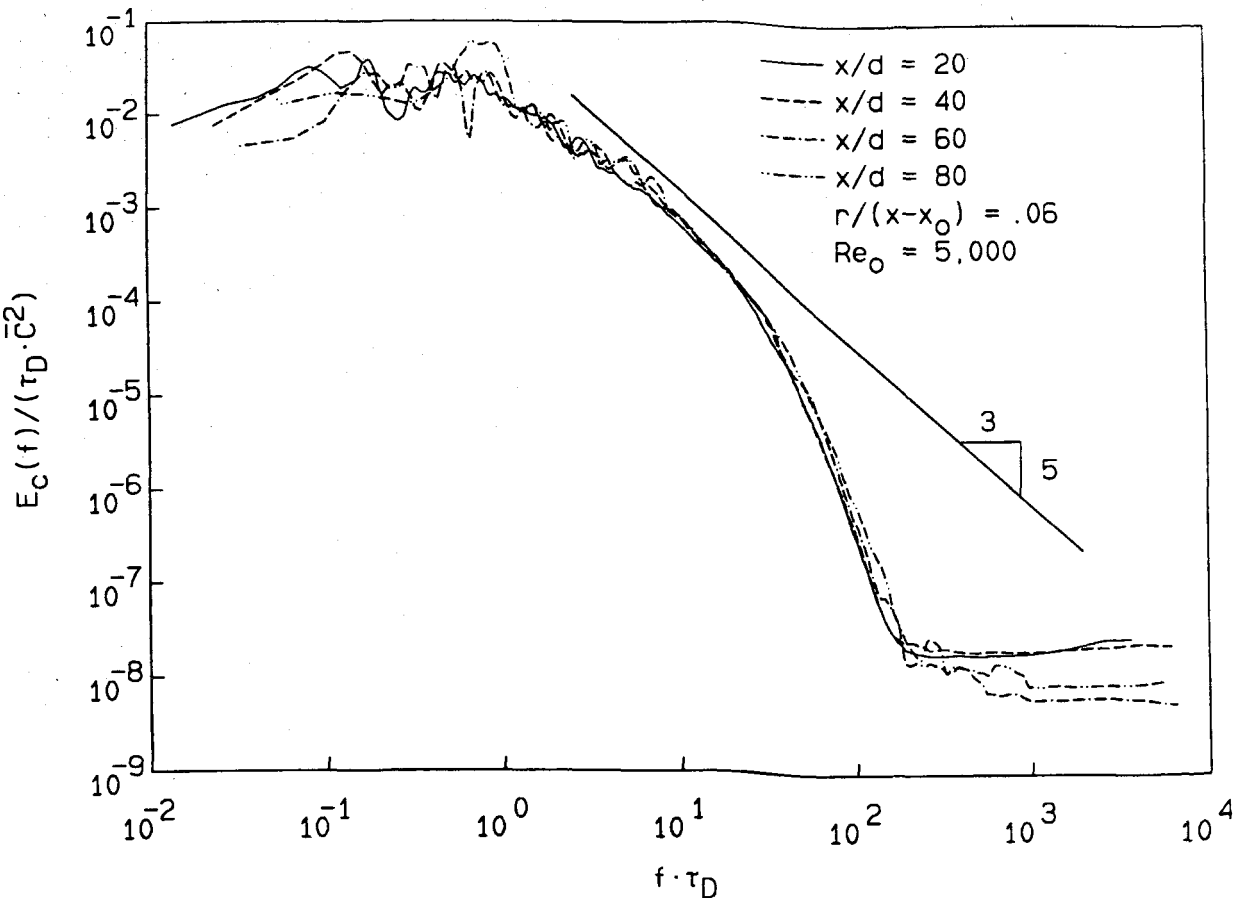

Figure 4-2. Scaled power spectra of the concentration fluctuations 3.4° off the jet centerline at Re_o = 5,000.

Chapter 3, Section 3). The nearly horizontal region of the spectra at the high values of $f \cdot \tau_D$ is the noise floor produced by the first stage of amplification in the photo-detection system. The small bumps that occur in the "noise-tails" are at the scaled values of 60 Hz, 120 Hz, and 360 Hz.

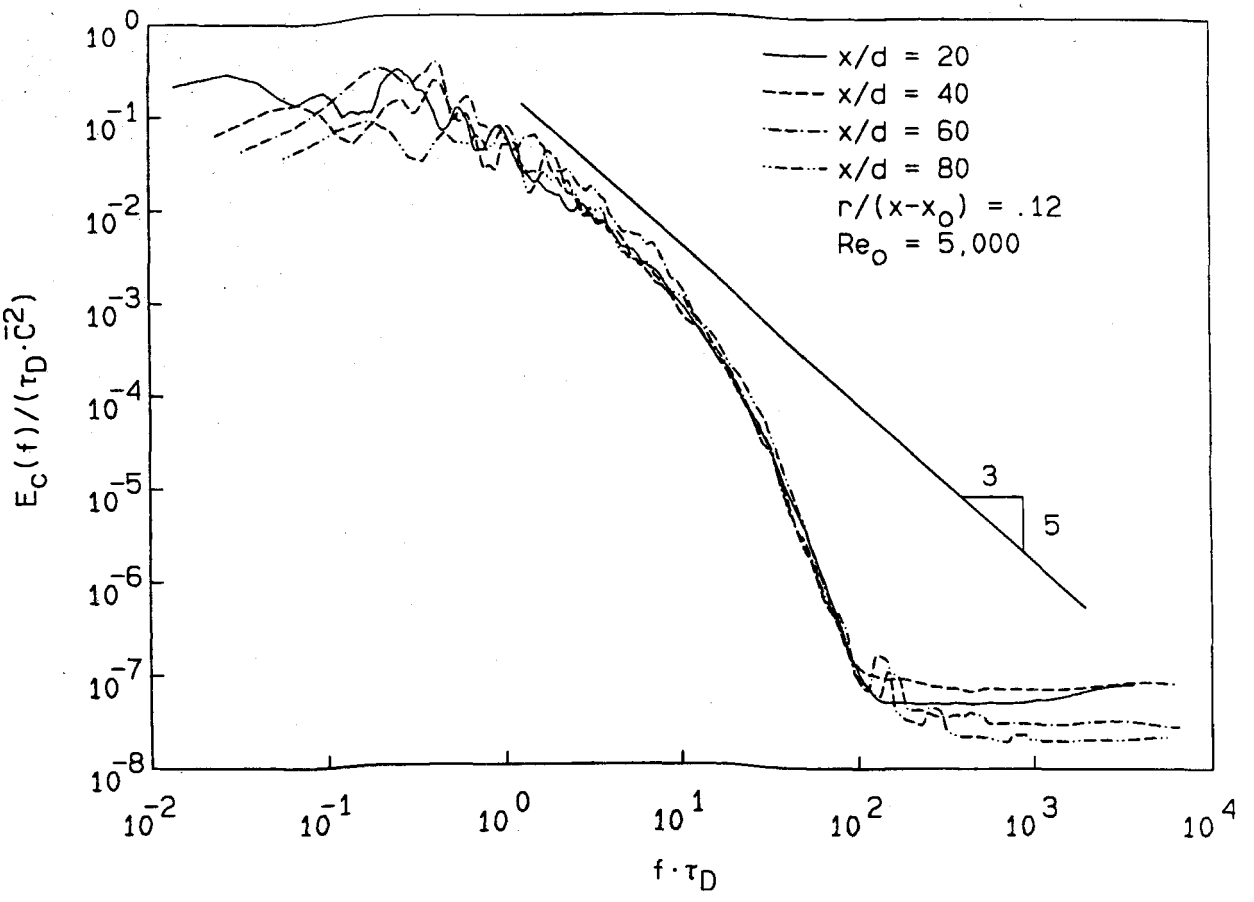

Figure 4-3. Scaled power spectra of the concentration fluctuations 7° off the jet centerline at Re_0 = 5,000.

The spectra collapse well in spite of the modest Reynolds number of the flow. Deviations, which are more evident as the edge of the jet is approached, are believed to be mainly due to decreased statistical convergence. In particular, for a fixed run time at a given downstream location, the total mass of fluid that passes through the focal volume

is roughly proportional to the local mean velocity. Consequently, the effective sample size of the run is smaller near the edge of the jet, where the mean velocity is lower. Other reasons for the deviations could be small variations in Re_0 from run to run, which slightly shift the frequency content of the jet's spectra, and minor angular differences ($\pm.2^0$) of the measurement locations from the exact positions along a given ray. The quality of the collapse displayed on Figures 4-1, 4-2, and 4-3 for the spectra of concentration fluctuations and Figure 3-5 for C'_{rms} is strong verification that *C'_{rms} and $\overline{C}$ have the same specific similarity throughout the jet*. $E_c(f)$ and C'_{rms} are related through Equation (4.1), so Figure 3-5 is an integral measure of the specific similarity of $E_c(f)$.

The adequacy of the temporal resolution of the measurements is evident in the spectra through the "noise-tails." The adequacy of the spatial resolution can also be inferred from the spectra. The diameter of the sensitive area of the photodiode utilized in each experiment, Δy, can be used along with $\overline{U}_{cl}$ to create an equivalent passage frequency, f_e, for length scales of size Δy ($f_e = \overline{U}_{cl}/\Delta y$). For the plotted data on Figures 4-1 to 4-3, $f_e \cdot \tau_D$ is greater than or equal to 650, so if there was any effect on the measurements from the finite spatial resolution of the detection system, it would be manifest in the spectra for $f \cdot \tau_D \gtrsim 650$. Because this region of the spectra falls within the "noise-tail" for all of the plotted results, the portion of the spectra at frequencies below $f \cdot \tau_D \approx 650$ and above the noise level are believed to be free of any resolution difficulties.

The value of the scaled Kolmogorov length-scale, passage frequency, $f_K \cdot \tau_D$, which should be the same as the scaled Batchelor length-scale, passage frequency, $f_B \cdot \tau_D$, at Sc = 1.0 (Batchelor 1959, Monin and Yaglom 1975), was calculated from the reservoir kinematic viscosity, ν_∞, the formula for the centerline energy dissipation rate, $\bar{\varepsilon}$, suggested by Friehe et al. (1971), and $\bar{U}_{cl}$, in particular:

$$f_K = \bar{U}_{cl}\left(\frac{\bar{\varepsilon}}{\nu_\infty^3}\right)^{1/4} \quad \text{or} \quad f_K \cdot \tau_D = 1.12\,\mathrm{Re}_0^{3/4} = \frac{D}{\lambda_K}, \tag{4.3}$$

The numerical value of $f_K \cdot \tau_D$ is about 670 at $\mathrm{Re}_0 = 5{,}000$. At high Reynolds number and a Schmidt number of order unity, the spectrum of turbulent scalar fluctuations should display a $-5/3$ power-law region and the Kolmogorov (Batchelor) length-scale, passage frequency should roughly correspond to the high frequency end of this region (Batchelor 1959, Gibson 1968, Monin and Yaglom 1975). While the plotted spectra are clearly not from a high Reynolds number flow, the scaled frequency range in which they begin to fall more rapidly than a constant power-law is more than an order of magnitude lower than 670. This discrepancy between the measured and calculated break points has also been reported by Clay (1973), who worked with data from a heated jet at a Reynolds number of almost 10^6.

At the low frequency end, $f \cdot \tau_D \leq 1$, the spectra are approximately flat or show a mild peak in the range $.1 < f \cdot \tau_D < 1$. While this behavior is consistent with the passage of structures whose scale is approximately the same as the local jet diameter, the most general conclusion to be drawn is that the fluctuations that occur at

frequencies below $1/\tau_D$ do not have a greater amplitude than those that occur near $1/\tau_D$. Consequently, the turbulent cascade at this Re_0 must start near $f \cdot \tau_D \approx 1$.

It is also worth noting that although the spectra collapse along rays when scaled by the mean concentration and τ_D, the spectra are different from ray to ray. In particular, the spectra along the ray at 7^0 show a longer power-law region with a slope closer to -5/3 than those for the inner rays. This latter behavior is also apparent in the spectra of Lockwood and Moneib (1980) at x/d = 20 in a heated air jet at $Re_0 = 50,000$. A more complete comparison with other experimental results will be presented in the next section.

For the data recorded at $Re_0 = 16,000$, the spatial and temporal resolution specifications, employed for the runs at $Re_0 = 5,000$, were relaxed by about a factor of 3. These adjustments were made based on the results of the $Re_0 = 5,000$ studies in order to take greater advantage of the experiment's diagnostic capabilities. The changes position the calculated value of $f_e \cdot \tau_d$ right near the low frequency edge of the spectral "noise-tails" for the results at $Re_0 = 16,000$.

The spectra from the data taken at $Re_0 = 16,000$ are displayed on Figures 4-4, 4-5, and 4-6 for x/d = 30 and 90 along the rays $r/(x - x_0) \approx$ 0, .06, and .11 (6.3^0 off the centerline). The slopes of the diagonal lines on these Figures were chosen by eye and do not have a theoretical backing. The axis scaling used in these plots is the same as for the

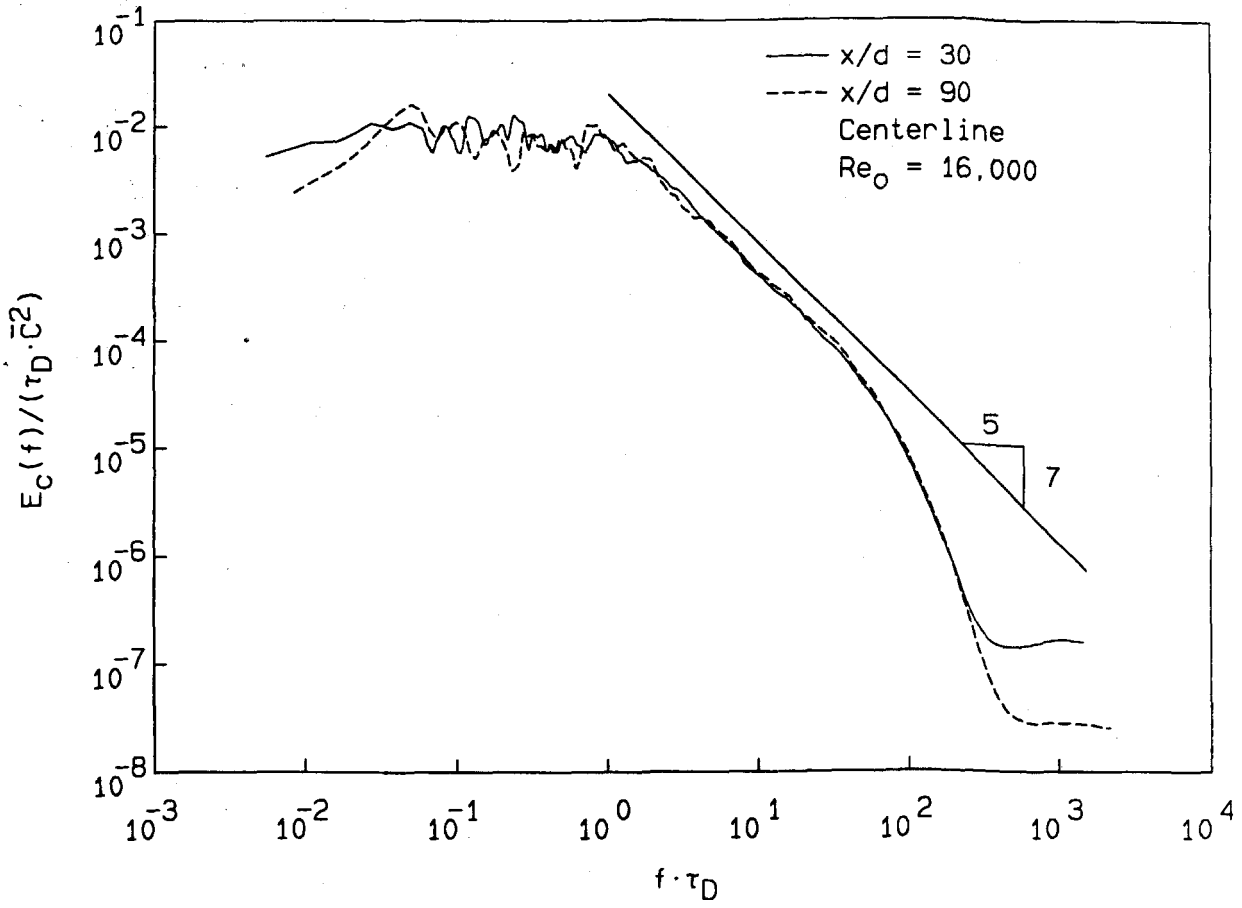

Figure 4-4. Scaled power spectra of the concentration fluctuations on the centerline of the jet at Re_0 = 16,000.

lower Reynolds number spectra except that the value of x_0 used to compute τ_D was derived from the mean-concentration profile collapse at $Re_0 = 16,000$. The quality of the collapse means that all of the conclusions from the lower Reynolds number concerning the specific similarity of C'_{rms} and $E_c(f)$ remain valid at $Re_0 = 16,000$. As before, incomplete statistical convergence, fluctuations in Re_0, and imperfect

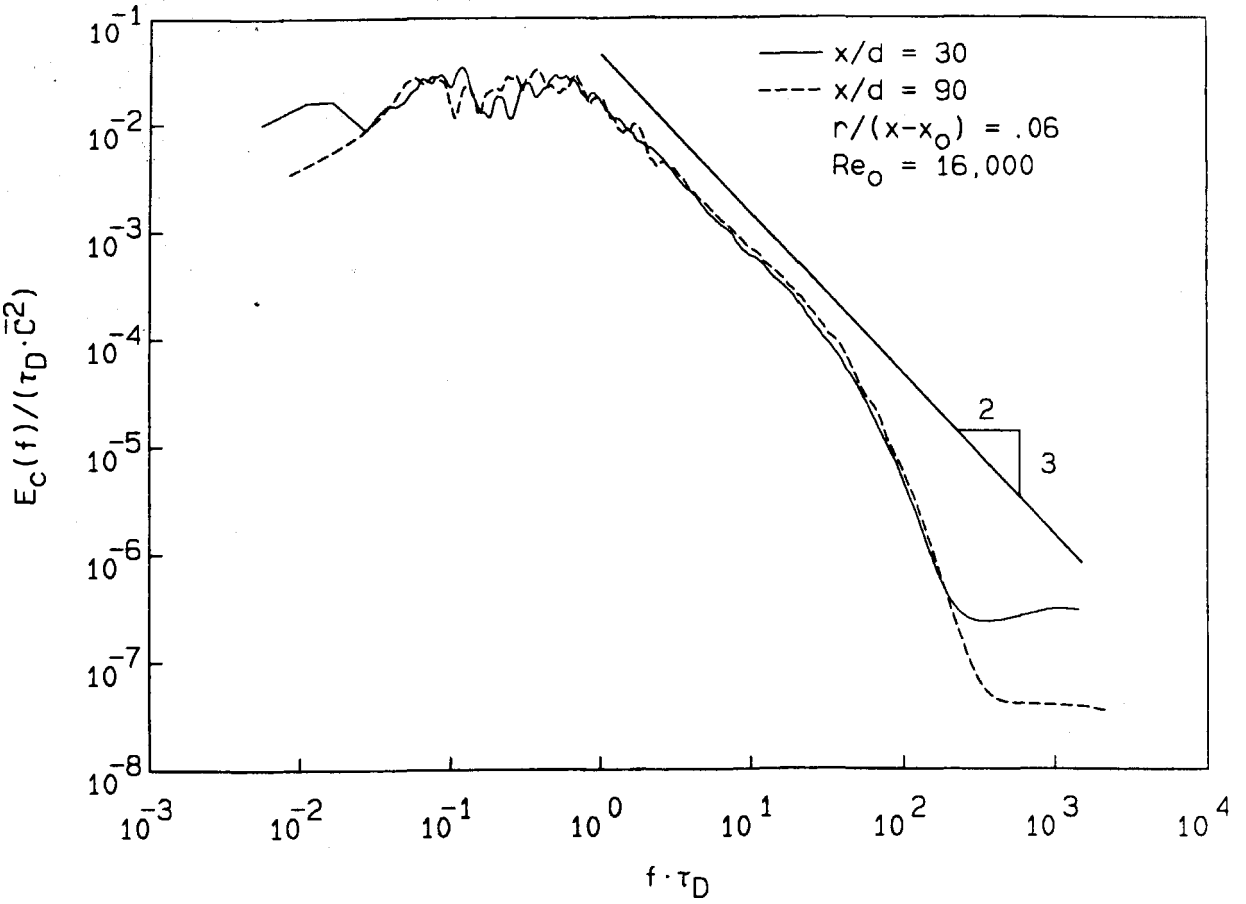

Figure 4-5. Scaled power spectra of the concentration fluctuations 3.4^{0} off the jet centerline at Re_{0} = 16,000.

angular alignment are probably responsible for the deviations from a perfect collapse. The value of $f_{e} \cdot \tau_{D}$ is about 490 for the data from x/d = 30 and about 580 for the data from x/d = 90. The estimate for $f_{K} \cdot \tau_{D}$ is 1,590 for Re_{0} = 16,000.

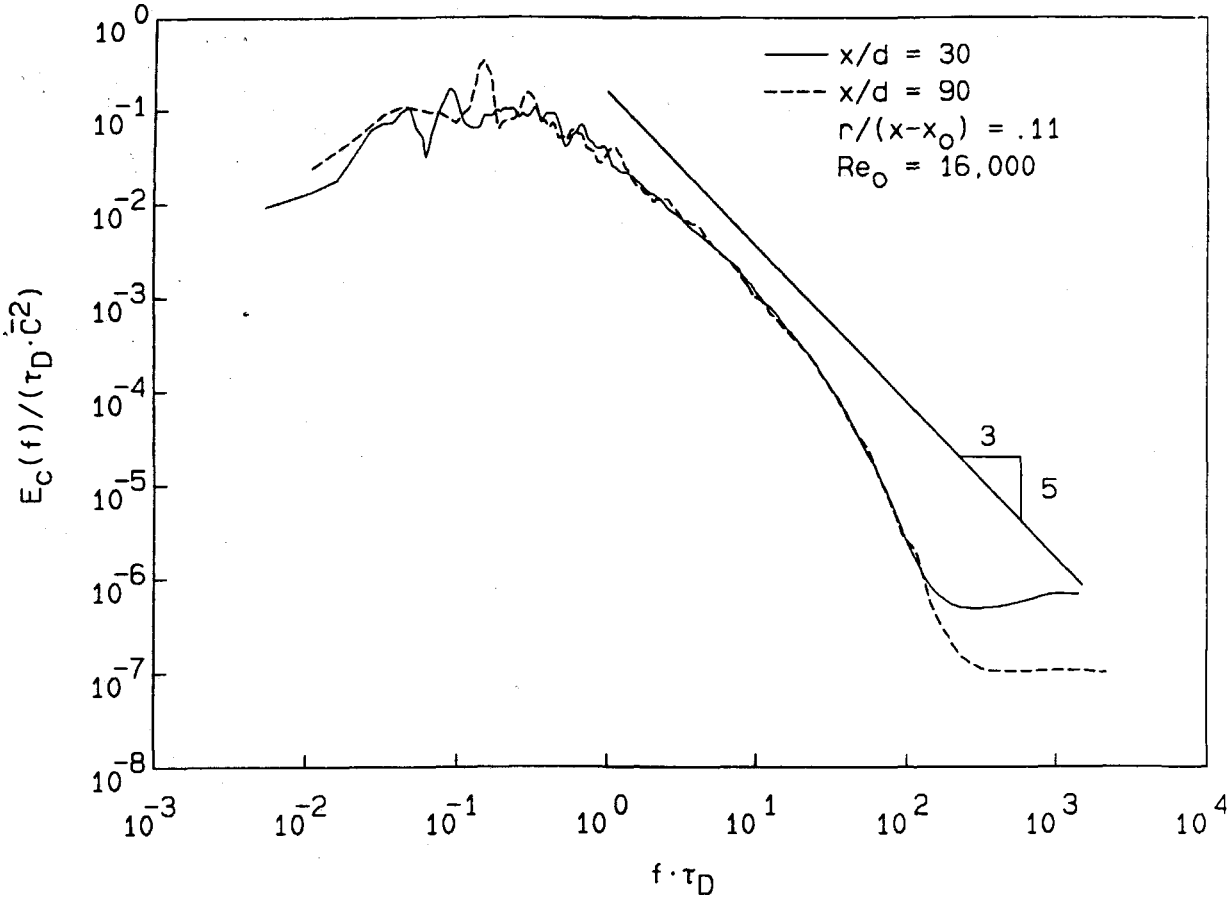

Figure 4-6. Scaled power spectra of the concentration fluctuations 6.3° off the jet centerline at Re_0 = 16,000.

These spectra show the same general shapes as those at $Re_0 = 5,000$ except for the appearance of a longer power-law regions, which extend the high frequency range of the spectra. The slope of the power-law region steepens as the edge of the jet is approached. The spectra from the centerline appear to have a slope of about -1.4, which decreases to

- 1.5 on the ray at $r/(x - x_0) = .06$, and the straightest part of the spectra from the ray at $r/(x - x_0) = .11$ has a slope close to - 5/3. The precise reasons for the emergence of power-law regions with powers other than - 5/3 are unknown and will be discussed further in Section 4 of this chapter. The low frequency end of the spectra has the same behavior as the spectra at the lower Reynolds number.

4.3 **Comparison of Scalar Power Spectra with Jet Scaling**

Figures 4-7 and 4-8 display the measured spectra from this experiment and other related jet experiments on the centerline and at $r/(x - x_0) = .12$. The scaling of the axes used in Figures 4-1 to 4-6 was retained because of the quality of the spectral collapse it produced at two different Re_0 over a range in x/d of 20 to 90. The parameters necessary to scale the spectra from other experiments, and make them satisfy the overall normalization (Equation 4.1), were taken from the author's papers in all but one case. The vertical location of the spectrum of Clay (1973) could not be determined because he did not include C'_{rms} among his results, nor report spectral values near $f \cdot \tau_D = 1$, where the other spectra seem to coincide (see Figure 4-7). The vertical location of Clay's spectrum on Figure 4-7 was chosen to match that of the spectrum of Becker et al. (1967), whose Reynolds number of 54,000 was closest to that of Clay's.

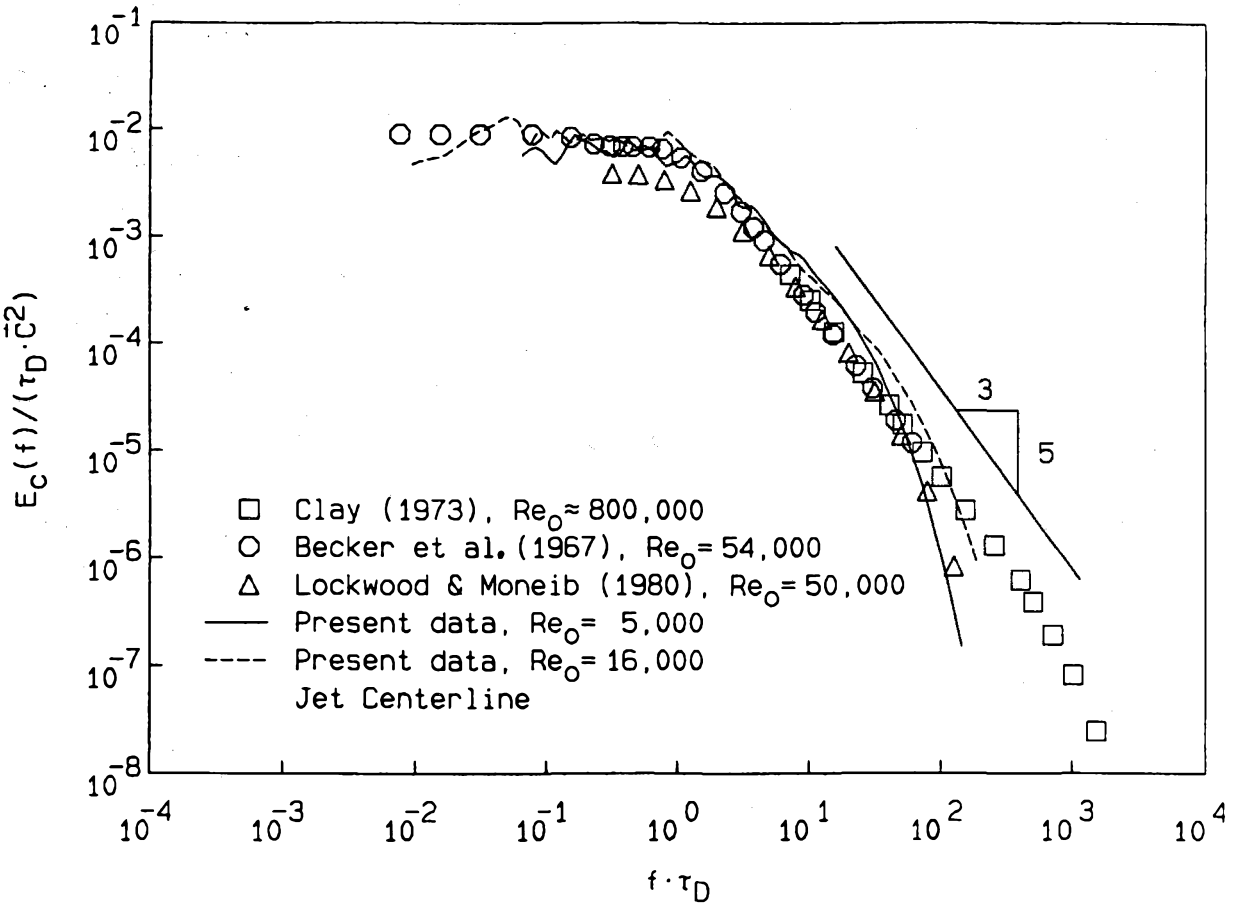

Figure 4-7. Comparison of the centerline concentration fluctuation power spectra to the results of other experiments with jet parameter scaling of the axes.

For the centerline spectra (Figure 4-7), the current results and those of Becker et al. agree quite well for $f \cdot \tau_D$ less than unity. This implies that the total amount of scalar fluctuation energy at the largest scales, with these normalizations, is independent of Re_0, beyond

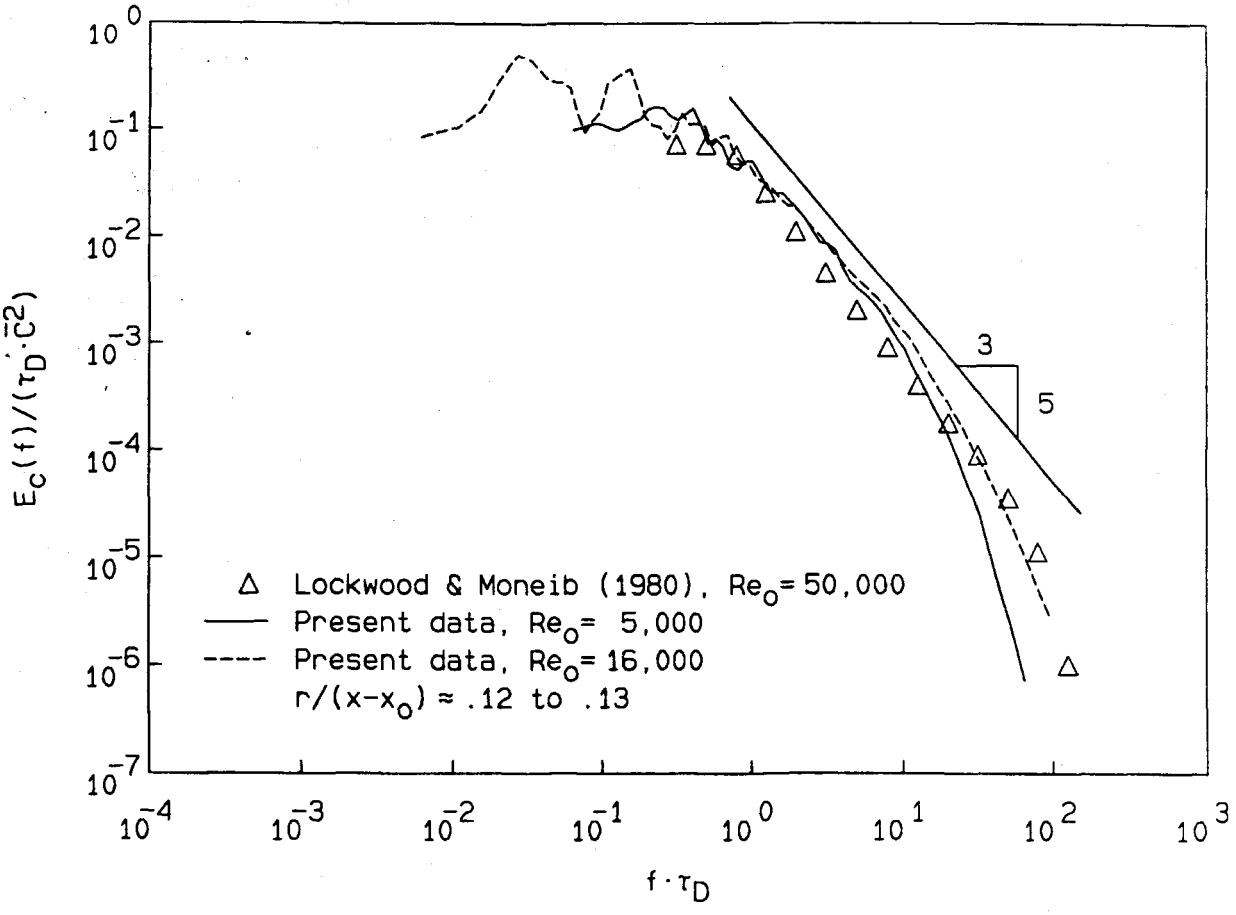

Figure 4-8. Comparison of the concentration fluctuation power spectra from -7° off the centerline to the results of Lockwood and Moneib (1980) with jet parameter scaling of the axes.

Re_o = 5,000. The centerline spectrum of Lockwood and Moneib (1980) probably falls below the others in this frequency range because their reported centerline rms level at the downstream location, where they measured their spectra (x/d = 20), is low ($C'_{rms} = .16\,\bar{C}$).

The spectra of Becker et al. and Clay follow a - 5/3 power law over a significant range, where as the results of the current studies do not. This may be due to Reynolds number effects, as will be seen more clearly in the next section. The spectrum of Lockwood and Moneib does not entirely coincide with that from Becker et al., even though their Reynolds numbers were very close. Table 3-1 contains the relevant parameters for these experiments. The observed mismatch might be the result of a resolution problem of some kind, since it is doubtful that the Schmidt number, which differed widely in these two studies, can affect the scalar fluctuation spectra at frequencies well below the dissipation range. It is worth noting that if the centerline spectrum of Lockwood and Moneib is raised so that its level is the same as that of the other spectra at $f \cdot \tau_D \approx 1$, it would be a close match with the current spectrum for $Re_0 = 16,000$.

Regardless of the exact spectral shapes or levels, two Reynolds number effects can be seen in Figure 4-7. The spectral level falls with increasing Reynolds number in the range $1 < f \cdot \tau_D < 10^2$ until a - 5/3 power-law behavior is reached. This power-law region matches smoothly to the Reynolds-number-independent, spectral level below $f \cdot \tau_D \approx 1$. The second effect is the movement of the break point, which is interpreted as the beginning of the dissipation range, where the spectrum starts to fall faster than a - 5/3 power-law, to higher frequency, as the Reynolds number is increased. The spectrum from Lockwood and Moneib was computed from data that were filtered above $f \cdot \tau_D \approx 50$, and therefore breaks from - 5/3 behavior at a lower frequency than expected.

If the dissipation break point is defined as the location at which the slope of the spectrum reaches -2, then, ignoring minor fluctuations, the break points of the current spectra are at $\log_{10}(f\cdot\tau_D) = 1.37$ and 1.73 for $Re_0 = 5{,}000$ and 16,000, respectively. The difference of these two is .36, which compares well to the logarithm of the expected ratio of Kolmogorov (Batchelor) length scales (see Equation 4.3), $\frac{3}{4}\log_{10}(16{,}000/5{,}000) = .38$. The dissipation break points of the spectra of Becker et al., and Lockwood and Moneib were not measured by these authors. Clay's dissipation break point is near $\log_{10}(f\cdot\tau_D) \approx 2.9$. The logarithm of the expected ratio of Batchelor scales for his flow and the current results at $Re_0 = 16{,}000$ is $\frac{3}{4}\log_{10}(800{,}000/16{,}000) = 1.27$, which compares reasonably well with the observed difference in location, $2.9 - 1.73 \approx 1.17$, of the break points of the spectra. The mismatch may result from Schmidt (Prandtl) number effects. A further discussion of this issue is taken up in the next section.

The present results for the location of the break point on the centerline concentration fluctuation spectra can be used to correct the dimensionless constant in the Kolmogorov length-scale, passage frequency formula:

$$\left(f_K\right)_{measured} = .0343 \pm .006\ \overline{U}_{cl}\left(\frac{\overline{\varepsilon}}{\nu_\infty^3}\right)^{1/4} \tag{4.4}$$

or equivalently,

$$\left(f_K\right)_{measured}\cdot\tau_D = .0384 \pm .007\ Re_0^{3/4}. \tag{4.5}$$

Spectra for the ray at $r/(x - x_0) \approx .12$ are depicted in Figure 4-8. The differences between the present results and those of Lockwood and Moneib are most likely due to differences in experimental resolution and possible misalignment with respect to the chosen ray. As mentioned before, the length of the portion of the spectra with a nearly constant slope is longer at higher values of Re_0, and the spectra from the present data display a longer -5/3 range when compared to the spectra from the centerline at the same Reynolds number.

4.4 Comparison of Scalar Power Spectra with Universal Scaling

Figure 4-9 is a plot of the current centerline spectra at both Reynolds numbers with the spectrum of Clay (1973) in the universal Kolmogorov coordinates suggested by Gibson (1968 II). The following definitions apply:

$$\Gamma_K(k) = \frac{\Gamma(k)}{\Sigma_K^2 \lambda_K} = \text{Universal scalar spectrum} \tag{4.6}$$

$$\text{with} \quad \int_0^\infty \Gamma(k)\, dk = C'^2_{rms}, \quad k = \text{wave number} \tag{4.7}$$

$$\lambda_K = \left(\frac{\nu_\infty^3}{\bar{\varepsilon}}\right)^{1/4} = \text{Kolmogorov length scale,} \tag{4.8}$$

$$k_K = \lambda_K \cdot k = \lambda_K \cdot 2\pi f\, U_{cl}^{-1} \approx 2\pi (f \cdot \tau_D)(\lambda_K/D) = \text{dimensionless wave number,} \tag{4.9}$$

$$\Sigma_K^2 = \bar{\varepsilon}_c \left(\frac{\nu_\infty}{\bar{\varepsilon}}\right)^{1/2} = (\text{Kolmogorov scalar scale})^2, \tag{4.10}$$

$$\bar{\varepsilon}_c = 6 D_{j\infty} \bar{U}_{cl}^{-2} \left(\overline{\dot{C}(t)^2}\right) = \text{estimated scalar dissipation rate.} \tag{4.11}$$

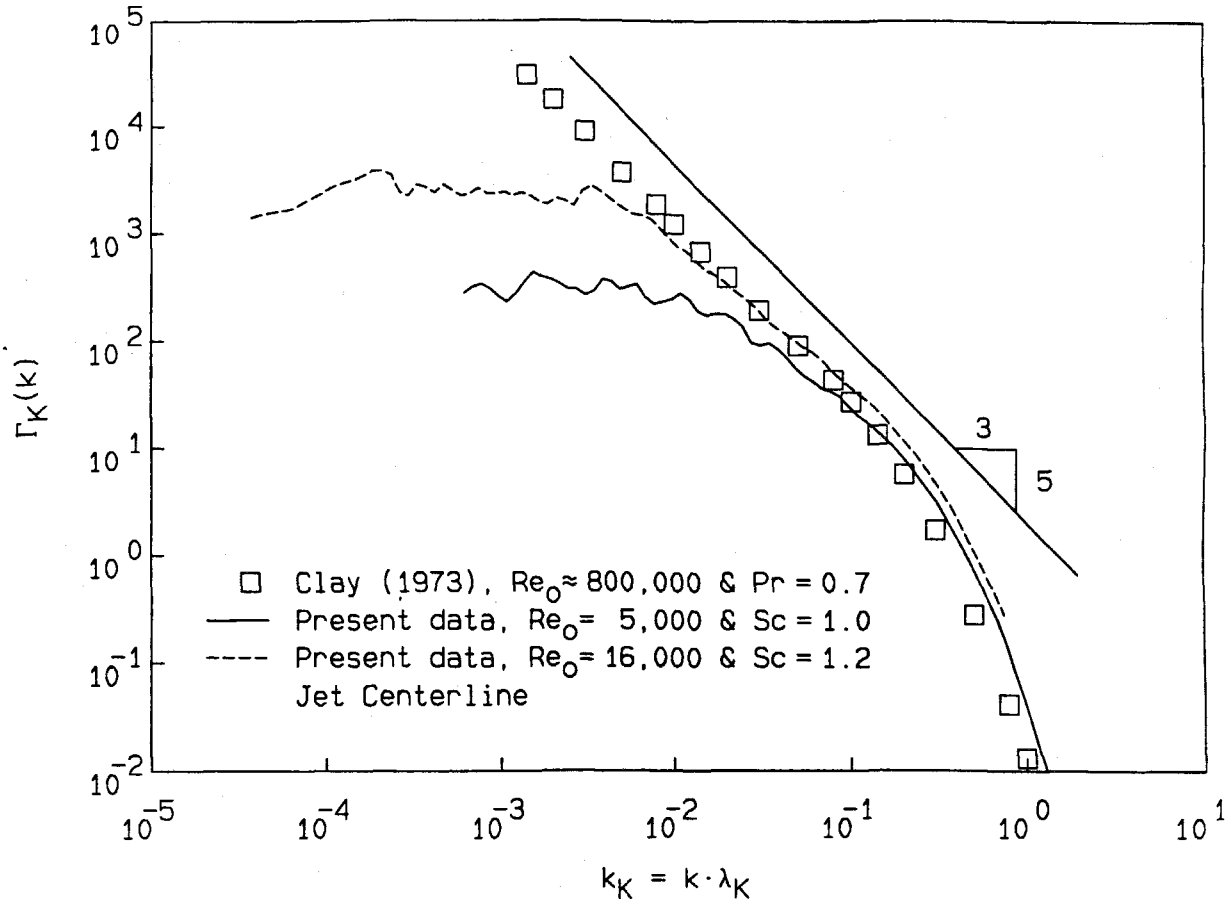

Figure 4-9. Comparison of the centerline concentration fluctuation power spectra to the results of Clay (1973) with universal Kolmogorov coordinate scaling of the axes.

Most of these symbols and definitions are the same as those used by Clay (1973). The universal Kolmogorov scaling of the spectrum is related to the jet parameter scaling on Figures 4-1 to 4-8 by:

$$\Gamma(k) = \frac{\bar{U}_{cl}}{\pi} E_c\left(\bar{U}_{cl} \cdot \frac{k}{2\pi}\right). \qquad (4.12)$$

The estimated scalar dissipation rate, ε_c, is the subject of Chapter 7. $D_{j\infty}$ is the diffusion coefficient of jet gas into reservoir gas. $\bar{\varepsilon}$ and $\bar{U}_{cl}$ are estimated from Friehe et al. (1971) and Chen and Rodi (1980), as was explained earlier.

The universal coordinates should collapse spectra with different Reynolds numbers, but with the same Schmidt number, in the dissipation range. The wave number scaling of the horizontal axis puts the value of k_K corresponding to the Kolmogorov length scale at $k_K = 2\pi$. Gibson's theory predicts that $\Gamma_K(k)$ in the dissipation range should shift to higher wave numbers as the Schmidt (Prandtl) number is increased. This shift is predicted to be proportional to the square root of the Schmidt (Prandtl) number ratio, when two flows with different Schmidt (Prandtl) numbers near unity are compared. Clay's spectrum is from a heated jet with Pr = 0.7 . The current results from $Re_0 = 5,000$ and 16,000 are for Sc = 1.0 and 1.2, respectively. The shift in $\log_{10}(k_K)$ between the current spectra at $Re_0 = 5,000$ and Clay's spectra near $k_K \approx 1$ on Figure 4-9 is slightly less than a tenth of a decade. This difference compares well to Gibson's theory, which would predict a shift of $.08 = \frac{1}{2}\log_{10}(1.0/.7)$. The predicted shift in $\log_{10}(k_K)$ between the current spectra at $Re_0 = 5,000$ and 16,000 is $.04 = \frac{1}{2}\log_{10}(1.2/1.0)$. In this case it is difficult to determine the actual shift precisely, but it appears to be very near the predicted value.

The universal collapse shows that Re_0 = 5,000 and 16,000 for the turbulent jet are not high enough to produce an inertial range in the measured scalar power spectra. Because Clay's spectrum and the spectrum of Becker et al. (see Figure 4-7), which were measured at much higher values of Re_0, do display an inertial range, it must be concluded that the rounded spectrum at Re_0 = 5,000 and the -1.4 power-law, found at Re_0 = 16,000 on the centerline of the jet, are artifacts of the particular values of Re_0. It is possible that the -1.4 slope at Re_0 = 16,000 might result from the near coincidence of the end of an "immature" turbulent cascade with the beginning of a dissipation range bump in the centerline spectrum.

Even though the current Reynolds numbers were not high enough to produce a classical inertial range cascade, Figure 4-9 shows that at scales in the dissipation range, the results from these studies match the predicted universal similarity behavior when compared to the dissipation range of Clay's spectrum. This feature of the current measurements implies that the results presented in Chapter 7 for the scalar dissipation rate might apply to flows with Reynolds numbers well above 5,000 or 16,000.

CHAPTER 5

PROBABILITY DENSITY FUNCTION OF CONCENTRATION

The power spectrum of concentration fluctuations for each data set was used to estimate the optimal filter (Wiener 1949) for that data set, following the procedure formula given by Press et al. (1986). After each data set was filtered, a histogram of the instantaneous concentration divided by the the local mean concentration, $C/\overline{C}$, was compiled by sorting the data into bins. This histogram was normalized; i.e.,

$$\int_0^\infty PDF(C/\overline{C})\, d(C/\overline{C}) = 1, \qquad (5.1)$$

to form a probability density function, $PDF(C/\overline{C})$. The variable, $C/\overline{C}$, was chosen because dividing C by $\overline{C}$ should remove the effects of the mean downstream concentration decay. At a fixed Reynolds number, the probability density function of $C/\overline{C}$ should depend only on $r/(x - x_0)$, if the statistical properties (higher moments) of the distribution of concentration fluctuations in the jet follow the same specific similarity as the first moment, $\overline{C}$.

5.1 **Results at Reynolds Number 5,000 and 16,000**

Figures 5-1, 5-2, and 5-3 display the measured probability density functions of $C/\overline{C}$ along three rays at $r/(x - x_0) \approx 0$, .06, and .12 for x/d = 20, 40, 60, and 80 at $Re_0 = 5{,}000$. The quality of the collapse of

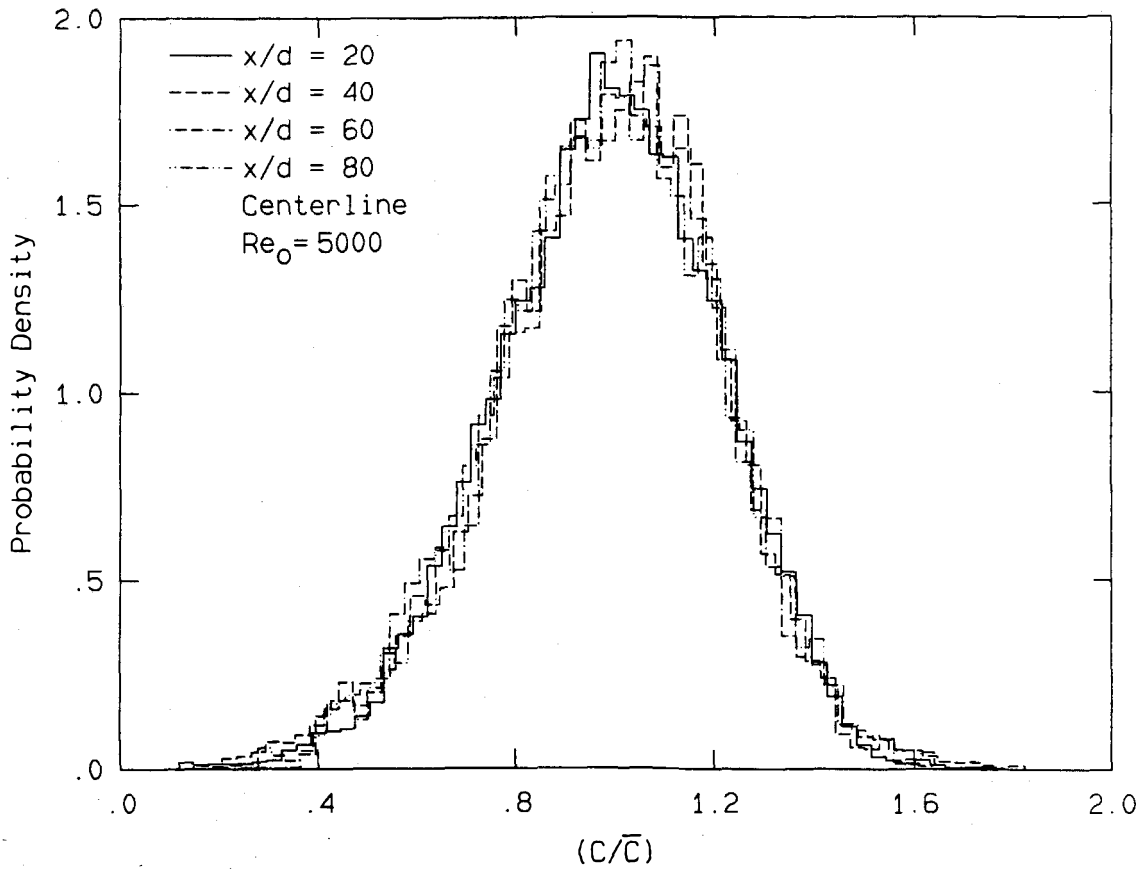

Figure 5-1. Probability density function of the scaled concentration on the jet centerline at Re_0 = 5,000.

the distributions along rays implies that $C/\overline{C}$ is the proper specific

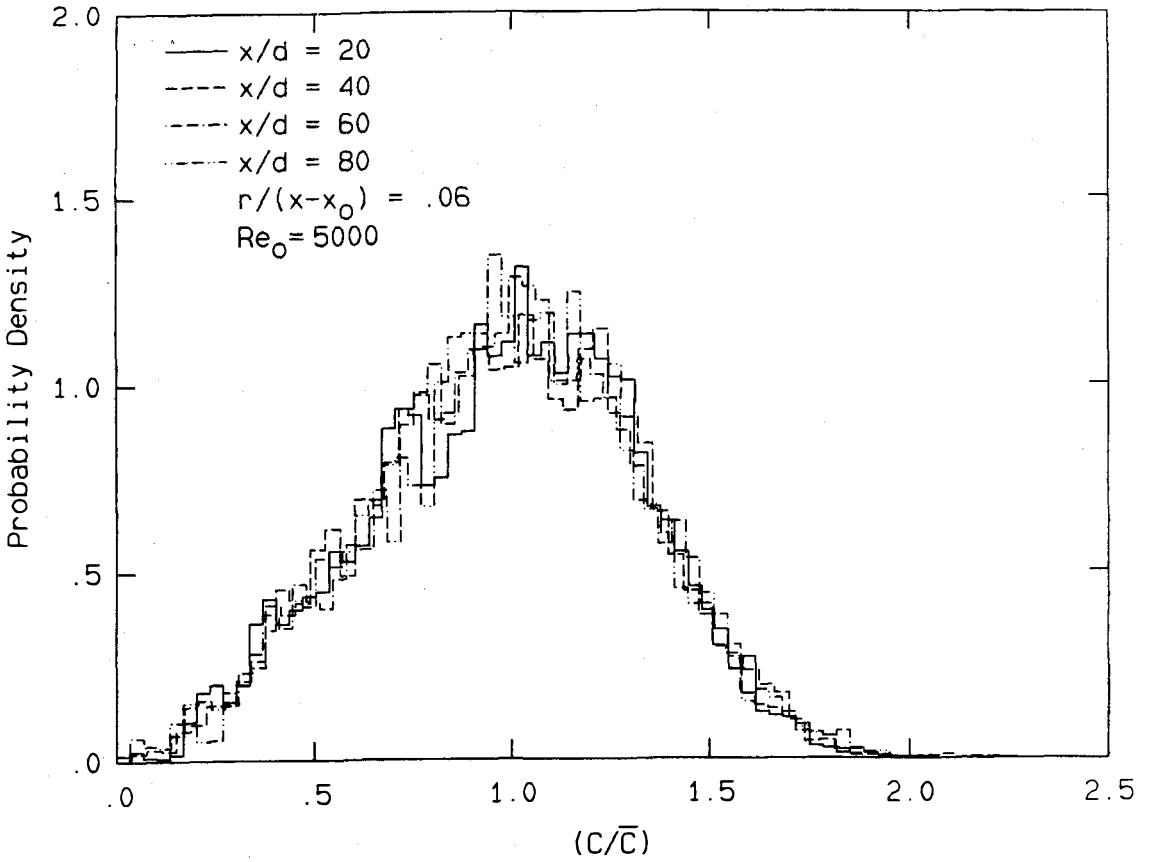

Figure 5-2. Probability density function of the scaled concentration 3.4^{0} off the jet centerline at Re_{0} = 5,000.

similarity variable and that the moments of the PDF($C/\overline{C}$) are independent of the downstream position in the jet. For example, the square root of the second moment of each PDF, taken about $C/\overline{C} = 1$, is $C'_{rms}/\overline{C}$, which was previously shown to depend only on $r/(x - x_0)$ (see Figure 3-5 and the discussion in Chapter 3, Section 2). Slight imperfections in the collapse are believed to be due to incomplete statistical convergence

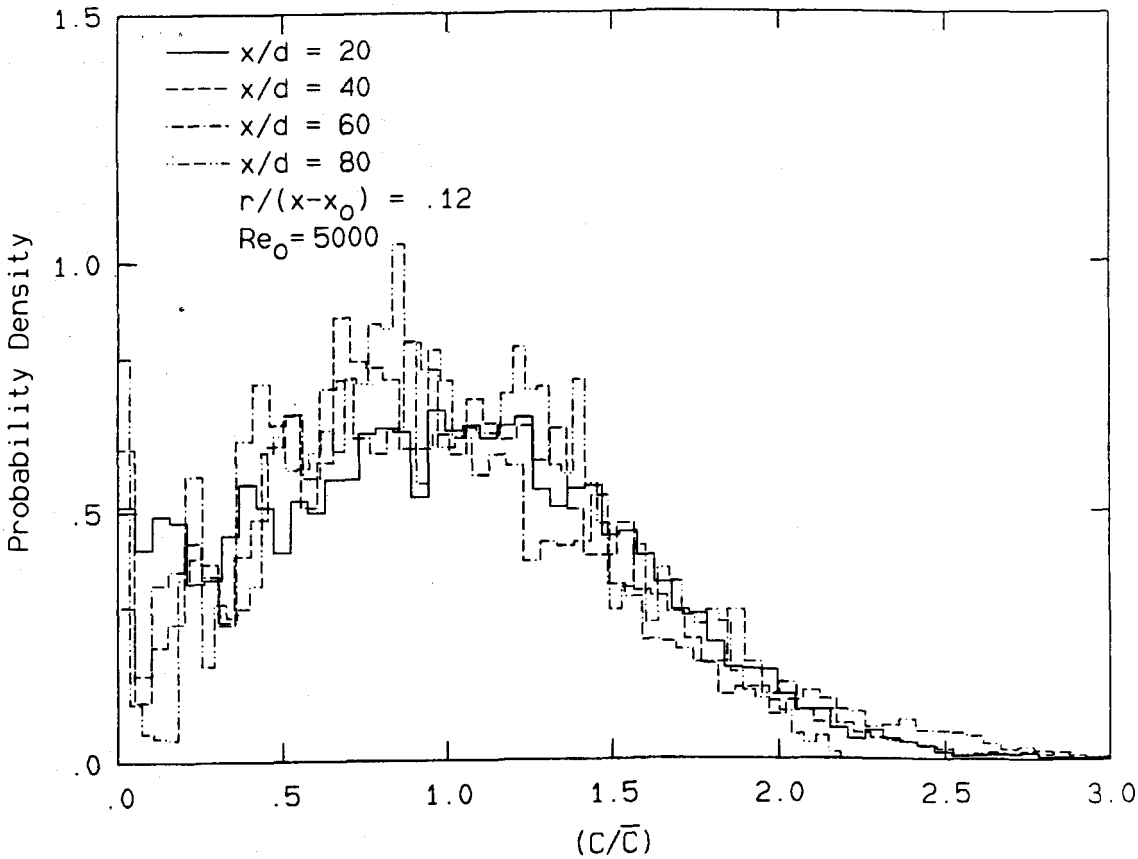

Figure 5-3. Probability density function of the scaled concentration 7° off the jet centerline at Re_0 = 5,000.

and possible imperfect alignment of the measurement point with respect to the chosen ray.

Figures 5-4, 5-5, and 5-6 display the measured probability density functions of $C/\overline{C}$ along three rays at $r/(x-x_0) \approx .00$, .06, and .11 to .12 for x/d = 30 and 90 at $Re_0 = 16,000$. The quality of the collapse is

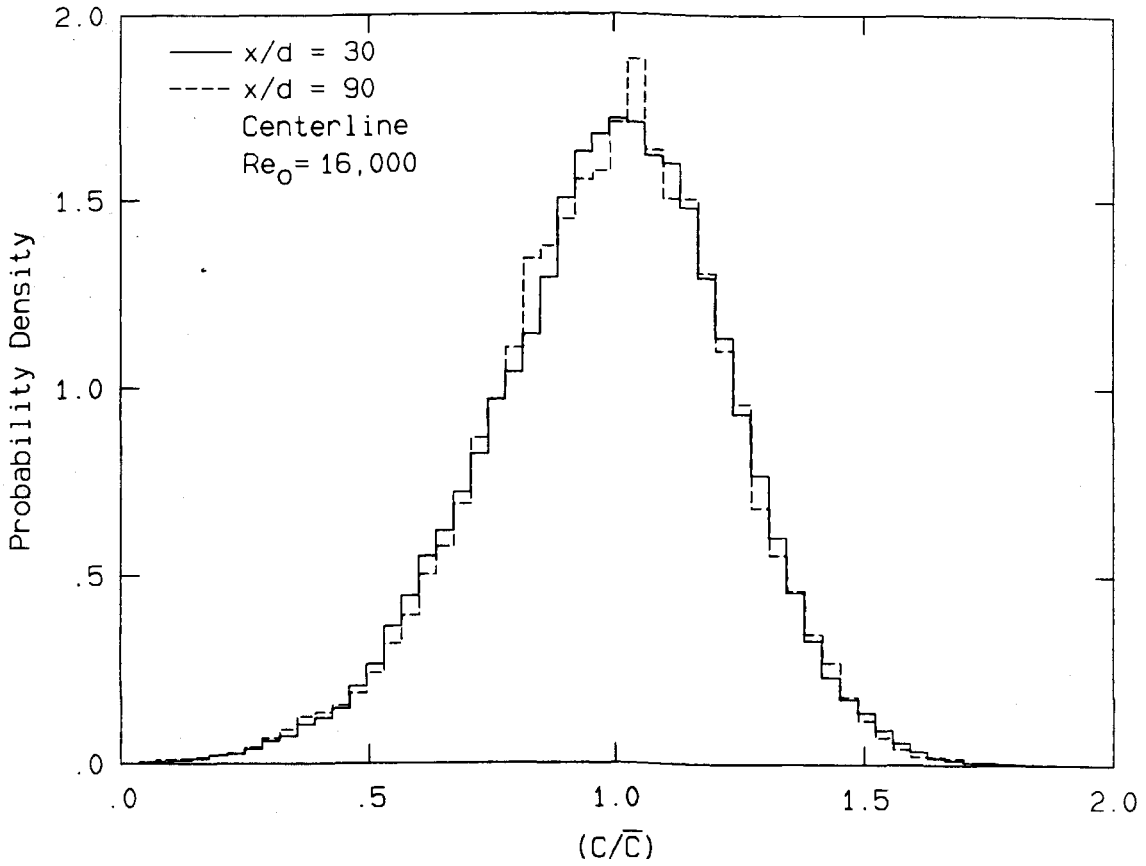

Figure 5-4. Probability density function of the scaled concentration on the jet centerline at Re_0 = 16,000.

good, implying that the proposed specific similarity variable, $C/\overline{C}$, for the PDF is a *general* similarity variable, even though the actual shape of the PDF might depend on Re_0. The Reynolds number dependence of the shape of the PDF of $\overline{C}/C$ and its consequences are discussed in Sections 2 and 4 of this chapter. Imperfections in the collapse at this Reynolds number may be attributed to the same problems mentioned above.

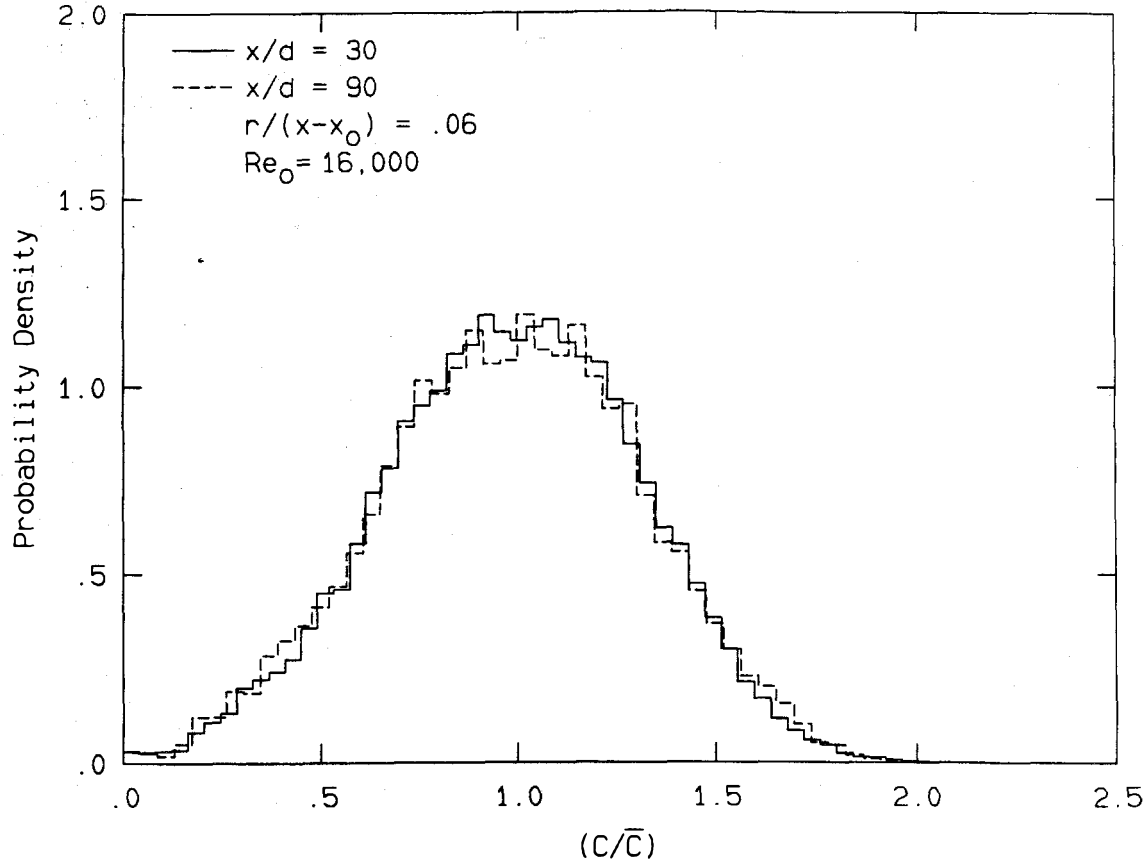

Figure 5-5. Probability density function of the scaled concentration 3.4^{0} off the jet centerline at Re_{0} = 16,000.

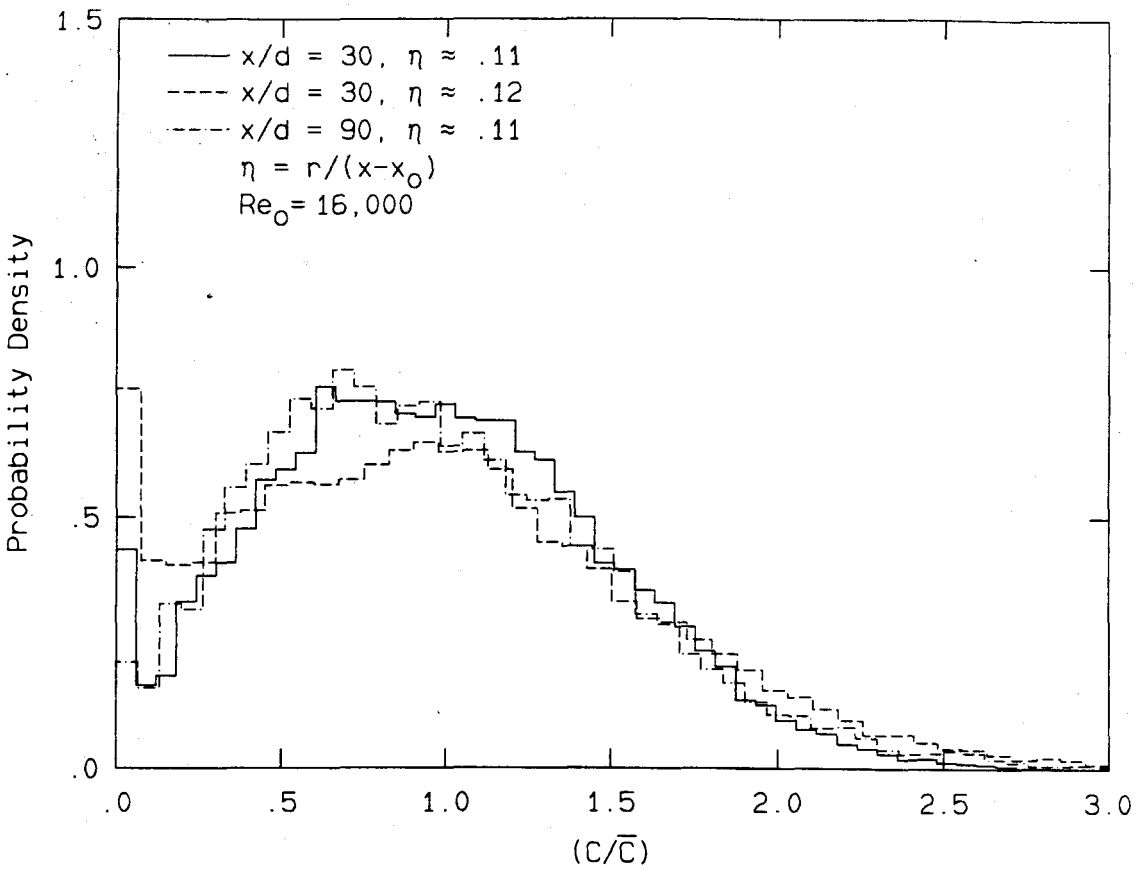

Figure 5-6. Probability density function of the scaled concentration 6.3^0 to 7^0 off the jet centerline at Re_0 = 16,000.

5.2 **Reynolds Number and Schmidt Number Comparisons**

Figure 5-7 is a comparison of the centerline PDF at the two Reynolds numbers. It was created from Figures 5-1 and 5-4 by averaging and smoothing the histograms. The differences in the two distributions

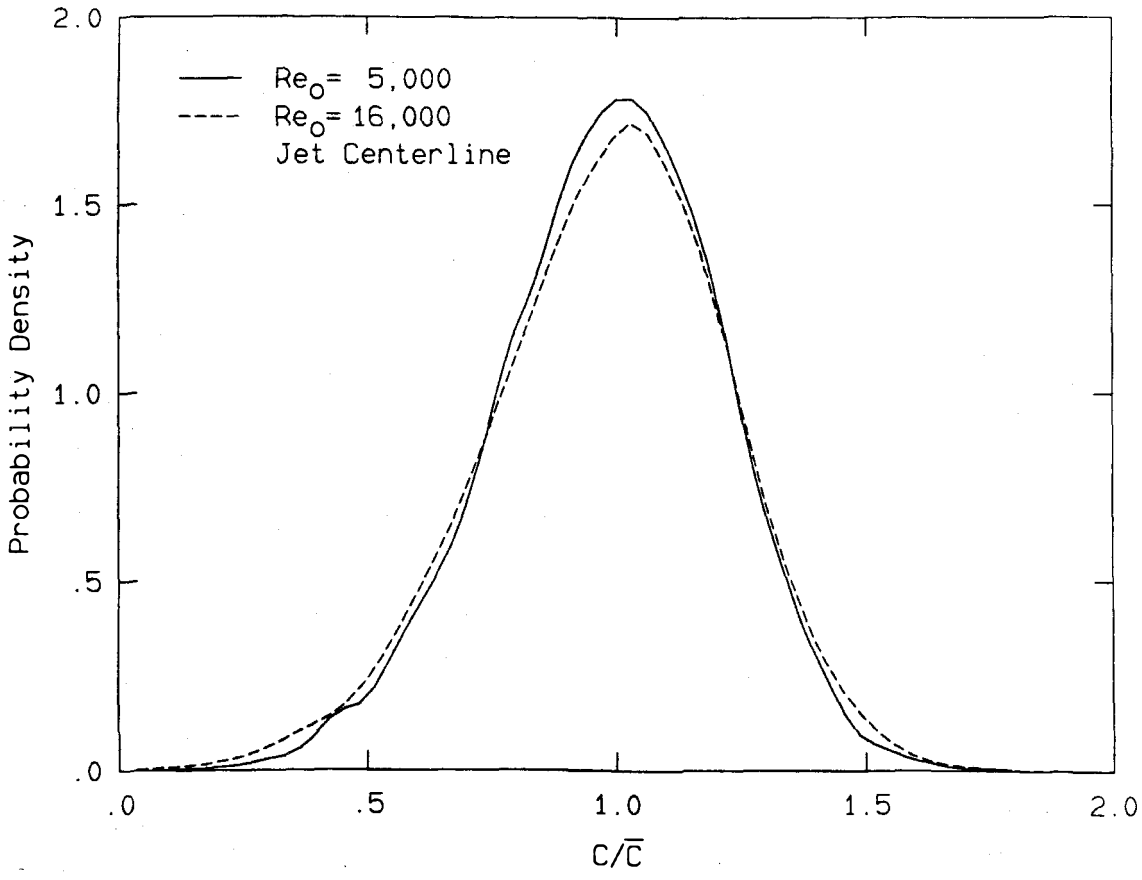

Figure 5-7. Averaged and smoothed probability density functions of the scaled concentration on the centerline of the jet at Re_0 = 5,000 and 16,000.

on Figure 5-7 are not large and are difficult to identify in the

statistical scatter of the individual histograms on Figures 5-1 and 5-4. This is also the case for the PDFs along the rays at $r/(x - x_0) = .06$ and .11 to .12. The principal difference seen on Figure 5-7 is that the PDF from the jet at $Re_0 = 16,000$ is slightly wider and a little shorter than the PDF from the jet at $Re_0 = 5,000$. This is consistent with the slightly higher value of $C'_{rms}/\overline{C}$ on the centerline at the higher Reynolds number.

Even though the estimated PDFs are in close agreement at both values of Re_0, the details of the mixing are not necessarily independent of Reynolds number. In particular, the value of the mean concentration decay constant, κ, is about 8% larger at $Re_0 = 5,000$ than at $Re_0 = 16,000$ (see Chapter 3, Section 1), and because the variable $C/\overline{C}$ removes this difference, comparisons between Figures 5-1 to 5-3, and 5-4 to 5-6 conceal this discrepancy. Additionally, the "inertial-range" portion of the power spectra of concentration fluctuations depends on Re_0, at least to values near 50,000 (see Chapter 4), so perhaps $PDF(C/\overline{C})$ does also, if only to a small extent.

At least one Schmidt number effect can be identified in $PDF(C/\overline{C})$ when the current results at $Re_0 = 5,000$ are compared to those of Dahm (1985), who worked at the same Reynolds number but at $Sc \approx 600$ to 800. He found pure reservoir fluid on the jet centerline a small fraction of the time. This is not the case for the current study in gas phase jets. *Pure reservoir fluid, $C/\overline{C} = 0$, was never found on the centerline in the $Re_0 = 5,000$, $Sc = 1.0$ jet.*

5.3 The Structure of the Probability Density Function

Figures 5-8 to 5-13 display time histories of the optimally smoothed concentration and the resulting accumulated PDF of concentration. The time span over which each PDF was accumulated is written at the top of each PDF plot. The displayed data on each Figure start from the same place in the chosen data sets so that the traces cascade from one plot to the next. For example, the top trace on Figure 5-9 corresponds to all of the data plotted on Figure 5-8 and the top trace on Figure 5-10 corresponds to all of the data plotted on Figure 5-9. The same pattern applies to Figures 5-11 to 5-13. Figures 5-8 to 5-10 are from the centerline of the jet at $x/d = 60$ and $Re_0 = 5,000$. Figures 5-11 to 5-13 are from the centerline of the jet at $x/d = 90$ and $Re_0 = 16,000$. In all of these plots, time is normalized by τ_D. The differences in the actual concentration levels on these plots are not important since the PDF is self-similar in the mean.

Both sets of plots show that the PDF of concentration is basically composed of many "spikes" of concentration. The "spikes" arise from portions of the data in which there is very little variation in concentration. Comparison of the shapes of the final PDFs on Figures 5-10 and 5-13 with the shape of the centerline similarity PDF, Figures 5-1 and 5-4 or Figure 5-7, shows that the convergence to a mean PDF is incomplete even after $16\,\tau_D$. It is also worth noting that within a particular large scale time, there are perhaps only about half a dozen individual concentration levels being mixed by the jet turbulence. This is best seen on the top plots of Figures 5-9 and 5-12, where the PDFs

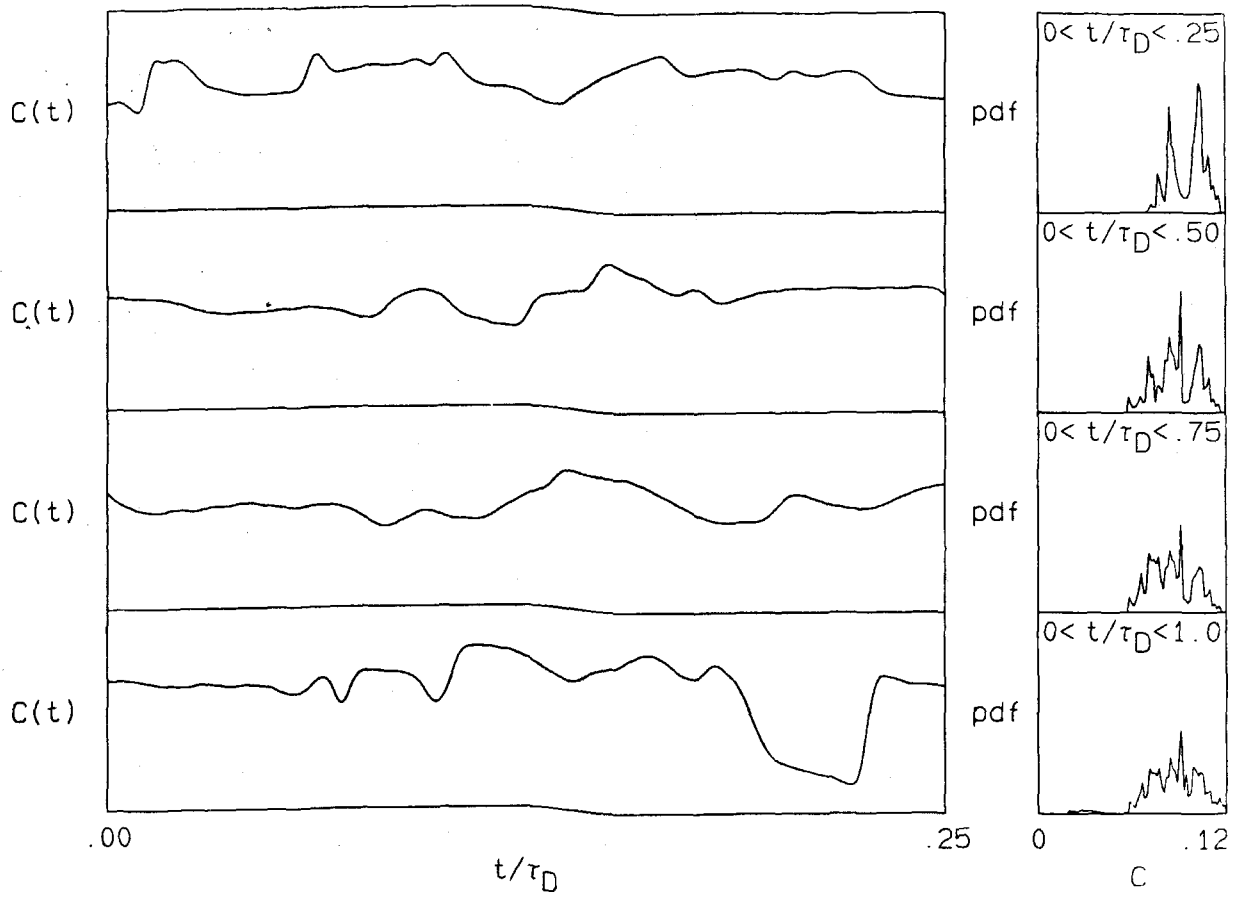

Figure 5-8. Time traces of C(t) and accumulated PDFs at Re_0 = 5,000 on the jet centerline with about .25 τ_D per line.

accumulated from a single large scale time are plotted.

Figures 5-8 to 5-13 also point out two differences in mixing at these two values of Re_0. The PDF of concentration appears to converge to a smooth shape more quickly at $Re_0 = 16,000$ than at $Re_0 = 5,000$, and the mixing at $Re_0 = 16,000$ takes place along a larger number of

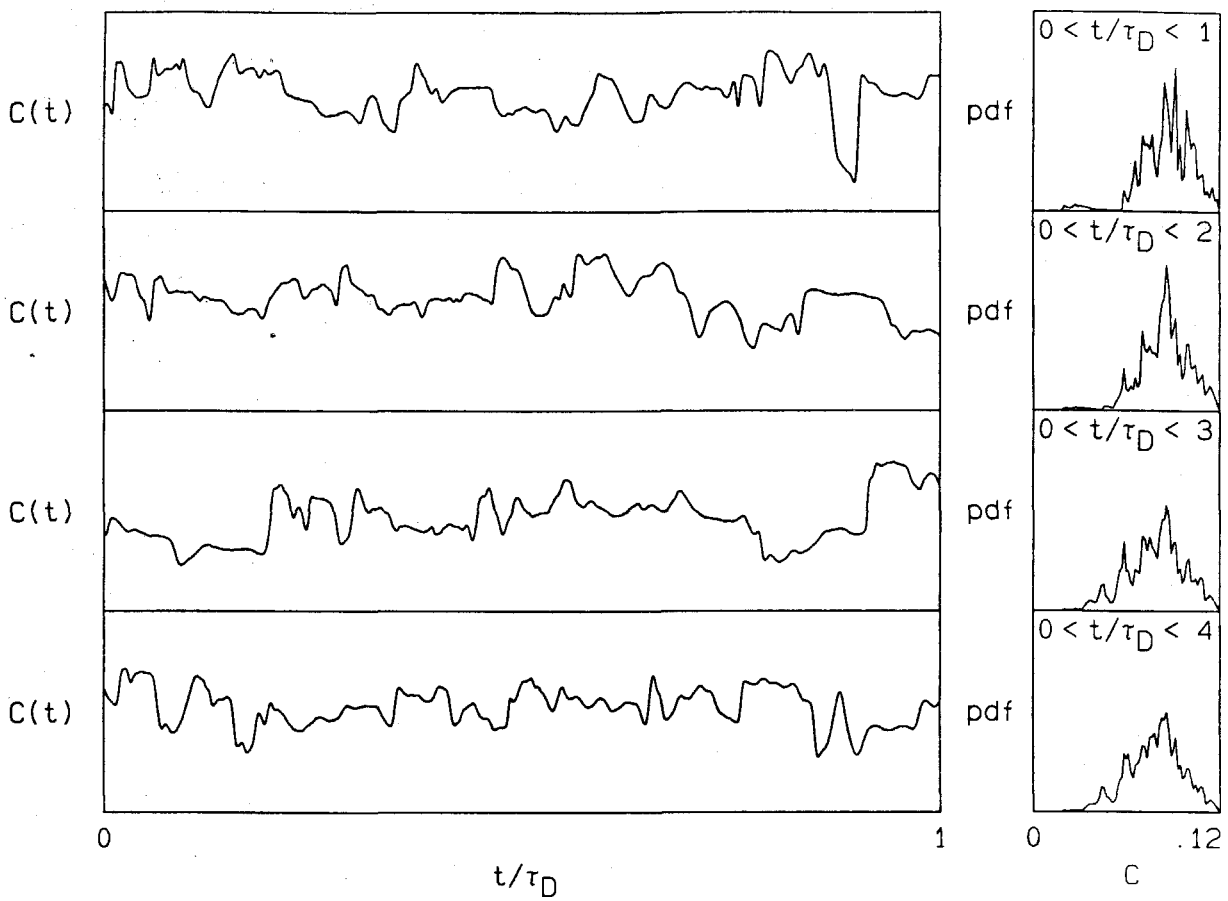

Figure 5-9. Time traces of C(t) and accumulated PDFs at Re_0 = 5,000 on the jet centerline with about 1 τ_D per line.

concentration gradients, per large scale time, than at $Re_0 = 5,000$. The latter of these differences is consistent with the increase in Re_0.

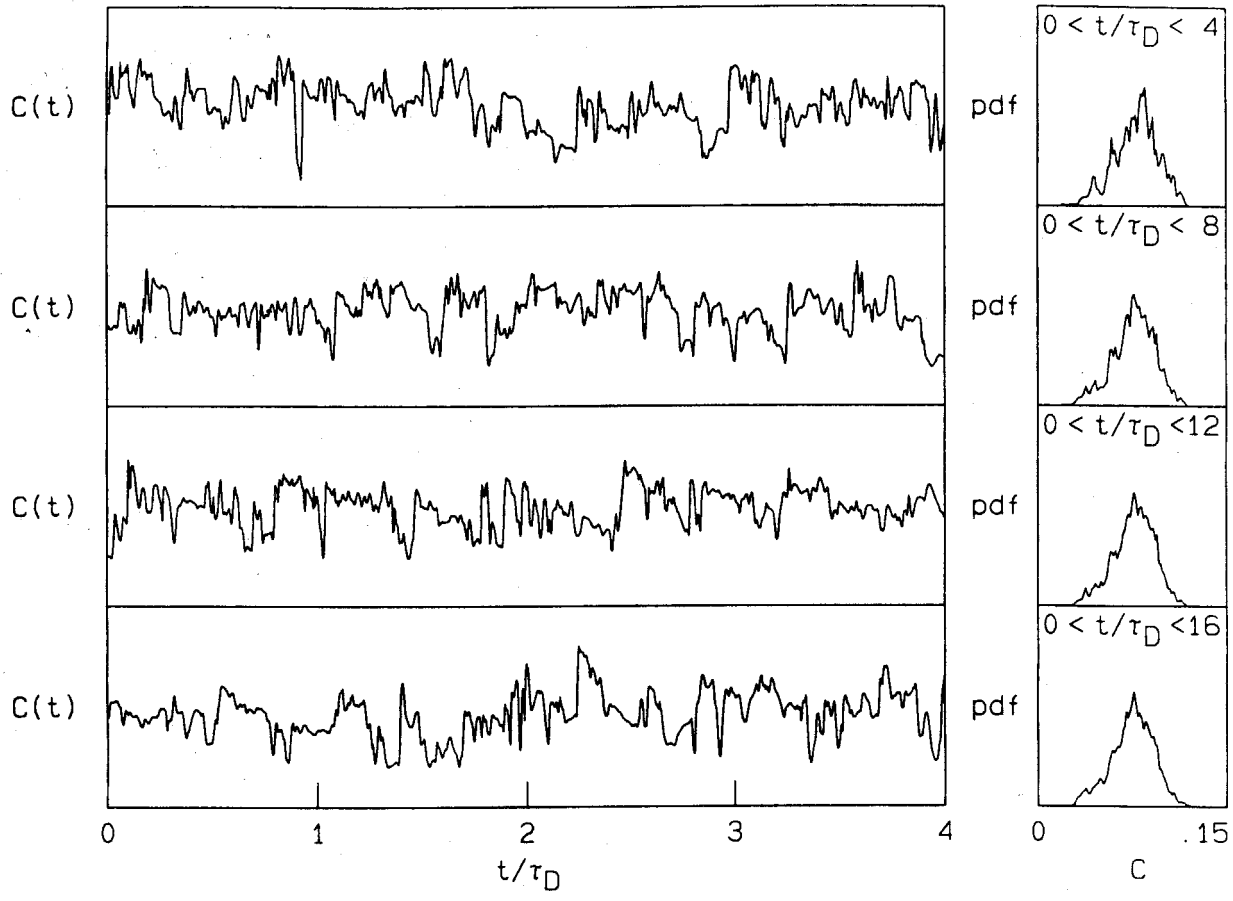

Figure 5-10. Time traces of C(t) and accumulated PDFs at Re_0 = 5,000 on the jet centerline with about 4 τ_D per line.

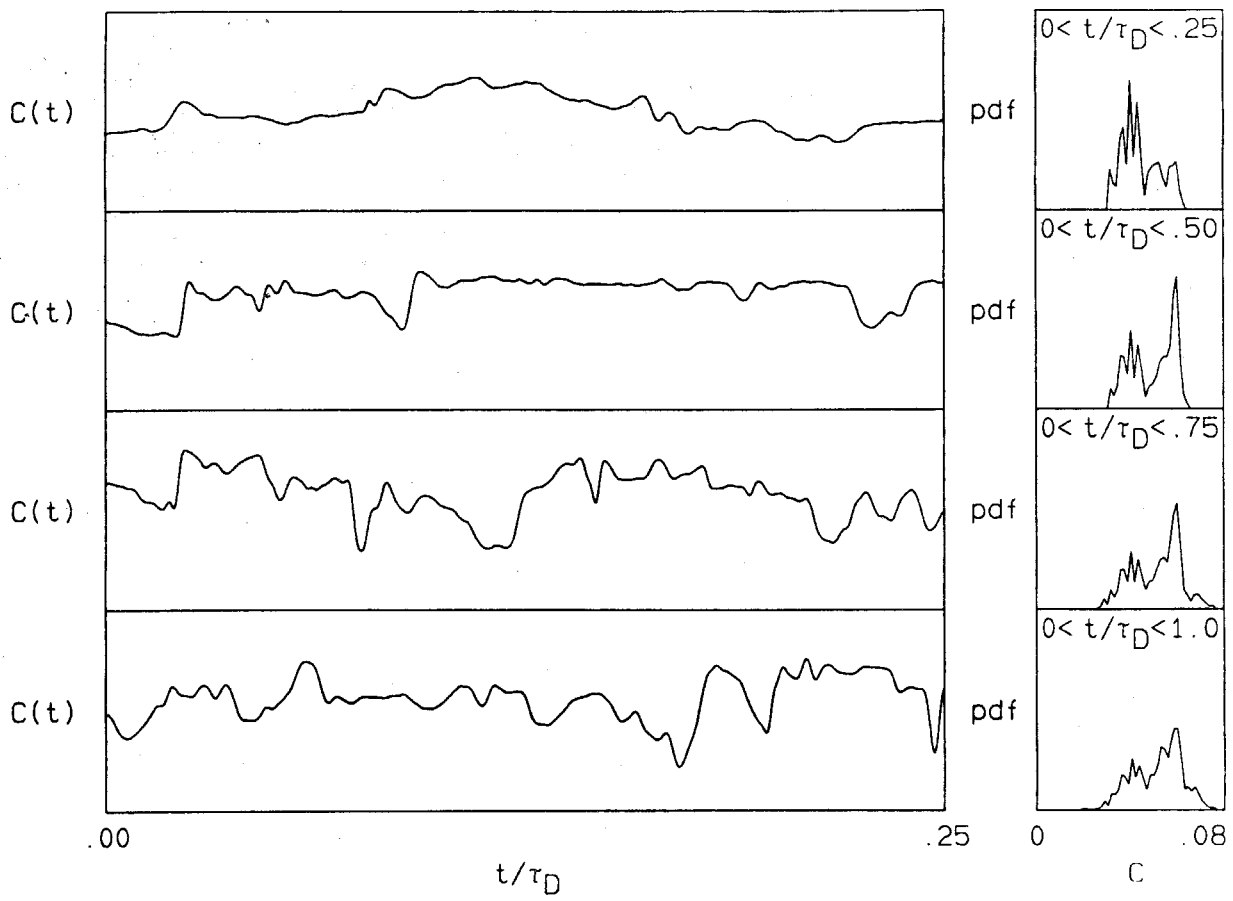

Figure 5-11. Time traces of C(t) and accumulated PDFs at Re_0 = 16,000 on the jet centerline with about .25 τ_D per line.

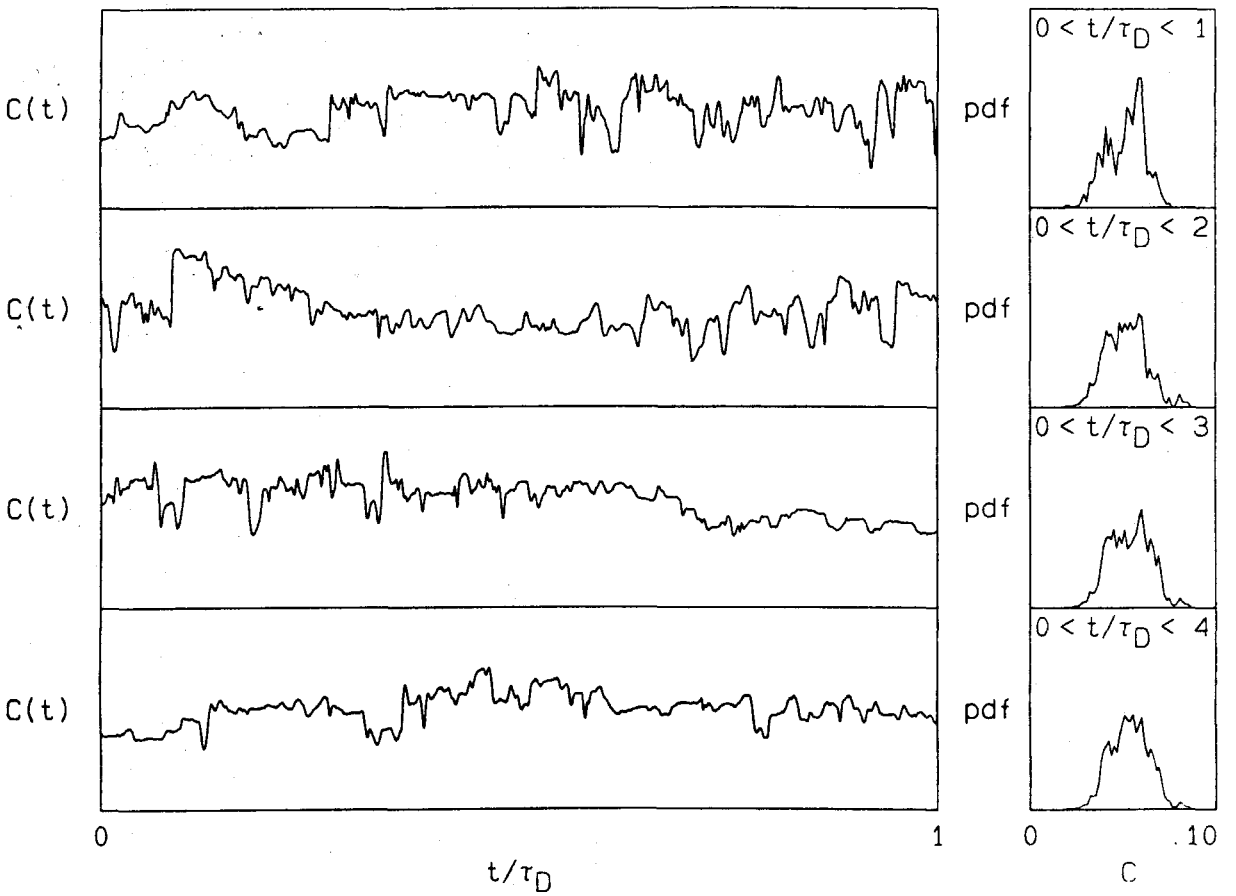

Figure 5-12. Time traces of C(t) and accumulated PDFs at Re_0 = 16,000 on the jet centerline with about 1 τ_D per line.

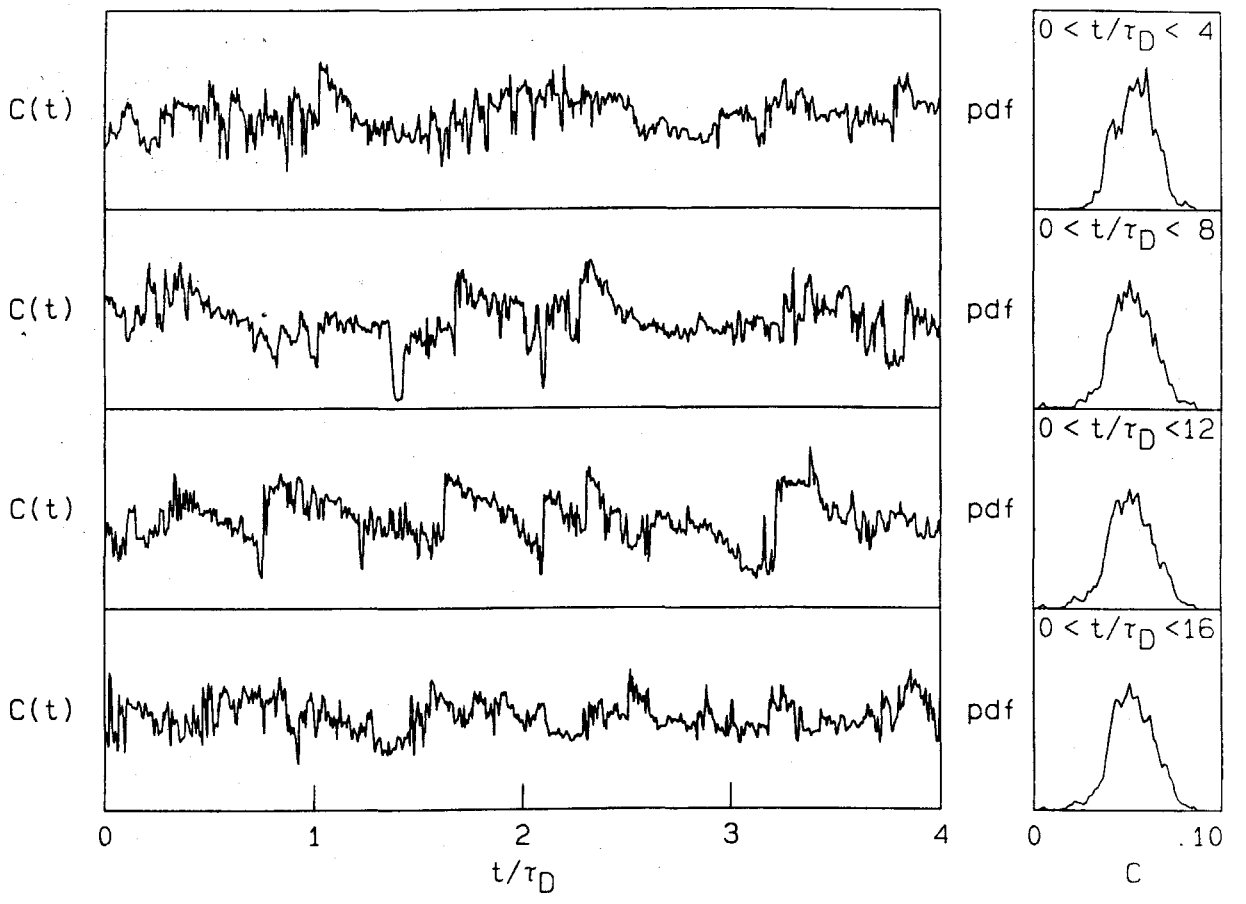

Figure 5-13. Time traces of C(t) and accumulated PDFs at Re_0 = 16,000 on the jet centerline with about 4 τ_D per line.

5.4 Implications for Turbulent Jet Mixing

The structure and shape of the probability density function of jet gas concentration at these two Reynolds numbers can be used to draw a few conclusions about turbulent jet mixing. The most important conclusion is that for the central part of the jet, $0 \leq r/(x - x_0) < .12$, the amount of molecularly mixed fluid, when scaled by the local mean concentration, is essentially independent of Reynolds number in the range studied. Even though there are fewer small-scale fluctuations per τ_D at $Re_0 = 5,000$ when compared to $Re_0 = 16,000$, the diffusion layers are thicker so that the tabulated amount and composition of the molecularly mixed gas, normalized by the local mean, is almost the same at the two Reynolds numbers.

This is not true at the edges of the jet, $r/(x - x_0) > .12$, where the rms levels, which are a measure of the width of the PDF of concentration, depend on Re_0 and Sc (see discussion in Chapter 3, Section 2). This radial dependence of the amount of mixed fluid at different Reynolds and Schmidt numbers can be seen in the current data by comparing the ratio of the local mean mixed fluid concentration and the local mean concentration, $\overline{C}_m/\overline{C}$, along rays near the edge and near the centerline, of the jet at the two Reynolds numbers. The local mixed fluid concentration was computed from the measured PDFs by ignoring the contribution of concentrations that were less than 5% of the local mean.

$$\overline{C}_m/\overline{C} = \frac{\int_{.05}^{\infty} (C/\overline{C})\ PDF(C/\overline{C})\ d(C/\overline{C})}{\int_{.05}^{\infty} PDF(C/\overline{C})\ d(C/\overline{C})} \qquad (5.2)$$

Table 5-1 displays the values of $\overline{C}_m/\overline{C}$ computed from the measured distributions. The values at $\eta \approx .18$ are not as reliable as for the

Table 5-1: Values of $\overline{C}_m/\overline{C}$

$\eta =$	.00	.06	.12	~.18
$Re_0 = 5{,}000$	1.00	1.001	1.016	$1.11 \pm .05$
$Re_0 = 16{,}000$	1.00	1.001	1.035	$1.16 \pm .05$

other 3 rays.

If the 8% difference in the mean concentration decay rate between Reynolds numbers is ignored, then the observed Reynolds number near-independence of the mixing would be consistent with the flame length studies of Weddell (1952) and Dahm et al. (1984). Their work points to $Re_0 \approx 3{,}000$ as the threshold where the degree of molecular mixing in the jet becomes independent of Re_0. In fact, all of the 8% difference in κ should not be ignored. It should be recognized that the flame length conclusions of Dahm et al. and Weddell require only that the high-concentration end of the PDF of $C/\overline{C}$ becomes independent of Re_0, beyond $Re_0 \approx 3{,}000$. Figure 5-7 shows that there is a slightly greater abundance of the high concentrations in the $Re_0 = 16{,}000$ jet than in the $Re_0 = 5{,}000$ jet. This increased abundance at high $C/\overline{C}$, however, offsets

part of the 8% loss in mean concentration when a flame length is estimated from the measured PDF of $C/\overline{C}$. It must be mentioned that only the maximum flame length can be estimated from the PDF of $C/\overline{C}$ because the the process of compiling the PDF removes temporal information, and only resolves the highest concentration excursions.

Figure 5-14 is a comparison of the flame length measurements of Dahm et al. (1984), with the maximum flame lengths estimated from the current mixing experiments. This was done by assuming that, if an infinitely fast reaction was to take place between the jet and reservoir gases, then the farthest downstream occurrence of the stoichiometric mixture ratio for the reaction, ϕ^*, would mark the flame tip. Because of the statistical error in the PDFs at very high values of $C/\overline{C}$, the calculations for Figure 5-14 were made assuming that a small percentage of gas was left unreacted at the flame tip. Of course, the actual percentage of gas left unreacted at the flame tip is zero.

The stoichiometric mixture ratio of the presumed reaction, ϕ^* = the number of parts of reservoir fluid needed to complete a reaction with one part of jet fluid, was estimated from the PDFs on Figure 5-7, using:

$$\phi^* = \frac{1 - C^*}{C^*} \quad , \quad C^* = \left(\frac{C}{\overline{C}} \right)^* \overline{C}, \tag{5.3}$$

where $(C/\overline{C})^*$ was determined from:

$$100\left[\int_{(C/\overline{C})^*}^{\infty} \mathrm{PDF}(C/\overline{C})\, d(C/\overline{C}) \right] = \text{\% unreacted @ the flame tip,} \tag{5.4}$$

and

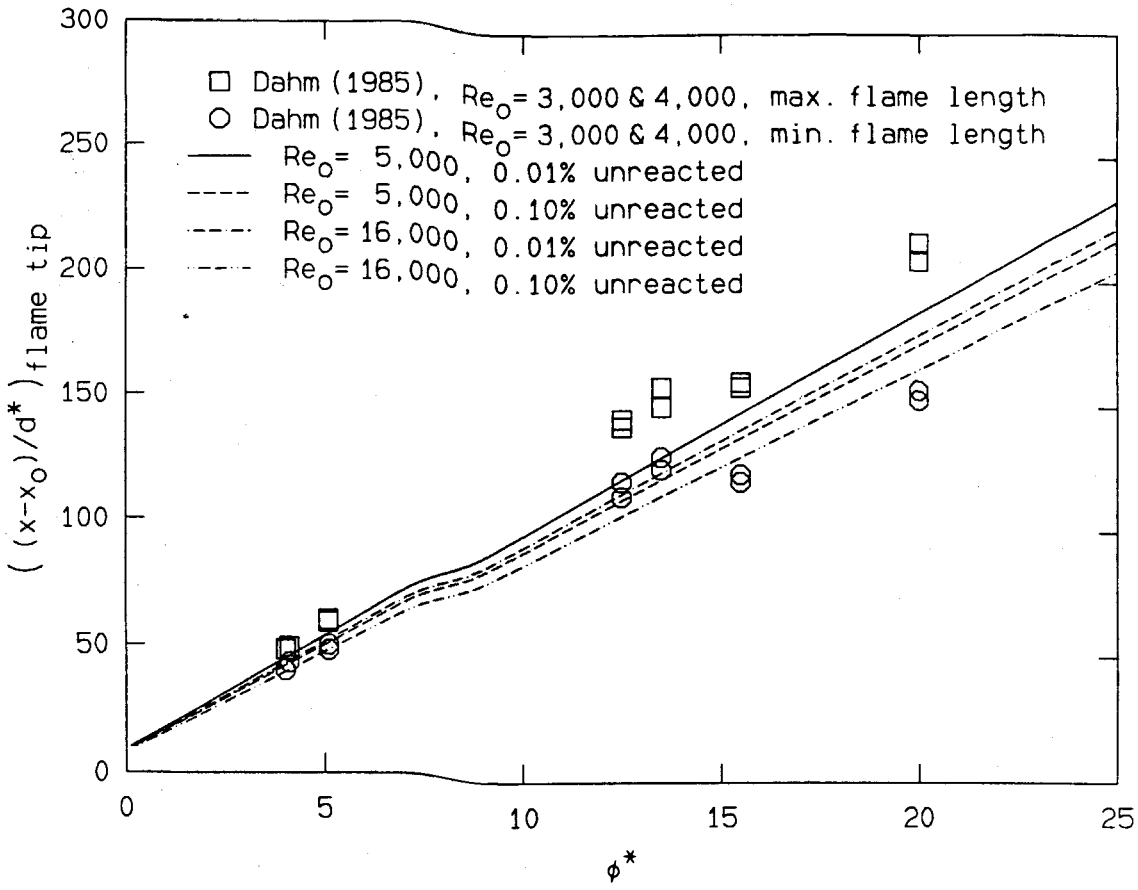

Figure 5-14. Comparison of flame lengths reported by Dahm et al. (1984) with those estimated from the measured PDFs of this study.

$$\overline{C} = \kappa C_0 d^*/(x - x_0), \qquad (5.5)$$

with κ and x_0 as specified in Chapter 3, Section 1. Substitution of Equation (5.5) into Equation (5.3) yields a formula for ϕ^* in terms of $(x - x_0)/d^*$, which can be inverted to give the expected value of $(x - x_0)/d^*$ at the flame tip for a given ϕ^*.

$$\left(\frac{x - x_0}{d^*}\right)_{\text{flame tip}} = \left(\frac{C}{\bar{C}}\right)^* \kappa C_0 (\phi^* + 1) \qquad (5.6)$$

Figure 5-14 shows the results at both of the current Reynolds numbers for two assumed values of the percentage of fluid left unreacted at the flame tip (.01% and .1%). The current predictions fall about 15% percent short of the measurements of the maximum flame length made by Dahm et al. (1984). A portion of this discrepancy can probably be ascribed to the fact that the current predictions were not made for 100% completion of the presumed reaction (zero percent unreacted). Perhaps the rest of the discrepancy can be attributed to the large difference in Schmidt number between the jet flows compared on Figure 5-14. Dahm worked with liquid phase jets at $Sc \approx 10^3$ and the current studies are for $Sc \approx 1$. Broadwell (1987) suggests that there should be a Schmidt number effect in jet mixing if the Reynolds number is low enough, so it is possible that the jet Reynolds numbers depicted in Figure 5-14 are not high enough to entirely eliminate a Schmidt number dependence of the flame length. It is worth noting that if the flame length does depend on the Schmidt number in the Reynolds number range presented on Figure 5-14, then the longer maximum flame length at the greater Schmidt number is consistent with the ideas presented by Broadwell. For the current studies, some of the disagreement between Reynolds numbers shown on Figure 5-14 might result from an error in the value of κ at $Re_0 = 16{,}000$ (see Chapter 3, Section 1).

As mentioned in the context of the mean concentration profile (Chapter 3, Section 1), the entrainment studies of Ricou and Spalding (1961) suggest that the threshold Re_0 for Reynolds number independent behavior of the jet's entrainment rate of reservoir fluid is about 25,000. Unfortunately, they only made measurements from the jet origin up to $x/d \approx 14$ and 26 so their results may not be free of near-field effects. Their measurements also show that the jet entrains relatively less reservoir fluid as Re_0 is increased. This is in clear contrast to the measured change in κ of the present studies, so a better understanding of the issues discussed here awaits new results.

A final conclusion, which does not depend on a subtle interpretation of Figures 5-1 to 5-6, is that the mixing process in the jet, when elucidated through the probability density function of jet fluid concentration, has the same specific similarity as the mean concentration of jet fluid. This can be concluded because the shape of the PDF of $C/\overline{C}$, at a fixed Reynolds number, is found to depend only on $r/(x - x_0)$. Additionally, the quality of the collapse achieved for the PDF of $C/\overline{C}$, at two different values of Re_0, suggests that $C/\overline{C}$ is the correct general similarity variable for the mixing process in the jet.

CHAPTER 6

THE TIME DERIVATIVE OF CONCENTRATION

The statistics of the time derivative of the concentration are important in this study as a check of the local isotropy of jet mixing because local isotropy is one of three assumptions that allow the scalar dissipation rate (or local mixing rate) to be estimated from measurements of $(dC/dt)^2$. The probability density function of dC/dt will be symmetric about $dC/dt = 0$, if the jet's turbulent concentration field is isotropic. It must also be mentioned that a description of the statistics and specific similarity of dC/dt is a necessary step on the computational path that starts with a time series of C(t) and ends at the estimated scalar dissipation rate, $\varepsilon_c(t)$, the subject of the next chapter.

The time derivative of concentration was computed from the optimally filtered data by convolution with the derivative of a Gaussian. The temporal width of the Gaussian was chosen to be less than that of the optimal filter kernel to prevent additional filtering of the data while the derivative was being computed. This convolution technique was chosen because it allowed the time derivative to be computed through an integration. Further discussion of the technique is contained in Appendix E, Section 4.

In accordance with the specific similarity found for the other properties of the jet turbulence (see Chapters 3, 4, and 5), dC/dt was scaled with jet variables to make it dimensionless. This meant multiplying by τ_D and dividing by $\overline{C}$. The statistical properties of $(dC/dt)(\tau_D/\overline{C})$ should depend only on $r/(x-x_0)$, if dC/dt has the same specific similarity behavior as the other statistical measures of the turbulent jet concentration field. To check this contention, the probability density function of $(dC/dt)(\tau_D/\overline{C})$ was compiled from each data set by sorting the instantaneous values into histograms and comparing different downstream locations. The histograms were normalized, i.e.

$$\int_{-\infty}^{\infty} PDF(\gamma)\, d\gamma = 1 , \qquad (6.1)$$

where γ represents the dimensionless time derivative, $(dC/dt)(\tau_D/\overline{C})$.

6.1 **Results at Reynolds Number 5,000 and 16,000**

Figures 6-1, 6-2 and 6-3 are plots of the probability density function of $(dC/dt)(\tau_D/\overline{C})$ at x/d = 20, 40, 60, and 80 along the three rays $r/(x-x_0) \approx .00$, .06, and .12. The quality of the collapse along rays implies that the chosen scaling removes the dependence on downstream distance in these distributions. Deviations are probably attributable to incomplete statistical convergence at the largest magnitudes of dC/dt and slight misalignment of the measurement point with respect to the chosen ray.

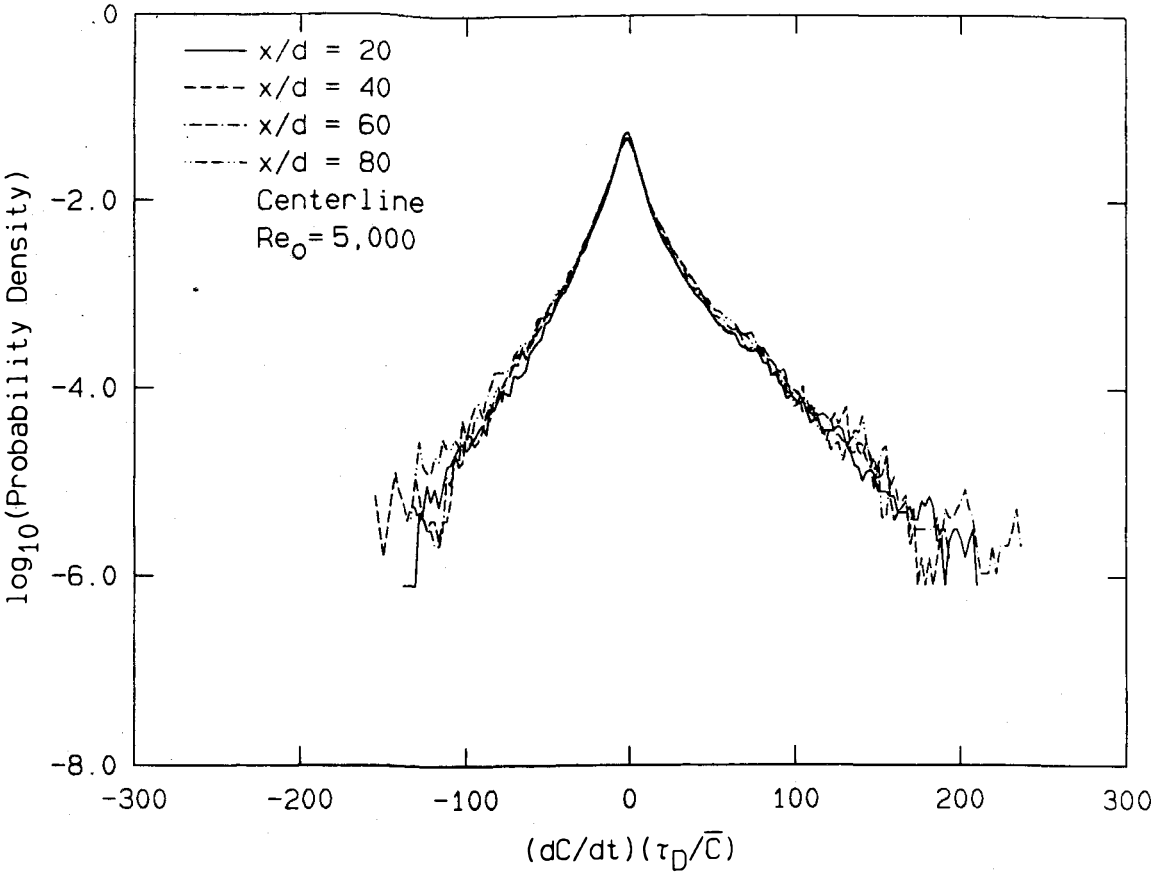

Figure 6-1. Probability density function of the scaled time derivative of concentration on the jet centerline at Re_0 = 5,000.

Figures 6-4, 6-5, and 6-6 display the measured probability density functions of $C/\bar{C}$ along three rays at $r/(x - x_0) \approx .00, .06,$ and .11 for x/d = 30 and 90 at $Re_0 = 16,000$. Imperfections in the collapse are attributed to the same problems mentioned above, and in addition, an overall bias may have been introduced in the scaling at this Reynolds

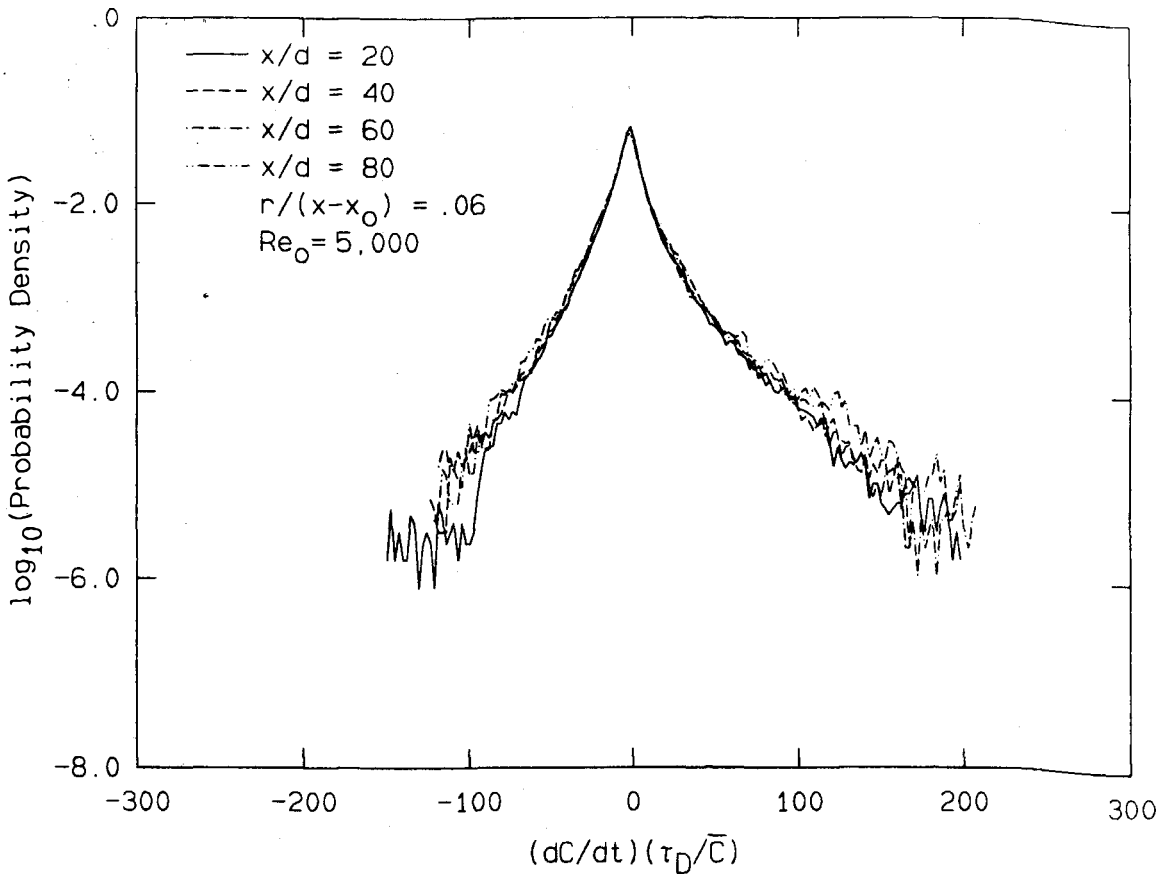

Figure 6-2. Probability density function of the scaled time derivative of concentration 3.4° off the jet centerline at Re_0 = 5,000.

number through any error in the value of x_0, which is used to compute τ_D. The value of x_0 is much more uncertain at this Reynolds number because it is based on measurements at only two downstream locations. Close examination of Figures 6-4 to 6-6 shows that for large values of |dC/dt|, the results from x/d = 90 usually fall above those from x/d = 30. While this might be caused by a possible error in τ_D transmitted

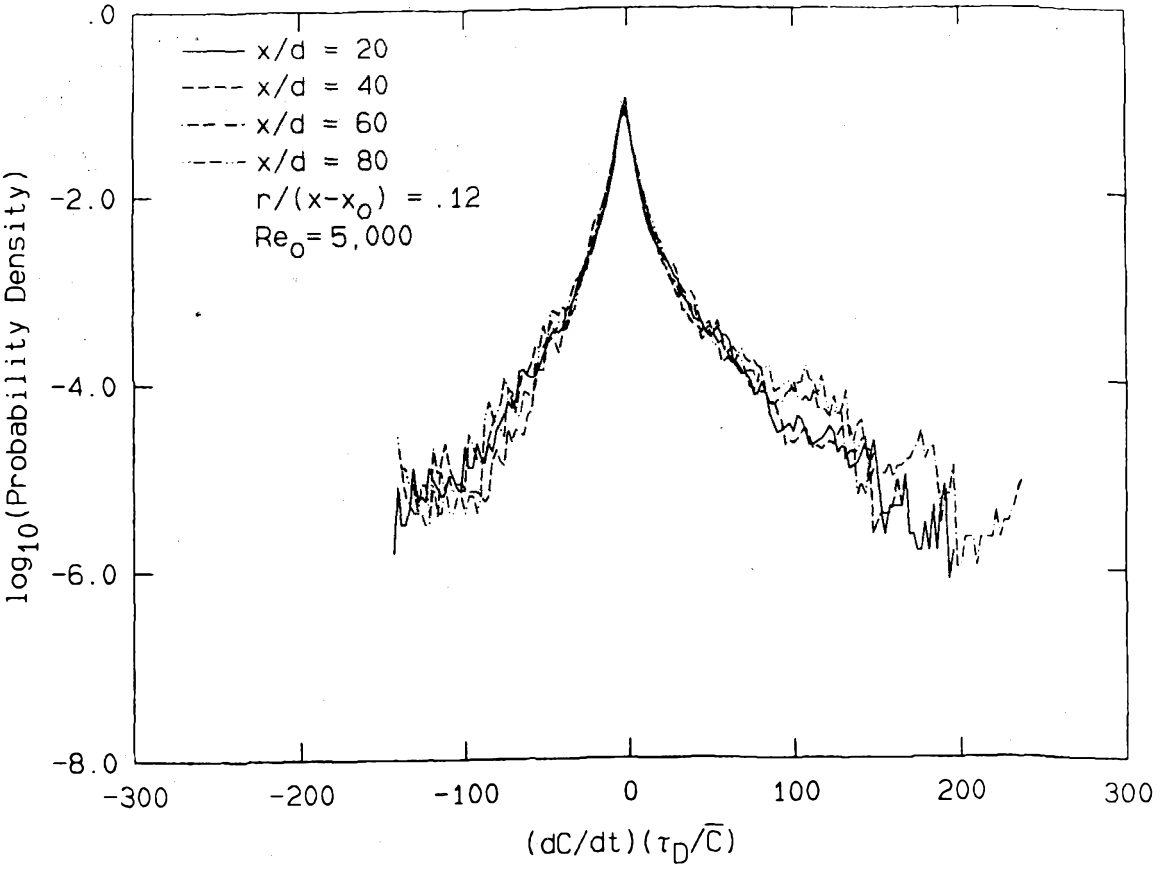

Figure 6-3. Probability density function of the scaled time derivative of concentration 7° off the jet centerline at $Re_0 = 5,000$.

via x_0, it could also be a result of the differing widths of the optimal filters. In particular, the "noise-tails" of the spectra at x/d = 30 start at a lower value of $f \cdot \tau_D$, so the width of the optimal filter kernels for these data sets were larger, relative to τ_D, than the kernel widths for the data sets at x/d = 90. In any case, the observed imperfections in the collapse are small and will not be mentioned

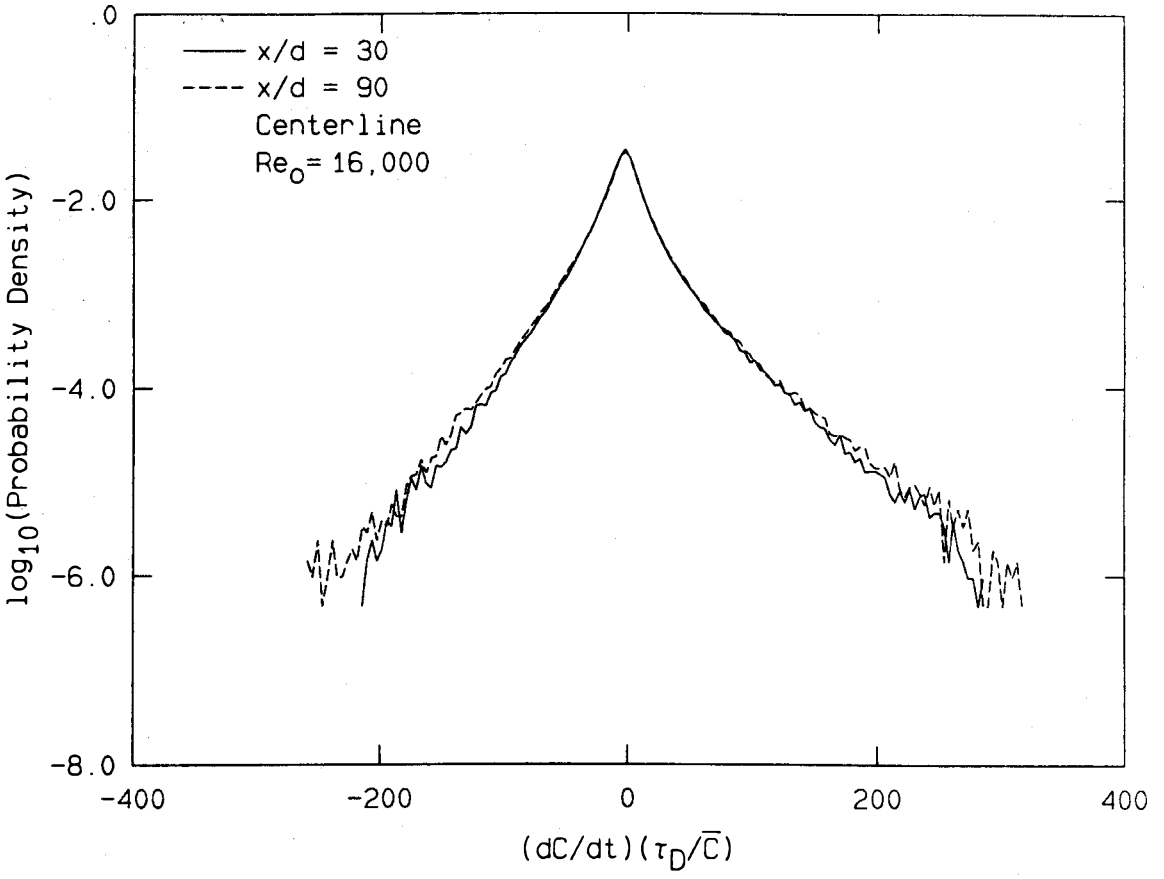

Figure 6-4. Probability density function of the scaled time derivative of concentration on the centerline of the jet at Re_0 = 16,000.

further.

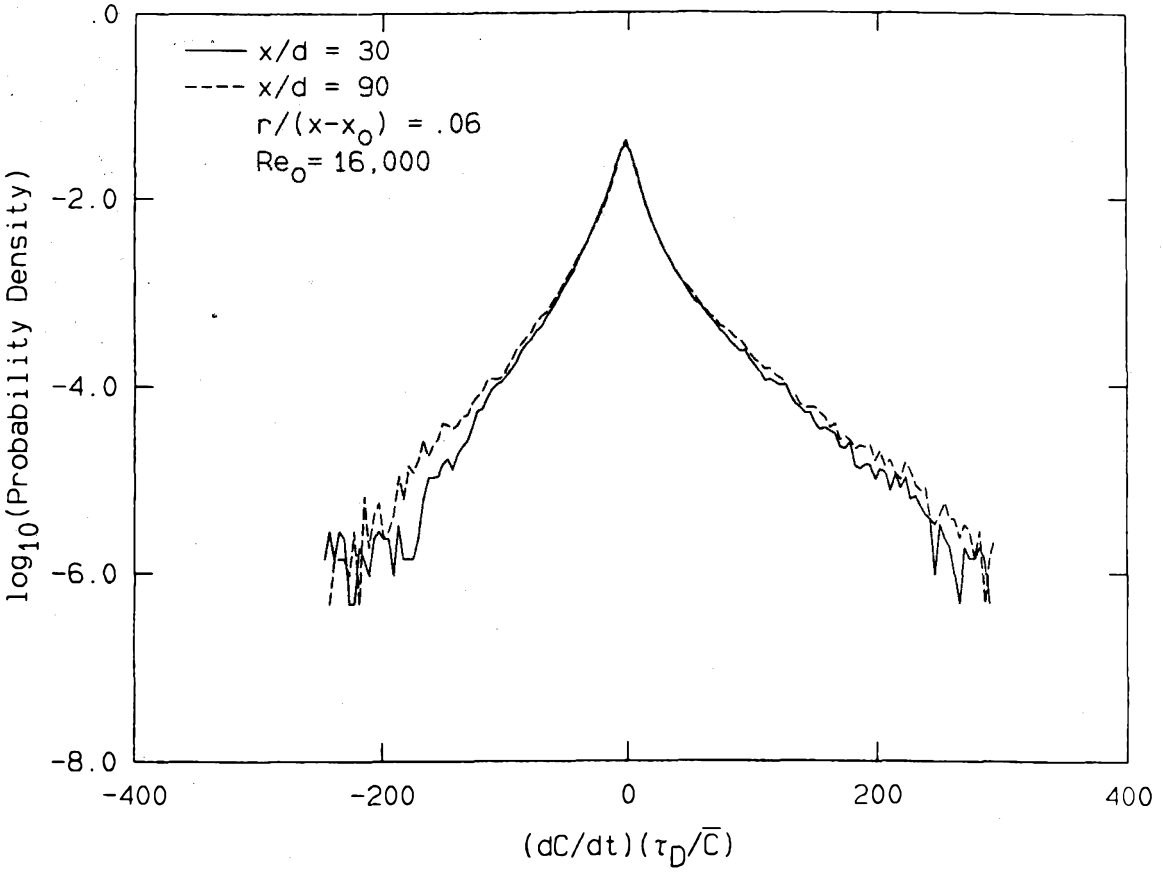

Figure 6-5. Probability density function of the scaled time derivative of concentration 3.4° off the jet centerline at Re_0 = 16,000.

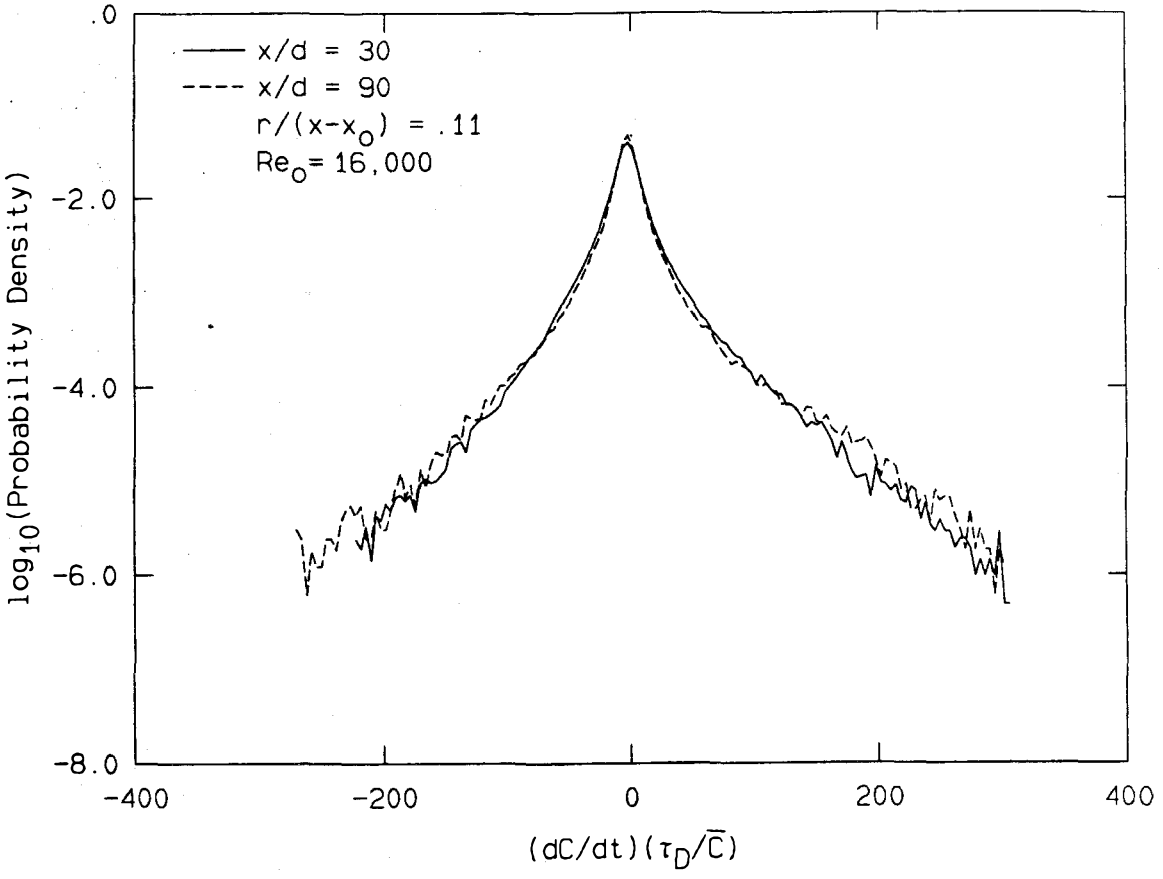

Figure 6-6. Probability density function of the scaled time derivative of concentration 6.3° off the jet centerline at Re_0 = 16,000.

6.2 Comparisons and Comments

The plotted PDFs at both Reynolds numbers show the same trends as the chosen ray is rotated toward the edge of the jet: The peak value increases slightly, and the width of the distribution also decreases slightly. The main difference between the results from the two Reynolds numbers is that the PDFs at $Re_0 = 16{,}000$ extend to higher values of the scaled time derivative of concentration.

Perhaps the most interesting characteristic of the distributions is the degree to which the "wings" are skewed toward large positive values of the scaled time derivative. The peaks of the distributions occur slightly below $dC/dt = 0$ to compensate for the asymmetry. This observation is supported by examination of the time traces of the instantaneous concentration on Figures 5-8 to 5-13, 6-7 and 6-8, where there is a greater prevalence of large positive values of dC/dt than large negative ones. Figures 6-7 and 6-8 are plots of the optimally filtered data from $Re_0 = 5{,}000$ and 16,000, respectively, along the ray at $r/(x - x_0) = .06$. The sections of the data on these two plots were chosen because they display some evidence of a large-scale motion. The general characteristics of this structure seem to be a relatively sharp rise in the concentration followed by a region where the concentration falls chaoticly, at a lower average rate, until the next sharp rise. The passage time for this structure is usually about τ_D and its strong asymmetry in time may be responsible for all or part of the measured asymmetry of the PDF of dC/dt. The small arrows on Figures 6-7 and 6-8 have been placed near the leading edges of the easily identifiable

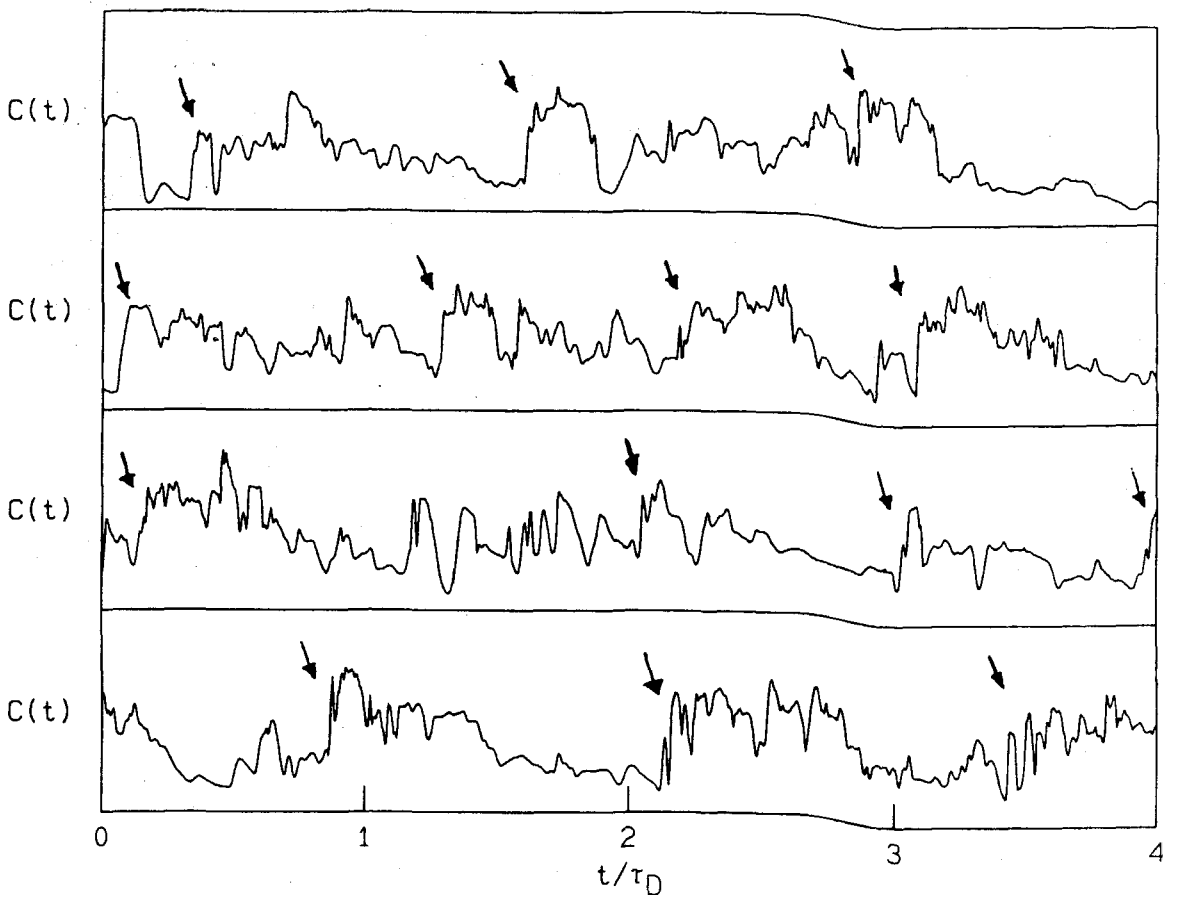

Figure 6-7. Time traces of C(t) 3.4^0 off the jet centerline at Re_0 = 5,000.

structures.

Gibson et al. (1977) report the presence of the same type of "ramp" structures in temperature measurements from many different shear flows, with Reynolds numbers ranging from 15,000 to 5,000,000, including axisymmetric turbulent jets at $Re_0 \sim 10^5$ and 10^6. They also discuss the asymmetry of the PDF of the time derivative of temperature and its

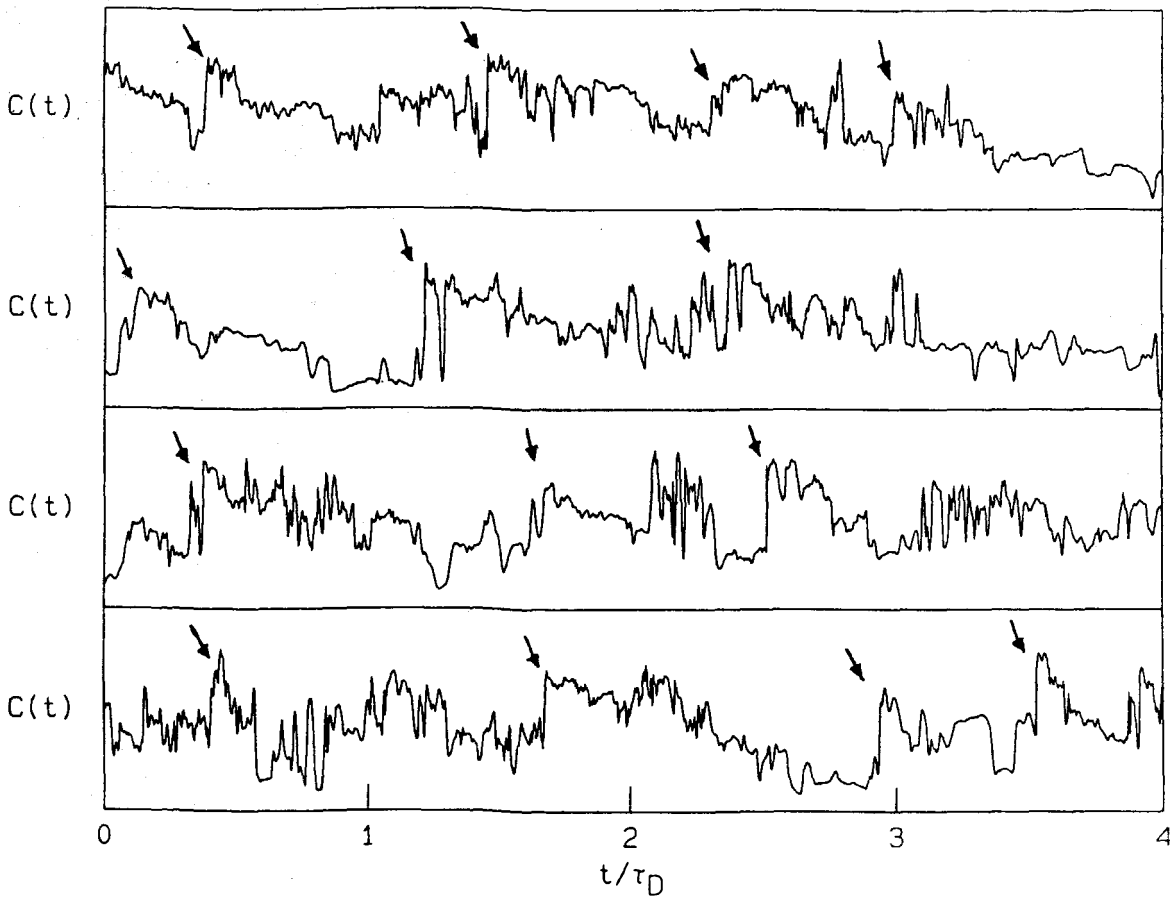

Figure 6-8. Time traces of C(t) 3.4° off the jet centerline at Re_0 = 16,000.

relation to the observed "ramps". Antonia, Anselmet et al. (1986), who worked in a heated plane jet at Re_0 = 7,550, find the same type of asymmetry in their PDFs of the spatial derivatives of temperature. Antonia, Chambers et al. (1986), also report the presence of "ramp" structures in their time traces of temperature from a heated plane jet.

CHAPTER 7

THE ESTIMATED SCALAR DISSIPATION RATE

The instantaneous estimated scalar dissipation rate, $\varepsilon_c(t)$, was computed from the optimally smoothed data by squaring and scaling the time derivative of concentration, i.e.

$$\varepsilon_c(t) = 6 D_{j\infty} \left(\frac{1}{\bar{U}_{c1}} \frac{dC(t)}{dt} \right)^2 \tag{7.1}$$

where $\bar{U}_{c1}$ is computed from the formula given by Chen and Rodi (1980), and the time derivative is calculated by convolution of the data with the derivative of a Gaussian (see Chapter 6 or Appendix E, Section 4).

The real scalar dissipation rate, $\zeta(t)$, is the rate at which fluctuations in the turbulent concentration field relax toward zero under the action of molecular diffusion. For this reason, $\zeta(t)$ is identified as the instantaneous mixing rate. The basic point of view taken in most of this chapter is that $\zeta(t)$ can be modeled by $\varepsilon_c(t)$, or equivalently, that $\zeta(t)$ is proportional to $(dC/dt)^2$. The validity and consequences of taking this point of view are also discussed.

One approach to defining $\zeta(t)$, reproduced here from Dimotakis (1984), uses an integral formulation for the conservation equation for the *scalar energy*, where:

$$\textit{Scalar Energy} = SE = \int_V \rho_\infty c^2 \, dV, \tag{7.2}$$

with V a fixed control volume in the jet flow. A factor of $\frac{1}{2}$ is

sometimes inserted inside the integral to make a more complete analogy with the kinetic energy of the fluid, $\frac{1}{2}\rho_\infty|\underline{u}|^2$ ($\underline{u}$ is the vector fluid velocity, $\underline{u} = \underline{U} + \underline{u}'$).

Taking the time derivative of Equation (7.2) yields:

$$\dot{SE} = \rho_\infty \int_V 2\,C \frac{\partial C}{\partial t}\, dV. \tag{7.3}$$

The conservation Equation for C in incompressible flow,

$$\frac{\partial C}{\partial t} + (\underline{u}\cdot\nabla)C = D_{j\infty}\nabla^2 C, \tag{7.4}$$

can be used to eliminate the time derivative of C inside the integral in Equation (7.3),

$$\dot{SE} = \rho_\infty \int_S \left[-C^2\underline{u} + D_{j\infty}\nabla C^2\right]\cdot d\underline{S} - 2\,\rho_\infty D_{j\infty} \int_V |\nabla C|^2\, dV, \tag{7.5}$$

where S is the surface of V and Gauss's divergence theorem has been used change the volume integral to a surface integral for the first two terms on the right hand side of Equation (7.5).

The surface integral terms in Equation (7.5) are identified as the flux of *scalar energy* across S resulting from convection and diffusion. The final term is identified as the diffusive dissipation of the *scalar energy* within V. Because V was not specified explicitly, Equation (7.5) must hold for all control volumes, so the dissipative effects of molecular diffusion on the *scalar energy* can be defined at every point in space. Dividing this dissipation function by the fluid density and V gives the mass specific rate of the dissipation of *scalar energy*,

$$\frac{\dot{SE}}{\rho_\infty V} = \zeta(t) = 2 D_{j\infty} |\nabla C|^2, \tag{7.6}$$

the scalar dissipation rate. In some references (Tennekes and Lumley 1972, Townsend 1976), ζ is defined in terms of the fluctuation concentration, $C'(t) = C(t) - \bar{C}$, i.e.,

$$\zeta(t) = 2 D_{j\infty} |\nabla C'|^2. \tag{7.7}$$

The difference between Equations (7.6) and (7.7), the contribution from the mean concentration gradients, $|\nabla \bar{C}|^2$, is very small compared to $|\nabla C'|^2$ for $Re_0 \gg 1$.

It was not possible to measure ζ directly, but some of its properties can be inferred from ε_c, even though ζ and ε_c differ in three important respects. One of these differences arises through the process of converting a temporal to a spatial derivative, which was accomplished for the present data by dividing dC/dt by the calculated value of $\bar{U}_{cl}$. This amounts to applying a form of Taylor's hypothesis (Taylor 1938),

$$\frac{dC}{dt} = -\bar{U}_x \frac{\partial C}{\partial x}, \tag{7.8}$$

without directly measuring the mean axial velocity $\bar{U}_x$. This approximation is not only subject to the limitations of Taylor's hypothesis applied in a turbulent flow (see Hinze 1975, and Lang 1985), but it might introduce a consistent bias in the results for ε_c, since the constant in the actual mean, centerline velocity decay law of the present jet flows may have been slightly different from the value of 6.2 suggested by Chen and Rodi (1980).

The second major difference between ε_c and ζ comes from the assumption that the statistical properties of each of the three spatial derivative terms in Equation (7.6) are same. If the turbulent field is isotropic, then this assumption is justified, but the results of the previous chapter suggest that the turbulent concentration field of the jet is not completely isotropic, especially for large values of $|dC/dt|$.

The third difference between $\zeta(t)$ and $\varepsilon_c(t)$, is the assumption that the square of the three spatial derivatives of the concentration field are completely correlated and can be represented by the scaled value of $(dC/dt)^2$, i.e.,

$$\left(\frac{\partial C}{\partial x_1}\right)^2 = \left(\frac{\partial C}{\partial x_2}\right)^2 = \left(\frac{\partial C}{\partial x_3}\right)^2 = \left(\frac{1}{\overline{U}_{cl}}\frac{dC}{dt}\right)^2, \qquad (7.9)$$

where x_1, x_2, and x_3 are cartesian coordinates. This assumption is adapted here only as a result of the need to present a connection between ε_c, computed from the one-dimensional measured time series, and ζ in the real three-dimensional turbulent flow. It is reasonable to expect that the three spatial derivatives of the concentration field will be correlated to some degree because they are linked through the conservation equation for the jet gas concentration, Equation (7.4). The statistics of ε_c between the two limits, completely correlated and uncorrelated derivatives, will be discussed in section 4 of this chapter.

Using these three approximations, Equation (7.1) can be obtained from Equation (7.6) by replacing $|\nabla C|^2$ with $3\cdot\left(\dot{C}(t)/\overline{U}_{cl}\right)^2$. When it is possible, the results in this chapter are displayed in terms of the unapproximated dimensionless quantity, $(dC/dt)^2(\tau_D/\overline{C})^2$, which differs from ε_c only by multiplicative constants. The errors introduced by the approximations leading to ε_c will be discussed in each section as appropriate.

7.1 The Mean Estimated Scalar Dissipation Rate

The mean value of ε_c was computed from the mean value of $(dC/dt)^2$ using Equation (7.1). The results are displayed on Figure 7-1 for data near the rays at $r/(x-x_0) = 0, .06, .12$ and for $r/(x-x_0) \geq .14$ at $Re_0 = 5{,}000$ and $16{,}000$. The axis scaling is consistent with that used by Friehe et al. (1971) for the mean energy dissipation rate. The axis scaling that would be obtained from nondimensionalizing ε_c with $\overline{C}$ and τ_D has the same functional dependence on $(x-x_0)$.

The collapse is not perfect for several possible reasons.

1. The instantaneous value of ε_c varies over many orders of magnitude and the rms fluctuation level of ε_c is typically 4 or 5 times larger than $\overline{\varepsilon}_c$. This means that the statistical convergence, especially for the outer ray where the effective sample size is smaller, may not be complete for all of plotted points.

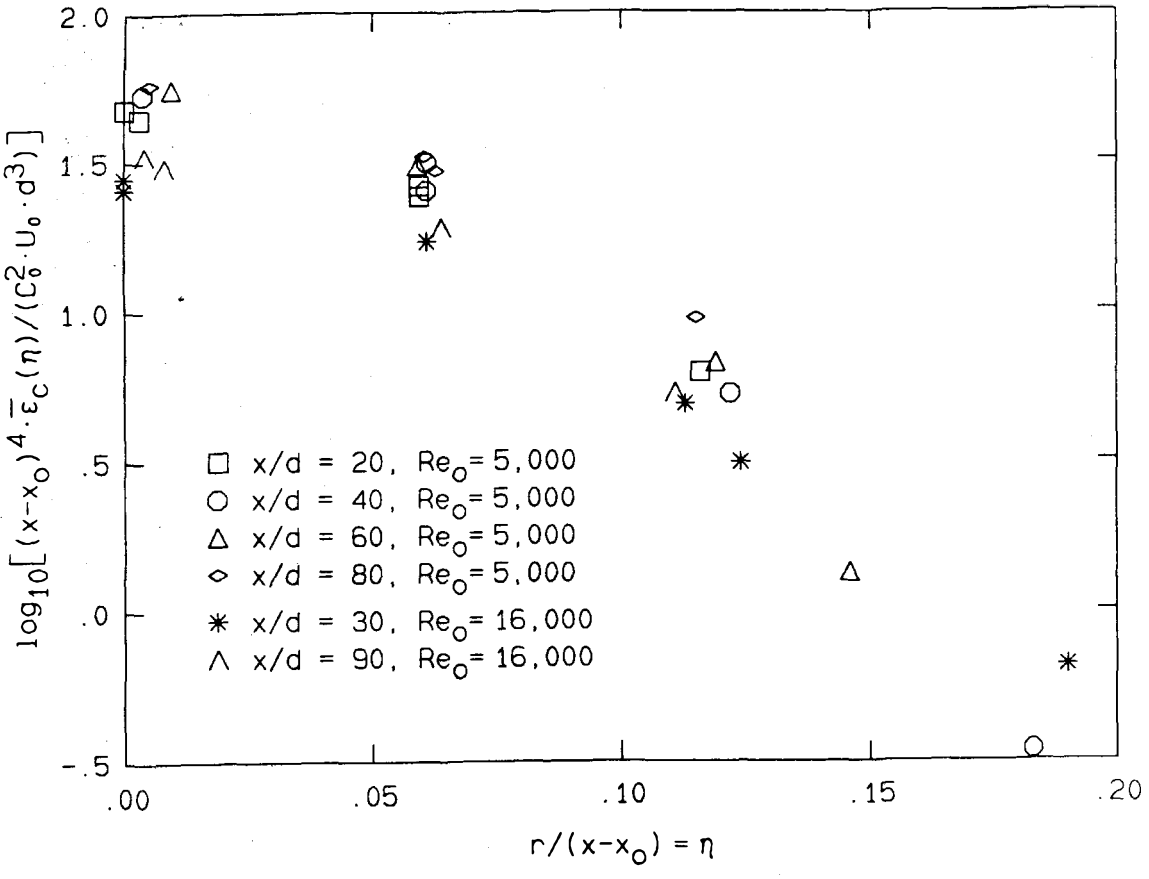

Figure 7-1. The scaled mean value of ε_c verses $r/(x - x_o)$.

2. Normalization of the plotted data by $(x - x_o)^4$ amplifies any small error in the value of x_o. In particular, the data at x/d = 30 and 90, for Re_o = 16,000, would collapse much better if x_o, for that Reynolds number, was decreased by 1.5 d.

3. As will be seen again in the next section, the results at x/d = 20 and Re_o = 5,000, may not be entirely free of near-field influences, and if these points are ignored, the collapse of

the results at Re_0 = 5,000 is improved.

4. The data at x/d = 90, Re_0 = 16,000, were taken with superior spatial resolution when compared to x/d = 30 at the same Reynolds number, and this might account for some of the consistent discrepancy between the results at x/d = 30 and 90.

Except for the first factor listed, all of these problems cause $\bar{\varepsilon}_c$ to be underestimated. Taking this into account, the best value of of κ_ε is 54 at Re_0 = 5,000 and 32 at Re_0 = 16,000, where κ_ε is defined by:

$$\bar{\varepsilon}_c\Big|_{\eta=0} = \kappa_\varepsilon \frac{C_0^2 U_0}{d} \left(\frac{x - x_0}{d}\right)^{-4}. \qquad (7.10)$$

These values of κ_ε and Equation (7.10) were used in the computation of the Kolmogorov scaling for the universal collapse of the scalar fluctuation spectrum (see Chapter 4, Section 4). It is worth noting that these values of κ_ε (54 & 32) are close to the one suggested by Friehe et al. (1971), $\kappa_{\bar{\varepsilon}} = 48$, for the mean kinetic energy dissipation rate in a round turbulent air jet at Re_0 = 120,000.

The difference in κ_ε between the results at the two Reynolds numbers is probably a Reynolds number effect. As can be seen in Figure 4-9, the power spectra of concentration fluctuations on the jet centerline do not display a Reynolds-number-independent, inertial cascade (power-law) region at either Re_0 = 5,000 or 16,000. This implies that it might be inappropriate to predict the small-scale properties of the flow, like ε_c or ζ, based on large-scale parameters and assume that the results will be *independent* of Re_0, when the

interaction of the large and small scales is clearly *dependent* on the Reynolds number. Figure 7-1 also shows that for $r/(x-x_0) \leq .12$, the ratio of $\overline{\varepsilon}_c$ at the two Reynolds numbers is nearly constant, within statistical fluctuations, but that for $r/(x-x_0) \geq .12$, $\overline{\varepsilon}_c$ at Re_0 = 5,000 falls below that of Re_0 = 16,000. A discussion of how this Reynolds number dependence of the mean mixing rate might be related to the PDF of $C/\overline{C}$ is contained in the next chapter.

The drop in $\overline{\varepsilon}_c$ with increasing $r/(x-x_0)$ is primarily a result of using only $\overline{U}_{cl}$ to scale the time derivative. If a local, off-centerline mean velocity is used, the mean value of $\overline{\varepsilon}_c$ is almost independent of $r/(x-x_0)$ for each Reynolds number.

The dominant error introduced by the scaling of the time derivative is probably a constant scale factor that would slightly modify the values of κ_ε. The error introduced by the assumption of isotropy is also likely to be only a small percentage of the reported mean. No error is produced in $\overline{\varepsilon}_c$ by the assumed correlation of squared derivative terms in this case, because the temporal average of a sum is the sum of the temporal averages. Hence, correlations between the terms of ζ are not reflected in $\overline{\zeta}$, and $\overline{\varepsilon}_c$ is presumed to be a fairly accurate measure of $\overline{\zeta}$.

7.2 The Instantaneous Value of $(dC/dt)^2$

Figures 7-2 and 7-3 are time traces of C(t) and $(dC/dt)^2$ from the jet centerline at Re_0 = 5,000 and 16,000. The trace of $(dC/dt)^2$ appears

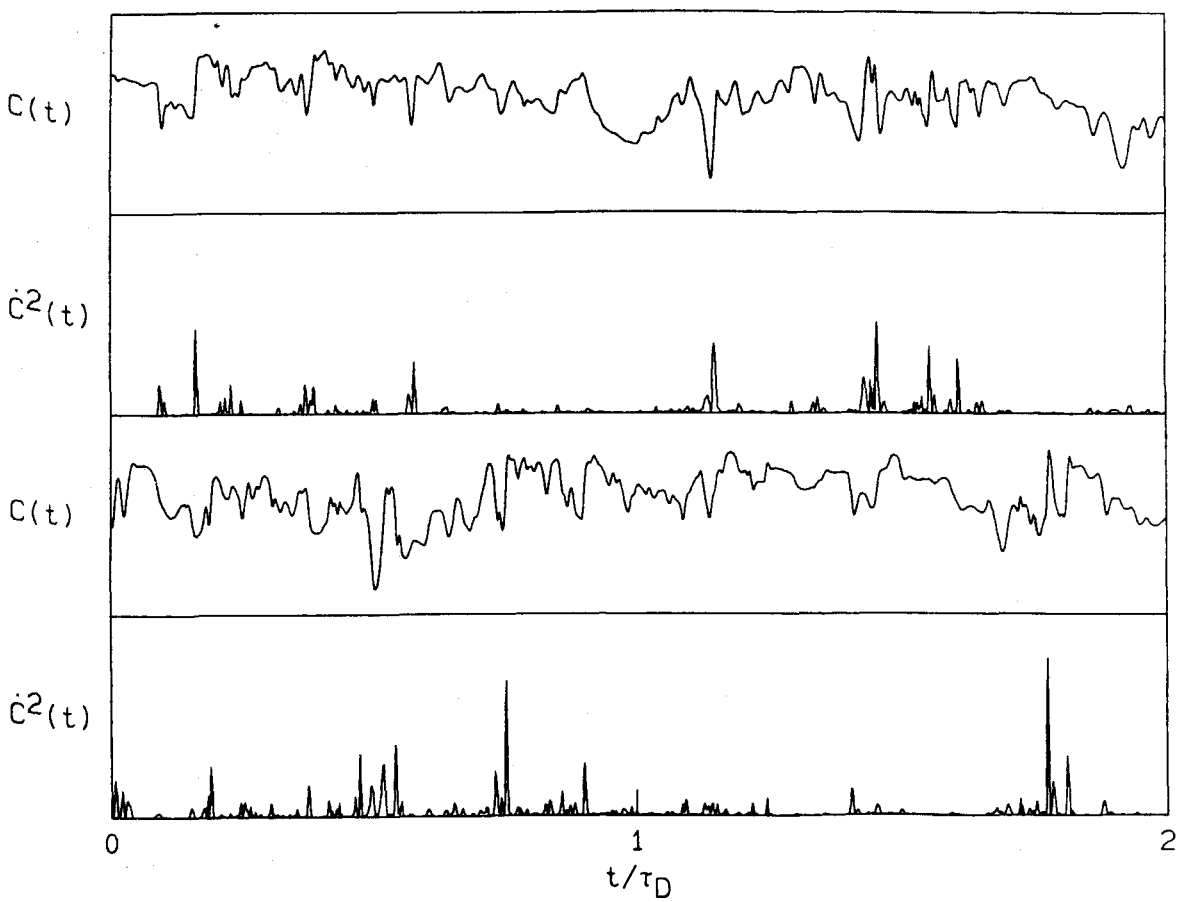

Figure 7-2. Time traces of C(t) and $\varepsilon_c(t)$ on the jet centerline at Re_0 = 5,000.

directly underneath the corresponding trace for C(t) on both Figures. The plotted data are continuous from the first line to the third line for C(t) and from the second line to the fourth line for $(dC/dt)^2$ on

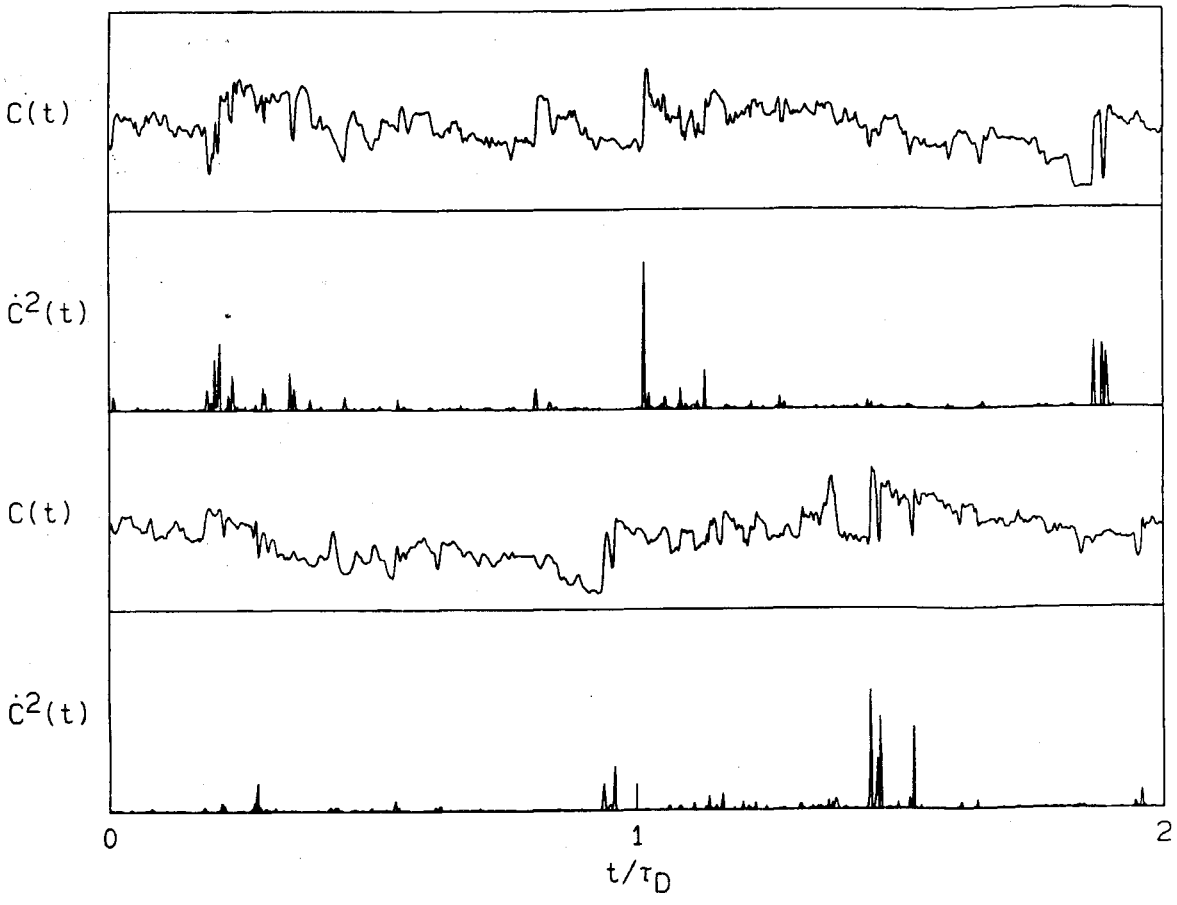

Figure 7-3. Time traces of C(t) and $\varepsilon_c(t)$ on the jet centerline at Re_0 = 16,000.

each of these plots. It should be noted that the maximum values of C(t) are about 1.7 times the mean concentration and the tallest peaks of $(dC/dt)^2$ are *one to two hundred times* the mean value of $(dC/dt)^2$.

The plotted time histories show the intermittent behavior of the local mixing rate as measured by $(dC/dt)^2$. The statistics of the extreme values of $(dC/dt)^2$ were investigated by making a histogram of

the time intervals between tall peaks and comparing it to the distribution that would result from a Poisson process with the same mean occurrence rate. Figure 7-4 is a comparison of this type. It was made from the data taken on the centerline of the jet at Re_0 = 16,000 and x/d

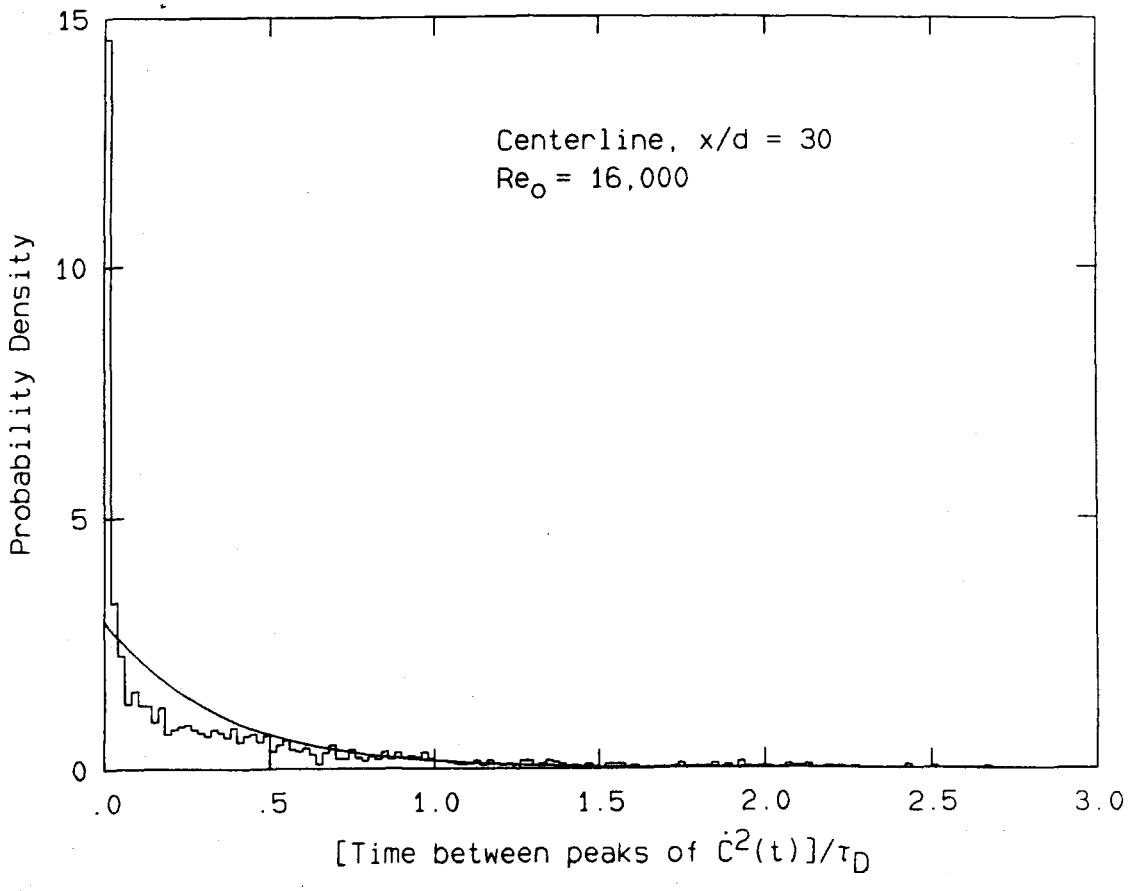

Figure 7-4. Distribution of time intervals between peaks of $(dC/dt)^2$

= 30, but is quite representative of results obtained throughout the jet at Re_0 = 5,000 and 16,000. A peak in $(dC/dt)^2$ was considered tall if it

was higher than a chosen threshold value. For the histogram on Figure 7-4, this threshold was set at twenty times the mean value of $(dC/dt)^2$. The smooth curve on Figure 7-4 is a decaying exponential, the expected shape of the PDF of peak separation times, if the peaks had Poisson statistics (Papoulis 1984).

As Figure 7-4 clearly shows, the time intervals between peaks of $(dC/dt)^2$ do seem to be described by Poisson statistics, especially for small times. This behavior was present in the measured histogram for a very wide range of threshold values, and implies that the peaks do not occur in an uncorrelated fashion but instead predominantly show up in small groups. This clustering of peaks of $(dC/dt)^2$ is seen in the time histories of $(dC/dt)^2$ on Figures 7-2 and 7-3. Further deviations from Poisson statistics are also apparent in the measured histogram. There is an underabundance of peak-separation intervals between about $.1\tau_D$ to $.8\tau_D$ and a mild excess of peak-separation intervals greater than τ_D. These deviations might be due to the large-scale "structures" of the flow (see Chapter 6, Section 2), which typically have high concentration gradients near their leading edges. The large scale "structures" could explain the observed deviations from Poisson statistics because they would cause clusters of peaks of $(dC/dt)^2$ to be separated by time intervals of approximately τ_D.

7.3 Power Spectra of ε_c

Figures 7-5 to 7-10 display the calculated power spectra of fluctuations in the estimated scalar dissipation rate, $E_{\varepsilon_c}(f)$, along the three rays $r/(x - x_0) \approx .00$, .06 and .11 to .12 for x/d = 20, 40, 60 and 80 at Re_0 = 5,000, and for x/d = 30 and 90 at Re_0 = 16,000. Each

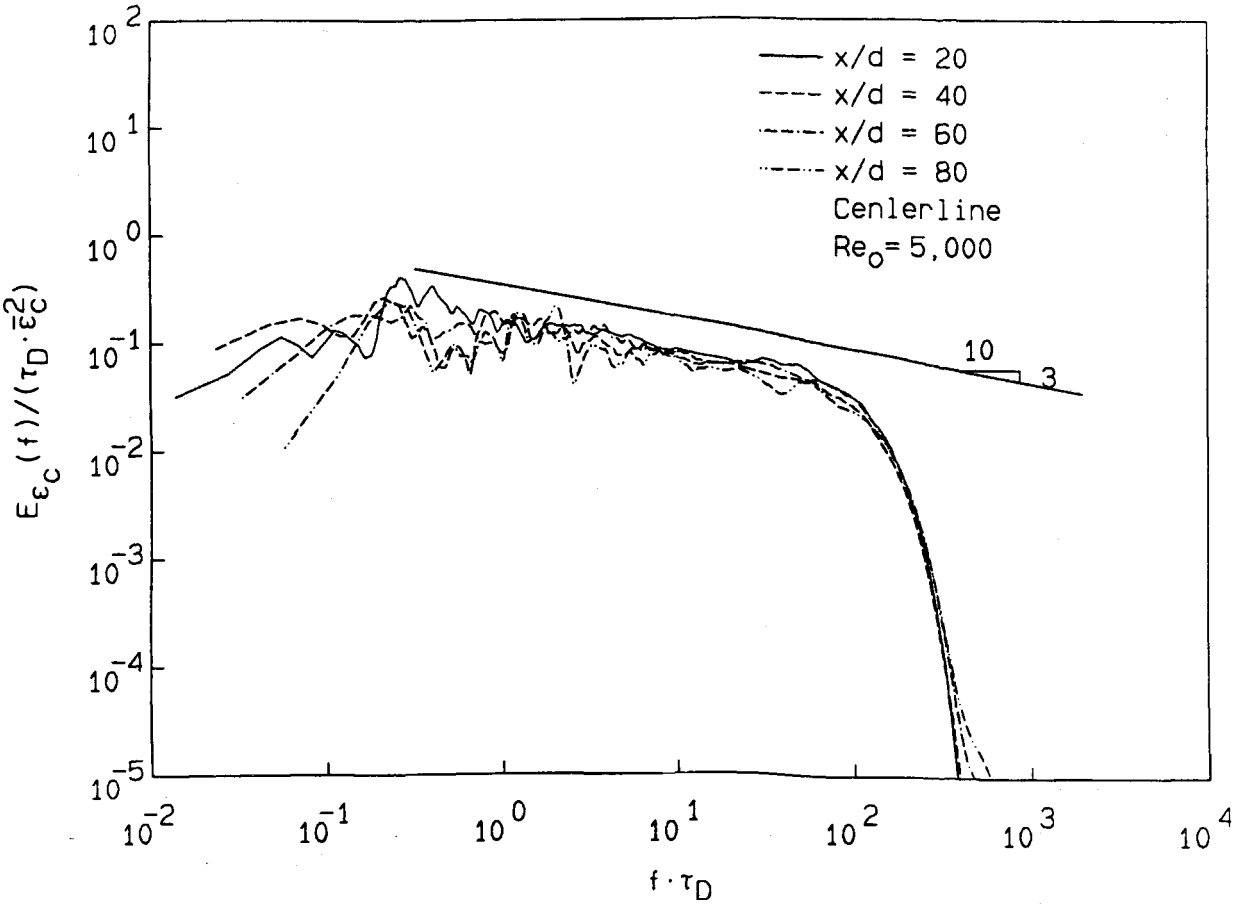

Figure 7-5. Power spectra of ε_c on the jet centerline at Re_0 = 5,000.

spectrum was computed with the same technique used to calculate the

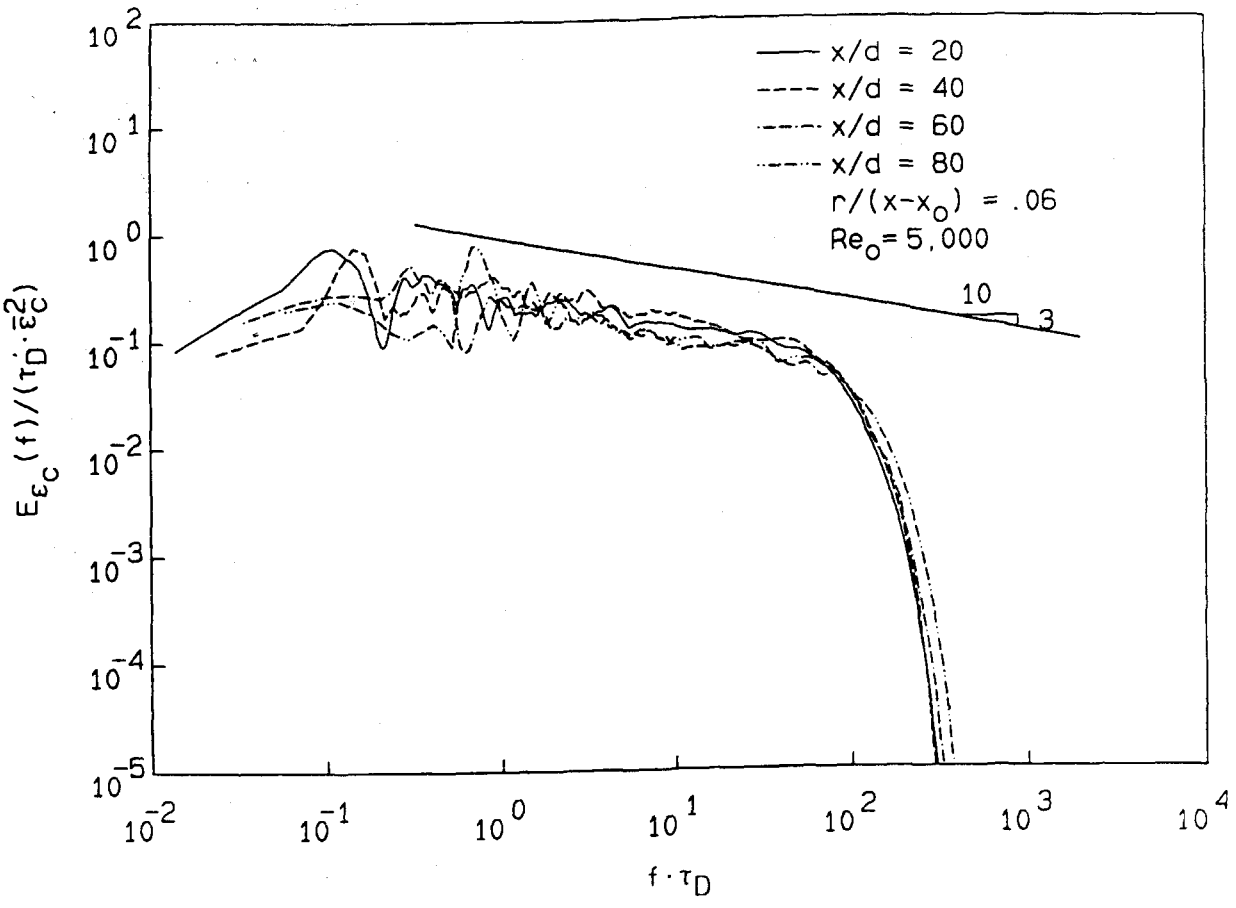

Figure 7-6. Power spectra of ε_c 3.4° off the centerline at Re_o = 5,000.

concentration fluctuation power spectrum, $E_c(f)$ (see Appendix C). The axis scaling on Figures 7-5 to 7-10 is the same as that for plots of $E_c(f)$ (Figures 4-1 to 4-6) with the local mean concentration, $\bar{C}$, replaced by the local mean estimated scalar dissipation rate, $\bar{\varepsilon}_c$. The slopes of the diagonal lines on Figures 7-5 to 7-10 were chosen by eye.

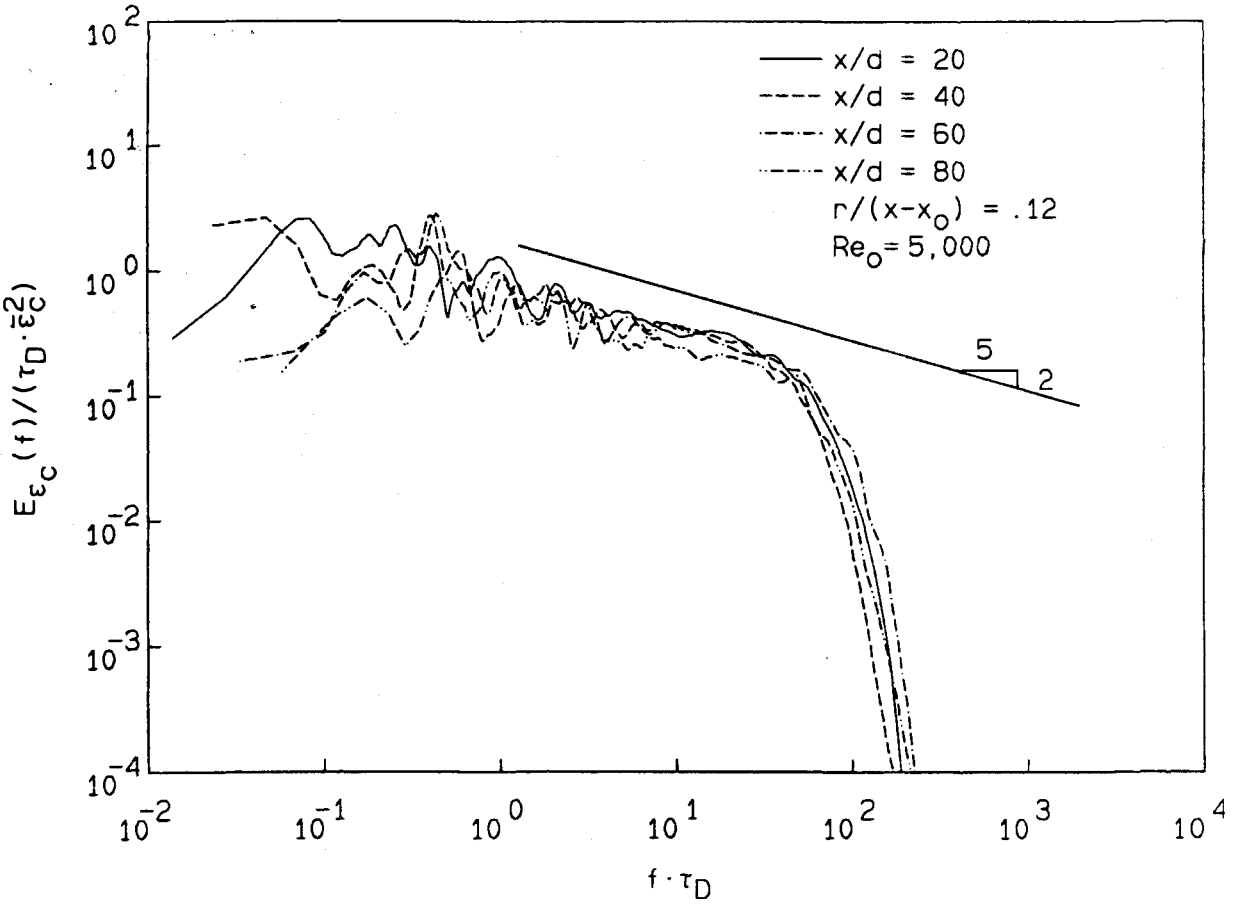

Figure 7-7. Power spectra of ε_c 7° off the centerline at Re_0 = 5,000.

Imperfections in the collapse are likely be the result of incomplete statistical convergence, misalignment of the measurement point with respect to the chosen ray, and the differing amounts of filtering done by the individual optimal kernels. In particular, the optimal filter entirely determines the shape and slope of each spectrum *beyond the point at which the spectrum turns sharply downward.* The

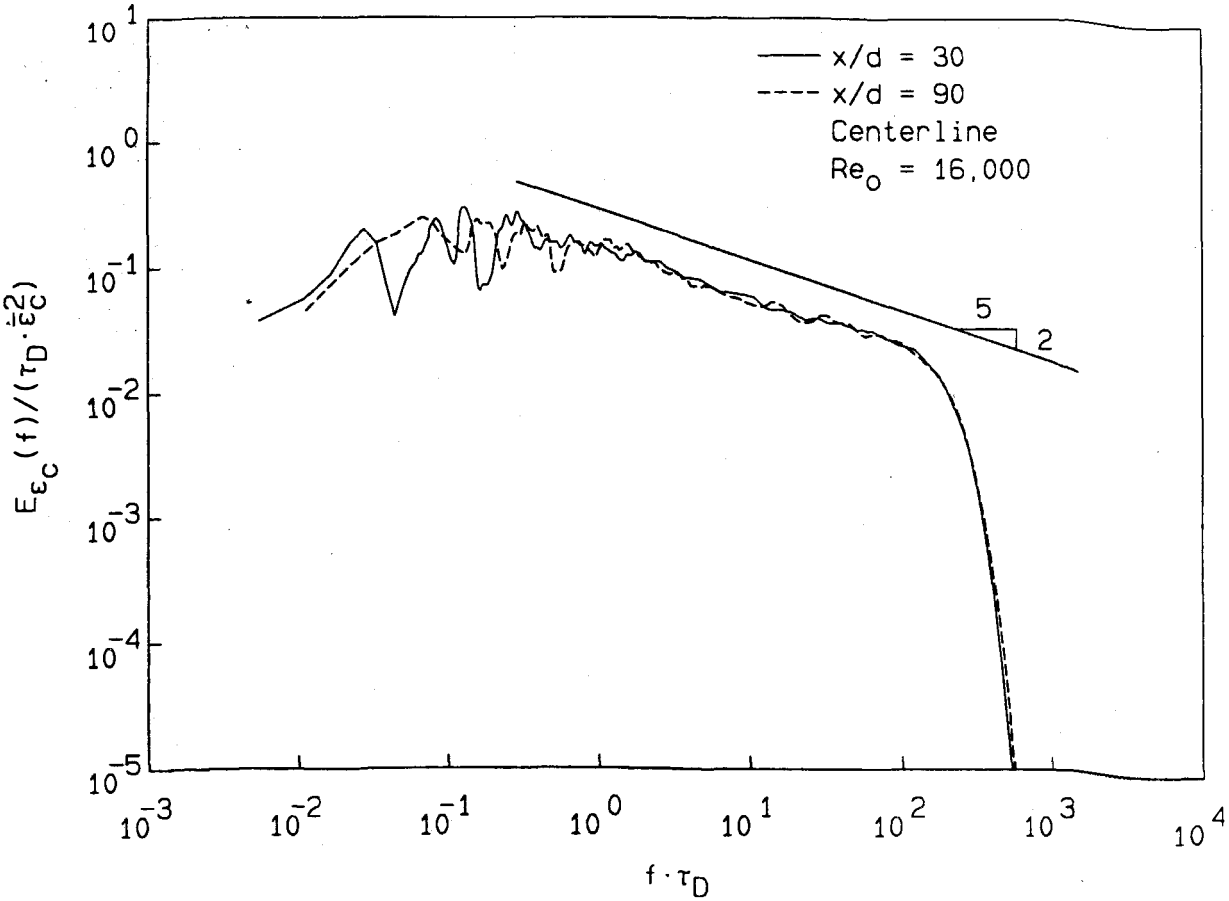

Figure 7-8. Power spectra of ε_c on the centerline of the jet at Re_0 = 16,000.

frequency location of the "knee", however, was found to be independent of the amount of filtering for kernels with a smaller effective width than the optimal kernel.

The quality and Reynolds number independence of the collapse aside, there are several noteworthy features of these spectra. The spectra of ε_c at Re_0 = 5,000 display a long power-law region, while the spectra of

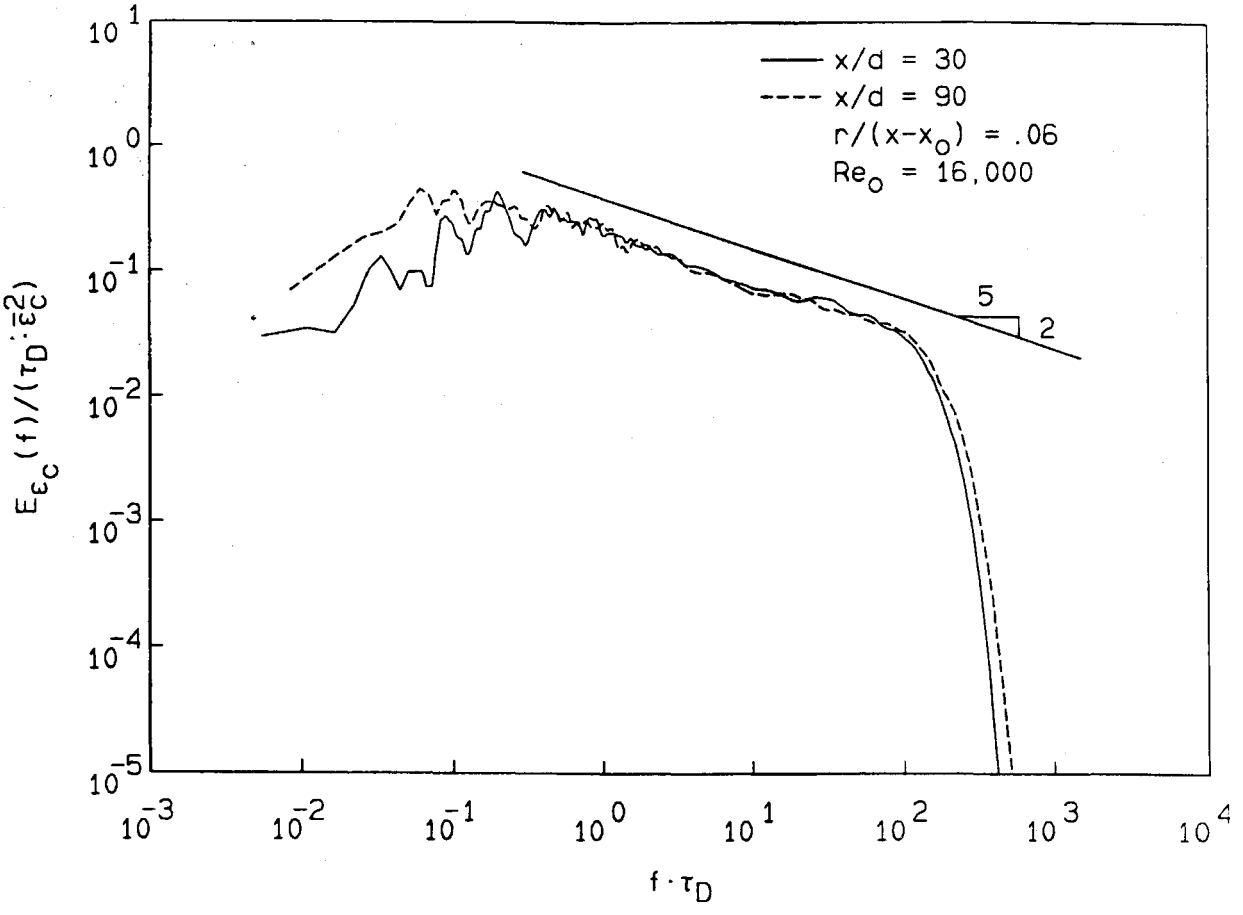

Figure 7-9. Power spectra of ε_c 3.4° off the centerline at Re_0 = 16,000.

fluctuations in C(t), at the same Reynolds number do not (see Figures 4-1 to 4-3). At both Reynolds numbers, the location of the knee frequency of $E_{\varepsilon_c}(f)$ is about a factor of three higher than the break-point frequency of $E_c(f)$. And finally, except for a small decrease in the slope as $r/(x - x_0)$ is increased, the shape of $E_{\varepsilon_c}(f)$ is almost independent of location within the jet.

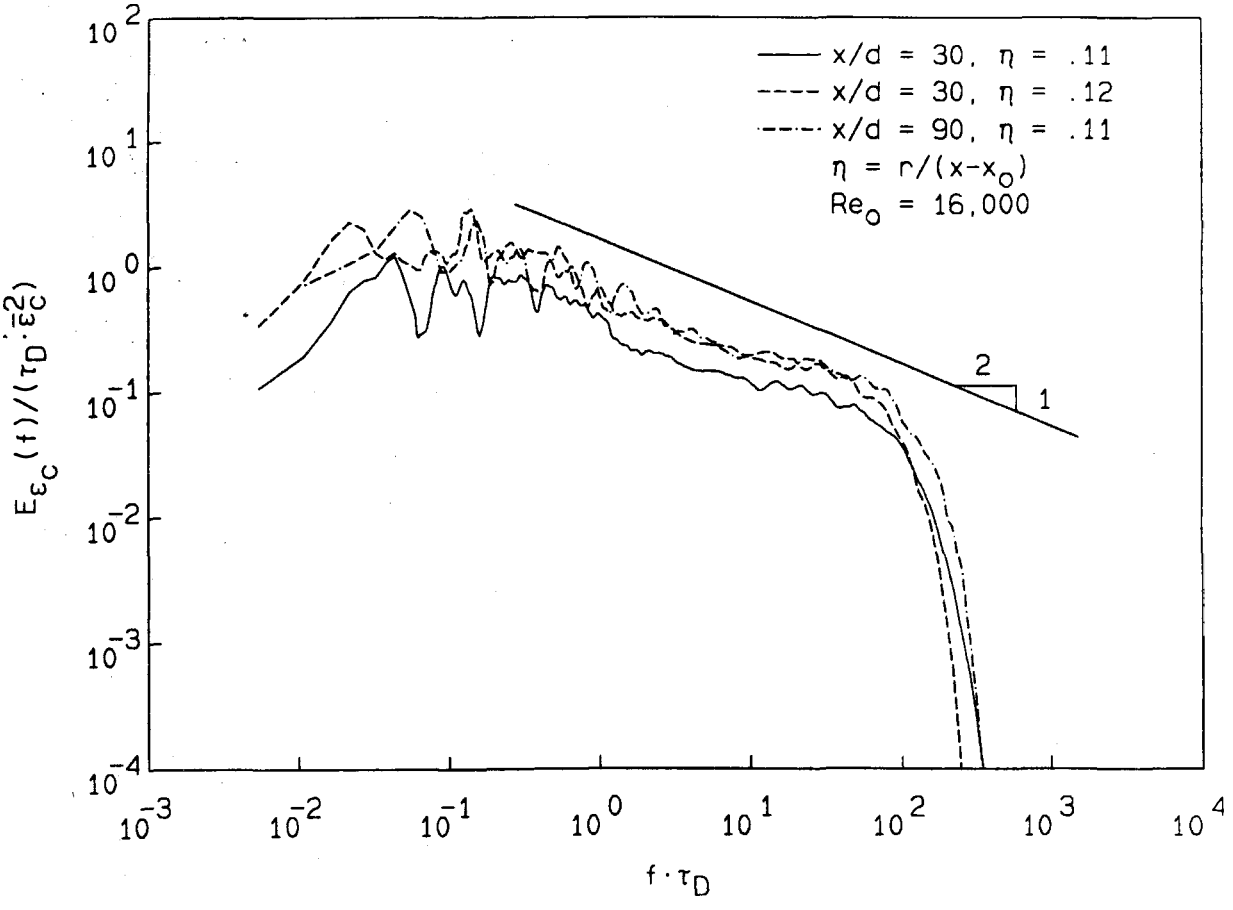

Figure 7-10. Power spectra of ε_c 6.3° to 7° off the centerline at Re_o = 16,000

Comparing the results of the different Reynolds numbers shows that the knee frequency is increased, and the slope of the spectra, up to the knee frequency, is decreased, as the Reynolds number is increased.

Classical theories of turbulence, as presented by Monin and Yaglom (1975) and the references cited therein, predict that the spectrum of the scalar dissipation rate, E_ζ, has the following form:

$$E_\zeta(k) \sim k^{\mu-1}, \tag{7.11}$$

at high Reynolds numbers in the scale-similarity range of wave numbers between the large scales and the dissipation scales. The exponent parameter, μ, should be a universal constant under these conditions.

Even though the current Reynolds numbers are probably not high for the classical theories to be applicable, they can be used to explore the lower Reynolds number limit for their validity. Equation (7.11), the current results for $E_{\varepsilon_c}(f)$, and the usual conversion between wave number and frequency ($k = 2\pi f/\bar{U}_{c1}$), imply that μ ranges from about .7 to .5, depending on the Reynolds number and the location within the jet. Masiello (1974) finds a value of $\mu = .42$ from the spectrum of the square of the temperature derivative measured near the centerline of a heated jet at $Re_0 = 810{,}000$. The differences in the experimental values of μ are probably the result of the large Reynolds number range spanned by the present data and those of Masiello. It is worth noting that the present results at least show a decrease in μ with increasing Re_0, which is consistent with the notion of the convergence of μ to a Reynolds number independent value that is perhaps close to the one reported by Masiello.

There is another way of computing μ from the statistical properties of ε_c (see Monin and Yaglom 1975, and references cited therein), which requires knowledge of $\varepsilon_c(t)$ and the probability density function of $\log(\varepsilon_c)$. This computation was not done because of problems surrounding the assumptions that produce Equation (7.1), and the poor agreement obtained by Masiello in calculating μ, using the two methods (.42 and .58), in spite of the large Reynolds number of his jet flow.

The errors produced in $E_{\varepsilon_c}(f)$ owing to the scaling of $(dC/dt)^2$ are probably small because the averaging involved in the computation of $E_{\varepsilon_c}(f)$ must correct for the portion of the velocity fluctuations that are uncorrelated with $(dC/dt)^2$. The scaling of $E_{\varepsilon_c}(f)$ in Figures 7-5 to 7-10 removes any biasing effect of the chosen formula for $\bar{U}_{cl}$. The error in $E_{\varepsilon_c}(f)$ that is due to the assumptions of isotropy and complete correlation of spatial derivatives is difficult to quantify. It probably leads to an increased fluctuation level in ε_c *as a result of the substantial overestimation of the number of zero-gradient points that result from using Equation (7.1) (see next section)*. This type of error would artificially raise the level of some portion of $E_{\varepsilon_c}(f)$ when compared to the spectrum of the true scalar dissipation rate, $E_\zeta(f)$.

7.4 The Probability Density Function of $\log[(dC/dt)^2]$

Classical theories of turbulence at high Reynolds number (Kolmogorov 1962, Obokhov 1962, and summarized in Monin and Yaglom 1975) have proposed that the probability density function of ζ, and by extension the probability density function of $(dC/dt)^2$ should be log-normal. The current data are at modest Reynolds numbers so they can, at most, provide a test to determine the lower Reynolds number limit of some of the classical ideas.

A log-normal distribution is Gaussian when plotted versus a logarithmic abscissa and a linear ordinate. Figures 7-11 to 7-16 show the probability density function of the logarithm of $(dC/dt)^2(\tau_D/\overline{C})^2$, along the three rays $r/(x-x_0) \approx .00$, .06 and .11 to .12 for x/d = 20, 40, 60 and 80 at Re_0 = 5,000, and x/d = 30 and 90 at Re_0 = 16,000. If the results from x/d = 20, Re_0 = 5,000 and $r/(x-x_0)$ = .12, are ignored because of possible near-field effects, the collapse of the plotted PDFs on Figure 7-13 is much improved. Because the factor $(\tau_D/\overline{C})^2$ goes like $(x-x_0)^6$, the chosen scaling is seen to collapse the PDF of $\log(dC/dt)^2$ over a large dynamic range in $(dC/dt)^2$. Note that $\overline{\varepsilon}_c$ required a scale factor of only $(x-x_0)^4$, since dividing $(dC/dt)^2$ by $\overline{U}_{cl}^2$ to produce ε_c introduces an additional factor of $(x-x_0)^2$.

As before, imperfections in the collapse are likely the result of misalignment of the measurement point with respect to the chosen ray, the differing widths of the optimal filters and any systematic bias introduced through the axis scaling by an error in the value of x_0, for

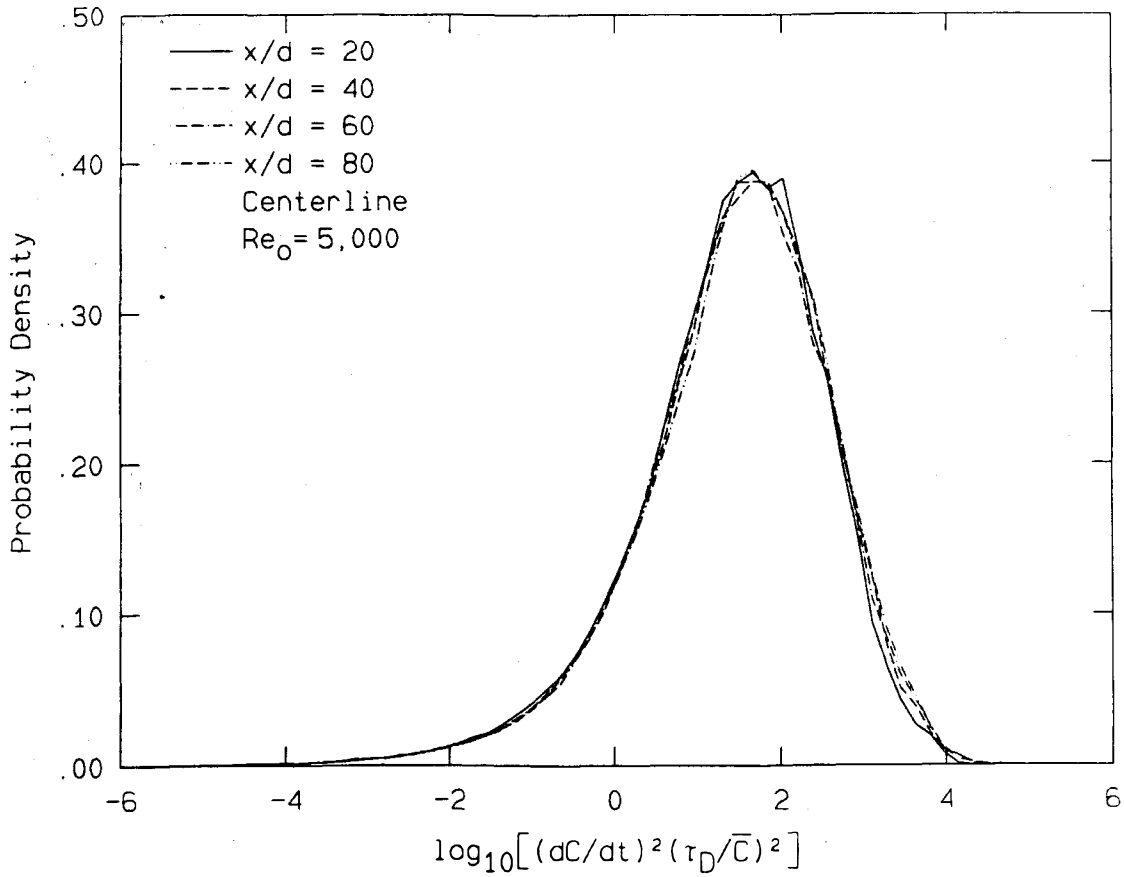

Figure 7-11. Probability density function of the logarithm of the scaled value of $(dC/dt)^2$ on the jet centerline at Re_0 = 5,000.

either Reynolds number.

These results show three consistent properties. First, the shape and width of the distributions appear to be nearly independent of Re_0 and $r/(x - x_0)$ even though the distributions are not centered on the same value of $\log_{10}[(dC/dt)^2(\tau_D/\overline{C})^2]$. For this distribution shape, the

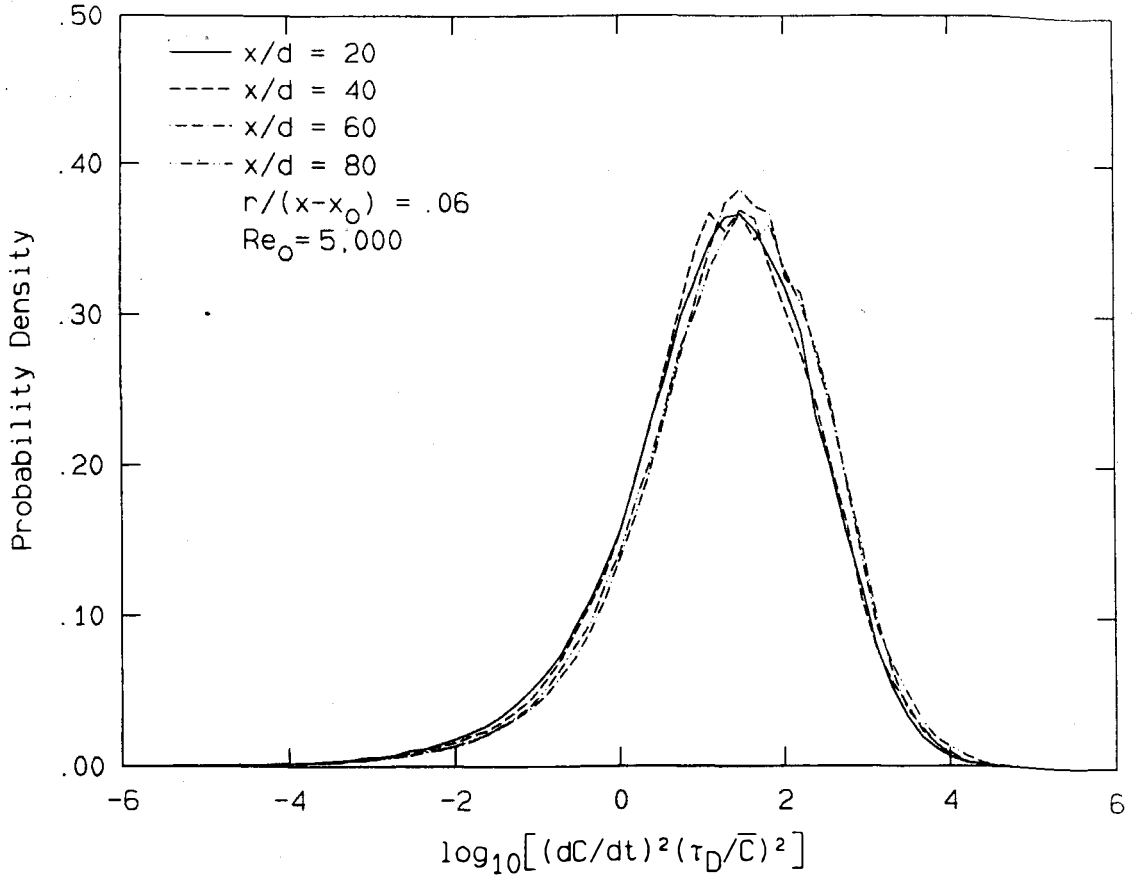

Figure 7-12. Probability density function of the logarithm of the scaled value of $(dC/dt)^2$ 3.4° off the jet centerline at Re_o = 5,000.

fraction of the total time that $(dC/dt)^2$ spends above its mean value is $.16 \pm .02$. Perhaps the most striking feature of these PDFs is their widths. *The full width at half-maximum for each distribution is about 3 orders of magnitude.* This means that if $(dC/dt)^2$ is proportional to $\zeta(t)$, then $\zeta(t)$ must also vary over many orders of magnitude, and this observation has important implications for the description and modeling

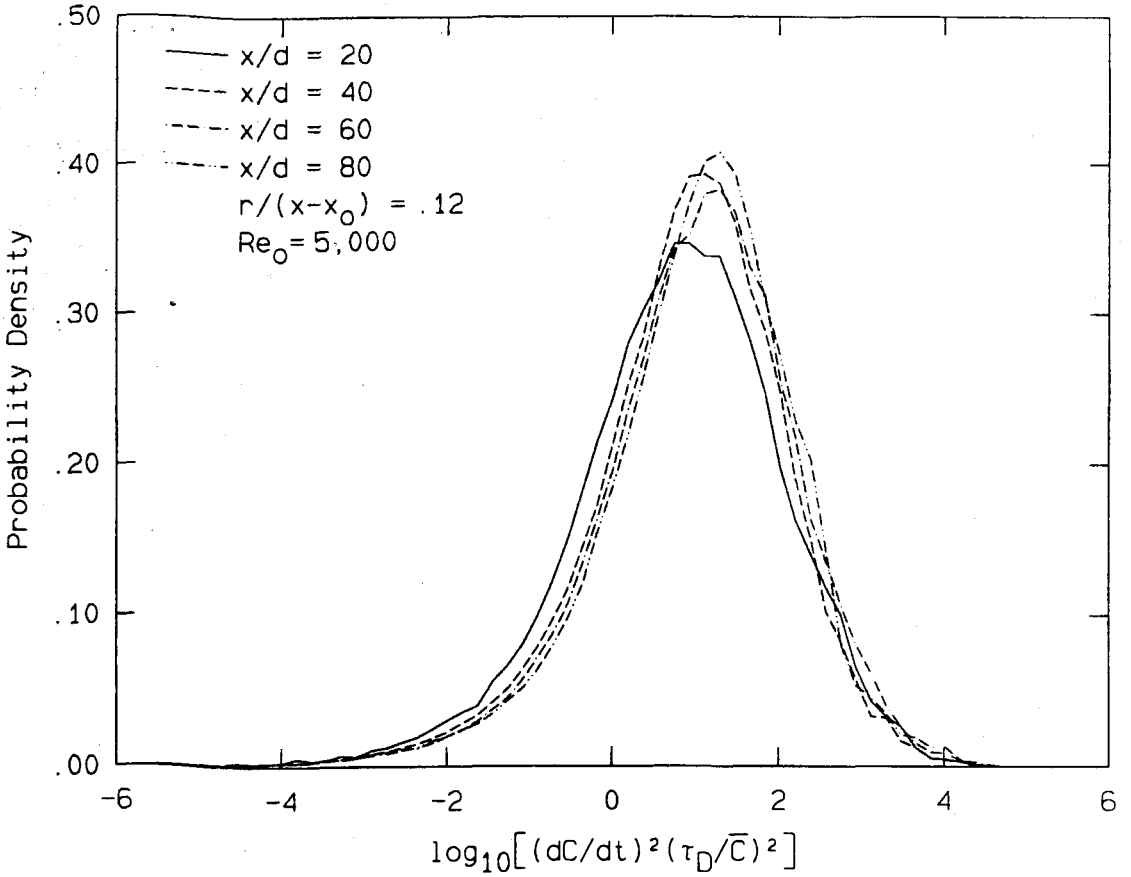

Figure 7-13. Probability density function of the logarithm of the scaled value of $(dC/dt)^2$ 7° off the jet centerline at Re_0 = 5,000.

of turbulent jet mixing with and without combustion.

A second observation concerning these distributions is that preponderant values are seen to shift toward higher values of $(dC/dt)^2$ for the larger Re_0, and toward lower values of $(dC/dt)^2$ as $r/(x - x_0)$ is increased. The shift to higher values of $(dC/dt)^2$ at the higher

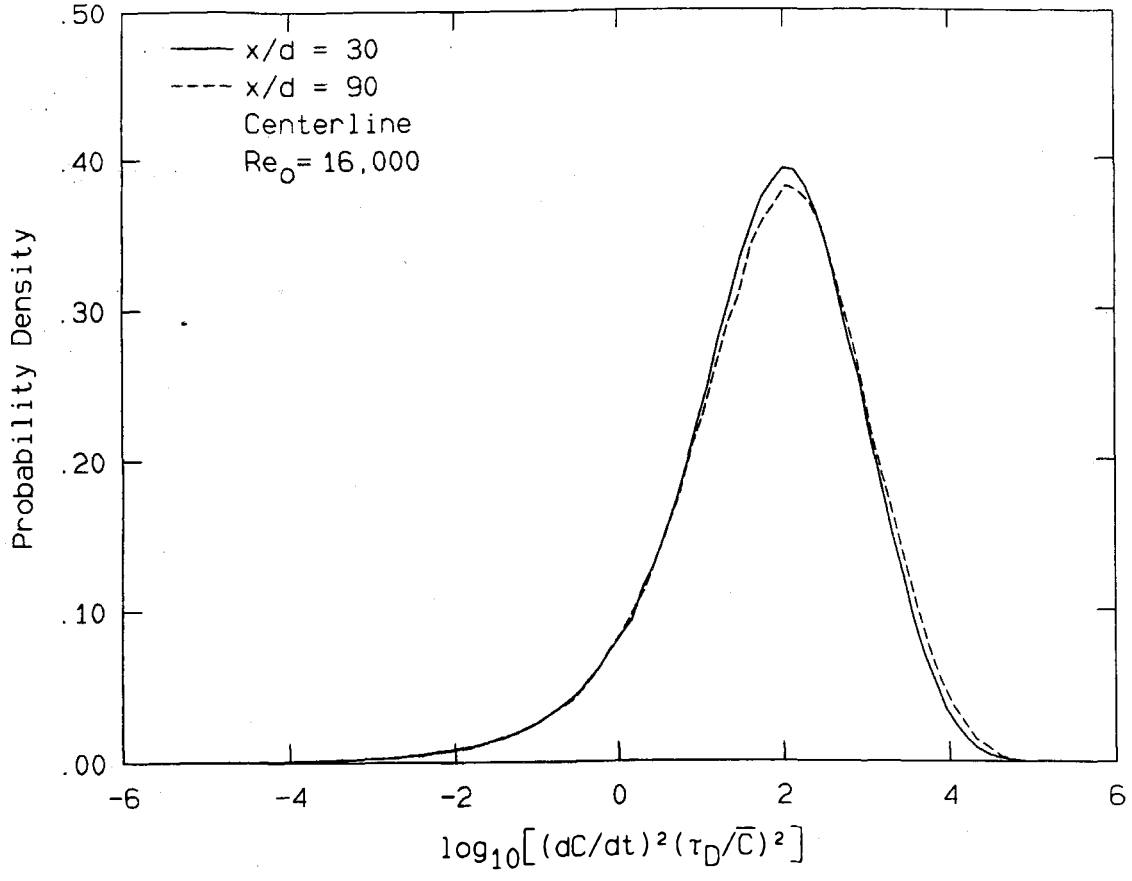

Figure 7-14. Probability density function of the logarithm of the scaled value of $(dC/dt)^2$ on the centerline of the jet at Re_0 = 16,000.

Reynolds number is more than offset by the scaling of $\bar{\varepsilon}_c$ with U_0 shown on Figure 7-1 so, that $\bar{\varepsilon}_c$ is actually lower at Re_0 = 16,000. The shift of the distributions to lower values of $(dC/dt)^2$, as $r/(x - x_0)$ is increased, results from the monotonic decrease in the mean convection velocity as the edge of the jet is approached.

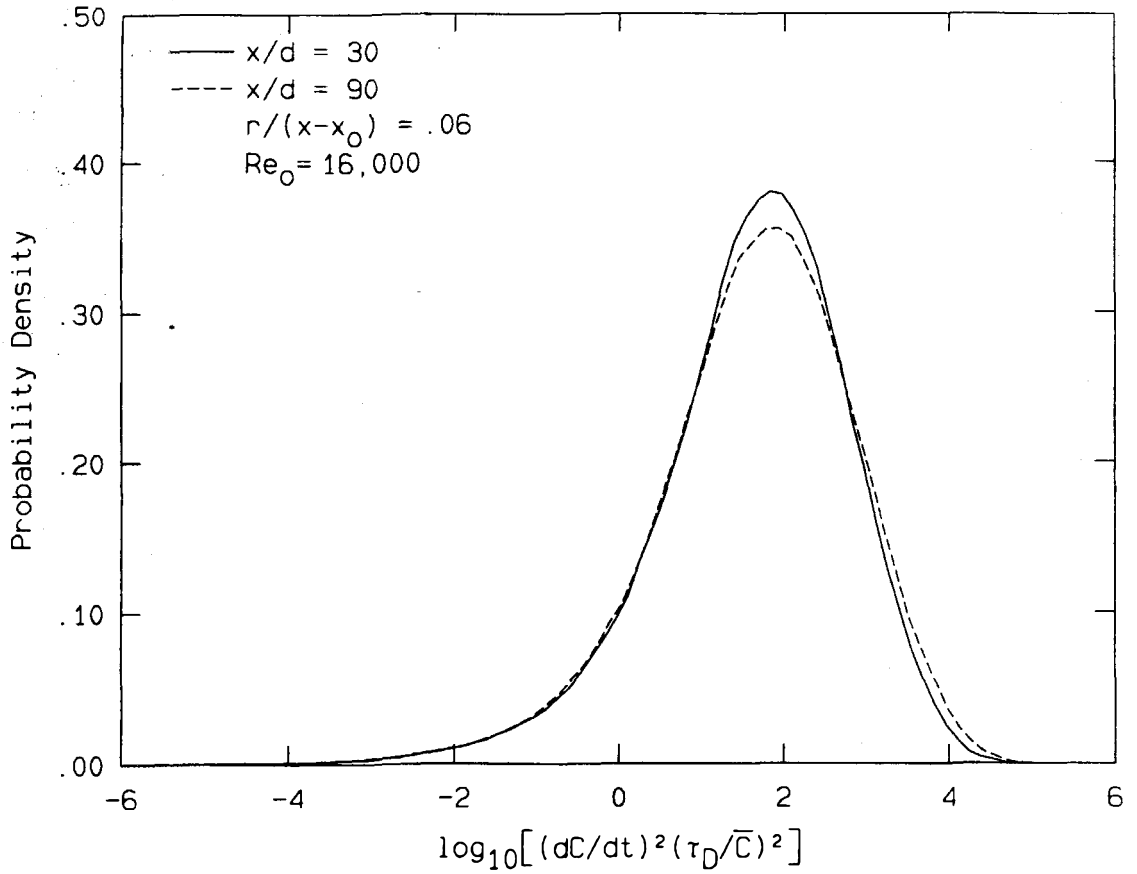

Figure 7-15. Probability density function of the logarithm of the scaled value of $(dC/dt)^2$ 3.4° off the centerline at Re_0 = 16,000.

And finally, the distributions on Figures 7-11 to 7-16 appear to be almost normal with a slight excess of low values and a slight deficit of high values. This last property was also noted by Masiello (1974) for the cumulative distribution function, CDF, of the square of the time derivative in a heated jet at Re_0 = 810,000. The CDF and PDF of a

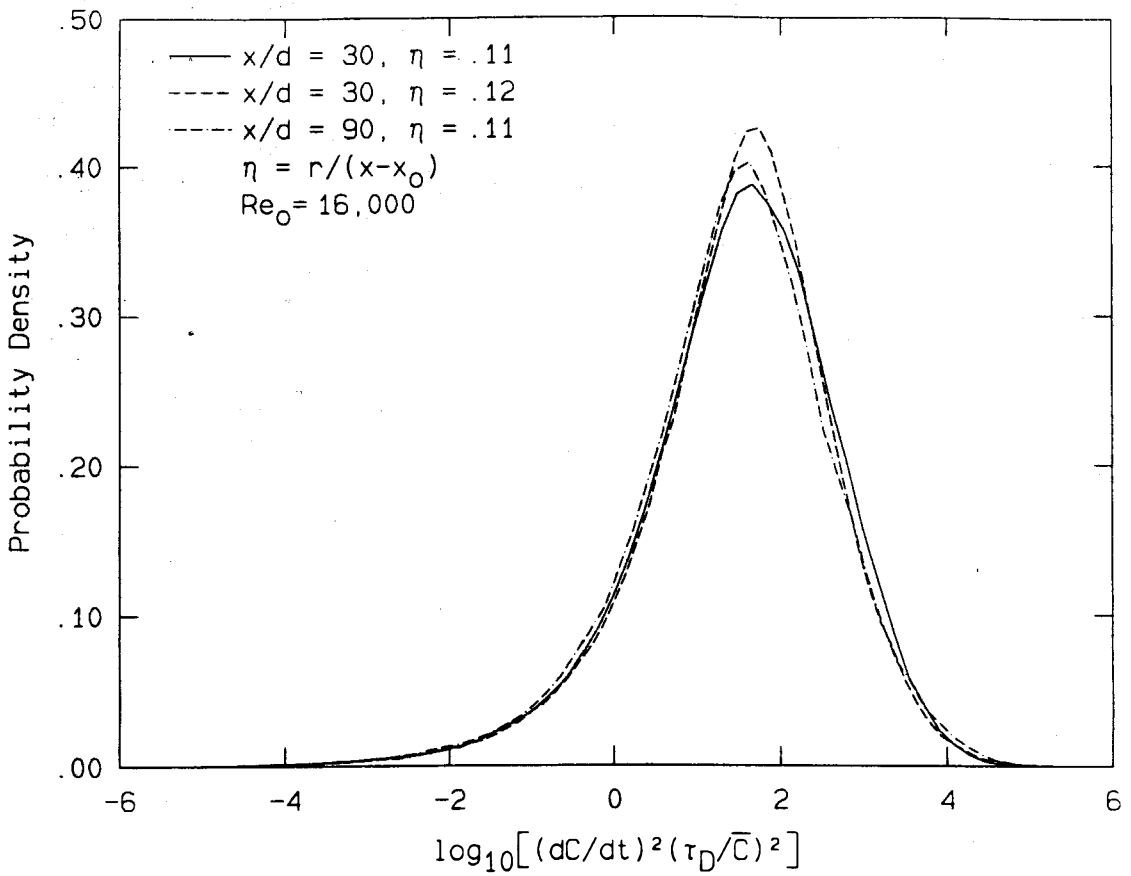

Figure 7-16. Probability density function of the logarithm of the scaled value of $(dC/dt)^2$ 6.3° to 7° off the centerline at Re_0 = 16,000.

random variable ξ, $0 \leq \xi < \infty$, satisfy:

$$CDF(\xi) = \int_0^{\xi} PDF(\xi')\, d\xi' \qquad (7.12)$$

where the normalization of the PDF(ξ) is set by CDF(∞) = 1.

The measured excess of low values and deficit of high values of $(dC/dt)^2$ and ε_c, must be independent of Re_0 because they are a direct result of the assumption that the three spatial derivative terms in ζ are completely correlated. This assumption allowed ε_c from Equation (7.1) to be postulated as a statistical basis for ζ and will be shown to be a major cause of the deviation from log-normality in the PDF of $(dC/dt)^2$ near $(dC/dt)^2 = 0$.

To display the statistical error that comes from using Equation (7.1) in the production of a probability density function for ζ, it is first necessary to derive a simple relationship between the probability density function of a random variable ξ, $0 < \xi < \infty$, and the probability density function of $\log\xi$, $-\infty < \log\xi < \infty$. This derived relationship, which does not depend on the identification of ξ as $(dC/dt)^2(\tau_D/\bar{C})^2$, will be used to determine the behavior of the PDF of $\log[(dC/dt)^2(\tau_D/\bar{C})^2]$ for small values of $(dC/dt)^2(\tau_D/\bar{C})^2$.

By definition, it can be chosen that:

$$\int_0^{\xi} \Phi_1(\xi')\, d\xi' = \int_{-\infty}^{\log\xi} \Phi_2(\log\xi')\, d(\log\xi'), \tag{7.13}$$

where $\log(\ )$ denotes the natural logarithm of $(\ )$, $\Phi_1(\xi)$ is the probability density function of ξ, and $\Phi_2(\log\xi)$ is the probability density function of $\log\xi$. Differentiate Equation (7.12) with respect to ξ to get:

$$\Phi_1(\xi) = \Phi_2(\log\xi) \cdot \frac{d(\log\xi)}{d\xi} = \Phi_2(\log\xi) \cdot \frac{1}{\xi}. \tag{7.14}$$

Now assume a power-law behavior for Φ_1 near $\xi = 0$, i.e. $\Phi_1(\xi) = \Phi_o \xi^s$, where Φ_o and s are constant real numbers. Equation (7.14) then becomes:

$$\Phi_o \xi^{s+1} = \Phi_2(\log\xi), \text{ as } \xi \to 0. \tag{7.15}$$

Taking the logarithm of both sides yields:

$$\log\Phi_o + (s+1)\log\xi = \log\Big(\Phi_2(\log\xi)\Big), \text{ as } \log\xi \to -\infty. \tag{7.16}$$

This means that a power-law behavior of $\Phi_1(\xi)$ for $\xi \to 0$ can be discovered from a plot of $\log(\Phi_2)$ versus $\log\xi$.

Figures 7-17 and 7-18 are plots of the logarithm of the PDF of $\log_{10}[(dC/dt)^2(\tau_D/\bar{C})^2]$ along the centerline of the jet at Re_o = 5,000 and 16,000. For small values of $\log_{10}[(dC/dt)^2(\tau_D/\bar{C})^2]$, both plots show a power-law behavior with a slope of $+\frac{1}{2}$ for many decades. Equation (7.16), with the formal identification of ξ as $(dC/dt)^2(\tau_D/\bar{C})^2$, then implies that $s = -\frac{1}{2}$, so the probability density function of $(dC/dt)^2$ must have an integrable singularity as $(dC/dt)^2 \to 0$ of the form $1/\sqrt{(dC/dt)^2}$. The PDFs of $\log[(dC/dt)^2(\tau_D/\bar{C})^2]$ on the rays at $r/(x - x_o)$ = .06, and .12 show exactly the same behavior as those from the centerline.

The square root singularity of the PDF of $(dC/dt)^2$ can be understood as a direct result of the parabolic geometry of $(dC/dt)^2$ near zero. Small values of $(dC/dt)^2$ come from the zero crossings of dC/dt. In fact, if dC/dt crosses zero with a finite slope S_o at t_o, then near t_o:

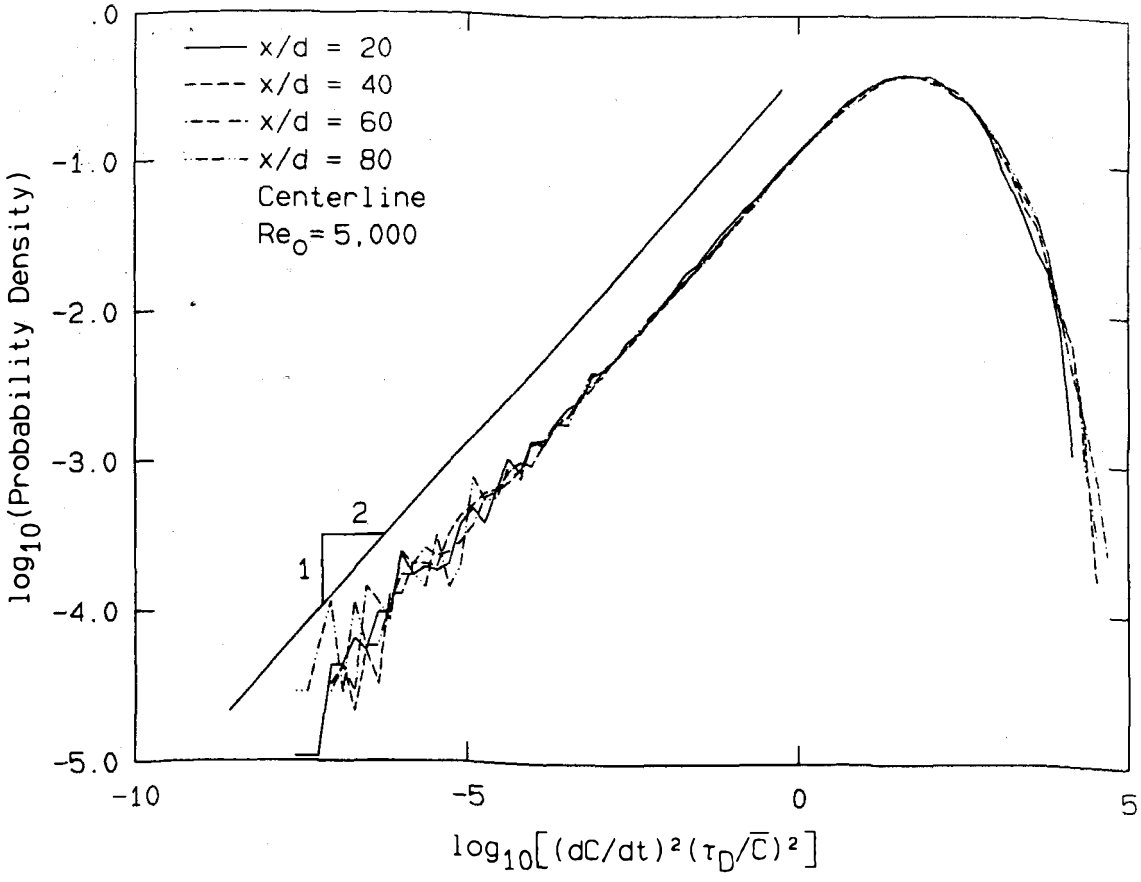

Figure 7-17. Logarithm of the probability density function of the logarithm of the scaled value of $(dC/dt)^2$ on the centerline at Re_o = 5,000.

$$\left(\frac{dC}{dt}\right)^2 = \dot{C}^2 = S_o^2(t - t_o)^2. \qquad (7.17)$$

The density of points, $\rho_1(t)$, along the curve of $(dC/dt)^2$ is constant with respect to time because the data sets were produced with a constant sampling rate. Hence:

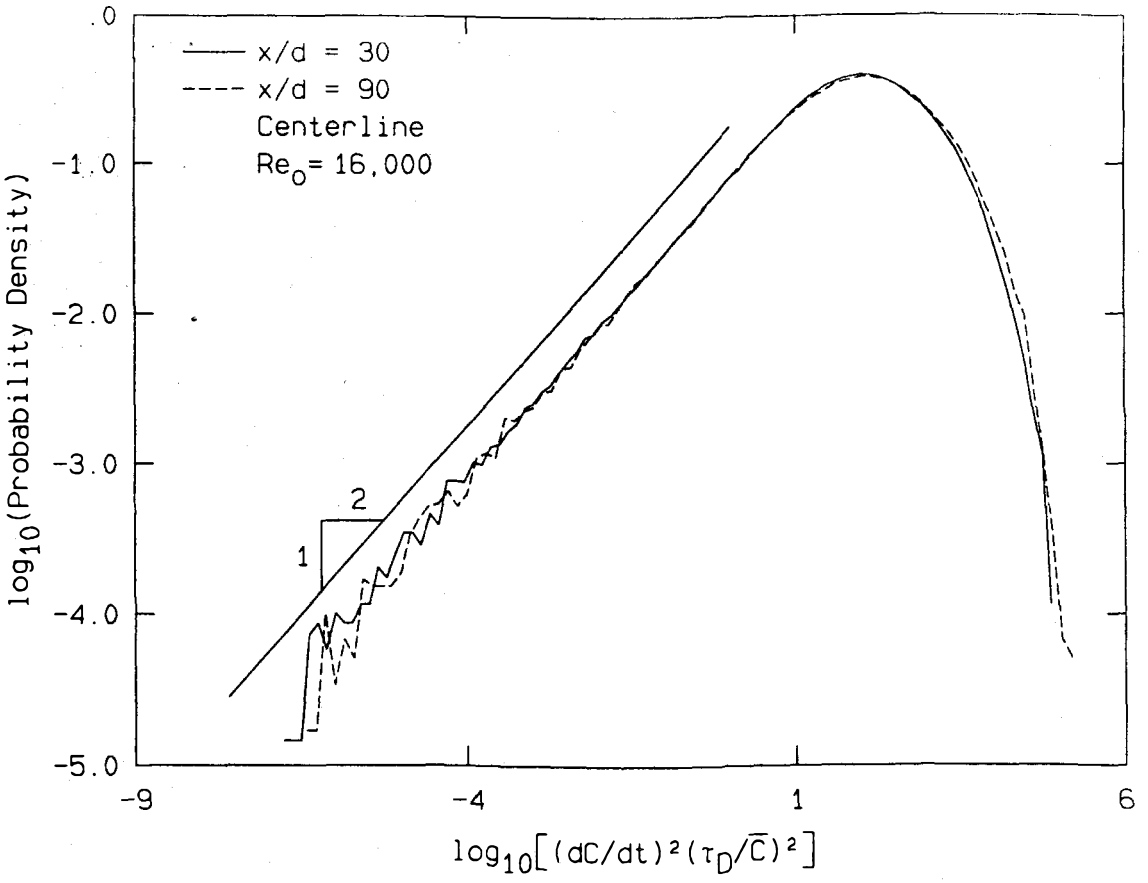

Figure 7-18. Logarithm of the probability density function of the logarithm of the scaled value of $(dC/dt)^2$ on the centerline at Re_0 = 16,000.

$$\rho_1(t)\, dt = \rho_0\, dt, \tag{7.18}$$

where ρ_0 is a constant. To determine how the density of sample points depends on $(dC/dt)^2$, differentiate and invert Equation (7.17):

$$d(\dot{C}^2) = 2 S_0^2 (t - t_0)\, dt\ , \quad (t - t_0) = \frac{1}{S_0} \left(\dot{C}^2\right)^{1/2}. \tag{7.19 \& 20}$$

Elimination of $t - t_0$ and dt on the right hand side of Equation (7.18) using Equation (7.19 & 20) gives:

$$\rho_1(t)\,dt = \rho_2(\dot{C}^2)\,d(\dot{C}^2) = \frac{\rho_0}{2S_0}\left(\dot{C}^2\right)^{-1/2} d(\dot{C}^2), \qquad (7.21)$$

where ρ_2 is the density of points with respect to $(dC/dt)^2$, given Equations (7.17) and (7.18). Because the slope of the concentration time history crosses zero many times, the compilation of the PDF of $(dC/dt)^2$ must involve the accumulation of data points in many regions that are well described by Equation (7.17) with differing values of S_0 and t_0. While the details of each region where Equation (7.17) applies are lost in the accumulation, the singular behavior of the local PDF of $(dC/dt)^2$, near $(dC/dt)^2 = 0$ ($\rho_2(\dot{C}^2)$ from Equation 7.21), is not. Note that the singular behavior of the local PDF occurs independently of the values of ρ_0, S_0, and t_0 so the excess of low values of the $(dC/dt)^2$ must be found if there are enough data points for proper statistical resolution of the full range of $(dC/dt)^2$.

The preceding discussion concerning the PDF of $(dC/dt)^2$ near $(dC/dt)^2 = 0$, was motivated by conversations with Dr. Roddam Narasimha.

The only way that the PDF of $(dC/dt)^2$ near $(dC/dt)^2 = 0$ could have a behavior different from that given by Equation (7.21) is if S_0 was zero at a significant number of the zeros of dC/dt. This actually does occur near the edges of the jet where the measured concentration spends a relatively large fraction of the time at $C = 0$ with $dC/dt = 0$. This is reflected in the PDF of $(dC/dt)^2$ by a further increase in the relative

abundance of the very lowest values of $(dC/dt)^2$, when compared to the PDF of $(dC/dt)^2$ from the centerline. The extent to which Equation (7.21) is followed by the plotted results on Figures 7-14 and 7-15 essentially proves that *dC/dt almost always crosses zero with a nonzero slope for* $r/(x - x_0) \leq .12$. The other extreme case, i.e. $S_0 \to \infty$, is be prevented by molecular diffusion.

If the PDF of $(dC/dt)^2$ (or ε_C) was actually log-normal it would appear as an inverted parabola in Figures 7-14 and 7-15,

$$\log\left(\text{PDF}(\dot{C}^2)\right) = -a_2(\log \dot{C}^2)^2 + a_1 \log \dot{C} + a_0, \tag{7.22}$$

where a_2, a_1, and a_0 are all real constants with $a_2 > 0$. This form for the PDF of $(dC/dt)^2$ goes to zero as $(dC/dt)^2 \to 0$ which is in clear contradiction with the measured distributions and the parabolic geometry of $(dC/dt)^2$ near $(dC/dt)^2 = 0$. However, the classical theories are supported by the measured PDFs shown on Figures 7-11 to 7-18 for values of $(dC/dt)^2(\tau_D/\overline{C})$ above 1, where the expected log-normal shapes are more closely realized than for values of $(dC/dt)^2(\tau_D/\overline{C})$ below 1. Recall that at large values of $(dC/dt)^2$ error from the the assumption of isotropy may also effect the results.

The physical reason for the failure of $(dC/dt)^2$, and therefore ε_C, to display something even close to log-normal statistics at the small values of $(dC/dt)^2$, comes from the serious overestimation of the number of points in the turbulent concentration field where the concentration gradient is zero, $\nabla C = 0$. By assuming that the three terms of $|\nabla C|^2$ are

completely correlated and that they can be represented by a scaled time derivative, ε_c is forced to have one-dimensional statistics which do not accurately model the three-dimensional character of the scalar dissipation, $\zeta = 2D_{j\infty}|\nabla C|^2$. In particular, the form of Equation (7.1) requires that ε_c is zero every time dC/dt is zero, while it is clear that the zeros of each of the three terms of ζ need not be coincident in time. ζ will be zero only at a zero gradient point. The importance of the number and distribution of zero gradient points in a turbulent flow that mixes a passive scalar is discussed in detail by Gibson (1968 I). It is quite possible that zero gradient points are extremely rare within the turbulent concentration field of the jet, and that the true PDF of ζ is very nearly log-normal.

It is probably a reasonable assumption that the scaled value of $(dC/dt)^2$ is an adequate estimate for one of the spatial derivative terms of ζ from Equation (7.6), since this requires only the validity of Taylor's hypothesis. Hence, the true statistics of ζ of might be realized by a sum of three squared time derivative terms with the correct amount of correlation between terms. To investigate this possibility, and to determine the effect on the statistics of ε_c from correlating the squared derivative terms, a grouping of three values of $(dC/dt)^2$, with a varying statistical weight for each term, was used in place of $(dC/dt)^2$ to compute probability densities.

In particular, this meant exchanging $(dC/dt)^2$ for the heuristic quantity, Σ_3:

$$\Sigma_3 = \sum_{i=1}^{3} \omega_i \left(\frac{dC}{dt} \right)_i^2 , \tag{7.23}$$

where $\omega_1 + \omega_2 + \omega_3 = 1$, and $\omega_1, \omega_2, \omega_3 \geq 0$. The three derivative terms, $(dC/dt)_i$, were chosen by sectioning a data set into three equal parts and sequentially drawing $(dC/dt)_1$ from the first section, $(dC/dt)_2$ from the second section, and $(dC/dt)_3$ from the third section. A one-parameter family for the weighting of the derivatives, ω_i, was constructed by allowing ω_1 to be the independent parameter and choosing $\omega_2 = \omega_3 = (1 - \omega_1)/2$. If $\omega_1 = 1$, then $\Sigma_3 = (dC/dt)_1^2$, and the case of complete correlation of derivative terms is recovered. For $\omega_1 = 1/3$, the three terms in Σ_3 are given equal weight. For $\omega_1 = 0$, the first term in Σ_3 is ignored and the second two are given equal weight. Note that if the mean value of $(dC/dt)^2$ is stationary within a data set, then $\bar{\Sigma}_3$ does not depend on the value of the free parameter, ω_1, because $\omega_1 + \omega_2 + \omega_3 = 1$.

The results of the parameter study for $0 \leq \omega_1 \leq 1$ are shown on Figures 7-19 to 7-22. As before, the multiplicative constants that change the sum of the time derivatives, Σ_3, to ε_c have been left out of the calculations and therefore do not appear in the axis scaling. Even though Figures 7-19 to 7-22 were made from a centerline data set at $x/d = 30$ and $Re_0 = 16{,}000$, the trends shown by changing ω_1 on these Figures are representative of those seen throughout the jet. The four plots (Figures 7-19 to 7-22) are for two ranges of ω_1: $1/3 \leq \omega_1 \leq 1$, where

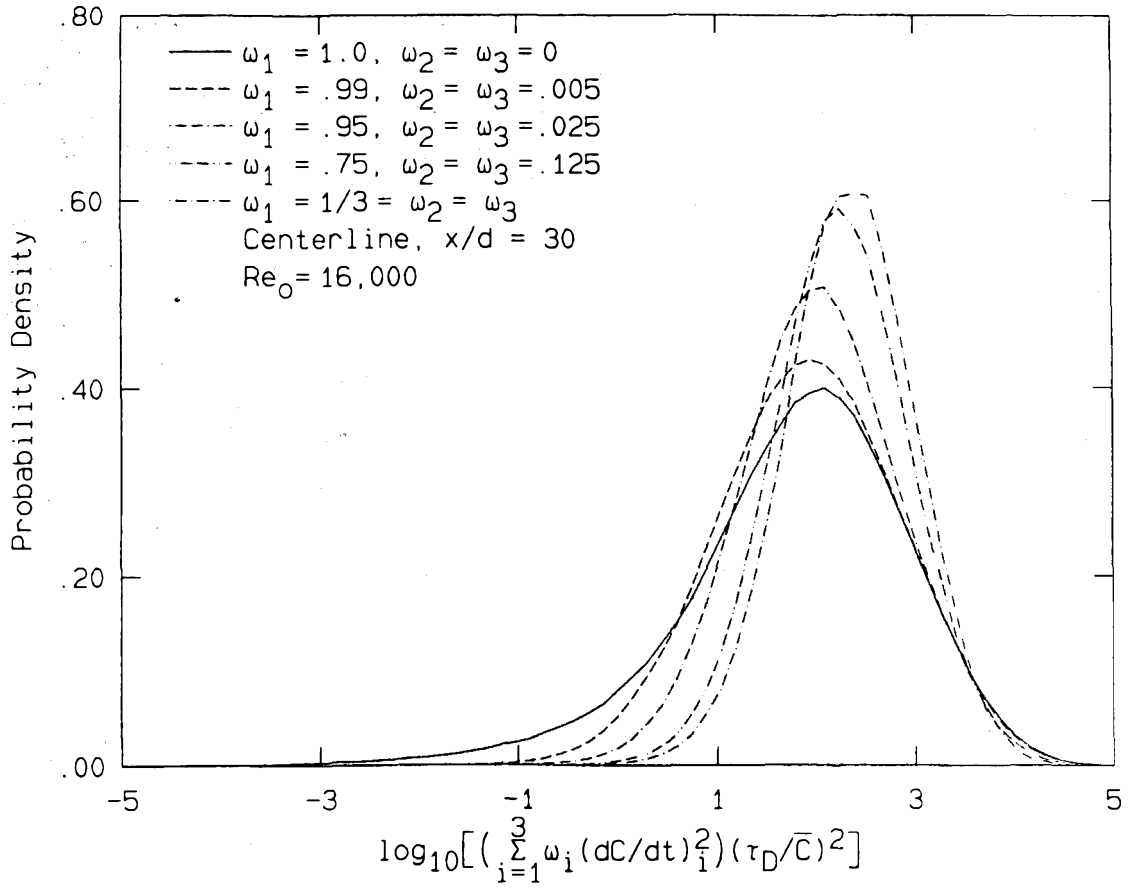

Figure 7-19. Probability density functions of the logarithm of Σ_3 for $\frac{1}{3} \leq \omega_1 \leq 1$.

the contribution from a single term dominates Σ_3, and $0 \leq \omega_1 \leq \frac{1}{3}$, where two terms in Σ_3 contribute equally and dominate the third term. At $\omega_1 = \frac{1}{3}$, the three terms have equal weight. Figures 7-19 and 7-20 show these two ranges with a linear ordinate, and Figures 7-21 and 7-22 show them with a logarithmic ordinate.

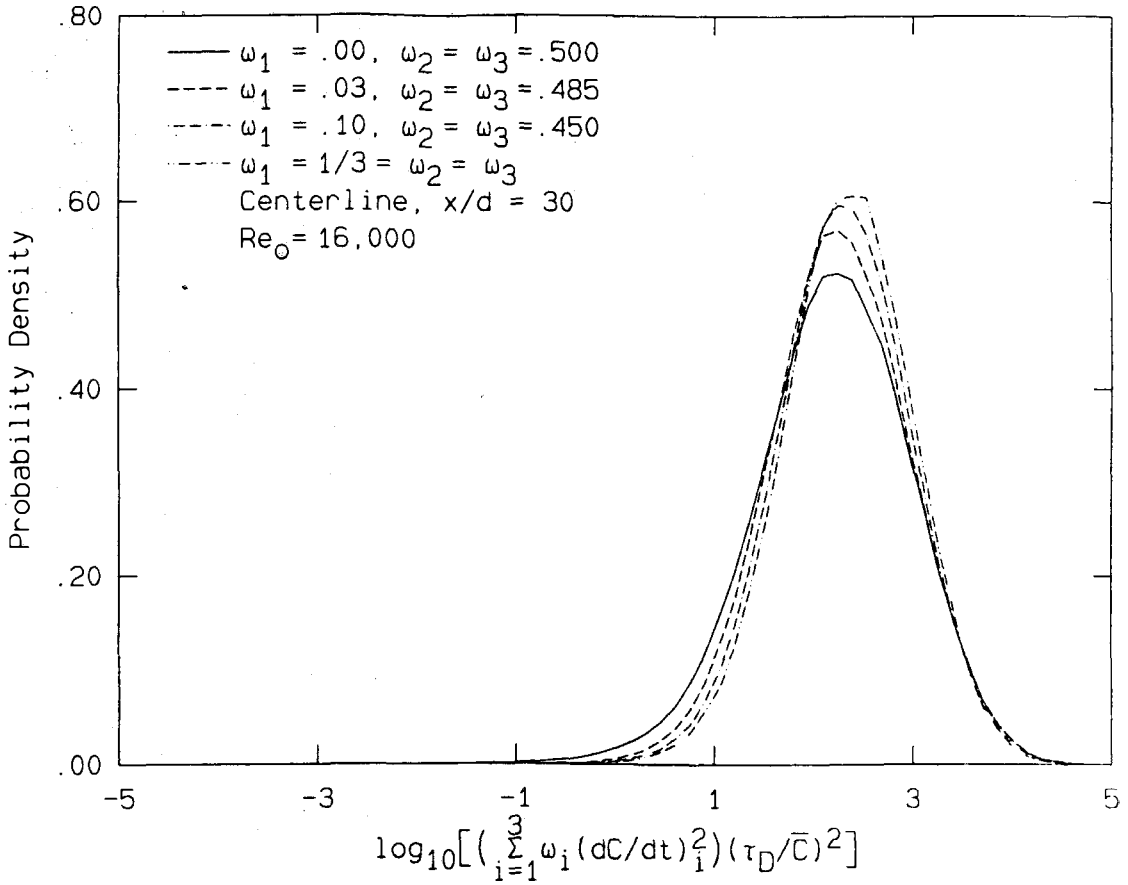

Figure 7-20. Probability density functions of the logarithm of Σ_3 for $0 \leq \omega_1 \leq 1/3$.

Several important characteristics of the PDF of the logarithm of Σ_3 become apparent on these Figures. The calculated distributions at small values of Σ_3 are very sensitive to the chosen value of ω_1 for ω_1 near one. Even introducing only .5% of the second and third terms in Σ_3 radically changes the PDF of $\log_{10}[\Sigma_3(\tau_D/\bar{C})^2]$ to a curve that is much more symmetric about its peak. In fact, for any value of $\omega_1 \neq 1$, the

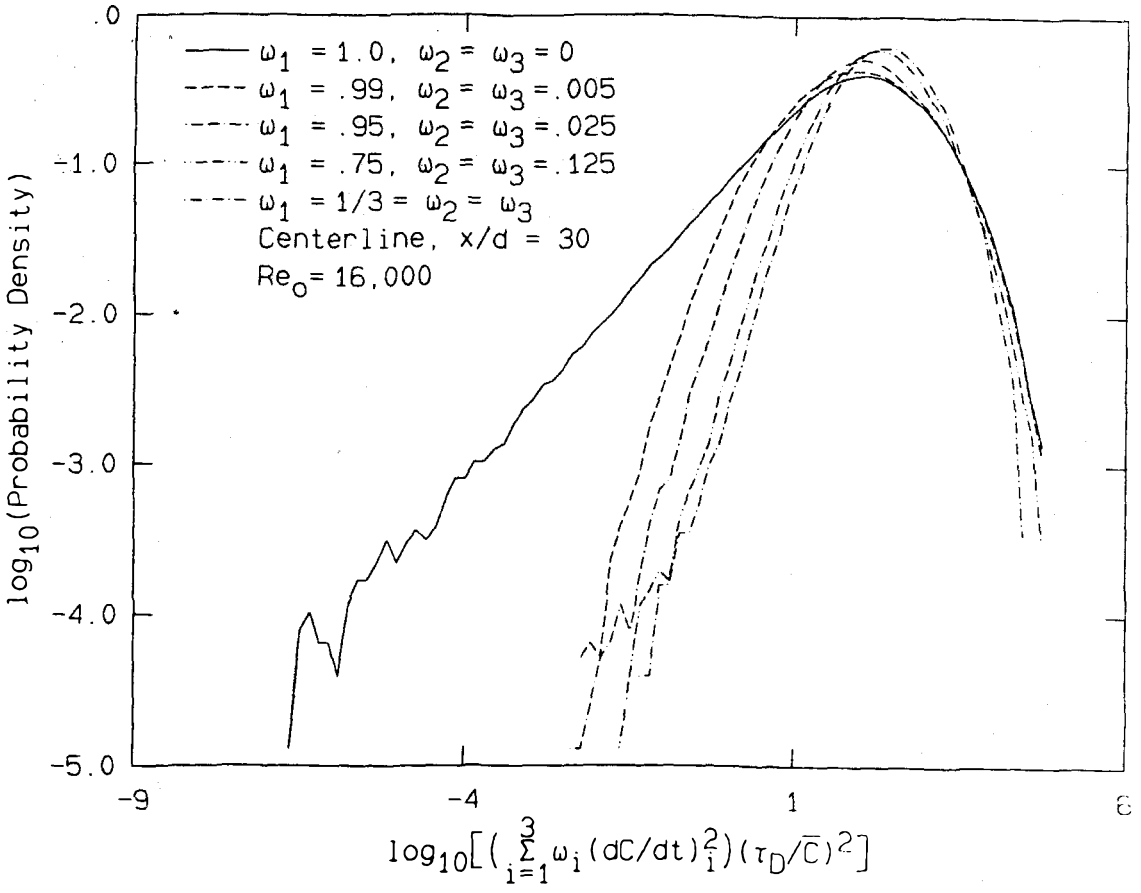

Figure 7-21. Logarithm of the probability density functions of the logarithm of Σ_3 for $\frac{1}{3} \leq \omega_1 \leq 1$.

PDFs of $\log_{10}[\Sigma_3(\tau_D/\bar{C})^2]$ are more symmetric about their peak than for $\omega_1 = 1$. The widths of the distributions on Figures 7-19 to 7-22 decrease and the peak values increase as ω_1 is decreased from unity until $\omega_1 = \frac{1}{3}$, where the trends are seen to reverse as ω_1 is decreased further.

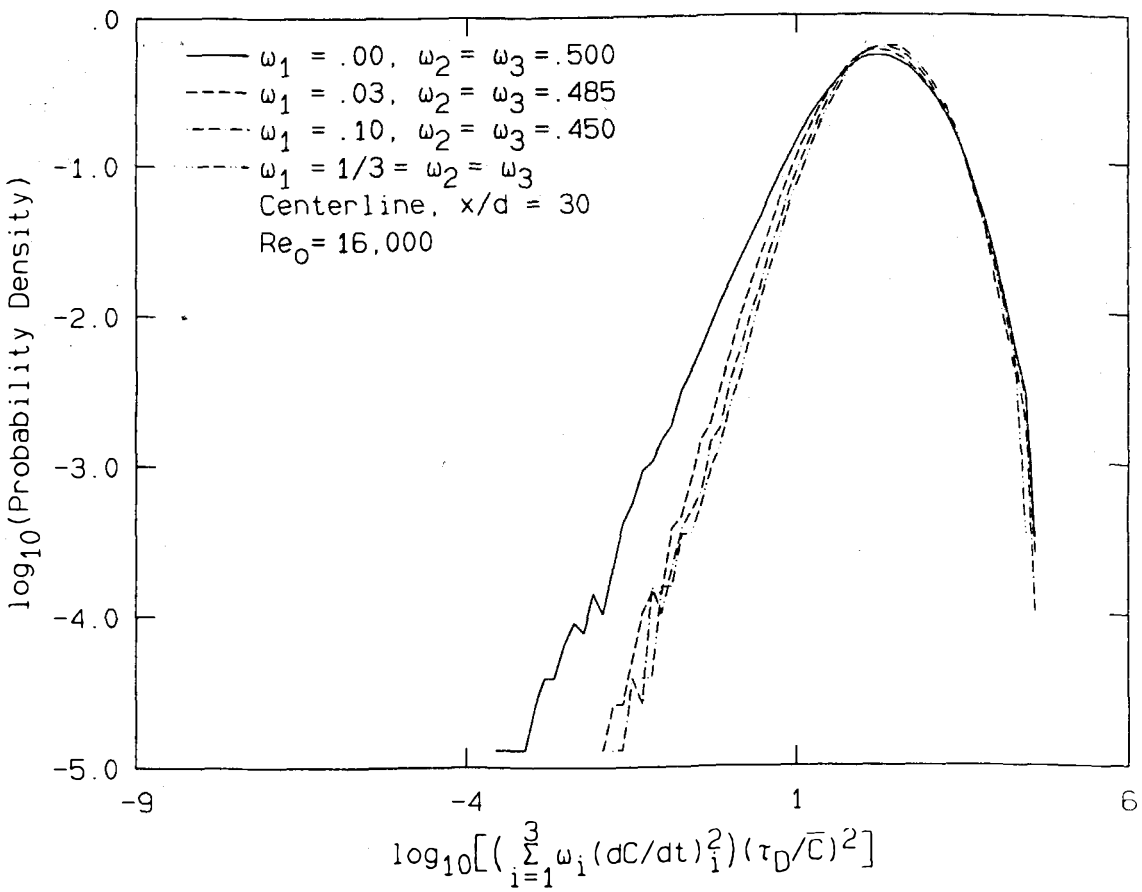

Figure 7-22. Logarithm of the probability density functions of the logarithm of Σ_3 for $0 \leq \omega_1 \leq 1/3$.

The shapes of the PDFs of Figures 7-19 to 7-22 for high values of Σ_3 are not as strongly affected by variations of ω_1 as the shapes of the PDF for low values of Σ_3. In fact, for values of ω_1 between .10 and .75, the whole PDF of $\log_{10}[\Sigma_3(\tau_D/\bar{C})^2]$ is almost unchanged. This independence is partially a result of the exponentially increasing bin sizes along the abscissa on Figures 7-19 to 7-22.

The major result of the parameter study presented here is that the shape of the PDF of ε_c as calculated from Equation (7.1) is strongly dependent on the assumption of complete correlation of derivatives ($\omega_1 = 1$ for Σ_3) that produce Equation (7.1) from Equation (7.6). When Σ_3 with $\omega_1 = 1/3$ is used in place of $(dC/dt)^2$ in Equation (7.1), the sensitivity of the PDF of the logarithm of Σ_3 to the chosen value of ω_1 is greatly reduced. This could be significant if real jet turbulence was known to produces a "true value" of ω_1 in the range where the shape of the PDF of the logarithm of Σ_3 is relatively independent of ω_1. However, Σ_3 with ω_1 near $1/3$ does not necessarily model the actual correlations between the squared spatial derivative terms in ζ produced by the flow field of the turbulent jet, even though basing ε_c on Σ_3 corrects some of the problems that result from the assumption of complete correlation of the three terms of $|\nabla C|^2$. In any case, the true shape of the PDF of ζ should fall in between the current results for the PDF of the logarithm of Σ_3 at $\omega_1 = 1$ and $\omega_1 = 1/3$. Determination of the PDF of ζ in any greater detail than this must await a proper experimental or computational characterization of the <u>three</u>-dimensional nature of the jet's turbulent mixing field. A step was made in this direction recently by Namazian et al. (1987), who used two-dimensional imaging techniques to measure two components of ζ in the near field of a turbulent jet. Their reported PDFs of ζ agree with the expected log-normal shape much better than those presented here for $(dC/dt)^2$.

The Reynolds number dependence of the shapes of the PDF of $\log_{10}[\Sigma_3(\tau_D/\bar{C})^2]$ are shown on Figures 7-23 to 7-25 for the centerline of the jet at Re_o = 5,000 and 16,000 and ω_1 = 1, 1/3, and 0. In all three

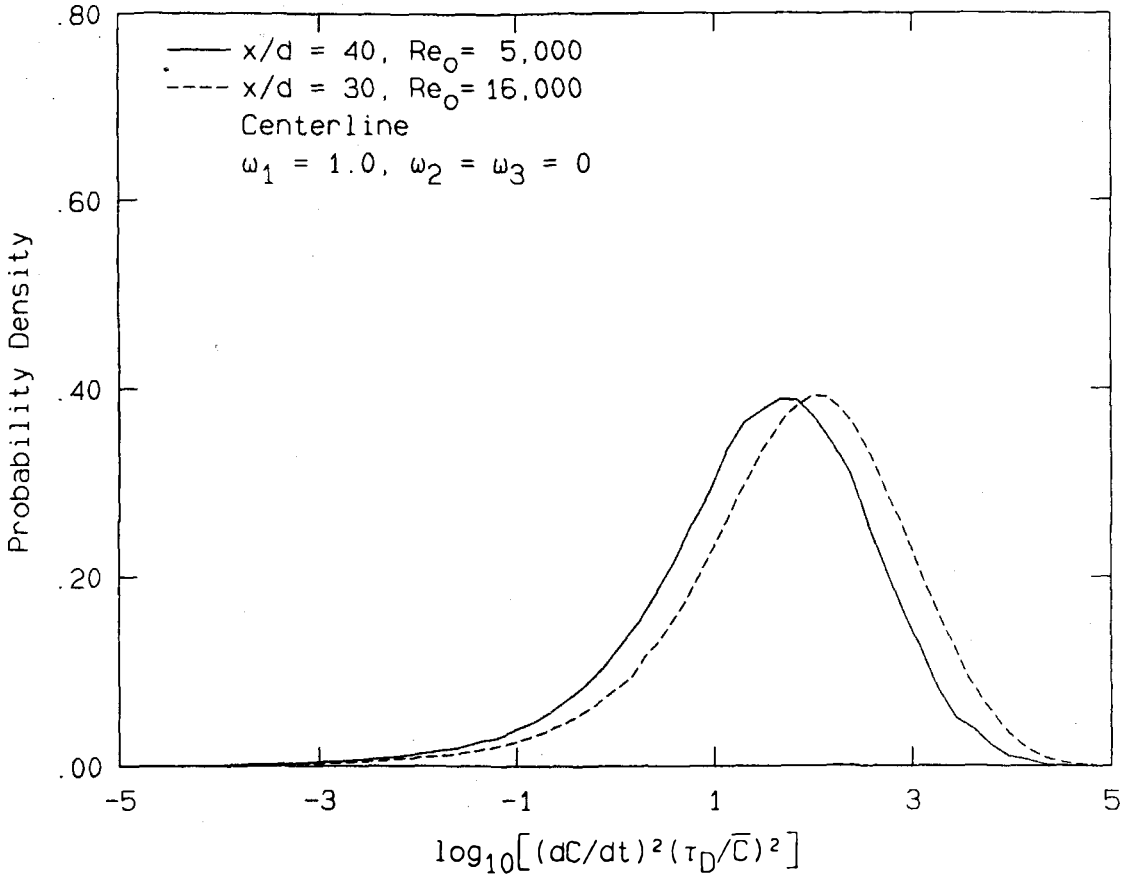

Figure 7-23. Reynolds number comparison of the probability density function of the logarithm of Σ_3 at ω_1 = 1 .

cases, the increase in Re_o shifts the whole PDF about one-third of a decade higher along the horizontal axis. Aside from the small

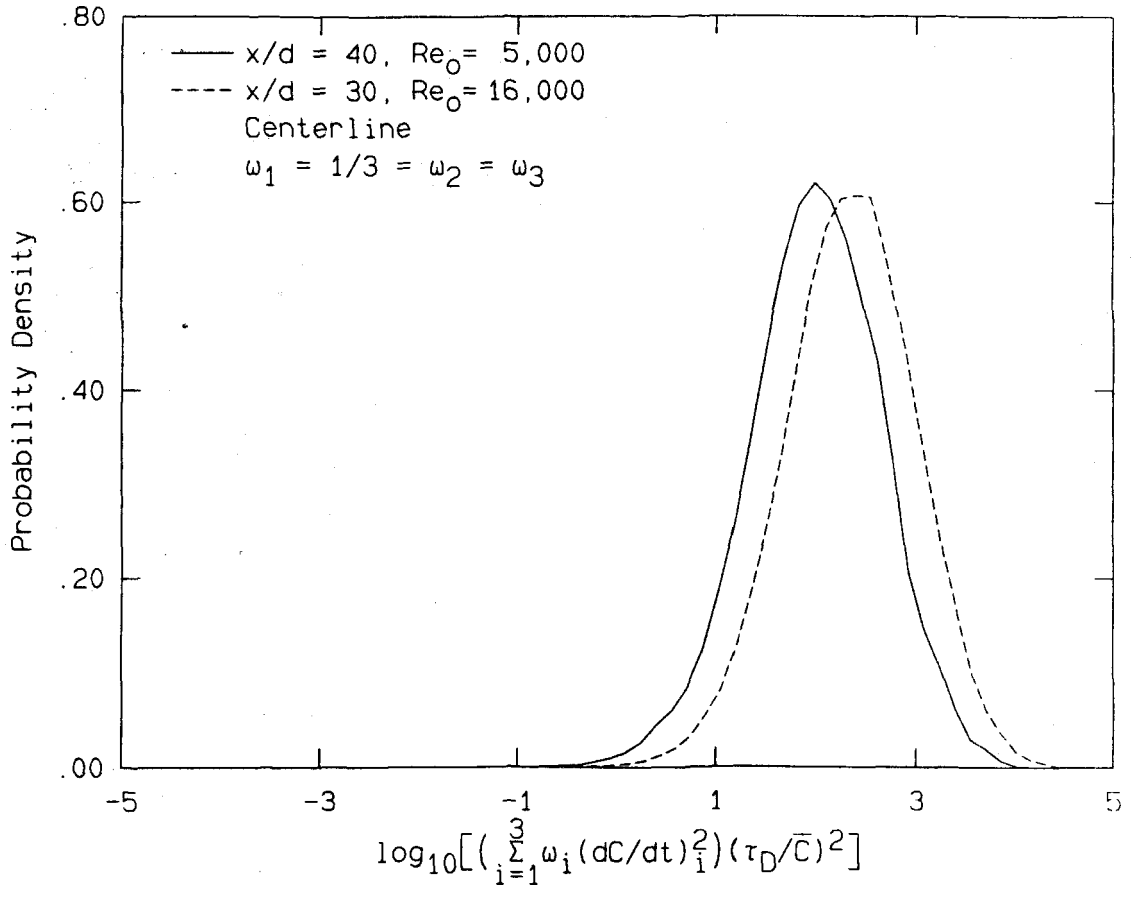

Figure 7-24. Reynolds number comparison of the probability density function of the logarithm of Σ_3 at $\omega_1 = 1/3$.

statistical differences between the compiled PDFs, this shift is the only effect of changing Re_o from 5,000 to 16,000.

Because all of the results of this section were presented without scaling the time derivatives with $\bar{U}_{cl}$, the chosen form of Taylor's hypothesis does not impact on these conclusions.

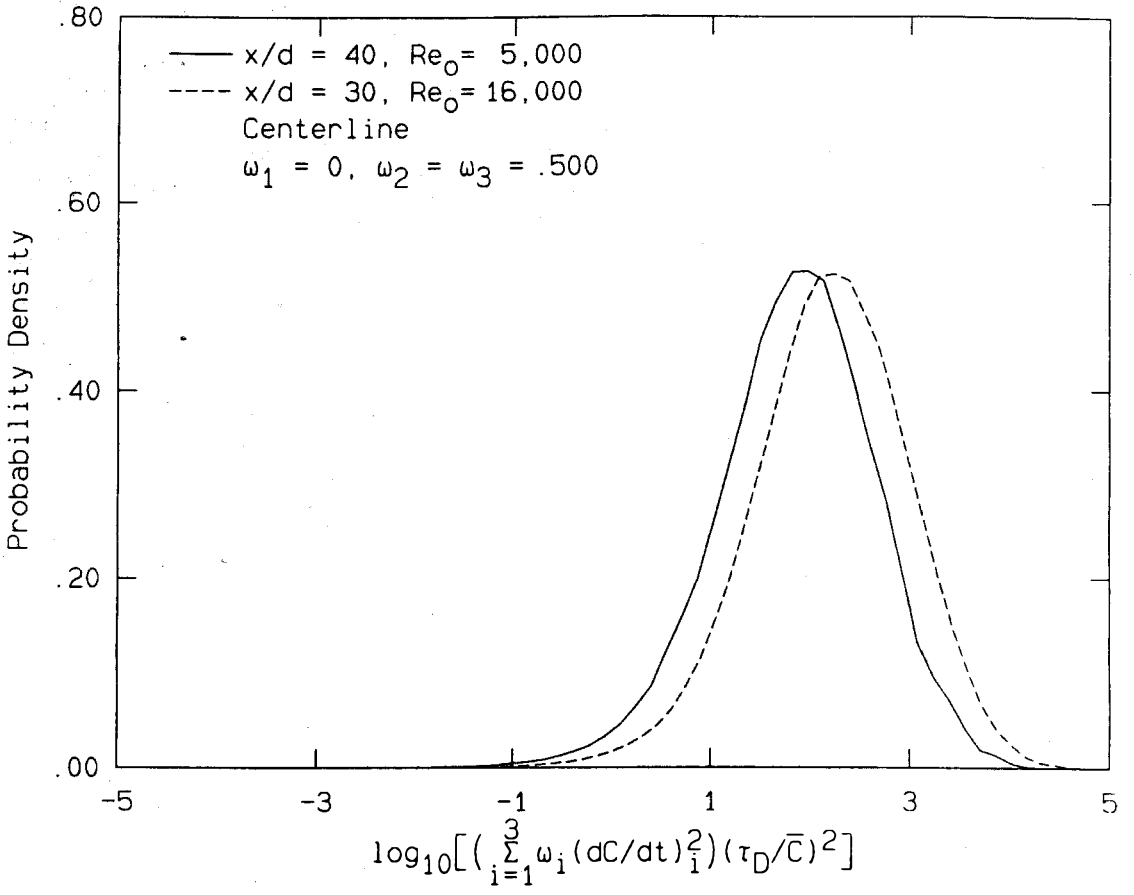

Figure 7-25. Reynolds number comparison of the probability density function of the logarithm of Σ_3 at $\omega_1 = 0$.

7.5 The Correlation of C(t) and $(dC/dt)^2$

Figure 7-26 is a contour plot of the joint probability density function of C(t) and $\log_{10}[(dC/dt)^2(\tau_D/\overline{C})^2]$. Each contour level is

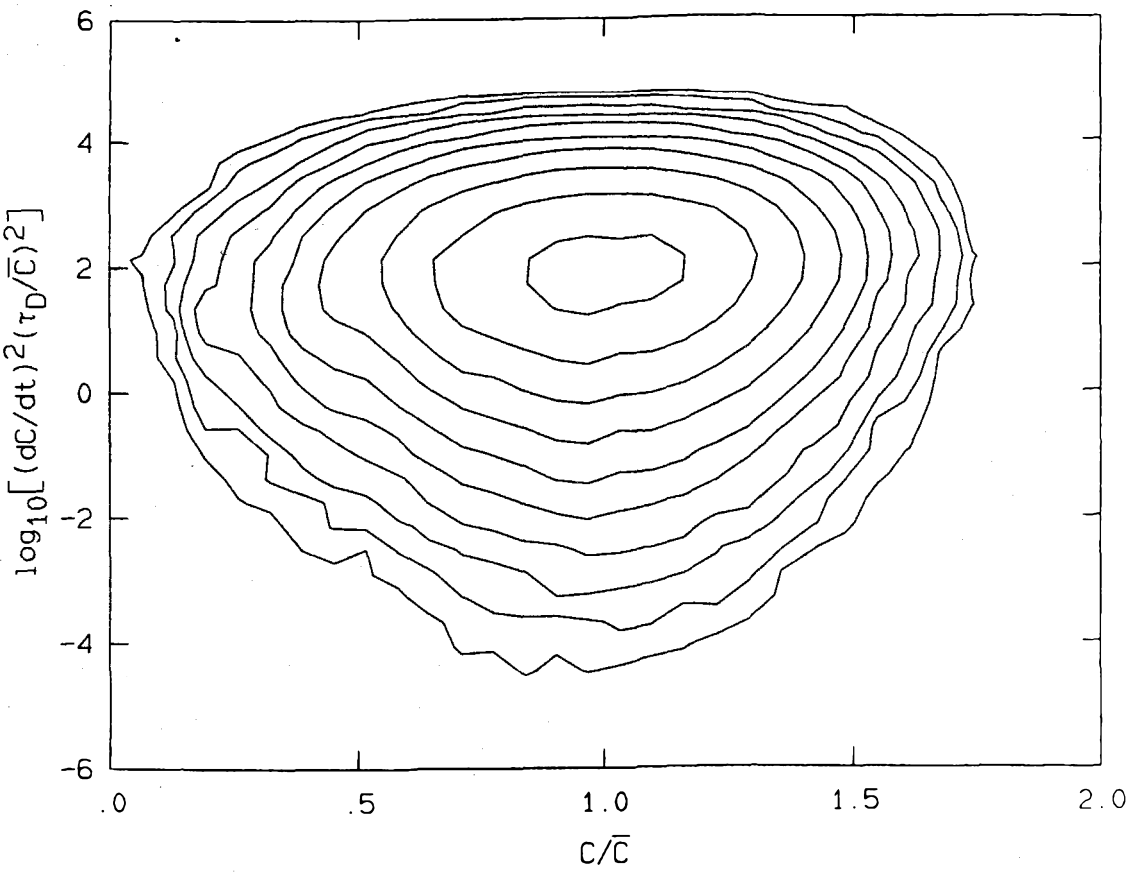

Figure 7-26. Contour plot of the joint PDF of $C/\overline{C}$ and the logarithm of the scaled value of $(dC/dt)^2$ on the jet centerline at Re_0 = 16,000.

separated from the one above it and below it by a factor of 2. The highest contour, the small rough oval near the middle of the Figure 7-26

is at 80% of the maximum value of the joint PDF. The data used to construct Figure 7-26 came from the centerline of the jet at Re_0 = 16,000 and x/d = 30. The symmetry of this figure suggests that on the centerline, C(t) and $\log(dC/dt)^2$ are not strongly correlated.

Figure 7-27 is a similar contour plot except that the data used to produce it were recorded on the ray $r/(x - x_0) = .12$, at Re_0 = 16,000 and x/d = 30. The diagonal nature of the contours suggests that high values of $(dC/dt)^2$ are more likely to occur at high values of C. The contours run into the vertical axis at $C/\overline{C} = 0$ because the bin structure of the underling PDF is not fine enough to show properly how they close on themselves.

The results for Re_0 = 5,000 are very similar to those presented here.

The assumptions leading to Equation (7.1) were not used in this section.

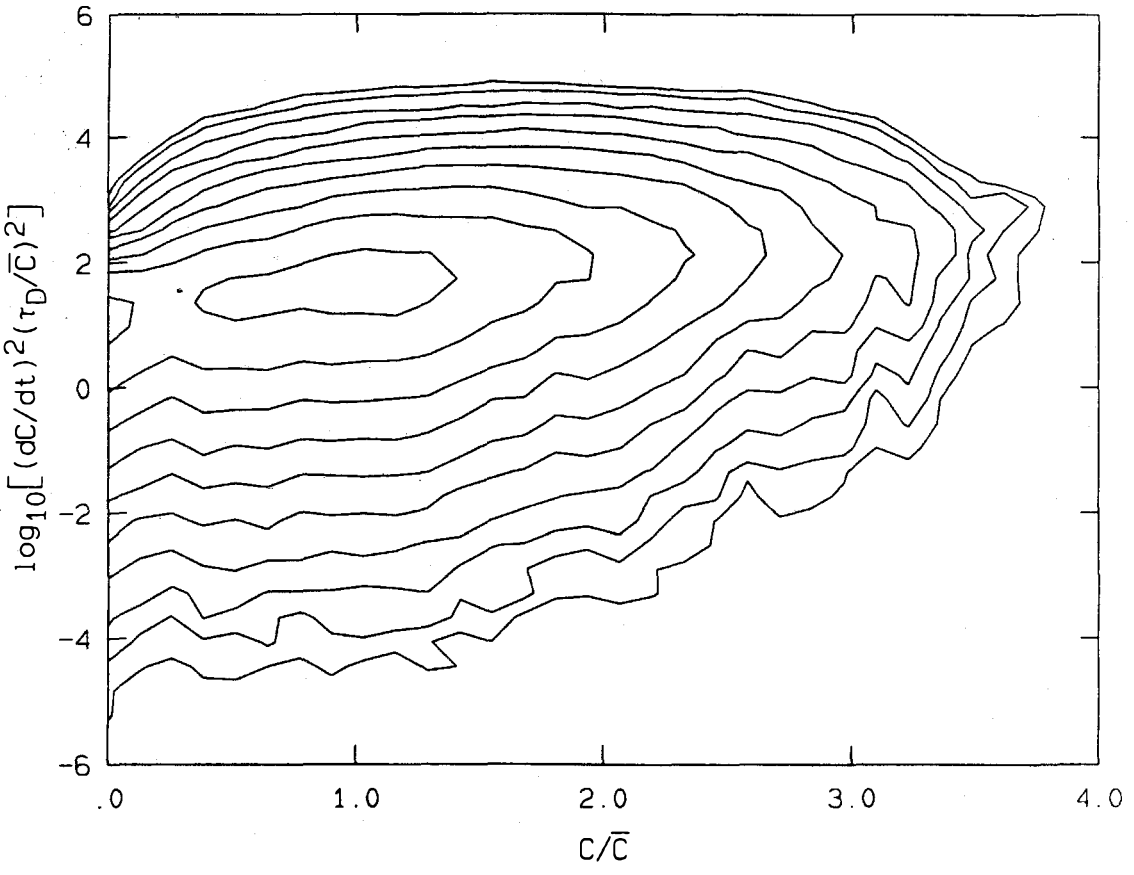

Figure 7-27. Contour plot of the joint PDF of $C/\overline{C}$ and the logarithm of the scaled value of $(dC/dt)^2$ 7° off the centerline of the jet at Re_0 = 16,000.

CHAPTER 8

CONCLUSIONS AND DISCUSSION

The conclusions that concern the specific similarity, the general similarity, and the mixing properties of the turbulent jet concentration field are summarized in the following list.

1. The mixing process in the far field of the momentum-dominated, free turbulent jet is specifically self-similar at all scales along rays that emanate from the virtual origin of the jet. Some of the shapes, profiles, and values of the statistical measures of the jet's turbulent concentration field are not independent of the Reynolds number for $5{,}000 \leq Re_0 \leq 16{,}000$.

2. The mean concentration, and a time scale that depends quadratically on the downstream coordinate are, in all likelihood, the general similarity scaling parameters for jet mixing. This conclusion is based on the strict collapse in downstream distance achieved with these scaling parameters for many different statistical measures of the fluctuating concentration field of the jet at two Reynolds numbers that differed by more than a factor of three.

3. The chosen Reynolds numbers of 5,000 and 16,000 are not high enough for the concentration field of the turbulent jet to display a $-5/3$ power law inertial range cascade in the power spectra of concentration fluctuations.

4. Many features found in the statistical measures of the fluctuating concentration field are explained by the existence of a large-scale structure in the jet that is roughly the same size as the local diameter of the jet. The support for this conclusion is provided by: (1) the "ramps" seen in the measured concentration time histories, (2) the asymmetry of the PDF of dC/dt, (3) the fact that the peaks of $(dC/dt)^2$ are not Poisson distributed, and (4) the fact that the power spectrum of the concentration fluctuations is essentially constant for frequencies below the reciprocal of the estimated passage time for length scales that are the size of the local jet diameter.

5. The scalar dissipation rate is <u>not</u> accurately modeled by assuming that the three, squared, spatial-derivative terms of $|\nabla C|^2$ are completely correlated. The classical theories of turbulence are not in accord with experimental results processed with this very restrictive assumption. However, any small deviation from complete correlation of the squared derivative terms brings the present results at Re_0 = 5,000 and 16,000 in line with the high Reynolds number predictions for the probability density function of the scalar dissipation rate.

6. The far field of the momentum-driven, free turbulent jet appears to begin about twenty nozzle diameters downstream when a smoothly contoured jet nozzle with a low exit turbulence level is used.

7. The distribution of compositions of molecularly mixed fluid in the gas phase turbulent jet, when scaled by the local mean concentration, is almost independent of the Reynolds number for $5,000 < Re_0 < 16,000$, $Sc \approx 1$, and $r/(x - x_0) \leq .12$.

8. The scaled value of the mean concentration, $\overline{C}/C_0$, on the centerline of the jet is found to depend on Reynolds number. Variation of the centerline value of $\chi \cdot \overline{C}/C_0$ $(= K)$ is also reported in the published literature (see Figure 3-4). This issue will be discussed in greater detail below.

The seventh conclusion, which is based on the measured probability density functions of concentration, seems to raise a paradox, since the same measurements show that the local mean mixing rate in the central portion of the jet decreases with increasing Reynolds number (see Figure 7-1). The resolution of the conflict lies in the contribution of the mixing realized at the edges of the jet.

It is quite clear that the amount of mixed fluid at a particular downstream location on the centerline of the jet depends on more than just the integrated centerline mixing rate, because mixed fluid is transported to and from the centerline, and exchanged with all parts of the jet by the large-scale motions of the jet flow. Even though the rate of mixing might be less near the edges of the jet, the time scales there are much longer, and the integrated product of the two determines the total production of mixed fluid. This integration would involve contributions from the entire upstream volume of the jet's turbulent

cone, and the volume inside $r/(x - x_0) = .12$ (the "core" of the jet flow), is only about a third of the total volume of the jet's turbulent cone, ($r/(x - x_0) \leq .21$ to .22). Hence, the amount of mixed fluid produced in the outer regions of the jet can be expected to represent a sizeable fraction of all of the mixed fluid produced within the jet.

One view of jet mixing that evolves from these ideas and resolves the paradox is that the central region of the jet does some mixing and nearly all of the convective transport of the mixed fluid. The edges of the jet provide a low-velocity environment that allows molecular diffusion to thoroughly mix the chunks of high concentration fluid, which are thrown out of the core of the jet by the turbulent velocity fluctuations. The large-scale motions in the jet flow provide these velocity fluctuations and the entrainment field that returns the thoroughly mixed fluid from the edges to the central region of the jet. In this picture, increasing the Reynolds number will increase the amount of mixed fluid produced at the edges of the jet when compared to the amount of mixed fluid produced in the core of the jet, so that the total amount of mixed fluid in the core of the jet remains nearly independent of the Reynolds number. Increasing the Schmidt number will likely produce the same type of shift in the localization of the dominant portion of the mixing process, but conflicting experimental results (see Figures 8-1 and 8-2) prevent any conclusions from being drawn about the Schmidt number dependence of the amount and composition of mixed fluid in the core of the jet.

The conceptual basis for understanding jet mixing would be much clearer, and perhaps better formulated, if the mean centerline concentration were known to be independent of the Reynolds number. Niwa et al. (1984) report that the scaled mean concentration, $\overline{C}/C_0$, at a fixed downstream location on the jet centerline, $x/d = 20$, does depend strongly on the product of the Reynolds number and the Schmidt number in the range $100 < Re_0 \cdot Sc < 3{,}000$. Some of the measured variation might result from a Reynolds number dependence of x_0 and d^* that may not have been accounted for by Niwa et al., but most of it probably comes from changes in the jet turbulence that affect the value of κ. While the present experiments were not intentionally set up to address this issue at higher Reynolds numbers than those explored by Niwa et al., the measured difference in κ at Re_0 = 5,000 and 16,000 exceeds the variation that could be accounted for by experimental error. As Figure 3-4 shows, the "κ problem" is not unique to this experimental study. For the current experiments, *the change in κ suggests that the jet entrains relatively more reservoir fluid as Re_0 is increased.*

It is unlikely that the variation in the reported values of κ (4.5 to 5.5) could come from differences between experiments in the density ratio of jet and reservoir fluids that are not accounted for by scaling the downstream coordinate with d^*. The reason for this is that any initial density difference quickly approaches zero, as the downstream distance is increased, because of the continuous dilution process in the jet. It is even less likely that differences in the Schmidt number between experiments are the cause of the reported variation in κ because

there does not appear to be a physical mechanism for the interaction of the species diffusivity and the large scale velocity fluctuations, which could account for a change in the jet's entrainment rate of reservoir fluid.

There is a clear need for further experimentation to determine the parameters that control κ. The value of κ is, perhaps, the most important measure of the mixed state of the jet. It is determined by the measured, mean, scaled concentration, $\overline{C}/C_0$, and can therefore be used, along with a PDF of $C/\overline{C}$ at a particular Re_0, to estimate the scaled concentration levels found throughout the turbulent jet far field at that Re_0. In fact, when the variation of κ between experiments is removed, the <u>entire</u> PDF of concentration nearly collapses. This collapse holds the promise that the shape of the centerline PDF of $C/\overline{C}$ might be a *general* similarity property of the jet, for a given Schmidt number. Figures 8-1 and 8-2 illustrate these contentions.

Figure 8-1 is a plot of the centerline PDF of the scaled concentration reported by several investigators, without any other scaling. Although the PDFs on Figure 8-1 were not measured at $(x - x_0)/d^* = 100$, the results have been referenced to $(x - x_0)/d^* = 100$, for the purposes of comparison, using the mean centerline concentration scaling law from each experiment and the assumption that the PDF of $C/\overline{C}$ is specifically self-similar in each experiment.

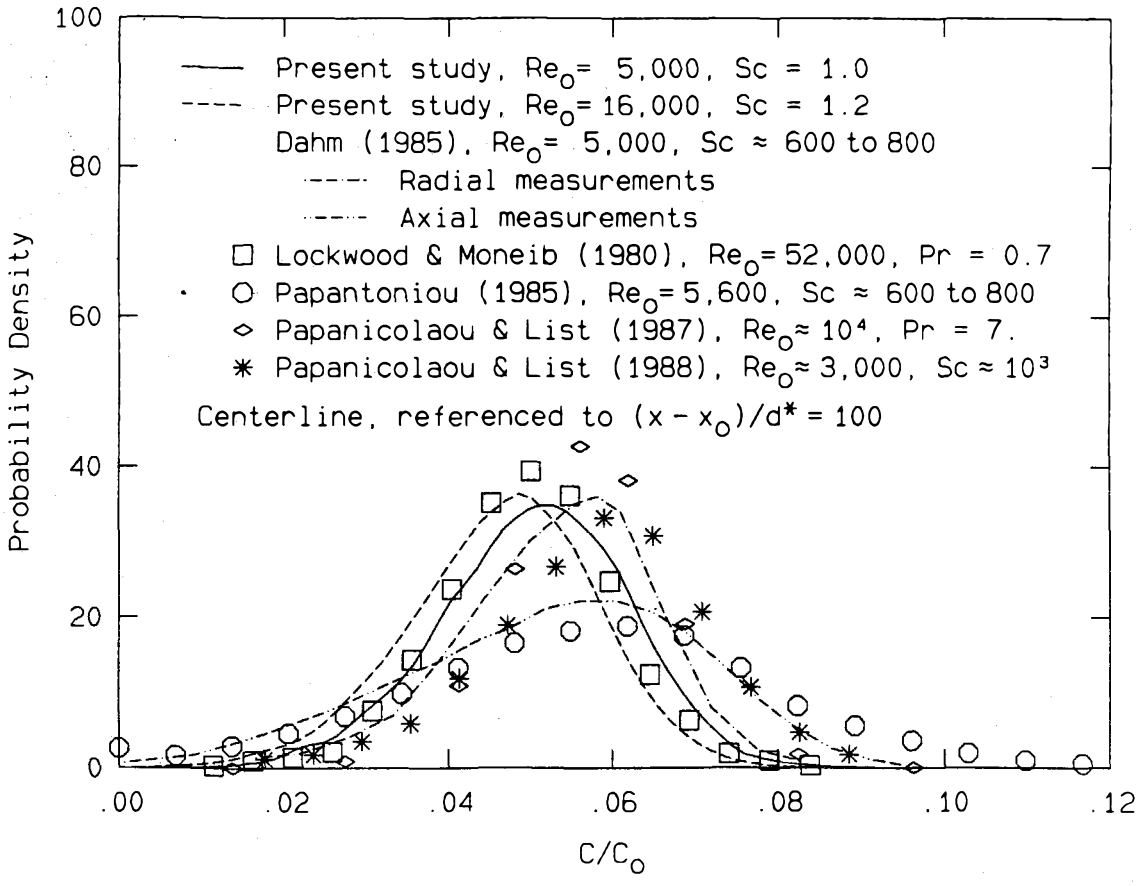

Figure 8-1. Comparison of reported probability density functions of scaled concentration for the centerline of the jet.

Figure 8-2 is a plot of the data from Figure 8-1 when the differences in κ have been normalized out by changing the horizontal coordinate from C/C_o to $C/\overline{C}$ and renormalizing each PDF. In the special case of Figures 8-1 and 8-2, this was done by multiplying values on the concentration axis of Figure 8-1 by 100, dividing them by the

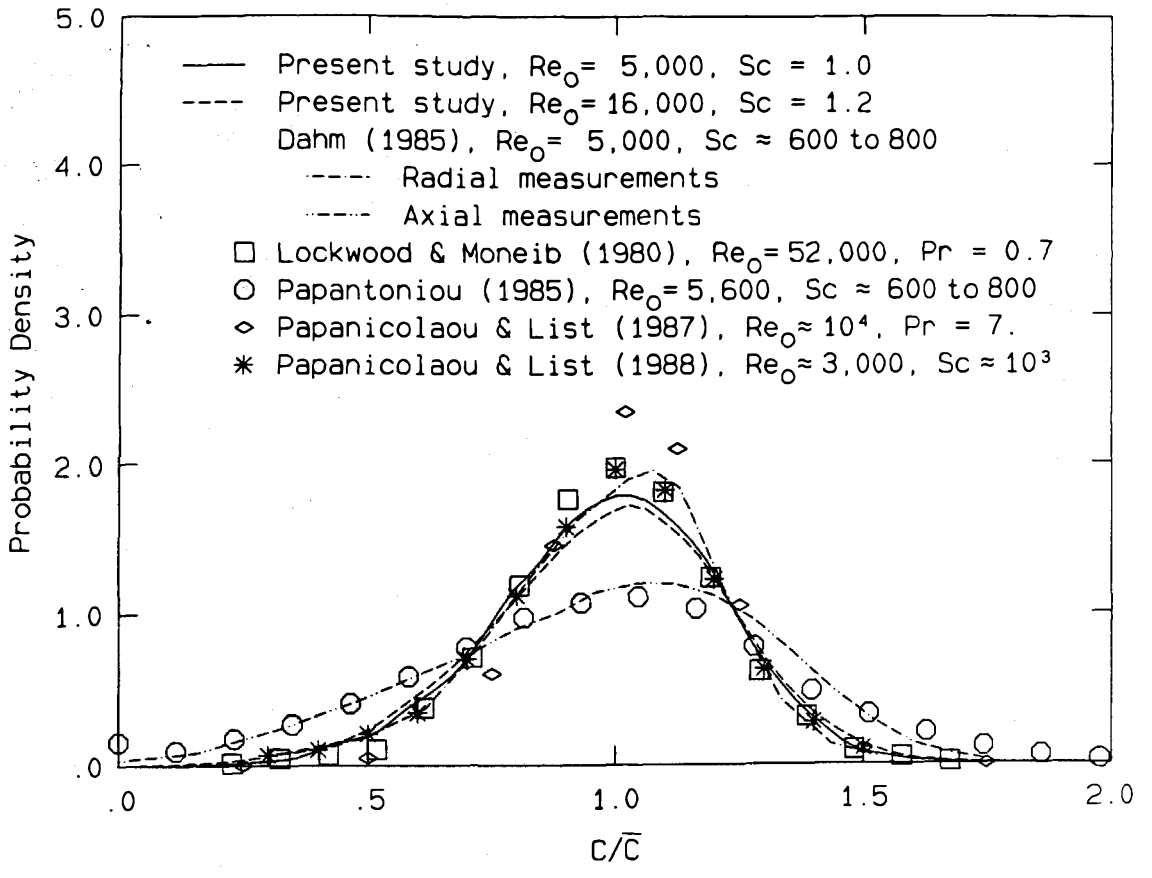

Figure 8-2. Comparison of reported probability density functions of concentration for the centerline of the jet with the concentration axis scaled by $\overline{C}$.

appropriate value of κ, and renormalizing each PDF so that its area was again equal to unity. Scaling with $\overline{C}$ (or κ) clearly brings the reported PDFs closer to a single curve. It is interesting to note that all of the PDFs on Figure 8-2 compiled from gas phase flows agree much better than the those compiled from liquid phase flows. The disagreement between liquid phase PDFs might result from the great difficulty of

producing an experimental diagnostic that is capable of Batchelor scale resolution (see Appendix A, Section 1) in a laboratory, liquid phase, mixing flow. It is entirely possible that all of the variation between the measured PDFs on Figure 8-2 results from differences in the time/space resolution of each experiment and differences in the Schmidt number of each jet flow. However, the evidence is not yet conclusive, so even though the unifying concept of a *general* similarity PDF of concentration on the jet centerline appears promising, it remains elusive.

As a final comment, the measured mean profile of concentration, Figure 3-3, seems to be nearly independent of the Reynolds number over the range where κ varies between 4.5 to 5.5. This implies that the jet velocity field and/or its correlation to the concentration field must change in a coordinated manner to permit the jet flow to conserve the passive scalar. In particular, for an incompressible flow, the total "volume flux" of conserved scalar from the jet nozzle that passes through any plane perpendicular to the jet axis, must be a constant equal to the nozzle exit "volume flux" of the scalar, $\dot{V}_C$. The total scalar "volume flux" will be made up of the contribution from the mean flow and the fluctuating components of the flow,

$$\dot{V}_C = \int_{A_j} (\bar{U}_x \bar{C} + \overline{u'_x C'}) \, dA, \tag{8.1}$$

where A_j is the area of the turbulent cone of the jet when the cone is sliced perpendicular to its axis. How the jet "rearranges" the relative importance of the two terms in Equation (8.1) for different Reynolds

numbers and values of κ is certainly a point for further investigation.

When the present results are viewed as a whole, one of the conclusions that can be drawn is that experiments in fluid mechanics, in some instances, can be completely integrated in order to maximize the quality of the results. For the present study this dictated that the jet Reynolds number, the nozzle exit diameter, the enclosure size, the choice of the jet and reservoir gases, and the minimum acceptable run time were based on calculated spatial and temporal resolution requirements for scalar mixing in the jet, the noise characteristics of the diagnostic, and the need to produce a purely momentum-dominated, free turbulent jet. The great wealth of existing experimental data for the free turbulent jet made the design of these experiments possible.

APPENDIX A

EXPERIMENTAL DESIGN AND PARAMETER SELECTION

The goal for these experiments was to measure the concentration field along the centerline of a round, momentum-driven, gas phase, turbulent jet with enough spatial and temporal resolution to capture the smallest diffusion scales. The design, which was not constrained by an existing apparatus, was subject to many specifications dictated by the need to achieve the measurement objective with the available funding.

The diagnostic chosen for these experiments was deemed to be the best for the stated research goal. Three alternatives were seriously considered; measuring temperature in a heated jet with cold wires, measuring thermal conductivity and local speed of sound with a Brown-Rebollo aspirating probe (Brown and Rebollo 1972), or measuring molecular number densities with laser-Rayleigh scattering. The cold-wire system was eliminated because the spatial resolution and signal-to-noise requirements could not both be met simultaneously in a momentum-driven jet. The aspirating probe was eliminated because its dynamic range was about 2 orders of magnitude too small for density-matched gas pairs. Laser Rayleigh scattering had been used in many previous jet studies (Dyer 1979, Escoda 1983, Pitts and Kashiwagi 1984, Pitts 1986) and was chosen as the main diagnostic for these experiments because it did not suffer from any of the previously mentioned problems, and it provided the greatest flexibility for the rest of the experimental design. What follows in this appendix is an

explanation of each requirement and how it was met, plus a final summary of the relevant numbers, sizes, rates, etc. for the completed measurements.

A.1 Resolution

The smallest velocity scale in a turbulent flow is the Kolmogorov scale λ_K,

$$\lambda_K = \left(\frac{\nu^3}{\bar{\varepsilon}} \right)^{1/4}, \quad \text{with} \quad \bar{\varepsilon} = \text{const} \frac{(\Delta U)^3}{L} , \tag{A.1}$$

where $\bar{\varepsilon}$ is the mean energy dissipation rate of the turbulence, L is the largest scale of the flow, ΔU is the velocity difference across L, and ν is the kinematic viscosity of the fluid. The smallest concentration scale in the flow is the Batchelor scale λ_B,

$$\lambda_B = \lambda_K / \sqrt{Sc} , \tag{A.2}$$

where Sc is the molecular Schmidt number (kinematic viscosity divided by species diffusivity). Unfortunately, the gas flows considered have $Sc \approx 1$, and Equation (A.2) was derived (see Batchelor 1959) for $Sc \gg 1$. By using empirical correlations taken from Reid et al. (1977) for the the diffusivities of gas pairs, the molecular Schmidt numbers of the gas pairs actually used were estimated to be .99 for ethylene and N_2 and 1.20 for propylene and argon.

By intuition one might expect that for $Sc \approx 1$ the smallest species-diffusion scale should be approximately the same size as the smallest momentum-diffusion scale. This agrees with the discussion presented by Batchelor in the paper in which he derives Equation (A.2), and with the discussion in Monin and Yaglom (1975, p. 383), so for the purposes of design it was assumed that $\lambda_B = \lambda_K$. This meant the experimental measurement volume had to be the same size or smaller than the local value of λ_K^3. To estimate λ_K, the result of Friehe et al. (1971) was used for the dissipation rate on the centerline of a turbulent jet:

$$\bar{\varepsilon} = 48 . \frac{U_0^3}{d} \left(\frac{x - x_0}{d} \right)^{-4}, \qquad (A.3)$$

where U_0 is the jet exit velocity, d is the jet exit diameter, x is the coordinate that starts at the nozzle exit and increases downstream along the centerline of the jet, and x_0 is the virtual origin of the jet. The far-field similarity of a turbulent jet can include a virtual origin (see Appendix F) to correct for the peculiarities of the near field of a particular nozzle. The virtual origin is usually only a few jet exit diameters (see Table 8 of Pitts 1986) and was assumed to be zero during the design phase of these experiments.

Equation (A.3) leads to an estimate for λ_K in terms of jet parameters,

$$\lambda_K = 0.38 (x - x_0) / Re_0^{-3/4}, \text{ where } Re_0 = U_0 d / \nu_\infty , \qquad (A.4)$$

and ν_∞, the kinematic viscosity of the reservoir gas.

By properly focusing the laser beam and by limiting the length of the laser beam from which scattered light was collected with a small aperture photodiode, the spatial resolution requirement was met at each measuring station for the first value of the Reynolds number studied (5,000). A different laser-beam focusing lens and/or photodiode was necessary for each measuring station. The focal length of each lens was chosen so that the geometry of the apparatus did not require the lens to be placed closer than about one local jet diameter from the measurement point. The width of the laser beam was checked by slicing the beam with a knife edge and recording the transmitted power as a function of knife-edge displacement. The results showed that the 2% to 98% beam width was usually about a factor of 2 smaller than the diameter of the sensitive area of the appropriate photodiode. The effective size of each photodiode was determined by simple shadowing. A knife edge on a micrometer traverse was used to slice a beam of parallel light rays that impinged on the sensitive aperture of the photodiode. The output signal from the photodiode and the knife-edge displacement were used to determine the diameter of the photoreceptive area. These measurements agreed with the photodiode manufacturer's (United Detector Technology) specifications and tolerances. The first section of Appendix E provides some more information about the photodiodes.

The quality of the lenses that were used to collect the Rayleigh scattered laser light and image it on the photodiodes was checked, even though the manufacturer claimed that it approached the diffraction limit. The technique for checking the lenses involved using the optical

setup shown schematically on Figure 2-5 in reverse. The lenses were placed in the optics pipe used for the jet experiments. Spherically diverging light was produced from a Helium-Neon laser beam, by passing it through some thin teflon that was taped to a precision pinhole. The pinhole was placed where the photodiode's active surface would have been normally located during concentration measurements. The image size of the pinhole produced on the other side of the lenses was carefully measured with a knife edge and power meter and was found to be the same as that of the precision pinhole within the tolerances quoted by the pinhole manufacturer. A schematic of this setup is shown in Figure A-1.

The temporal resolution requirement for the measurements was determined by the passage time (τ_K) of scales of the size of λ_K. The decay law for the mean centerline velocity, $\bar{U}_{cl}$, of momentum-driven, density-matched jets is reported by Chen and Rodi (1980) as:

$$\bar{U}_{cl} = 6.2\, U_0 \left(\frac{x - x_0}{d} \right)^{-1}. \qquad (A.5)$$

In this formula, d should really be replaced by d^*, the momentum diameter of the jet (see Chapter 2, Section 2), but for properly designed nozzles, and density-matched jet and reservoir gases: $d^* \approx d$. Since the mean fluctuation level of the centerline velocity is roughly thirty percent of the local mean (Wygnanski and Fiedler 1969), a conservative estimate for τ_K was obtained by multiplying Equation (A.5) by 1.3 and dividing it into Equation (A.4), i.e.,

$$\tau_K = .047 \frac{d^2}{\nu_\infty} \left(\frac{x - x_0}{d} \right)^2 Re_0^{-7/4}. \qquad (A.6)$$

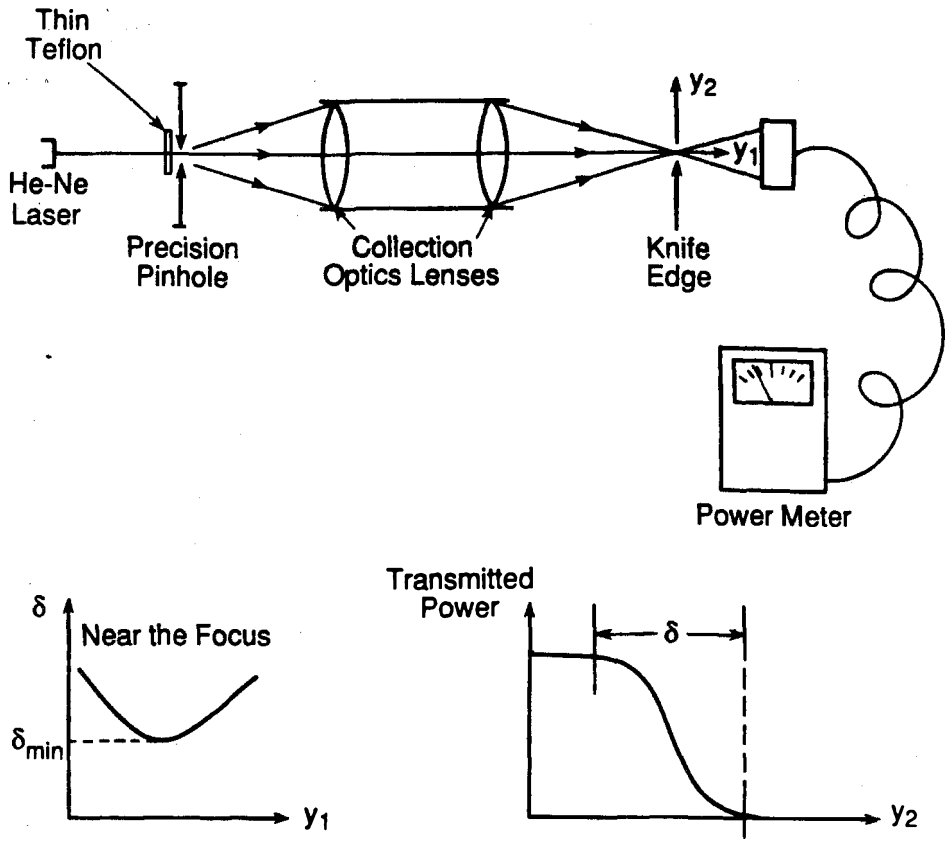

Figure A-1. Schematic of collection lens testing setup.

To insure that information from frequencies near $1/\tau_K$ were included in the sampled data, the output signal from the sensory electronics was filtered above $4/\tau_K$ and sampled at twice the filtering frequency, usually a bit more that $8/\tau_K$, in accordance with the Nyquist criterion.

A.2 Spatial Range and Similarity

The work of Weddell (1952), Becker et al. (1967) and Dahm (1985) suggests that the far-field scaling laws are applicable for $x/d \geq 20$, so this was chosen as the location of the first measuring station. It was decided that increasing x/d from 20 by two factors of two, to a final measuring station at $x/d = 80$, would provide adequate spatial range along the jet axis to properly investigate similarity. This requirement was addressed by correctly sizing the apparatus.

Another way of checking the similarity behavior of the jet was flow visualization. For these experiments, the shadowgraph method was chosen because it was the simplest, the cleanest (no dust or smoke is needed), and it works well with the gas pairs chosen for their Rayleigh scattering properties. The need for this type of flow-visualization was reflected in the design by the placement of two large windows on opposite sides of the test section. A sketch of the shadowgraph setup is given as Figure 3-9.

A.3 Reynolds Number

Many competing factors entered into the choice of Re_0. From Equations (A.4) and (A.6) it is easy to see that the resolution requirements become easier to attain by lowering Re_0, but the significance of the experimental results would be greater for higher values of Re_0. Since one aspect of this investigation was the identification of the effect of the Schmidt number in jet mixing, being

able to match Re_0 with one of the two chosen by Dahm for his liquid phase experiments (1985) was important.

The entrainment studies of Ricou and Spalding (1961) suggest that the jet reaches a Reynolds number independent state above $Re_0 = 25,000$. The flame length work of Weddell (1952) and Dahm (1985) suggests, at least for high Schmidt number fluids, that this limit is about an order of magnitude lower. A design Reynolds number of 5,000 was chosen because it was not possible to satisfy the calculated resolution requirements at $Re_0 = 25,000$. This choice satisfied Dahm's criterion for Reynolds number independent behavior of the jet mixing and also matched one of the Reynolds numbers he extensively investigated in liquid phase jets.

After the results from $Re_0 = 5,000$ were available and the degree to which the experiment had been "overdesigned" became obvious, the spatial resolution requirement, i.e. Equation (A.4), was relaxed by about a factor of 3. This allowed Re_0 to be increased to 16,000 with only minor modifications to the rest of the experiment.

A.4 **Run Time**

Since most of the results from this experiment would be statistical, it was essential that data could be collected continuously for many local large-scale passage times. The local large-scale passage time (τ_D) was calculated by dividing the local jet diameter by the mean centerline velocity:

$$\tau_D = \frac{d^2}{3.1\,\nu_\infty}\left(\frac{x - x_0}{d}\right)^2 \tan\theta_j\, Re_0^{-1}, \qquad (A.7)$$

where the half-angle of the jet's turbulent cone, θ_j, is about 12^0 (White 1974, and Chapter 3, Section 3). Identifying τ_D as the largest fluctuation time scale in the jet is consistent with the flame length fluctuation measurements of Dahm and Dimotakis (1987).

The Rayleigh scattering diagnostic required that the experiment be as free from dust as possible, so the gases used in the test section had to be filtered and enclosed. Estimates were made for the time that it would take recirculation of the jet mixing products to "pollute" the on-going measurements for several different enclosure sizes. The discouraging results of these estimates and the finite amount of available laboratory space necessitated the addition of extra ambient (reservoir) gas to the test section during a run to prevent recirculation of mixed gases through the measuring station. This extra reservoir gas was added by means of a mild uniform coflow applied to the entire cross section of the test section. The uniformity of the coflow was produced by a special shower head with 900 small orifices and the pressure drop across a one-inch thick slab of open-pore foam. The total

volume flux of the coflow was chosen to meet the total entrainment requirement of the jet, Q_v, down to x/d = 90 for the $Re_0 = 5,000$ studies. The entrainment requirement of the jet was estimated from Ricou and Spalding's result (1961),

$$Q_v = .332\, Q_0 \left(\frac{x - x_0}{d} \right), \quad \text{where } Q_0 = \frac{\pi d^2}{4} U_0. \tag{A.8}$$

Since the farthest downstream measurements anticipated were to be made at x/d = 80, there would be no recirculation of mixed gases back to the measuring station, because the entrainment needs of the jet would be met by the fresh supply of reservoir gas from the weak coflow.

The apparatus was a "blow-down" facility, and some time had to be allowed for filling the jet plenum and for the establishment of a steady-state jet in the test section. The plenum-filling time was calculated by dividing the volume of the plenum by the volume flux of the jet. The startup time for the jet was estimated to be twice the time that it takes jet fluid to first reach the measuring station.

Unfortunately, the stability of the coflow became suspect after about 45 seconds, and this placed an upper limit on the run time. For the runs at $Re_0 = 5,000$, this meant that about 40 τ_D were captured at x/d = 20 and 40, about 30 τ_D were captured at x/d = 60 and about 16 τ_D were captured at x/d = 80.

Section 6 of this Appendix is a discussion of how the effects of the coflow on the turbulent jet were estimated for this study.

A.5 Momentum and Buoyancy

To be sure that momentum forces dominated in the jet, it was necessary to determine when buoyancy would become important. Although the gas pairs considered for these experiments were closely matched in density, small differences did exist. To properly scale the effects of such density differences in the earth's gravitational field, a buoyancy length scale was found. The following derivation follows the one found in Fischer et al. (1979).

The exit momentum flux from the jet (J_0) is given by:

$$J_0 = \int_{A_0} \rho_j U_j^2 \, dA \, , \tag{A.9}$$

where ρ_j is the density of the jet gas, U_j is the exit velocity profile and A_0 is the source area. The exit, excess-density flux when multiplied with gravity ($g \approx 9.8$ m/sec^2) gives the exit buoyancy flux, B,

$$B = g \int_{A_0} (\rho_j - \rho_\infty) U_j dA \, , \tag{A.10}$$

where ρ_∞ is the density of the reservoir fluid. A buoyancy length scale, L_b, can be formed from J_0, B, and ρ_∞, using dimensional analysis, i.e.,

$$L_b = \frac{(J_0/\rho_\infty)^{3/4}}{(B/\rho_\infty)^{1/2}} \, . \tag{A.11}$$

If the exit profiles of ρ_j and U_j are uniform, and if the source is round,

$$J_0 = \rho_j U_0^2 A_0 , \tag{A.12}$$

$$B = g(\rho_j - \rho_\infty) U_0 A_0 , \tag{A.13}$$

$$A_0 = \frac{\pi d^2}{4} , \tag{A.14}$$

then L_b can be rewritten as:

$$L_b/d = \left(\frac{\pi}{4}\right)^{1/4} (\rho_j/\rho_\infty)^{1/4} (\rho_j U_0^2/\Delta\rho g d)^{1/2}, \tag{A.15}$$

where $\Delta\rho = \rho_j - \rho_\infty$. Papanicolaou and List (1987 and 1988) showed in their research that jets are essentially momentum dominated for values of x/L_b below one. Chen and Rodi derive the same length scale (without the factor of $(\pi/4)^{1/4}$) by a different argument but make the sightly more restrictive statement $x/L_b \leq .53$ for completely momentum-dominated jet flow. For the work presented here, care was taken in the choice of gas pairs, jet velocities and nozzle sizes so that all the measurements were performed with $x/L_b \leq .4$. Efforts were also made to insure that the jet, which always contained the slightly denser of the two gases, pointed in the same direction as gravity. This prevented any buoyancy effects from deflecting the axis of the jet.

A.6 Momentum and Coflow

Coflowing jets are known to have different growth rates and decay laws than free jets. The effect of the introduction of coflow on these measurements was estimated from the results of Reichardt (1964).

The conserved momentum flux from a coflowing jet (J_C) is given by:

$$J_C = \int_{A_0} \rho_j (U_j - U_C) U_j dA , \tag{A.16}$$

where U_C is the coflow velocity (see Hinze 1975). For round jets, a momentum thickness, Θ_C, can be formed from J_C by division with $\rho_\infty U_C^2$ and $\pi/4$.

$$\Theta_C^2 = 4J_C/\pi\rho_\infty U_C^2 \tag{A.17}$$

If the exit velocity and density profiles are uniform, Θ_C simplifies to:

$$\Theta_C/d = \sqrt{r_u(r_u - 1)\rho_j/\rho_\infty} , \tag{A.18}$$

with $r_u = U_0/U_C$. The plots in Reichardt's paper show that the velocity half-width of the jet is unchanged from free jet, growth rates for values of x/Θ_C less than about one.

To be completely sure that the coflow was not affecting the jet, it was required that the value of x/Θ_C always be less than .50, or equivalently, that Θ_C always be greater than twice the distance from the nozzle exit to the measurement location. This was easily satisfied by making the inlet supply area for the coflow gas large enough so that the necessary volume input could be achieved with a velocity that was much

smaller than the jet exit velocity. In fact, for the runs at Re_0 = 16,000, U_0/U_C was about 500, which produced $x/\Theta_C \approx .2$ at x/d = 90.

A.7 **Signal-to-Noise Ratio**

A high signal-to-noise ratio is important for any measurement, so a requirement for the minimum allowable "SNR" was needed. It was planned that one of the main results of this work would be the compilation of the probability density function (PDF) of jet gas concentration from the measured data. This PDF would be the convolution of the true PDF of jet gas concentration with the PDF of the experimental measurement noise. Maximizing the quality of the experimentally measured PDF meant minimizing the width of the noise PDF. A practical requirement derived from this thinking is that the rms noise level should be smaller than the size of a bin to compile a reliable estimate of the true PDF from the measured data. A minimum signal-to-noise ratio of 30 was chosen so that it would be realistic to use 30 bins for the measured PDF. The details of how the signal-to-noise ratio was defined predicted and maximized for these experiments are the subject of the Appendix B.

A.8 **Laboratory**

The laboratory had to have certain electrical and ventilation capabilities. For the Rayleigh scattering diagnostic to be effective, a lot of laser power was needed. This usually comes at the expense of large amounts of electrical power because of the low efficiencies of most lasers. Some of the gases chosen for the jet were explosive hydrocarbons, so it was essential that they were properly contained at all times, and a safe method of venting the experimental exhaust was available.

The laboratory space that was eventually chosen had both positive and negative aspects. It was electrically equipped to run a CR-10 laser system which could be coaxed to deliver about 20 watts of laser power, at the expense of 20,000 watts of electrical power. Unfortunately, the laboratory was in the subbasement, making it necessary to install a special system for venting the products of the experiment. An explosion-proof suction line had to be run all the way to the roof of the building (5 floors up), to satisfy safety codes. Figure 2-4 is a reduction of the blue prints of this system. For safely handling explosive gases, high-sensitivity, combustible gas detectors were installed near the main experimental apparatus, and quick-disconnect fittings were used on the jet gas delivery lines to allow the hydrocarbon cylinder to be easily removed from the lab if necessary.

The nine and a half foot floor to ceiling distance in the laboratory limited the length of the test section. This constraint and the spatial range requirement forced the choice of the jet diameter to be smaller than one inch. The spatial resolution and signal-to-noise requirements at $Re_0 = 5,000$ could be reached for nozzle diameters larger than 1/2". Fortunately, a precision-machined, plexiglass nozzle was available, which had an exit diameter of 3/4". With this nozzle size and the chosen value of Re_0, all of the other parameters, sizes, rates and time intervals could be calculated for any gas pair.

This arithmetic quickly led to the realization that the internal volume of the experiment would exceed 100 cubic feet. Nitrogen and argon were the only two pure gases that could be obtained easily and cheaply enough for regular use as the reservoir gas. Matching the density of these two gases with the appropriate gases for Rayleigh scattering measurements finalized the choice of gas pairs for the momentum-dominated jet studies. These pairs were: argon/propylene, and nitrogen/ethylene. Although the hydrocarbon compound propadiene ($CH_2=C=CH_2$, $M_w = 40.$) is a closer density match with argon than propylene (C_3H_6, $M_w = 42.$), it was not available with high enough purity at an acceptable price.

A.9 **The Jet Nozzles**

Two nozzles were used in these studies and the inner contours of both were designed using a method developed by Professor Paul Dimotakis. The 3/4" nozzle, used for the $Re_0 = 5,000$ experiments, was produced entirely under his direction for a water fountain project, while the 0.30" nozzle was produced specially for the experiments at $Re_0 = 16,000$. The results of the design calculations for the 0.30" nozzle are plotted in Figure A-2.

The inner contour of both nozzles was a fitted 6^{th} order polynomial:

$$r_i(z) = c_0 + c_1 z + c_2 z^2 + c_3 z^3 + c_4 z^4 + c_5 z^5 + c_6 z^6, \qquad (A.19)$$

where $r_i(z)$ is the internal radius of the nozzle and z is a coordinate that is zero at the beginning of the nozzle contraction and increases to z_e at the nozzle exit. Six boundary conditions were imposed on $r_i(z)$:

$$r_i(0) = \text{entrance radius } (r_0), \qquad r_i(z_e) = \text{exit radius } (r_e)$$

$$r_i'(0) = 0, \qquad r_i'(z_e) = -\tan(4^0)$$

$$r_i''(0) = 0, \qquad r_i''(z_e) = 0,$$

leaving one degree of freedom. The entrance boundary conditions insure a smooth transition to the nozzle contour from the assumed upstream parallel flow and the exit boundary conditions produce a smooth, beneficial, exit pressure gradient.

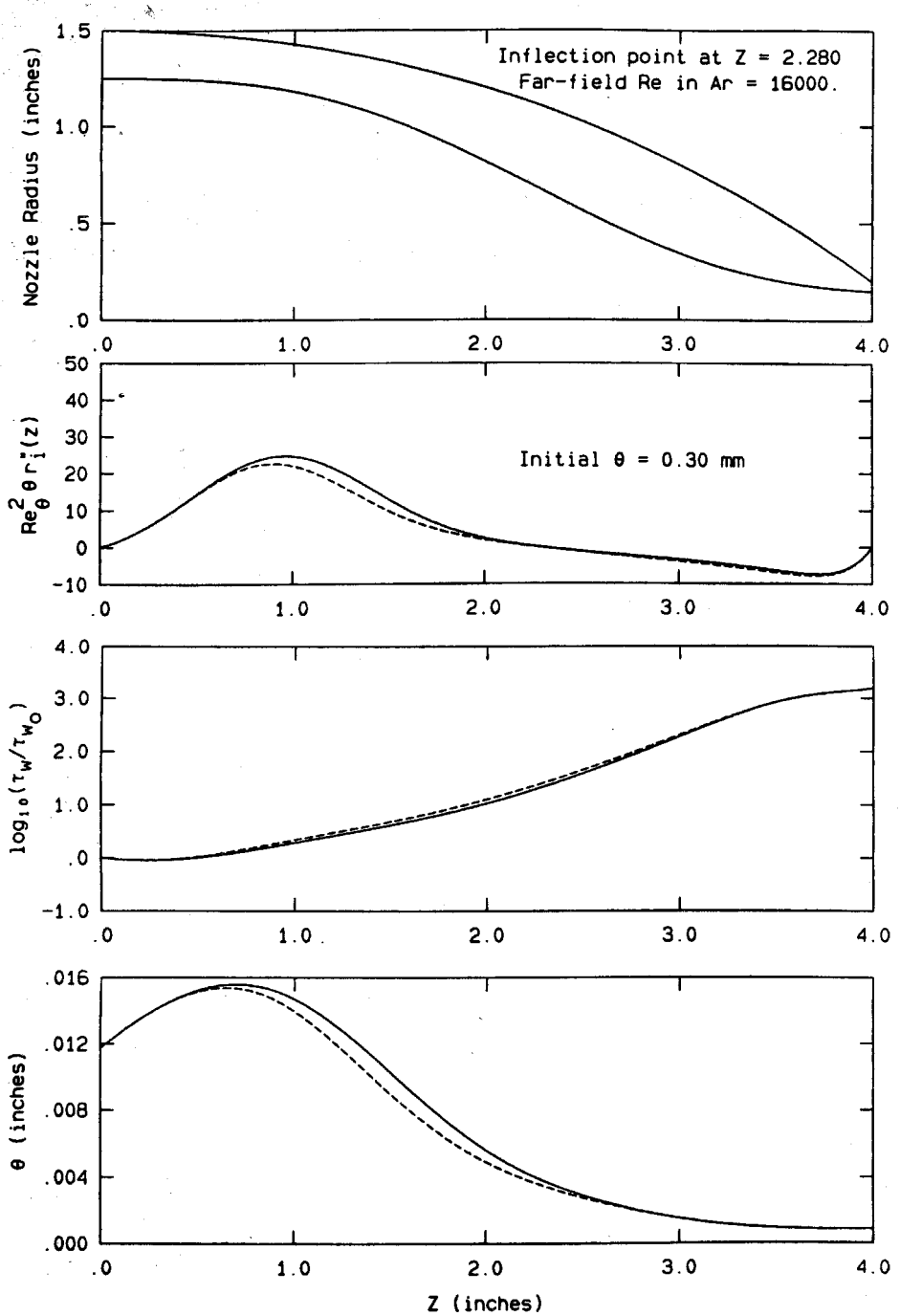

Figure A-2. Results of the design analysis for the 0.30" nozzle.

The final degree of freedom was spent locating the inflection point of $r_i(z)$ by graphically comparing the results of an axisymmetric, laminar, boundary layer calculation (Schlichting 1979, p. 240). Two "outer flow" velocities were used in the calculations. The first, which is represented by the solid lines in the plots of Figure A-2, is the mean axial velocity, U_m, in the nozzle computed from the continuity equation, assuming incompressible flow.

$$U_m(z) = U_0\left(\frac{r_i(z)}{r_e}\right)^2$$

The second, which is represented by the dashed lines in the plots on Figure A-2, is a corrected mean velocity that takes into account the slope of the nozzle wall. The 2 velocities are related by:

$$U_{corrected} = U_m\sqrt{1 + r_i'^2(z)} \ ,$$

It was hoped that these 2 velocities would bound the true velocity, obtainable only from a 3-D potential flow solution for the nozzle and its settling chamber. The boundary layer calculations were used to predict the momentum thickness of the boundary layer on the inside contour of the nozzle (θ), the shear stress (τ_w), and the Görtler parameter, G, used by Liepmann (1943) in his study of the transition of a laminar boundary layer on a curved surface:

$$G = Re_\theta^2\,\theta\,r_i''(z), \qquad (A.21)$$

where Re_θ is the Reynolds number based θ. The location of the inflection point was "optimized" against the need to make θ evolve smoothly, force τ_w to be monotonically increasing, and keep G below 50.

For the .30" nozzle, the internal entrance diameter (2.5") was chosen to be the same as the existing hardware built for the .75" nozzle, and the length (4.00") was the longest possible that could be machined with the local expertize and equipment.

A.10 **Experimental Parameters**

Tables A-1 and A-2 summarize the values, sizes and parameters used at the two Reynolds numbers: 5,000, and 16,000. The values in parentheses are the calculated values from the appropriate design equations, with the measured values of x_0: $-3.7\,d$ at $Re_0 = 5{,}000$ and $.5\,d$ at $Re_0 = 16{,}000$. The actual design work was done with $x_0 = 0$.

Table A-1

Parameter Summary for Re_0 = 5,000

Jet exit diameter (d) = 0.75 inches

Jet nozzle contraction ratio = 100/9

Jet exit turbulence level (N_2 at Re_0 = 5,000) ≤ .002

Jet gas : Ethylene, C_2H_2, M_w = 28.054, purity = 99.5%

Reservoir gas : Nitrogen, N_2, M_w = 28.013, purity = 99.995%

$\Delta\rho/\rho_\infty$ = .0015

L_b/d = 227

Coflow velocity = 2.4 cm/sec

Jet exit velocity = 4.04 m/sec

Θ_c/d = 170

	x/d=20	x/d=40	x/d=60	x/d=80
λ_K (μm)	(288)	(532)	(775)	(1020)
diode size (μm)	200 & 500	500	500	1000
τ_D (sec)	(.182)	(.618)	(1.31)	(2.27)
τ_K (msec)	(.209)	(.711)	(1.51)	(2.61)
A/D rate (KHz)	96 & 40, (38.3)	20, (11.25)	10, (5.30)	5, (3.07)
focal length (mm) of laser beam lens	200	400	400	500
Beam waist (μm) (2% to 98% thickness)	120±10	210±10	210±10	260±10
# of τ_D captured	40 & 100	40	30	16

Table A-2

Parameter Summary for Re_o = 16,000

Jet exit diameter (d) = 0.30 inches

Jet nozzle contraction ratio = 69.4

Jet exit turbulence level (N_2 at Re_o = 16,000) ≤ .002

Jet gas : Propylene, C_3H_6, M_w = 42.08, purity = 99.5%

Reservoir gas : Argon, M_w = 39.948, purity = 99.999%

$\Delta\rho/\rho_\infty$ = .053

L_b/d = 443

Coflow velocity = 5 to 6 cm/sec

Jet velocity = 28.6 m/sec

$\Theta_c/d \approx 500$

	x/d=30	x/d=90
λ_K (μm)	(60)	(182)
diode size (μm)	200	500
τ_D (sec)	(.0160)	(.146)
τ_K (μsec)	(7.67)	(70.6)
A/D rate (KHz)	180	30
focal length of laser beam lens (mm)	200	400
Beam waist (μm) (2% to 98% thickness)	120±10	210±10
# of τ_D captured	180	120

APPENDIX B

PERFORMANCE PREDICTION AND MEASUREMENT

The experimental measurement system was designed to produce high quality data from which the probability density function of jet gas concentration, PDF(C), could be compiled without resolution error. The number of bins between $C = 0$ (pure reservoir fluid) and $C = C_{max}$ (C_{max} = the local maximum concentration), which are justified in such a compilation, can be estimated from:

$$\text{Number of bins} = C_{max}/\delta C \equiv \text{RSNR}, \qquad \text{(B.1)}$$

where δC is the maximum rms uncertainty of the concentration measurements. This estimate for the number of bins was renamed the relative signal-to-noise ratio (RSNR) and served as the primary measure of photodetection system performance.

The RSNR, as defined above, depends on both the capabilities of the chosen measurement system and the fluid mechanics of the jet turbulence. What follows in this appendix is an explanation of how the RSNR was calculated and how the results of these performance calculations influenced the choice of the photosensor that was eventually used in the jet. In order to choose the best system, all of the work presented in this appendix leading up to Figure B-4 had to be completed before any archival quality runs were made in the turbulent jet.

B.1 Relating Current, Concentration, and the RSNR

The parameters of the conventional signal-to-noise ratio, SNR, provide a starting point for a discussion of the RSNR. The SNR was defined as:

$$SNR = I_S/\sqrt{i_n^2 \Delta\nu}\,, \tag{B.2}$$

where I_S is the signal photocurrent, i_n is the total noise current in Amps/$\sqrt{Hz}$, and $\Delta\nu$ is the bandwidth of the signal in Hertz. To maximize the RSNR, it was important to be able to predict I_S and i_n from the experimental design parameters, as well as to relate them to C_{max} and δC.

The Rayleigh scattered light intensity is a linear function of the mole fraction of jet molecules in the focal volume. The photodetectors utilized in these studies produced electrical currents that were linearly related to the amount of light power incident on them. Combining these facts yields:

$$I_S - I_r = m C_n\,, \tag{B.3}$$

where C_n is the mole fraction of jet gas molecules, I_r is the residual current that the system produces when $C_n = 0$ and the slope, $m = \frac{\partial I}{\partial C}$, is taken to be constant for each particular configuration of the data acquisition system. Because the gases chosen for this experiment were nearly density-matched, it was assumed that $C_n \approx C$ for the performance calculations. Conversion between C_n, the molecular number-weighted concentration, and C, the mass-weighted concentration, is explained in

Appendix E, Section 3.2 . The residual current is the sum of the leakage currents of the photosensor and the first-stage amplifier, plus the photocurrent resulting from the detected Rayleigh scattered light from the pure reservoir gas.

For a small change in C, δC, Equation (B.3) produces the relation for the accompanying small change in I_S, δI:

$$\delta I = m\,\delta C. \tag{B.4}$$

With this, the RSNR can be expressed as:

$$RSNR = (I_{max} - I_r)/\delta I. \tag{B.5}$$

As will be seen a little farther on (Equations B.13 and B.18), the rms noise current in a fixed bandwidth increases with signal current, but at a less than linear rate, so the peak signal-to-noise ratio and the maximum rms noise current both occur at the highest signal level. Therefore, δI in Equation (B.5) can be identified with $\left(\sqrt{i_n^2 \Delta\nu}\right)\Big|_{I_S=I_{max}}$ $(= \delta I_{max})$, allowing the RSNR to be written in terms of the maximum SNR and the ratio of the residual current and the maximum rms value of the noise current.

$$RSNR = SNR_{max} - \left(I_r/\delta I_{max}\right) \tag{B.6}$$

To properly predict this difference, the peak, local, jet gas concentration had to be estimated, the properties of the jet and reservoir gas pairs had to be known, and the capabilities of the

detection system had to be understood.

B.2 **The Dynamic Range of the Jet**

The mean dilution properties of the jet were estimated from experimental results. For uniform-density, momentum-driven, jet mixing, Chen and Rodi (1980) suggest:

$$\overline{C}_{cl} = 5.\, C_0 \left(\frac{x - x_0}{d} \right)^{-1}, \tag{B.7}$$

where x is the coordinate that is zero at the jet nozzle exit and increases downstream, C_0 is the exit concentration of the jet gas, and $\overline{C}_{cl}$ is the mean centerline concentration in the jet. Actually, d in Equation (B.7) should be replaced by d^*, the momentum diameter of the jet (see Chapter 1, Section 1), but for properly designed nozzles, and density-matched jet and reservoir gases: $d \approx d^*$. The unpublished result of Dowling and Frieler (1983),

$$C_{max} = 1.7\, \overline{C}_{cl}, \tag{B.8}$$

provided the estimate for the maximum local jet gas concentration C_{max}. The lower limit of the dynamic range of C was assumed to be zero.

B.3 The Intensity of Rayleigh Scattered Light

The amount of Rayleigh scattered radiation from a gas was expressed in terms of the extinction coefficient, α. It can be calculated from the index of refraction of the gas, n, the wave number of the incident light, k, and the number density of the gas molecules, N, as:

$$\alpha = \frac{2k^4}{3\pi N}(n-1)^2. \tag{B.9}$$

A derivation of this formula can be found in Jackson (1975). For a monochromatic beam of light traveling in the y direction through a gas with extinction coefficient α, the power in the beam, P(y), varies as an exponential,

$$P(y) = P(0)e^{-\alpha y}. \tag{B.10}$$

The light that is lost by the beam is the Rayleigh scattered light. A short segment of the beam ($\alpha \Delta y \ll 1$) at $y = 0$ radiates power ΔP:

$$\Delta P = P(0)\alpha \Delta y . \tag{B.11}$$

For most gases α is smaller than 10^{-4}/meter, so that a beam of light is not appreciably attenuated for many meters. Because all of the relevant path lengths in the experiment were less than a meter, the linear form (Equation B.11) was used to estimate system performance with P(0) taken as the output power of the laser.

For the optical setup used, Δy in Equation (B.11) corresponded to the length of the laser beam from which Rayleigh scattered light was collected. The spatial resolution requirement (Equation A.4) set the

size of Δy, so the amount of scattered light was determined by P(0) and the α's for the chosen jet and reservoir gas pair.

The laser system for the experiment was a Coherent Radiation CR-10 argon-ion system with an Innova-10 plasma tube. When properly tuned up, it delivered more than 20 watts from all of the laser lines. For the purposes of performance estimation, a slightly more conservative Figure of 16 watts was assumed for P(0). The laser system produced most of its power at two wavelengths near 500 nanometers (488 and 514.5 nm). For calculation of α from Equation (B.9), the mean wavelength and the mean photon energy of the two lines were used to represent the laser light's characteristics.

The selected jet and reservoir gas pairs were: propylene and argon, and ethylene and nitrogen. These choices were made on the basis of optical properties, density differences, available purity, and costs (see Sections A.5 and A.8). The amount of Rayleigh scattering done by a mixture of two gases is the proportional sum of their molecular number-weighted, extinction coefficients (= A, the available Rayleigh scattering cross section),

$$A = \alpha_j C_n + \alpha_\infty (1 - C_n), \qquad (B.12)$$

where jet and reservoir extinction coefficients are denoted by α_j and α_∞. As mentioned earlier, the difference between C_n and C was not taken into account in the performance calculations because the jet and reservoir gases were nearly density-matched.

One option for increasing the intensity of the Rayleigh scattered light that was not exploited would have involved performing the experiments at greater than atmospheric pressure. For most gases, N and (n-1) are proportional to the pressure. This makes α proportional to the pressure (see Equation B.9), so that raising the pressure has the effect of increasing the absolute magnitude of the extinction coefficients of both the jet and reservoir gases. While this is definitely a beneficial effect, it was offset by the cost and difficulty of producing a large pressure vessel for use as the main experimental platform.

The intensity of the Rayleigh scattered light, δP, for the experiments was predicted to be 2.4×10^{-8} watts radiated per watt of incident argon-ion laser power, for every millimeter the beam traversed through a mixture of 10% ethylene and 90% nitrogen. This Figure is about 3.4×10^{-8}/mm for 10% propylene and 90% argon.

B.4 **The Two Light Sensing Systems**

Performance calculations were made for 2 different light sensing systems and compared to the requirement of a minimum RSNR of 30 (see Appendix A, Section 7). The first system, which was used for all of the measurements, was based on a photodiode. The second one, based on a photomultiplier tube, was used in most of the preliminary work. The performance of each system was also measured to check the accuracy of the calculations.

B.4.1 **The Photodiode System**

The photodiode's main advantage over the photomultiplier tube was its high quantum efficiency of nearly 70% at the laser light wavelengths used. Its main deficiency was that it provided no signal amplification and therefore required a special, low-noise amplifier to raise its signal to working levels. The special transimpedance amplifiers used were designed by Dr. Dan Lang.

Following the noise analysis of Lang (1985), who made laser Doppler vorticity measurements with photodiodes and transimpedance amplifiers, the rms noise current of the photodiode system was calculated from:

$$i_n^2 = 2q_e(I_S + I_L) + i_a^2 + e_a^2\left[1/R_L^2 + (\omega C_t)^2\right] + 4k_B T/R_L , \quad (B.13)$$

where

q_e = charge of an electron (1.602×10^{-19} coulombs)

I_L = the total leakage current from the photodiode and the input of the first-stage op-amp. (.10 to .15 nano-amps)

i_a = amplifier input noise current (10^{-14} amps/$\sqrt{Hz}$)

e_a = amplifier equivalent noise voltage (noise voltage at the amplifier output with the input shorted to ground divided by the amplifier gain) in volts/$\sqrt{Hz}$ (12 nano-volts/$\sqrt{Hz}$)

R_L = load resistance in ohms (100 megaohms)

ω = frequency in radians per second ($2\pi\Delta\nu$)

C_t = total input capacitance of the photodiode, op-amp and load resistor (about 10 picofarads)

k_B = Boltzmann's constant (1.38×10^{-23} joules/K)

T = absolute temperature in Kelvin (295 K)

The values in parentheses were the ones used to estimate i_n^2. The first group of terms in Equation (B.13) is the shot noise contribution to the total noise current. The term headed by e_a^2 is the amplification noise term, and the final term is the Johnson noise contribution of the load resistor. The low frequency (1/f) noise term was believed to be too small to include.

All of the parameters in Equation (B.13) except I_S could be easily estimated, found on the manufacturer's data sheets, looked up, or measured. An estimate for I_s was obtained from:

$$I_S = q_e \eta_d \zeta A \beta t_1^6 \frac{\Omega}{4\pi} \phi \gamma \psi \Delta y P_L / E_{ph} = q_e \eta_d \dot{N}, \qquad \text{(B.14)}$$

where

η_d = quantum efficiency of the photosensitive surface (.68)

ζ = transmissivity of detector window (.95)

A = available cross section for the mixture of gases in the focal volume

β = the geometrical factor for the focal volume (.66 to .74)

t_1 = transmissivity of a coated glass surface (.99)

Ω = collection solid angle of the sensor optics ($\Omega/4\pi = 10^{-2}$)

ϕ = pressure ratio (ξ = 1 implies atmospheric conditions)

γ = polarization recovery factor (1.5)

ψ = number of beam passes through the focal volume (1)

P_L = laser power (16 watts)

E_{ph} = photon energy (3.97×10^{-19} joules)

Δy = the length of laser beam from which scattered light is collected (the diameter of the pinhole or photodiode used, 200 to 1000 μm)

$\dot{N}$ = the number of photons incident on the photosensory surface (between 1.5 and 7 billion per second)

As before, the values in parentheses were the ones used in the computations.

Several parameters in (B.13) need further explanation. The α values of the gases that enter the Equation for I_S through the available cross section A were calculated using Equation (B.9) with: $N = 2.48 \times 10^{25}$ molecules/m^3, $k = 1.255 \times 10^7 m^{-1}$, $n_{Ar} = 1.000261$, $n_{N_2} = 1.000277$, $n_{C_2H_4} = 1.000673$, and $n_{C_3H_6} = 1.00100$. The geometrical

factor for the focal volume, β, was used to predict the effective length of the laser beam from which scattered light was detected. It was calculated, based on the intersection of a Gaussian intensity distribution in the laser beam and a Gaussian sensitivity profile from the sensory optics. After performing the volume integrals, the result appears as:

$$\beta = \frac{\sqrt{\pi}}{2}\left(1 + 4\left(\frac{w}{\Delta y}\right)^2\right)^{-1/2}, \qquad \text{(B.15)}$$

where w is half the distance between 1/e points on the laser beam intensity profile. The polarization factor enters the formula for I_S, because the form of α was derived for randomly polarized light and the laser light employed for these experiments was strongly polarized.

When C_{max} from Equation (B.8) is used for C_n in Equation (B.12), Equations (B.13) and (B.14) allow the calculation of the maximum SNR and δI_{max} for the diode system with an arbitrary bandwidth for any downstream location in the jet. I_r is obtained by using α_∞ for A in Equation (B.14). Putting this all together yields:

$$\text{RSNR} = \left(\eta_d \zeta \beta t_1^6 \frac{\Omega}{4\pi} \phi\gamma\psi\Delta y P_L / E_{ph}\right)(\alpha_j - \alpha_\infty) C_{max} / \left(\sqrt{i_n^2 \Delta\nu}\right)\Big|_{I_S = I_{max}}. \qquad \text{(B.16)}$$

It is worth noting that the α's enter the numerator as a difference and the denominator as a sum in the estimate of i_n through I_{max}.

The bandwidth of the signal, $\Delta\nu$, was chosen to meet the temporal resolution requirement (see Appendix A, Section 1) and was set in the output electronics by a 3-pole Butterworth low-pass filter. The knee

frequency, f_0, was set above $4/\tau_K$. For 3-pole Butterworth low-pass filters:

$$\Delta\nu = 1.05\, f_0. \tag{B.17}$$

With all of these definitions and estimates in place, Equations (B.1), (B.6), (B.12), and (B.13) to (B.17) comprise the performance calculation for the diode system with Equation (B.16) as the main result.

B.4.2 **The Photomultiplier Tube System**

The photomultiplier tube (PMT) system was used for most of the preliminary measurements that lead up to the actual jet experiments. It has a lower quantum efficiency than the photodiode, but its dark current is insignificant and it provides considerable amplification of the signal current ($G_{PMT} \approx 10^4$). For the PMT system, i_n^2 is well approximated by:

$$i_n^2 = \frac{2\theta_t}{\theta_t - 1}\, q_e\, I_S\,, \tag{B.18}$$

where θ_t is the stage gain of the tube (typically about 2.5). The Johnson noise term from the first load resistor was too small to include. If θ_t was infinite, then (B.18) would be the form of i_n^2 for a shot-noise-limited process. The signal current for the PMT system, I_S was estimated from Equation (B.14), with the photodiode quantum efficiency replaced by the PMT photocathode quantum efficiency

($\eta_t = .09$). The spatial resolution of the PMT system was determined by a precision pinhole, since the diameter of the PMT's sensitive area was 3/4".

The rest of the arithmetic that leads to the RSNR of the PMT system is the same as for the photodiode system, so Equations (B.1), (B.6), (B.14), (B.17) and (B.18) provide the predicted performance for the PMT system.

B.4.3 **Measurements and Comparisons**

For selected conditions, the performance of each system was measured and compared to the calculated performance. Figure B-1 is a plot of the signal current versus laser power for both systems. It was not possible to measure I_S for the PMT, because the exact gain of the tube (G_{PMT}) was unknown and the measured current is the product $I_S G_{PMT}$. The best estimate of G_{PMT} would put the measured I_S versus laser power line about 20% below the predicted line on Figure B-1. The small deviations from linearity in the measured results for the photodiode are probably produced by the imprecision of the laser power meter. The discrepancy between the predicted and the actual photodiode system sensitivity is probably due to imperfect characterization of the delivery of scattered light to the photodiode's sensitive surface in the performance calculation. Earlier studies in a special pressure vessel, not described here, showed that the linearity of the output current versus mole fraction characteristic for the PMT system was very good.

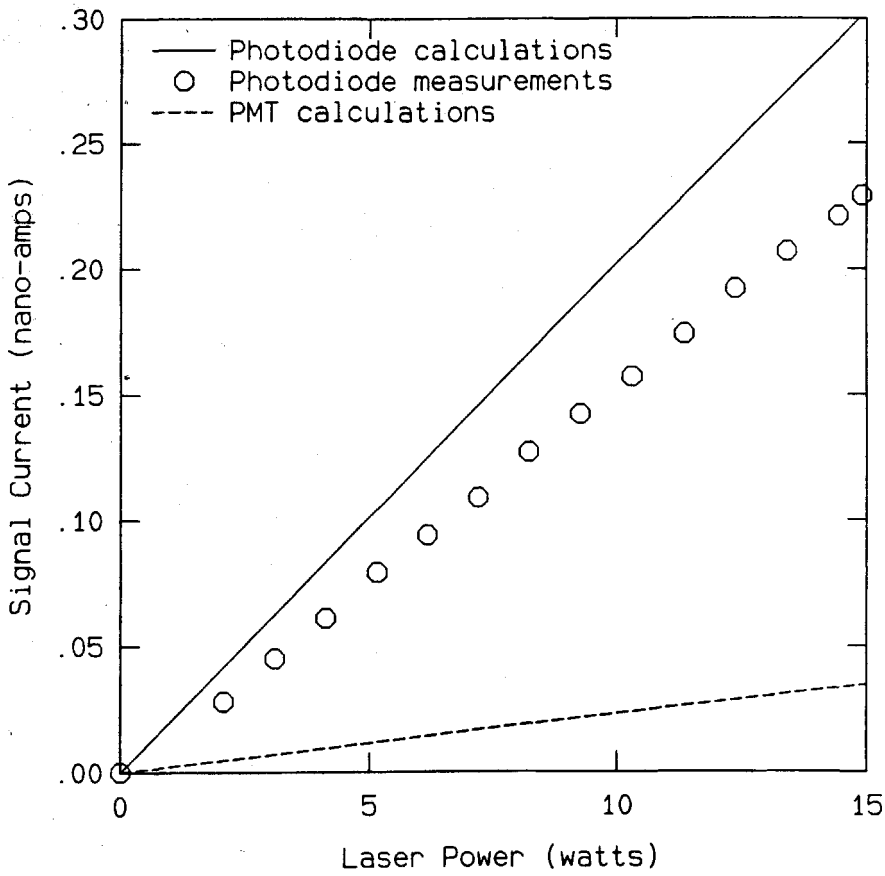

Figure B-1. Linearity of the photodetectors.

These studies were done to check that m, from Equation (B.3) was indeed a constant.

The noise characteristics were also measured for each system and compared with the predictions. The results for the rms noise current from the photodiode system are displayed in Figure B-2. The rms noise current could not be directly measured for the PMT system because of the large uncertainty in G_{PMT}, so the SNR of the PMT system is plotted in Figure B-3. The SNR is a ratio of amplified quantities, making it independent of the PMT's gain. It is worth noting that although none of

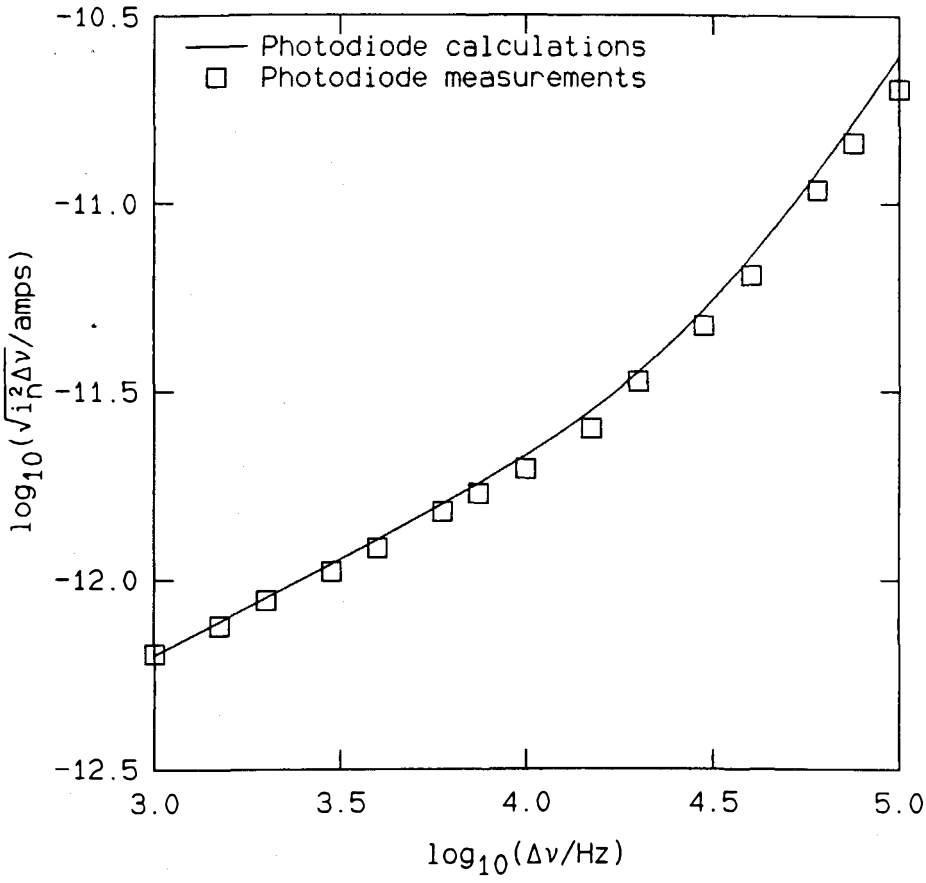

Figure B-2. Comparison of the measured and predicted rms noise current from the photodiode system.

the predictions for either the signal current or the total noise current exactly coincide with the measured results, they do have the correct shape and/or slope. This means that much better agreement could be obtained by inserting the correct multiplicative constants.

When this was done, the "fitted" theoretical formulas were used to to predict the RSNR of each system for the two gas pairs considered. It was not possible to measure the RSNR directly, because that would have

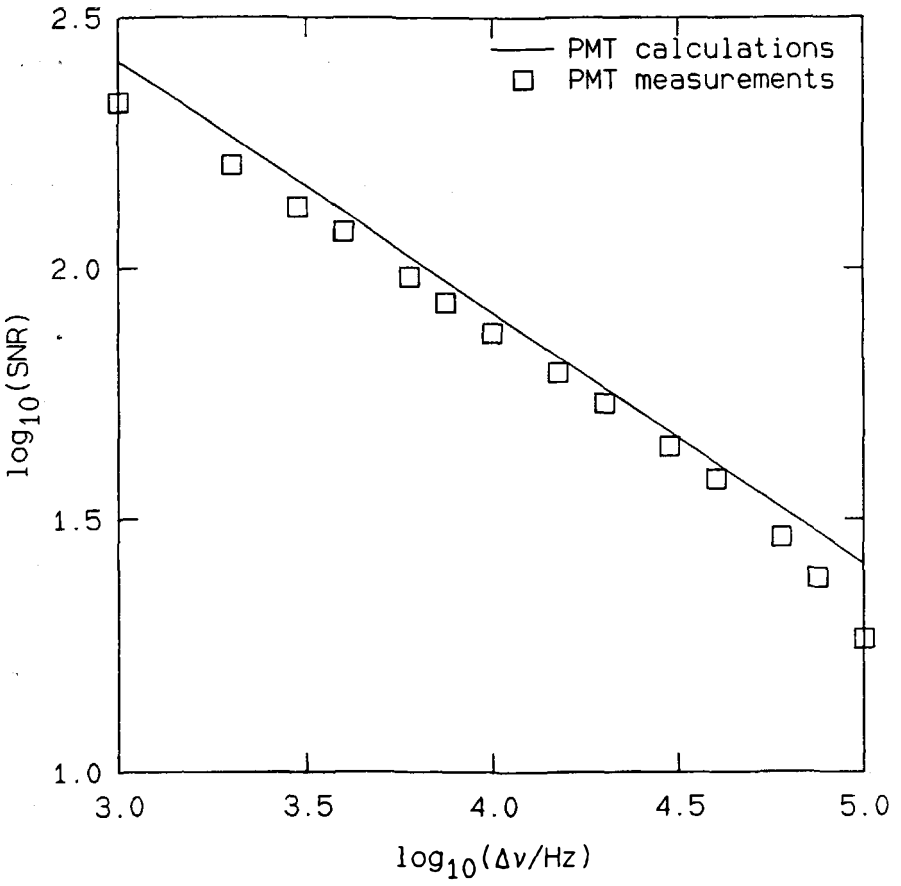

Figure B-3. Comparison of the measured and predicted signal to noise ratio for the photomultiplier tube system.

required the production of many precise mixtures of the various jet and reservoir gases. Figure B-4 shows the results of these predictions. Since this plot was used to determine which sensory system would be used for the concentration measurements in the turbulent jet, it was necessary to use the spatial and temporal resolution requirements dictated by the fluid mechanics of the jet (see Appendix A, Section 1) in determining Δy and $\Delta \nu$. For a fixed jet Reynolds number (5,000), and Δy and $\Delta \nu$ fixed by the fluid mechanics of the jet, the downstream

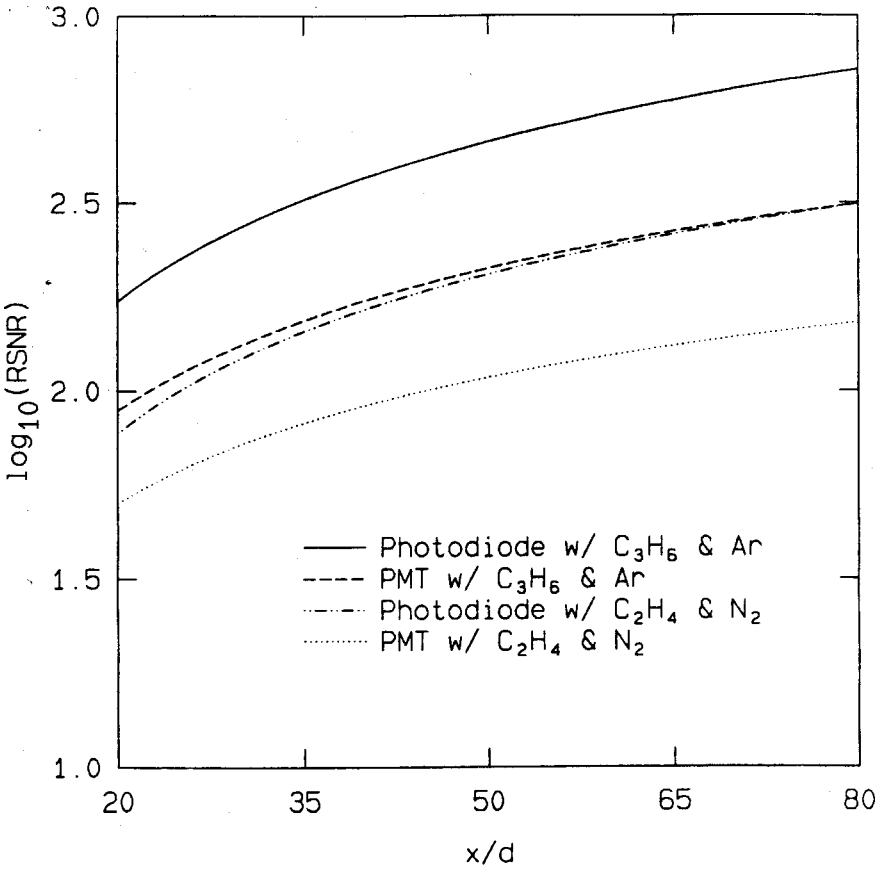

Figure B-4. Comparison of the expected RSNR from the two photodetection systems for both of the chosen gas pairs.

measurement location becomes the independent variable. Figure B-4 was constructed with $x_0 = 0$, $\Delta y = .6667\,\lambda_K$, and $\Delta\nu = 2/\tau_K$ and is the basis for the decision to use the photodiode system exclusively as the main experimental diagnostic.

After the development of the power spectrum software described in Appendix C, an additional comparison was made between the two systems described above and a new, second generation, photodiode system, which was used for the measurements in the jet at Re_0 = 16,000. The major change in the second generation photodiode system was the use of a better input stage for the transimpedance amplifier, which decreased the value of e_a by almost an order of magnitude. The new amplifier was also designed by Dr. Dan Lang.

Figure B-5 is a plot of the noise power spectra of each system. The upper two spectra in Figure B-5 were obtained under identical conditions for the PMT and first photodiode systems. The Rayleigh scattered light came from 200 μm of a 17.5 watt laser beam passing through still argon at room temperature and pressure. The most important observation from Figure B-5 concerning the upper two spectra is that the noise spectrum from the first photodiode system is roughly a factor of two less than the PMT system's from about 20 Hz to about 10 KHz. In fact, the noise spectrum from the first photodiode system is right on the Johnson noise limit from about 300 to 3000 Hertz. Beyond 3000 Hertz, the "roll-up" in the noise spectrum from the first photodiode system is due to amplification noise.

A second observation concerning the two upper spectra is that both are strange below 20 Hz. The funny business was caused by slight beam steering and power fluctuations in the laser. These problems arose from an optically large speck (probably a small fragment of the tube's

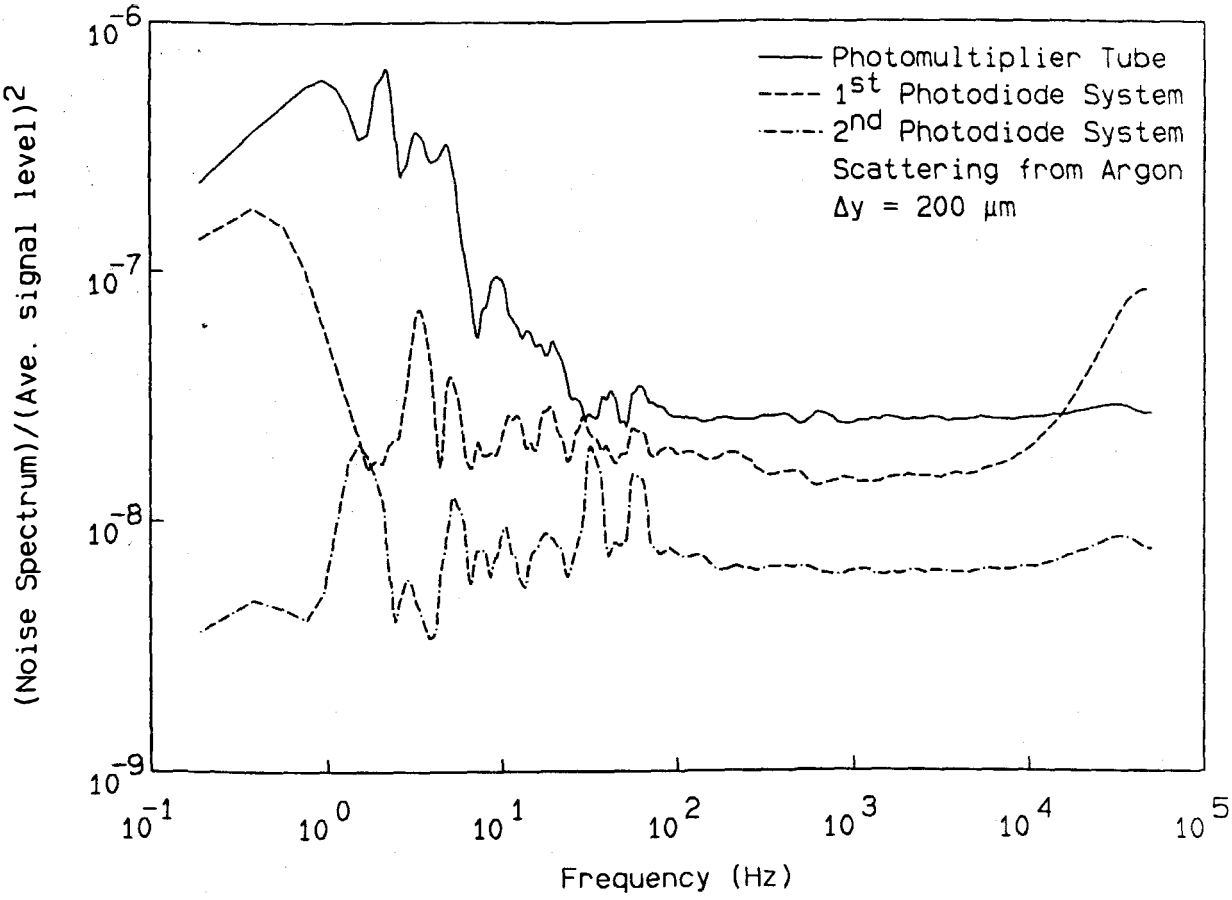

Figure B-5. Comparison of the noise power spectra from the photomultiplier tube system and the 1st and 2nd photodiode systems.

cathode), on the inside of the laser's front Brewster angle window, whose dynamic thermal/optical properties destabilized the laser's light output. The details of the spectrum of these disturbances were not reproducible. Although this unsteadiness could have been a factor for extremely critical measurements, the power spectrum of the concentration fluctuations was typically about 4 or 5 orders of magnitude higher than

the laser fluctuations in the frequency range where the laser problems were the worst. This put the laser problems in perspective and they were ignored as much as possible. Their most important impact on the experiment was to set the absolute concentration calibration uncertainty at about .3%.

The lowest spectrum on Figure B-5 was taken with the 200 μm photodiode hooked to the second-generation transimpedance amplifier. The wild fluctuations at low frequency are no longer detectable, because the laser tube with the window problems had been replaced since the first two noise spectra were measured. The laser power for this final spectrum was about 23 watts, so it falls below the others because the DC signal level was higher. The peak at 30 Hertz is due to one of the building's vibrational modes or some type of outside electrical discharge, because the same frequency appears in spectra from another experiment in the same laboratory, using a completely different diagnostic. The peak sightly above 30 Hertz occurs at 60 Hertz. The amplification noise from the second generation photodiode system does not affect the noise spectrum until about 20,000 Hertz. In fact, the the second generation photodiode system noise spectrum falls on the Johnson noise limit from about 10 Hertz to 10^4 Hertz.

APPENDIX C

COMPUTATION OF POWER SPECTRA

The computation of the power spectrum of concentration fluctuations for each data set was based on Equation (C.1). The accuracy of this formula, especially for low frequencies, is determined by the length of the available data record, since the limit of $\Upsilon \to \infty$ is unobtainable by experiment.

$$E_c(\omega) = \lim_{\Upsilon \to \infty} \frac{1}{2\Upsilon} \left| \int_{-\Upsilon}^{+\Upsilon} e^{-i\omega t} C(t)\, dt \right|^2 \qquad (C.1)$$

$E_c(\omega)$ = true power spectrum of the process $C(t)$

2Υ = time interval over which $C(t)$ is known

ω = temporal radian frequency = $2\pi f$

t = time

$C(t)$ = concentration of jet gas as a function of time

In Equation (C.1) the finite Fourier transform was approximated by a conventional, fast Fourier transform, computer algorithm designed for use with sampled data sets.

To insure that all of the relevant fluid mechanical time scales of the jet were well represented by the estimate of the concentration-fluctuation power spectrum, the complete data acquisition interval for the experiment was many local large scale times of the jet,

typically 30 or 40 τ_D at Re_0 = 5,000 and more that 100 τ_D at Re_0 = 16,000. With the data acquisition rate set by the requirement for adequate resolution of the smallest predicted diffusion scales, the number of individual concentration measurements made in a typical run was 524,288 ($=2^{19}$).

Because this amount of data far exceeded the largest available array size on the PDP 11/44 used for processing, it was necessary to break the long data record into smaller pieces and to develop a technique for independent estimation of the high and low frequency portions of the spectrum. The necessary sectioning and sampling of the long data set into smaller records of 4096 (4K) data points was found to be optimum for data management and computational efficiency. The use of this record length also allowed nearly one and a half decades of overlap between the the high and low frequency estimates of the spectrum.

C.1 **High Frequency Spectral Estimation**

The method used for estimation of the high frequency part of the spectrum is based on the one proposed by P. D. Welch (1972), with a few refinements. A small portion of the entire record is selected, in this case 4096 (4K) measurements. A parabolic least-squares fit of the data is calculated and then subtracted out. This prevents contamination from frequencies that are too low to have their spectral contribution properly estimated by a fast Fourier transform (FFT). Because the spectra computed for this study normally roll off quite strongly ($\omega^{-5/3}$

or faster), it was necessary to prewhiten the data in order to prevent the finite accuracy of the computer arithmetic from affecting the results. This was accomplished by taking a first difference of the data. Centered differencing was found to depress the calculated spectrum at high frequencies, so it was not used. To prevent the entry of spurious frequency components from mismatch of the data at the ends of the 4K record, the data were multiplied by a window function, W(i), which in this case was a half sine wave.

$$W(i) = N_w \sin\left[(i - .5)\pi/4096\right] \qquad (C.2)$$

W(i) = window function

i = index that runs from 1 to 4096

$N_w = \sqrt{2}$

The value of N_w results from the need to have $\sum_{1}^{4096} W^2(i) = 1$. After these preparations, the fast Fourier transform of the 4K record was computed. The real and imaginary components of each point were normalized, squared and added to produce a power spectrum. The effect of the prewhitening introduced by the first difference operation was removed by a division with $4 \sin^2(\omega/2)$ (the correct inversion of a first difference). Since the important results to be obtained from the computed spectra were the values of slopes and the location of break points (and not the shape nor the height of peaks), the final step was a convolution with a triangular filter function defined by Equations (C.3).

$$Trg(j-2) = 0.00 \quad \text{(C.3a)}$$

$$Trg(j-1) = 0.25 \quad \text{(C.3b)}$$

$$Trg(j) = 0.50 \quad \text{(C.3c)}$$

$$Trg(j+1) = 0.25 \quad \text{(C.3d)}$$

$$Trg(j+2) = 0.00 \quad \text{(C.3e)}$$

Trg(j) = Triangular filter function centered on point number j

This smoothing also repairs some of the imperfections produced by the windowing and the other operations (Blackman and Tukey 1958). The rest of the long data set was processed in exactly the same manner in a sequential fashion. The first point of each 4K record was the midpoint of the previous 4K record, except for the first 4K record, which started on the first point of the long data set. This method of overlapping successive small records, in conjunction with the windowing operation, insured that every part of the entire long data set would receive equal statistical weight, except for the very beginning and very end, where no overlap is available. Figure C-1 is a flow chart of this method of spectral estimation.

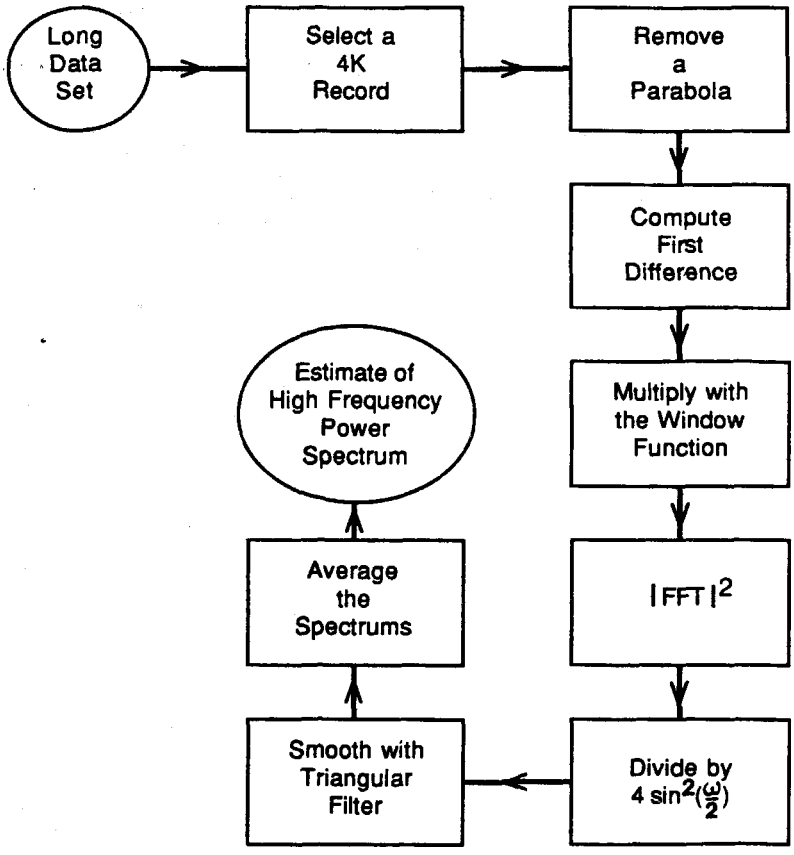

Figure C-1. Flow chart for the high frequency portion of the spectral estimation software.

C.2 **Low Frequency Spectral Estimation**

The method used to estimate the low frequency portion of the power spectra is basically the same as the high frequency method. The major differences are the manner in which the 4K records are removed from the long data set and the extent of the filtering performed.

To prevent aliasing of high frequency information down to the lower frequencies, where this method computes the spectrum, the long data set was convolved with a broad Gaussian. The pass band of this filtering process was chosen to end at the highest frequency for which the low frequency method could provide spectral information. From the long, filtered data set, equally spaced data points were selected to fill a 4K record. The spacing between samples was typically 128 points; for example, the first 4K record was composed of the first point, the one hundred twenty-ninth point, the two hundred fifty-seventh point, continuing up to the $524,161^{st}$ point of the long, filtered data set. This 4K record was then subjected to a process similar to the high frequency method of estimation. After having its least-squares parabola removed, the 4K record was first differenced, windowed, and fast Fourier transformed. The square of the magnitude of the transform was computed, divided by $4 \sin^2(\omega/2)$ and smoothed with the triangular function. The rest of the long filtered data set was processed in exactly the same fashion except for a shift, typically 16 points, in the sampling used to produce subsequent 4K records. The second 4K record, for example, would typically start with the seventeenth point of the long, filtered data set and end on the $524,177^{th}$, the third 4K record would start with the thirty-third point of the long, filtered data set, and this process was continued until the selection of data points for the last 4K record. The results from each of these 4K records, typically 8 in number, were normalized and averaged to form the low frequency estimate of the power spectrum. It is probably worth noting that the window (see Equations C.4) used in this method was chosen to give equal statistical

emphasis to as large a portion of the data set as the high frequency routine did.

$$W(i) = \frac{1}{2} N_w \left[1-\cos\left((i-.5)\pi/16\right)\right] \qquad \text{for } 1 \le i \le 16 \qquad \text{(C.4a)}$$

$$W(i) = 1.00\, N_w \qquad \text{for } 17 \le i \le 4080 \qquad \text{(C.4b)}$$

$$W(i) = \frac{1}{2} N_w \left[1-\cos\left((4096.5-i)\pi/16\right)\right] \qquad \text{for } 4081 \le i \le 4096 \qquad \text{(C.4c)}$$

Here the value of N_w is about 1.00245. This choice of the window and its normalization are important for a good match with results from the high frequency routine. A flow chart of this method of spectral estimation is given as Figure C-2.

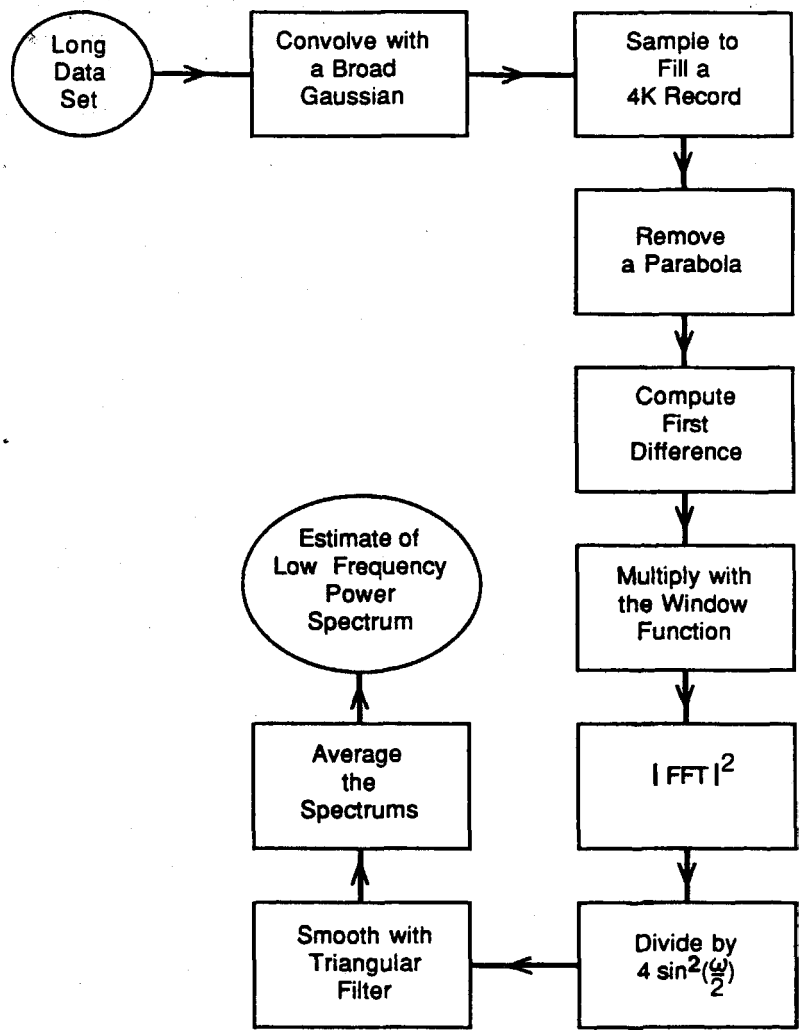

Figure C-2. Flow chart for the low frequency portion of the spectral estimation software.

C.3 **Comments**

The results of the two methods formed the estimate of the power spectrum. For log-log plotting purposes, the spectra were smoothed with a one-tenth decade filter, and linear interpolation was used to "fair-in" a curve in the matching region.

As a global check of the complete method of power-spectral estimation, the rms concentration fluctuation level was computed directly from the long data set and from the estimate of its spectrum using Equation (4.1). The value computed from the spectrum was usually less than the value computed directly, but the two answers typically differed by less than one percent. This small discrepancy was traced to the details of the lowest frequency portion of the computed power spectrum, which is sensitive to the finite record length, the windowing, and the removal of the parabolic trend. It is worth noting that for any individual 4K record, the mean-fluctuation level computed from its estimated spectrum without the windowing or parabolic trend removal agreed with that computed directly from the 4K record to 3 or more significant figures.

APPENDIX D

THE COFLOW TEMPERATURE CONTROL SYSTEM

Before the control system was built, the temperature of the coflow gas, which was supplied by high-pressure cylinders, would drop during a run at the rate of 1.5 ^{0}C per minute. This cooling trend was the result of the isentropic expansion and Joule-Thompson throttling processes taking place in the cylinders and the delivery plumbing. Because the coflow gas entered the test section at the top, the cooling trend would cause a layer of colder (denser) gas to form over warmer (lighter) gas. In the earth's gravitational field, this is an unstable arrangement of densities, and the resulting buoyancy currents were unacceptable. To prevent these currents, which were observed in the laboratory, it was necessary to develop a means of controlling the temperature of the coflow gas during a run, to insure that the background fluid mechanical aspects of the experiment were stable.

In addition to reversing the cooling trend, the temperature control system was required to be compatible with the other sensitive electric components of the experiment. This eliminated any "off-the-shelf" commercial systems that rely on high-speed switching of large electrical currents. The system also had to be easy to use so that its addition to the experimental apparatus did not necessitate an increase in manpower to run the entire experiment. These requirements were met with a design based on a single thermocouple sensor and a resistive heater.

This custom system was a basic P-I (proportional and integral) feedback control system except that the actuator, the resistive heater, was a nonlinear element. The sensory thermocouple produced a voltage V_{tc} that was linearly related to the difference between its own temperature T_{tc} and the temperature of a reference junction T_{ref},

$$V_{tc}(t) = \sigma (T_{tc}(t) - T_{ref}). \tag{D.1}$$

The reference junction for this system was provided by bulky electrical connectors in the upper part of the coflow settling chamber. The sensory thermocouple was Alumel-Chromel, so σ in Equation (D.1) was equal to $40\,\mu V/^{0}C$ in the range of temperatures encountered. The thermocouple voltage was subtracted from a set-point voltage to form an error signal $\varepsilon(t)$.

$$\varepsilon(t) = V_{sp} - V_{tc}(t) \tag{D.2}$$

The error signal was separately amplified and integrated. These two signals were then recombined and sent to a custom DC power amplifier, which produced the voltage applied to the heater V_h. Equation (D.3) summarizes these manipulations.

$$V_h = G_h\left[\varepsilon(t) + \frac{1}{\tau}\int_0^t \varepsilon(t)\,dt\right] \tag{D.3}$$

The power amplifier regulated V_h with several large transistors, so the current passed to the resistive heater was smooth, and no electrical interference was created. To obtain the best possible frequency response from the heater, it was made from a coil of bare nichrome wire supported inside the coflow delivery plumbing by a ceramic rod. The

"cold" resistance of the heater was about 5 Ω. The sensory thermocouple was placed downstream of the heater, and the increase in temperature, ΔT, of the flowing gas closed the feedback loop when it passed by the thermocouple,

$$\dot{Q} = \dot{m} c_p \Delta T = \frac{1}{R_h} V_h^2, \tag{D.4}$$

where:

$\dot{Q}$ = rate of heat input by the resistive heater

$\dot{m}$ = mass flow rate of the coflow gas

c_p = specific heat of the coflow gas

R_h = electrical resistance of the heater

V_h = Voltage applied to the heater by the DC power amp.

The heat was well mixed throughout the flowing gas before it reached the sensory thermocouple by the turbulence created in the tortuous interior path of the solenoid valve used to initiate the coflow. A schematic of this system is shown in Figure D-1.

Because the heater was nonlinear and delivered heat proportional to the square of the voltage applied to it, the values of the loop gain (G_h), the time constant for the integration (τ), and the magnitude of the initial difference between the thermocouple and set-point voltages ($\varepsilon(0)$) could be predicted only approximately. Heat transfer into and along the delivery plumbing that carries the coflow gas created

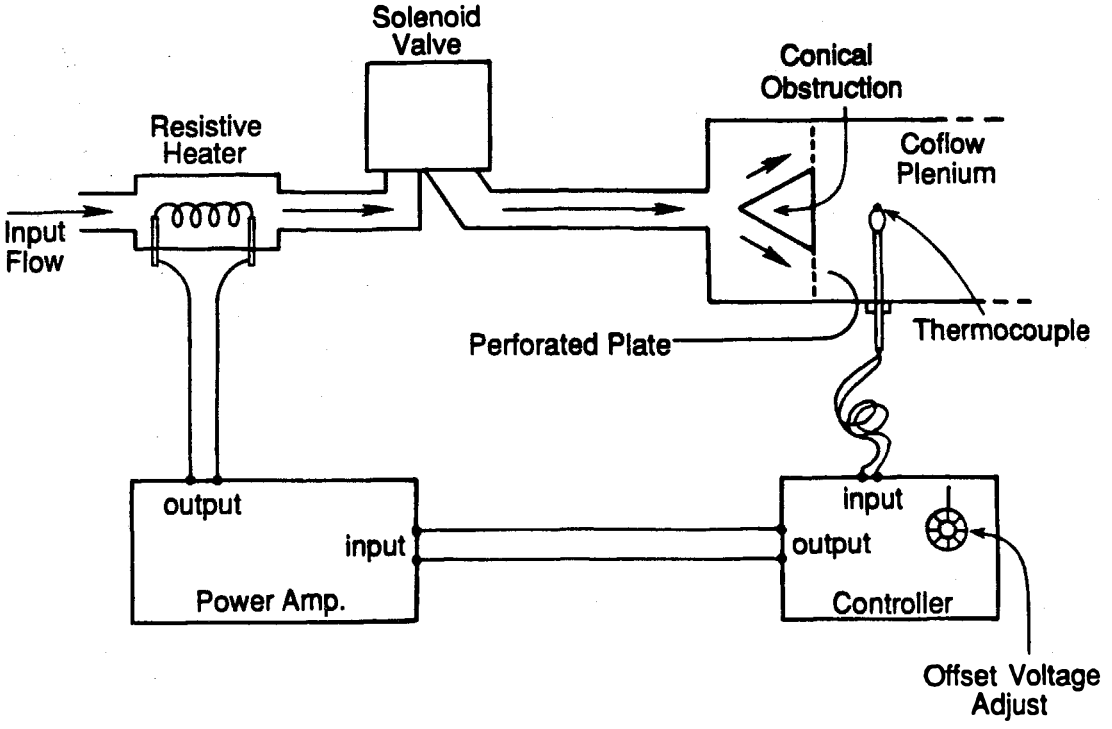

Figure D-1. Schematic of the coflow temperature control system.

additional uncertainty in these estimates. To realize optimum performance, several trial runs were made, the parameters were adjusted and a 300 watt heating tape was added to provide some uncontrolled bulk heating of the delivery plumbing. These are the values that were used:

$$G_h = 950{,}000$$

$$\tau = 3.67 \text{ seconds}$$

$$\varepsilon(0) \approx 10 \text{ to } 16 \ \mu V.$$

The final system delivered about 1300 watts without any effect on the other electrical components of the experiment. It was operated from the same remote switch that was used to open the coflow solenoid valve. The turn-on transient was typically composed of one overshoot bump in V_h, which lasted less than one second. Since the mixing time for the coflow plenum was about 6 seconds, this short transient did not cause any problems. The system forced the temperature of the coflow gas to achieve a preset temperature rise to within 1/5 ^{0}C. This preset temperature rise, ΔT_p, was directly proportional to the initial difference between the thermocouple voltage and the set-point voltage.

$$\Delta T_p = \varepsilon(0)/\sigma = \left(V_{sp} - V_{tc}(0)\right)/\sigma \qquad (D.5)$$

The set-point voltage was usually chosen to produce ΔT_p in the range from .25 to .40 ^{0}C.

The temperature regulation lasted typically for about a minute for the runs at $Re_0 = 5{,}000$ and for about 15 to 20 seconds for the runs at $Re_0 = 16{,}000$ before being saturated. This was allowed more than 30 large-scale times to be captured in a single run for every measurement location at both Reynolds numbers except $x/d = 80$ and $Re_0 = 5{,}000$, where about 16 large-scale times were recorded in each run.

APPENDIX E

DATA ACQUISITION SYSTEM AND PROCESSING TECHNIQUES

E.1 The First-Stage Electronics

The first-stage electronics consisted of the photodiode and its matched transimpedance amplifier. The photodiodes used in this study were from the United Detector Technology PIN-HSxxx series. They were operated in the photoconductive mode with a constant reverse bias voltage of about 15 volts. Two different transimpedance amplifiers were used with the photodiodes in these experiments. The first one was employed for the runs at $Re_0 = 5,000$, and the second one, which was an upgrade of the first, was employed for the runs at $Re_0 = 16,000$. Both transimpedance amplifiers were carefully matched to the diode's characteristics to provide low-noise performance and enough bandwidth to meet the temporal resolution requirement (Equation A.4). The gain of both amplifiers was 10^8 volts/ampere, and they worked with a typical signal current of about one-third of a nano-ampere. The measured frequency response of both of the photodiode/amplifier systems was flat (3 percent peak variation) from 10 Hz to 40 Khz. For higher frequencies stray capacitance "rolled-off" the response (see Figure E-1). The frequency at which the response had dropped to 70% of its peak value was about 110 KHz for the first photodiode/amplifier system and about 130 KHz for the second photodiode/amplifier system. The measurements shown on Figure E-1 were made by illuminating the photodiode with light from a red light-emitting diode (LED), which was driven by a sinusoidal voltage

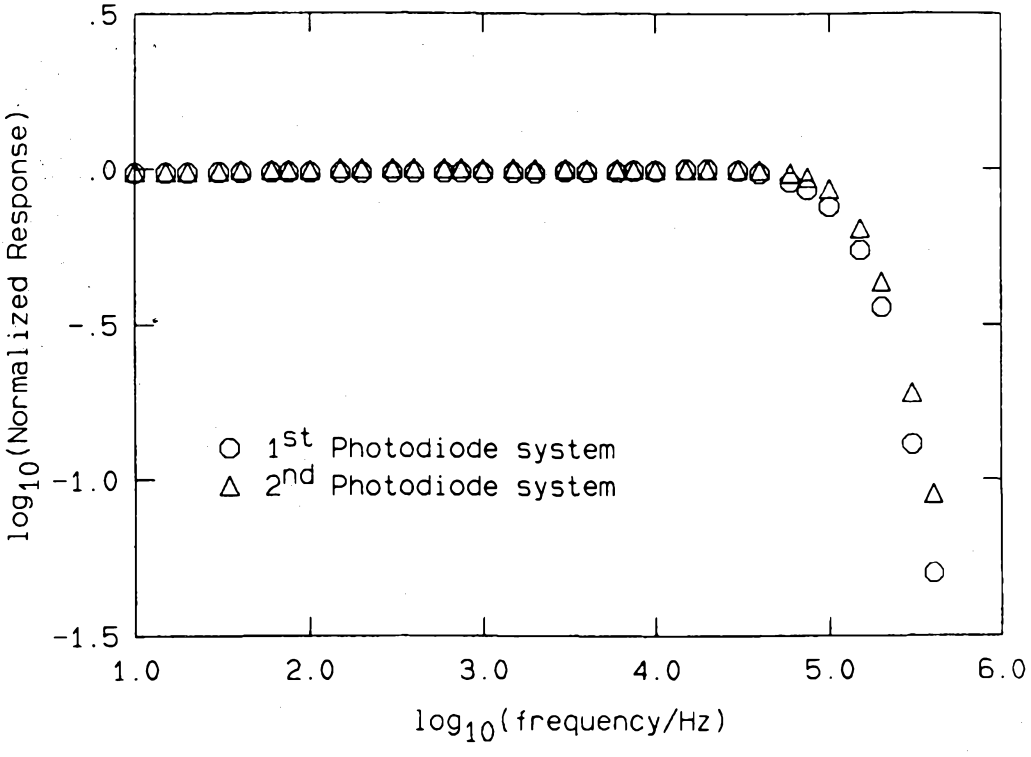

Figure E-1. Frequency response of the first and second photodiode systems.

with a DC offset. Figure B-1 is a plot of the linearity of the first photodiode system's DC response. The small deviations from perfect linearity of the measured response are probably the result of uncertainty from the laser-power meter. The performance of both photodiode systems is discussed in Appendix B.

E.2 **Analog Processing**

Before digitization, some analog processing was performed by the second-stage electronics to match the incoming signal to the voltage range of the A/D converter (see Figure 2-3). The signal from the first-stage electronics was DC compensated to remove the signal voltage produced by the Rayleigh scattered light from the reservoir gas alone, and was sent to a variable gain amplification stage used to set the voltage range of the output signal to roughly 10 volts. This compensated and amplified signal was offset again to put the system's "zero-concentration" voltage level at about -8 or -9 volts. As a final step, the signal was filtered with a 3-pole Butterworth filter, whose knee frequency was chosen based on the Nyquist criterion and the sampling rate. The gain offsetting done by the electronics was intentionally chosen to insure that the concentration signal approximately filled the lower half of the ±10 voltage range of the A/D converter. This made the occasional sharp peaks from the Mie scattering of dust particles, which rose above the nearby molecularly Rayleigh scattered data, easy to detect and remove in later processing.

E.3 **Digital Processing**

The scaled and filtered signal was then fed to a Data Translation 3382 12-bit, 250 KHz analog-to-digital converter board. The digitized values from the converter were initially stored in memory and then transferred to a hard disc after the run was complete. The data acquisition process was controlled by software running on an LSI

11/73-based computer system, which was also used for initial data processing.

E.3.1 **Analog-to-Digital Converter Corrections**

The first step in this processing involved the removal of the A/D converter's peculiarities from the data. The voltage characteristic of the A/D converter was measured immediately after each run by digitizing a large integer number of cycles of a triangular wave form having a low frequency relative to the digitization rate and an amplitude spanning the A/D voltage range. This digitized signal was used to construct a histogram of the number of digitizations at each of the 4096 levels (12 bits). The histogram was normalized, ignoring the end points, to produce a look-up table for the size of each of the A/D converter's bins. The partial sum of the look-up table to each bin then provided a corrected A/D number for that bin. This procedure allowed digitized concentration data to be interpreted through an almost perfect linear characteristic. To remove the sampling bias associated with unequal bin sizes in the A/D converter, a random number with a uniform density function spanning the bin of the conversion was added to the partial sum of the look-up table for the previous bin to produce the final corrected A/D number for that conversion. Although this added a small amount of noise to the data, it uncoupled the A/D converter's voltage characteristic from the statistics of the data.

E.3.2 Conversion to Mass-Weighted Concentration

The second processing task performed was the conversion of the corrected A/D numbers to molecular number-weighted concentration (mole fraction), C_n. The sensitivity of the entire data acquisition system was calibrated by alternately introducing pure reservoir and pure jet gases into the focal volume by means of a small laminar jet with the system gain set to achieve a 15-volt difference in these levels. To accurately record the concentration dynamics in the far field of the jet where concentrations are low, it was necessary to change the system gain for data acquisition to insure that the signal would span a significant portion of the A/D range. The calibration was anchored at the higher gain by recording the reservoir gas signal level again. The conversion from A/D number to mole fraction proceeded as follows.

$$C_n(i\Delta t) = 10^4 \frac{(M_i - RH)}{\frac{GH}{GL}(JL - RL)} \qquad (E.1)$$

$C_n(i\Delta t)$ = mole fraction of the i^{th} measurement in parts per 10^4

Δt = time between measurements, $(\text{A/D conversion rate})^{-1}$

M_i = corrected A/D # of the i^{th} measurement

RH = corrected A/D # for the reservoir gas level at the higher gain

GH = higher gain

GL = lower gain

JL = corrected A/D # for the jet gas level at the lower gain

RL = corrected A/D # for the reservoir gas level at the lower gain

JL, RL and RH were measured before and/or after each run with the average value for each being used in the conversion process when both measurements were made. The ratio of GH to GL was determined by the 2 resistor values that were alternated in the gain-setting position of the variable gain stage of analog amplification.

The mole fraction data were converted to mass fraction, C, using:

$$C(t) = \frac{\rho_j C_n(t)}{(\rho_j - \rho_\infty) C_n(t) + \rho_\infty}, \qquad (E.2)$$

where ρ_j and ρ_∞ are the densities of the jet and reservoir gases. The density ratio of the jet and reservoir gases, ρ_j/ρ_∞, was 1.0015 for the runs at Re_0 = 5,000, and 1.053 for the runs at Re_0 = 16,000.

E.3.3 **The Removal of the Effects of Particles**

The scattering cross sections of dust particles are typically a few orders of magnitude larger than the Rayleigh scattering cross sections exploited by the diagnostic in the measurements. Unfortunately, there was always a small number of dust particles (10 to 100) that would wander through the focal volume during data acquisition and would appear in the recorded data as sharp peaks. To find these peaks, a filter shaped like a Mexican hat was convolved with the data and when the convolution value exceeded a threshold, the location in the data set was noted. A detected dust spike was removed by placing a straight line

across its base and adding noise to the line from a nearby portion of the data set. The top three plots of Figure E-2 illustrate these manipulations. The first plot is of 512 data points with some typical dust peaks. The second is the output of the Mexican hat filter for the same data. The third plot is the data with the dust peaks removed. The fourth plot on Figure E-2 is explained below. This whole process of convolution and peak removal was repeated in an iterative fashion, with a decreasing threshold, until naturally occurring concentration or noise fluctuations were the only features exceeding the threshold.

After the dust was removed, the local mean was checked throughout the data set to make sure that no trend had developed during the run. A slowly increasing or decreasing local mean could be indicative of recirculation of mixed gases to the measuring station or of unsteadiness caused by separation of the coflow from the inner walls of the experiment.

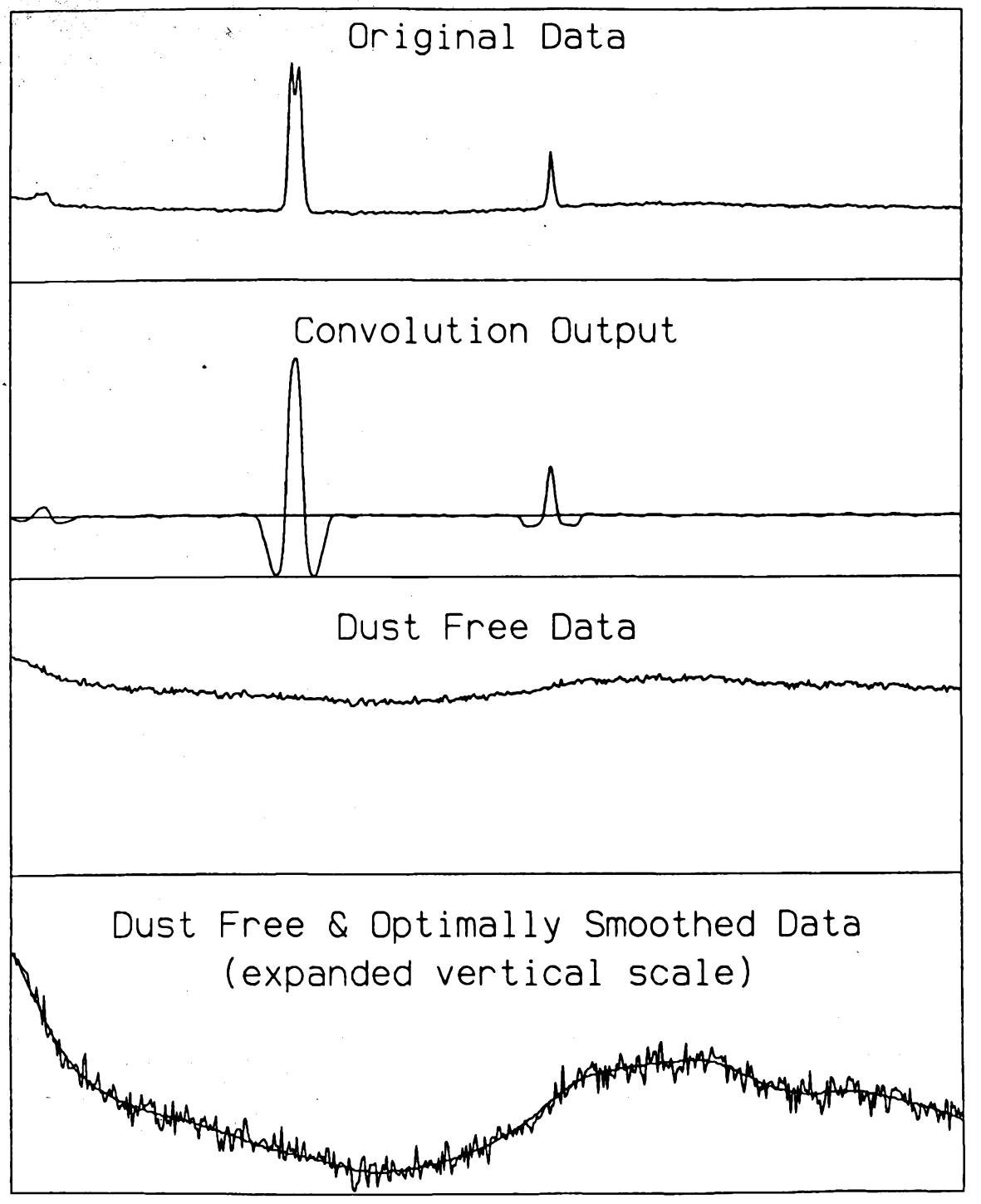

Figure E-2. The effects of dust removal and optimal filtering on the instantaneous concentration signal

E.4 Statistical Processing

The method of power-spectral estimation from the converted and "cleaned" data is explained in Appendix C. To further improve the quality of the data, optimal Wiener filtering (Wiener 1949) was performed. The estimated optimum filter, computed from the power spectrum of the data following the recipe given by Press et al. (1986), was used to push the noise floor in the data down to the round-off error produced by the integer storage format.

The formula used to compute the optimal filter kernel, F(f), in the frequency domain was:

$$F(f) = \frac{M(f) - N(f)}{M(f)} \qquad (E.3)$$

where M(f) is the measured power spectrum (signal and noise), and N(f) is the power spectrum of the noise alone. In practice, $E_c(f)$ was used for M(f), and N(f) was taken to be a constant noise level that matched the "noise tail" level of $E_c(f)$. A fast Fourier transform was used to switch the filter kernel to the time domain, where the filtering was performed through a point by point convolution of the kernel and the sampled data. The time domain version of an optimal kernel is shown on Figure E-3. This particular one was created from and used on the data from the jet at $Re_0 = 16{,}000$ and $r/(x - x_0) = .12$.

The effect of the optimal filtering is illustrated by the lower two plots on Figure E-2. The jagged trace on the bottom plot is the same data as the trace above it except that the vertical scale has been

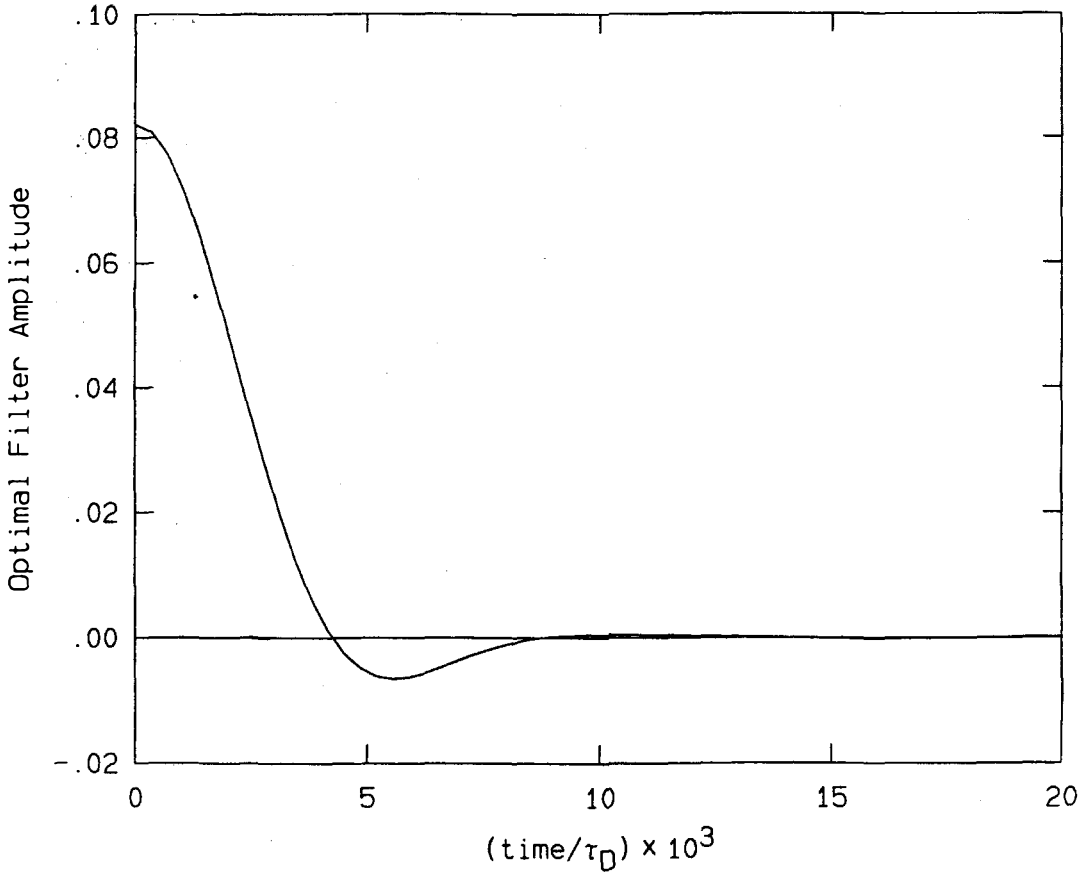

Figure E-3. A typical optimal kernel in the time domain. ($\Delta t/\tau_D \approx 3.47 \times 10^{-4}$)

changed. The smooth curve on the bottom plot is the optimally filtered result of the jagged trace. Small jumps in the smooth curve result from compressing the dynamic range of the data for plotting purposes.

The probability density function was compiled from the optimally filtered data by sorting the data into 60 bins. While the signal-to-noise ratio of the filtered data may have exceeded 60, the

statistical resolution of the data usually did not, because the experiment could be run for only a finite length of time.

The first derivative of the filtered data was computed by convolving it with the first derivative of a Gaussian.

$$\frac{dC(t)}{dt} = -\int_{-\infty}^{+\infty} C(t') \frac{(t-t')}{\sqrt{2\pi}\,\upsilon^3} \exp\left(\frac{-(t-t')^2}{2\,\upsilon^2}\right) dt' \qquad (E.4)$$

The width parameter of the kernel, υ, was chosen in a fashion that was consistent with the local sampling, in both time and space, with respect to the local jet resolution requirements, and was typically between $2\,\Delta t$ and $6\,\Delta t$. Care was taken to be sure that the effective width of the Gaussian in Equation (E.3) did not exceed the width of the central hump in the optimal filter kernel. The square of the first derivative was used to compute the instantaneous estimate of the scalar dissipation rate from Equation (7.1). The power spectrum of the estimated scalar dissipation rate was computed with the same software used for the concentration fluctuation power spectrum. The PDF of the logarithm of $(dC/dt)^2$ was computed by taking the logarithm of each value of $(dC/dt)^2$, sorting the ensemble of data points into bins and normalizing the resulting histogram.

Figure E-4 provides some insight into how these manipulations change the character of the data. All four traces on Figure E-4 are from the same portion of the same data set used to make Figure E-2. The top trace is a 512 point sample of data after conversion to concentration, removal of dust "spikes," and optimal smoothing. The

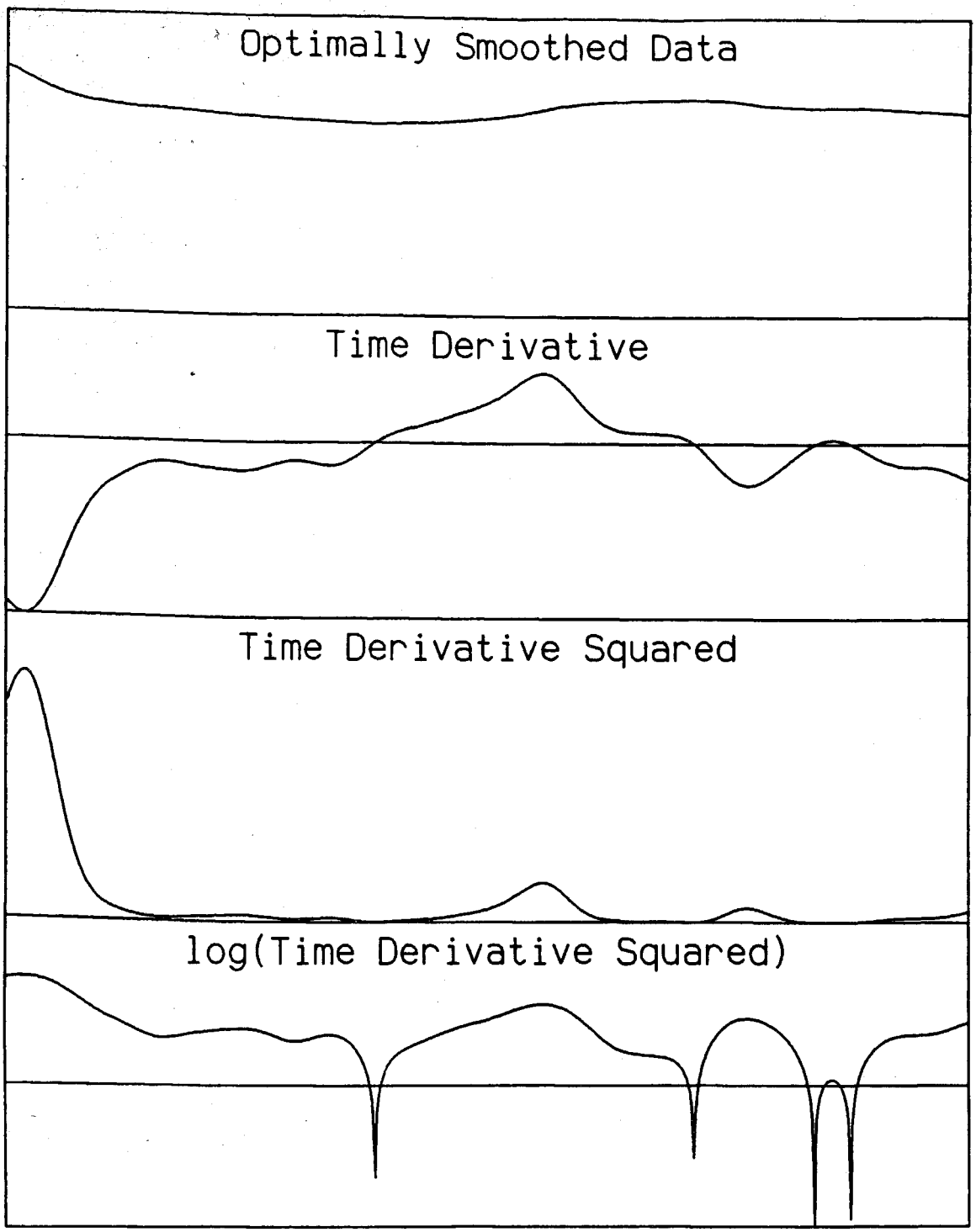

Figure E-4. Effects on the optimally filtered concentration of taking the time derivative, squaring the time derivative, and taking the logarithm of the square of the time derivative.

second trace is the time derivative of the first one. The third trace is the square of the time derivative of the first trace, and the bottom trace is the logarithm of the data plotted on the third trace.

APPENDIX F

A MOMENTUM-INTEGRAL ANALYSIS OF THE FREE-JET MEAN VELOCITY FIELD

This appendix is a presentation of one way that the general similarity behavior of the mean velocity field of the momentum-driven, free turbulent jet can be massaged out of the equations of motion for an incompressible fluid. A different version of this discussion is given in a more compact form by Landau and Lifshitz (1959).

Start with the Reynolds-averaged, integral form of the momentum equation for a control volume V, contained by a surface S, in a constant density flow, with mean velocity vector, $\underline{U}$, fluctuating velocity vector, $\underline{u}'$, and mean pressure P.

$$\int_S \rho_\infty \underline{U}\,\underline{U}\cdot d\underline{S} = -\int_S P d\underline{S} + \int_S (\underline{\underline{\tau}} - \rho_\infty \overline{\underline{u}'\underline{u}'})\cdot d\underline{S} + \int_V \rho_\infty \underline{f} dV + \underline{J} \qquad (F.1)$$

The outward-directed area element is $d\underline{S}$, the fluid density is ρ_∞, the viscous stress tensor is $\underline{\underline{\tau}}$, and $\underline{J}$ is sum of any momentum sources within V. The body force, assumed to be steady, is denoted by $\underline{f}$. The overbar represents a time average.

For an infinite medium in the absence of any momentum sources, the fluid will be still and Equation (F.1) will reduce to:

$$-\int_S P_o d\underline{S} + \int_V \rho_\infty \underline{f} dV = 0\,, \qquad (F.2)$$

where P_o is the pressure distribution when the velocity is everywhere zero. Subtracting Equation (F.2) from Equation (F.1) eliminates the

body-force term at the expense of introducing P_o in the pressure integral.

$$\int_S \rho_\infty \underline{U}\,\underline{U}\cdot d\underline{S} = \int_S (P_o - P)\, d\underline{S} + \int_S (\underline{\underline{\tau}} - \rho_\infty \overline{\underline{u'}\,\underline{u'}})\cdot d\underline{S} + \underline{J} \qquad (F.3)$$

Now represent the jet by a single point source of momentum of magnitude J_o placed inside V. Choose V to be a spherical volume of radius R centered on the point momentum source, and introduce spherical coordinates with the polar axis aligned with the direction of momentum input, radial coordinate r, and polar angle θ. The polar axis will be called the x-axis, to be consistent with the rest of this manuscript.

Before proceeding further, it is necessary to estimate the importance of some of the terms on the right side of Equation (F.3). A Reynolds number can be formed for the flow from J_o, ρ_∞, and ν_∞, the kinematic viscosity of the fluid.

$$Re = \frac{\sqrt{J_o/\rho_\infty}}{\nu_\infty} \qquad (F.4)$$

For high Reynolds numbers, the turbulent stress will dominate the viscous stress, so $\underline{\underline{\tau}}$ will be dropped from the last integral in Equation (F.3). As R is increased, the pressure integral and the turbulent stress integral are expected to be, at most, constant. The absolute magnitude of these constants should depend on the value of Re, since the two integrals are zero when Re is zero. If the pressure and turbulent stress integrals are divergent for increasing R, then an infinitesimal force could be seen to cause unbounded pressure forces or

velocity fluctuations. The component of Equation (F.3) in the x-direction can now be written:

$$\int_0^{\pi} \rho_\infty (U_r^2 \cos\theta - U_r U_\theta \sin\theta) 2\pi R^2 \sin\theta d\theta = J_\infty \quad \text{for} \quad R \to \infty , \qquad (F.5)$$

where the x-components of the constants from the pressure and turbulent stress integrals have been combined with J_o and given a new name J_∞. This new constant represents the total amount of momentum transferred to the fluid in the far field of the jet by mean momentum transport, pressure forces and turbulent momentum transport. The exact relationship between J_o and J_∞ will depend on the Reynolds number. The symmetry of the boundary conditions insures that there will be no mean angular momentum in the flow, so the mean azimuthal velocity must be zero.

At high Reynolds numbers, the dissipation rate of kinetic energy into heat provides a clue about the evolution of the velocity profile. The energy dissipation rate is always positive and all of the energy in this flow is produced at the origin through the work done by the momentum source. A consequence of these facts is that the mean kinetic energy flux crossing the surface S will decrease as R increases. In particular, this means that the peak values, and widths of the parts of the profiles of U_r and U_θ which contribute positively in the integration specified by Equation (F.5), will increase and decrease, or decrease and increase, respectively, with increasing r in a manner that maintains the validity of Equation (F.5) and allows for the effects of the energy dissipation rate.

A form of the mean radial velocity profile that allows for these variations with r is:

$$U_r(r,\theta) = \frac{1}{b(r)} G[a(r)\theta] , \tag{F.6}$$

where a(r), b(r) and G are unknown functions. Substituting this in the Reynolds-averaged integral form of the continuity equation, i.e.

$$\int_S \rho_\infty \underline{U}\cdot d\underline{S} = 0, \tag{F.7}$$

yields:

$$\frac{2\pi\rho_\infty R^2}{b(R)} \int_0^\pi G[a(R)\theta]\sin\theta d\theta = 0. \tag{F.8}$$

To learn something about a(r), assume that the factor outside the integral in Equation (F.8) is not equal to zero, divide it out, and replace $a(R)\theta$ in the integral by v. The result is:

$$\frac{1}{a(R)} \int_0^{\pi a(R)} G(v)\sin\left(\frac{v}{a(R)}\right) dv = 0. \tag{F.9}$$

In the integrand, the sine function is always positive-definite regardless of the value of a(R). This forces G(v) to contribute exactly the correct amount of positive and negative value over an interval in v that varies with a(R). This is impossible for $G \neq 0$, so a(R) must be a constant function, independent of R. Replacing a(r) by a constant in Equation (F.6) and absorbing the constant into the unknown function G simplifies the assumed form for the mean radial velocity profile to:

$$U_r(r,\theta) = G(\theta)/b(r). \tag{F.10}$$

If this decomposition of variables is also valid for the mean angular velocity, the radial dependence of the integrand in Equation (F.5) can be determined from a simple argument: The surface area of the integration in Equation (F.5), like R^2, increases and the total value of the integral remains equal to J_∞; therefore, the integrand must decrease like $1/R^2$. In mathematical notation, this conclusion looks like:

$$U_r^2\cos\theta - U_r U_\theta \sin\theta \sim F(\theta)/R^2 \quad \text{for} \quad R \to \infty, \tag{F.11}$$

where $F(\theta)$ is an unknown function such that:

$$\int_0^\pi \rho_\infty F(\theta)\, 2\pi \sin\theta d\theta = J_\infty . \tag{F.12}$$

Equation (F.11) can be further decomposed to:

$$U_r^2 \sim g^2(\theta)/R^{2\xi} + F_1(\theta)/R^2 \quad \text{for} \quad R \to \infty \tag{F.13a}$$

$$U_r U_\theta \sim g^2(\theta)\cot(\theta)/R^{2\xi} + F_2(\theta)/R^2 \quad \text{for} \quad R \to \infty, \tag{F.13b}$$

where $\xi < 1$, $g(\theta)$ is an unknown function and

$$F_1(\theta)\cos\theta - F_2(\theta)\sin\theta = F(\theta). \tag{F.14}$$

Equations (F.13a and b) allow for the possibility that there is a common component in the two terms in the integrand of Equation (F.5), which decays less quickly than $1/R^2$ as R increases.

To leading order, equations (F.13a and b) yield:

$$U_r \sim g(\theta)/R^\xi, \quad \text{for} \quad R \to \infty \tag{F.15a}$$

$$U_\theta \sim g(\theta)\cot\theta/R^{\xi}, \quad \text{for} \quad R \to \infty . \tag{F.15b}$$

If these forms for U_r, and U_θ are checked in the differential form of the continuity equation,

$$\frac{1}{r^2}\frac{\partial}{\partial r}(r^2 U_r) + \frac{1}{r\sin\theta}\frac{\partial}{\partial\theta}(\sin\theta U_\theta) = 0, \tag{F.16}$$

an equation for $g(\theta)$ is produced:

$$(1-\xi)g(\theta) + (\cot\theta)g'(\theta) = 0. \tag{F.17}$$

The solution is:

$$g(\theta) = \text{const}(\cos\theta)^{1-\xi}, \tag{F.18}$$

which yields:

$$U_r \sim \text{const}\, R^{-\xi}(\cos\theta)^{1-\xi} \quad \text{for} \quad R \to \infty \tag{F.19a}$$

$$U_\theta \sim \text{const}\, R^{-\xi}\frac{(\cos\theta)^{2-\xi}}{\sin\theta} \quad \text{for} \quad R \to \infty. \tag{F.19b}$$

While these expressions are mathematically allowed, they are physically unrealistic because U_θ is singular at $\theta = 0$. This implies that Equations (F.15a and b) are an improper form for the velocity field, so the constant of integration in Equation (F.18) must be chosen to be zero. Therefore, each term of the integrand in Equation (F.5) must, like $1/R^2$, decay as R increases since it is physically impossible for a larger common term, that cancels in the subtraction, to exist. This means that the first terms on the right side of Equations (F.13a and b) should be ignored, leaving:

$$U_r \sim \frac{\sqrt{J_\infty/\rho_\infty}\, f(\theta)}{R} \quad \text{for} \quad R \to \infty \tag{F.20a}$$

$$U_\theta \sim \frac{\sqrt{J_\infty/\rho_\infty}\, h(\theta)}{R} \quad \text{for} \quad R \to \infty, \tag{F.20b}$$

where $f(\theta)$ and $h(\theta)$ are related to $F_1(\theta)$ and $F_2(\theta)$ by:

$$f(\theta) = \left(\frac{\rho_\infty F_1(\theta)}{J_\infty} \right)^{1/2} \tag{F.21a}$$

$$h(\theta) = F_2(\theta) \left(\frac{\rho_\infty}{F_1(\theta)\, J_\infty} \right)^{1/2}. \tag{F.21b}$$

Equations (20a and b) describe the self-similarity of the free-jet, mean velocity field for large R. It should be mentioned here that the profile functions, $f(\theta)$ and $h(\theta)$, could depend on the Reynolds number.

In experiments, some type of nozzle with a finite exit area is used to produce the jet flow. Because laboratory jets do not originate from a point source of momentum, the origin of the proper coordinate system for a similarity collapse is not known before the measurements are made. This means that the arguments presented above allow the introduction of a virtual origin, x_0, with respect to the nozzle location to collapse laboratory data properly. In practice, the virtual origin is usually located only a few nozzle diameters upstream or downstream of the nozzle exit.

A second difference between the material in this appendix and real jet flows is that real jets have a nonzero, positive, net mass flux, $\dot{m}_o$. This parameter can be used to create a length scale, d^*, that depends only on the exit parameters of the nozzle:

$$d^* = \frac{2\dot{m}_o}{\sqrt{\pi \rho_\infty J_o}}, \tag{F.22}$$

where the factors of 2 and π have been added to so that d^* reduces to the geometrical nozzle exit diameter for density-matched jet and ambient fluids, and a perfect "top-hat" exit velocity profile. This length scale, d^*, is the proper length scale for normalizing the downstream distance in the jet. It was introduced by Thring and Newby (1953), used by Avery and Faeth (1974) and modified to the present form by Dahm and Dimotakis (1987).

The introduction of $\dot{m}_o$ should not affect the similarity arguments presented above as long as the effects of $\dot{m}_o$ are small in the far field. This idea implies that a definition of the far field for real jet flows could be based on $\dot{m}_o$, J_o, ρ_∞, and R. First, define the mass flux associated with jet flow, ignoring $\dot{m}_o$, at a distance R by:

$$\dot{m}(R) = \int_0^{\theta_m} \frac{\sqrt{\rho_\infty J_\infty}}{R} f(\theta) 2\pi, R^2 \sin\theta d\theta \qquad (F.23)$$

where θ_m is the angle for which $\dot{m}(R)$ is maximum. and Equation (F.20a) has been used for U_r. Note that $\dot{m}(R) \sim R$ as $R \to \infty$, so a practical definition of the far field of the jet can now be stated as the region of the flow where $\dot{m}_o$ is negligible compared to $\dot{m}(R)$:

$$\frac{\dot{m}(R)}{\dot{m}_o} \gg 1, \qquad (F.24)$$

or equivalently, after substitution from Equation (F.23) and recalling that the ratio J_∞/J_o, which depends only on the Reynolds number, is a constant in the far field:

$$R/d^* \gg 1. \qquad (F.25)$$

On the jet centerline this becomes:

$$\chi = (x - x_0)/d^* \gg 1. \qquad \text{(F.26)}$$

The exact point at which Equation (F.24) or Equation (F.25) is sufficiently satisfied for Equations (F.20a and b) to be applied must be determined by experiment.

Whatever the actual threshold may be, the results of the point-source, jet analysis should be valid in the far field of the a laboratory jet. For laboratory jets there are only two small modifications to the results of the present point-source analysis: Equations (F.20a and b) should be set in a coordinate system whose origin is at x_0, and the implied limit for reaching the far field is given by Equation (F.24) or (F.25), instead of just $R \to \infty$.

The results of the point source analysis presented above can also be extended to the case of a free jet in a coflowing stream, at the expense of placing a limit on the downstream range for which Equations (F.20a and b) are valid. Hinze (1975) presents a similar discussion to the one that follows here.

If U_c is a uniform velocity of the entire reservoir in the the direction of the jet's discharge, then Equation (F.5) becomes:

$$\int_0^{\pi} (U_c + U_r\cos\theta - U_\theta\sin\theta)(U_c\cos\theta + U_r)2\pi R^2\sin\theta d\theta = \frac{J_\infty}{\rho_\infty} \text{ for } R \to \infty, \qquad \text{(F.27)}$$

where as before U_r and U_θ are the mean radial and angular velocities

produced by the point source of momentum. If the integral form of the continuity equation in the presence of the uniform coflow,

$$\int_0^{\pi} (U_c\cos\theta + U_r)\, 2\pi R^2 \sin\theta = 0, \qquad (F.28)$$

is multiplied by U_c, and subtracted from Equation (F.27), then Equation (F.29) is obtained.

$$\int_0^{\pi} (U_r\cos\theta - U_\theta\sin\theta)\,(U_c\cos\theta + U_r)\, 2\pi R^2 \sin\theta d\theta = \frac{J_\infty}{\rho_\infty}, \text{ for } R \to \infty \qquad (F.29)$$

If the $U_c\cos\theta$ term in the integrand could be dropped, then Equation (F.29) would be identical with Equation (F.5). This means that Equations (F.20a and b) will hold if:

$$U_r \gg U_c\cos\theta. \qquad (F.30)$$

Using Equation (F.20a) for U_r, and taking $\theta = 0$, Equation (F.30) can be rewritten in terms of J_∞, U_c and the downstream distance:

$$\frac{f(0)}{x - x_0}\,\frac{\sqrt{J_\infty/\rho_\infty}}{U_c} \gg 1. \qquad (F.31)$$

If Equation (F.29) is applied to a laboratory jet and extrapolated back to jet nozzle exit conditions, then the momentum length scale for a coflowing jet, see Equations (A.16) and (A.17), can be substituted into Equation (F.31), to get:

$$\sqrt{\pi/4}\, f(0)\left(\frac{\Theta_c}{x - x_0}\right) \gg 1. \qquad (F.32)$$

Equations (F.30) to (F.32) restrict the downstream distance in the jet for which Equations (F.20a and b) are valid in the presence of a uniform coflow. Appendix A, section 6 contains a discussion of how Θ_c was used

to scale the effects of the coflow for the present study, but it is worth mentioning here that the grouping of terms on the left hand side of (F.32) was greater than 10 for all of the current experiments. As a final comment, it must be recognized that Equation (F.30) must be satisfied in $0 \leq \theta \leq \pi$ for the jet to be completely unaffected by the coflow.

When Equations (F.24) and (F.30) are satisfied, one conclusion concerning the concentration field of the jet can be drawn from Equation (F.23). If the fluid that comes from the jet nozzle carries a conserved passive scalar, then the mean concentration of this scalar within the jet flow must, like 1/R, decrease since the mass flux in the jet increases linearly with R. In terms of the centerline coordinate, $x - x_0$, this implies:

$$< C >_{jet} \sim C_0/(x - x_0) \sim C_0 \chi^{-1}, \quad \chi \gg 1, \qquad (F.33)$$

where C is the mass fraction concentration, the brackets imply averaging across the lateral extent of the jet, and C_0 is a reference concentration. In most experiments, C_0 is chosen to be the concentration of the nozzle fluid at the exit of the jet nozzle.

Experimental verification of the similarity forms presented here can be found in many references, for example Chen and Rodi (1980) and the references cited therein.

REFERENCES

ANTONIA, R.A., ANSELMET, F., and CHAMBERS, A.J. 1986, "Assessment of local isotropy using measurements in a turbulent plane jet," J. Fluid Mech., 162, 365-391.

ANTONIA, R.A., CHAMBERS, A.J., BRITZ, D. and BROWNE, L.W.B. 1986, "Organized structures in the turbulent plane jet: topology and contribution to momentum and heat transport," J. Fluid Mech., 172, 211-229.

AVERY, J.F. and FAETH, G.M. 1974, "Combustion of a submerged gaseous oxidizer jet in liquid metal," Fifteenth (International) Symposium on Combustion, The Combustion Institute.

BATCHELOR, G.K. 1959, "Small-scale variation of convected quantities like temperature in turbulent fluid," J. Fluid Mech., 5, 113.

BECKER, H.A., HOTTEL, H.C. and WILLIAMS G.C. 1967, "The nozzle fluid concentration field of the round turbulent jet," J. Fluid Mech., 30, 285-303.

BIRCH, A.D., BROWN, D.R., DODSON, M.D., and THOMAS, J.R. 1978, "The turbulent concentration field of a methane jet," J. Fluid Mech., 88, 431-449.

BLACKMAN, R.B. and TUKEY, J.W. 1958, The Measurement of Power Spectra (Dover Publications Inc., New York).

BROADWELL, J.E. 1987, "Molecular mixing and chemical reactions in turbulent shear flows," presented at the NATO Advanced Study Institute on Disorder and Mixing at the Institut D'Etudes Scientifiques de Cargese, Corscia, June 12-27. To be published in Disorder and Mixing edited by GUYON, E., POMEAU, Y., CHARLAIX, E. and NADIAL J.P. (Martinus Nijhoff Publishers).

BROWN, G.L. and REBOLLO, M.R. 1972, "A small fast-response probe to measure composition of a binary gas mixture," AIAA Journal, 10(5), 649-652

CHEN, C.J. and RODI, W. 1980, Vertical Turbulent Buoyant Jets: A Review of Experimental Data (Pergamon Press, New York).

CLAY, J.P. 1973, "Turbulent mixing of temperature in air, water and mercury," Ph.D. Thesis, University of California San Diego.

CORRSIN, S. and UBEROI, M.S. 1950, "Further experiments on the flow and heat transfer in a heated turbulent air jet," NACA Report 998.

DAHM, W.A. 1985, "Experiments on entrainment, mixing and chemical reactions in turbulent jets at high Schmidt number," Ph.D. Thesis, Caltech.

DAHM, W.A. and DIMOTAKIS, P.E. 1987, "Measurements of entrainment and mixing in Turbulent jets," AIAA J. 25(9), 1216-1223.

DAHM, W.A., DIMOTAKIS, P.E. and BROADWELL, J.E. 1984, "Non-premixed turbulent jet flames," AIAA paper # 84-0369.

DIMOTAKIS, P.E. 1984, "Lectures in Ae 239: Turbulent shear flows," (unpublished) course lecture notes, Caltech.

DOWLING, D.R., and FRIELER C.E. 1983, "Temperature measurements in a round heated turbulent jet," (unpublished) Ae 104c report, Caltech.

DYER, T.M. 1979, "Rayleigh scattering measurements of time-resolved concentration in a turbulent propane jet," AIAA Journal, 17, 912.

ESCODA, M.C. and LONG, M.B. 1983, "Rayleigh scattering measurements of the gas concentration field in turbulent jets," AIAA Journal, 21, 81.

FISCHER, H.B., LIST, E.J., KOH, R.C.Y., IMBERGER, J., and BROOKS, N.H. 1979, Mixing in Inland and Coastal Waters (Academic Press, New

York).

FRIEHE, C.A., VAN ATTA, C.W., and GIBSON, C.H. 1971, "Jet turbulence: dissipation rate measurements and correlations," AGARD Turbulent Shear Flows, CP-93, pp. 18-1 to 18-7.

GIBSON, C.H. 1968, "Fine structure of scalar fields mixed by turbulence. I. Zero-gradient points and Minimal gradient surfaces," Physics of Fluids, 11(11), 2305-2315.

GIBSON, C.H. 1968, "Fine structure of scalar fields mixed by turbulence. II. Spectral theory," Physics of Fluids, 11(11), 2316-2327.

GIBSON, C.H., FRIEHE C.A., AND McCONNELL, S.O. 1977, "Structure of sheared turbulent fields," Physics of Fluids, 20(10), S157-S167.

HINZE, J.O. 1975, Turbulence, 2nd ed. (McGraw-Hill Book Company, New York), p. 46, pp. 520-523.

JACKSON, J.D. 1975, Classical Electrodynamics, 2nd ed. (Wiley, New York), p. 423.

KOOCHESFAHANI, M.M. 1984, "Experiments on turbulent mixing and chemical reactions in a liquid mixing layer," Ph.D. Thesis, Caltech.

KOLMOGOROV, A.N. 1941, "Local Structure of turbulence in an incompressible viscous fluid at very high Reynolds numbers," Dolk. Akad. Nauk SSSR 30, 299, reprinted in Usp. Fiz. Nauk 93, 476-481 (1967), transl. in Sov. Phys. Usp. 10, no. 6, 734-736 (1968).

KOLMOGOROV, A.N. 1962, "A refinement of the previous hypotheses concerning the local structure of turbulence in a viscous incompressible fluid at high Reynolds number," J. Fluid Mech. 13, 82-85.

KUETHE, A.M. 1935, "Investigations of the turbulent mixing regions formed by jets," Journal of Applied Mechanics, Transactions of the AMSE, Vol. 2, no. 3, 87-95.

LANDAU, L.D. and LIFSHITZ, E.M. 1959, Fluid Mechanics (Pergamon Press, New York).

LANG, D.B. 1985, "Laser doppler velocity and vorticity measurements in turbulent shear layers," Ph.D. Thesis, Caltech.

LIEPMANN, H.W. 1943, "Investigations on laminar boundary layer stability and transition on curved boundaries," NACA report WRW-107.

LIEPMANN, H.W. and ROSHKO, A. 1957, Elements of Gasdynamics (John Wiley, New York), pp. 162-163.

LIU, H.T., LIN J.T., DELISI. D.P., and ROBBEN, F.A. 1977, "Application of a fluorescence technique to dye-concentration measurements in a turbulent jet," NBS special publication number 484 in Proc. Symp. on Flow in Open Channels and Closed Conduits.

LOCKWOOD, F.C. and MONEIB, H.A. 1980, "Fluctuating temperature measurements in a heated round free jet," Comb. Sci. Tech., 22, 63-81.

MASIELLO, J.P. 1974, "Intermittency of the fine-structure of turbulent velocity and temperature fields at high Reynolds number," Ph.D. Thesis, University of California San Diego.

MONIN, A.S., and YAGLOM A.M. 1975, Statistical Fluid Mechanics II (MIT Press, Cambridge), Chapter 8.

NAMAZIAN, M., SCHEFER, R.W. and KELLY, J. 1987, "Scalar dissipation measurements in the developing region of a jet," Sandia report no. SAND87-8652, submitted to Combustion and Flame.

NIWA, C., ICHIZAWA, J., YOSHIKAWA, N., and OHTAKE, K. 1984, "Time-resolved concentration measurements of jets by laser Rayleigh method - Comparison of He, $C0_2$, and CCl_2F_2 jets," Proc. Fourteenth Int. Symp. on Space Technology and Science, Tokyo.

OBOKHOV, A.M. 1962, "Some specific features of atmospheric turbulence," J. Fluid Mech. 13, 77-81.

PAPANICOLAOU, P.A. and LIST E.J. 1987, "Statistical and spectral properties of tracer concentration in round buoyant jets," Int. J. Heat Mass Transfer, 30(10), 2059-2071.

PAPANICOLAOU, P.A. and LIST E.J. 1988, "Investigations of round turbulent buoyant jets," to appear in the Journal of Fluid Mechanics.

PAPOULIS, A. 1984, Probability, Random Variables and Stochastic Processes, 2nd ed. (McGraw Hill, New York), p. 362.

PITTS, W.M., and KASHIWAGI T. 1984, "The application of laser-induced Rayleigh light scattering to the study of turbulent mixing," J. Fluid Mech., 141, 391.

PITTS, W.M. 1986, "Effects of global density and Reynolds number variations on mixing in turbulent axisymmetric jets," NBSIR 86-3340.

PRESS, W.H., FLANNERY, B.P., TEUKOLSKY, S.A., and VETTERLING, W.T. 1986, Numerical Recipes (Cambridge University Press, New York), pp. 417-419.

REICHARDT, H. 1964, "Turbulenten Strahlausbreitung in gleichgerichteter Grundstromung," Forsh. Ing.-Wes, 30, 133-139; topic developed in: Zur Problematik der turbulenten Strahlausbreitung in einer Grundstromung, Mitt. MPI und AVA, Gottingen, Nr. 35, 1965.

REID, R.C., PRAUSNITZ, J.M., and SHERWOOD, T.K. 1977, The Properties of Gases and Liquids, 3rd ed. (McGraw-Hill Book Company, New York), p. 554.

RICOU, F.P., and SPALDING, D.B. 1961, "Measurements of entrainment by axisymmetrical turbulent jets," J. Fluid Mech. 11, 21.

ROBBEN, F.A., LIN J.T., DESILI, D.P. and LIU H.T. 1976, "Feasibility study of a dye-fluorescence technique for measuring concentrations in fluids," Flow Research Note No. 91, Flow Research Inc.

RUDEN, P. 1933, "Turbulente aurbreitungsvorgange im freistrahl, Die Naturwissenshaften," Jahrg. 21, Heft. 21/23, 375-378.

SCHLICHTING, .H. 1979, Boundary Layer Theory (McGraw-Hill Book Company, New York), p. 240.

TAYLOR, G.I. 1938, "The spectrum of turbulence," Proc. Roy. Soc. Lon., A164, 476-490.

TENNEKES, H. and LUMLEY, J.L. 1972, A First Course In Turbulence (MIT Press, Cambridge Mass.), p. 95.

THRING, M.W. and NEWBY, M.P. 1953, "Combustion length of enclosed turbulent jet flames," Fourth (International) Symposium on Combustion, The Williams and Wilkins Co., p. 789.

TOWNSEND, A.A. 1976, The Structure of Turbulent Shear Flow, 2nd ed. (Cambridge University Press, Cambridge).

WEDDELL, D.S. 1952, in Hottel, H.C., "Burning in laminar and turbulent fuel jets," Fourth (International) Symposium on Combustion, The Williams and Wilkins Company, p. 97.

WELCH, P.D. 1967, "The Use of Fast Fourier Transform for the Estimation of Power Spectra: A Method Based on Time Averaging Over Short, Modified Periodograms," IEEE Transactions in Audio Electroacoustics, AU-15, 70-73.

WHITE, F.M. 1974, Viscous Fluid Flow (McGraw-Hill Book Company, New York), pp. 505-510.

WIENER, N. 1949, Extrapolation, Interpolation, and Smoothing of Stationary Time Series (Technology Press, MIT & John Wiley).

WILSON, R.A.M. and DANCKWERTS, P.V. 1964, "Studies in turbulent mixing - II, A hot air jet," Chem. Engr. Sci., 19, 885-895.

WYGNANSKI, I. and FIEDLER, H.E. 1969, "Some measurements in the self-preserving jet," J. Fluid Mech. 38, 577-612.